UNIVERSITY OF GHANA

# DETERMINATION OF GOLD MINERALIZATION TRENDS AND PATTERNS IN THE KIBI GOLD ZONE, GHANA

A thesis submitted to University of Ghana, Department of Earth Science

in Partial Fulfillment of the Requirements for the Degree of Doctor of Philosophy (PhD) in

Earth Science.

BY

Michael Kwasi Dwumfuor

Index No. 10440121

October 2023

# DECLARATION

This is to certify that this thesis is the result of research undertaken by Michael Kwasi Dwumfuor (Index No. 10440121) towards the award of the PhD in Earth Science in the Department of Earth Science, University of Ghana.

Signature ………………………………… Date 13/01/2025………
Michael Kwasi Dwumfuor (10440121)
(STUDENT)

Signature ………………………………… Date 13: 01: 2025………
Prof. Prosper Mackenzie Nude
(Principal supervisor)

Signature ………………………………… Date 13\01\2025……
Prof. Johnson Manu
(Co-supervisor)

Signature ………………………………… Date 13|01|2025……
Prof. Frank Kwakye-Nyame
(Co-supervisor

# ABSTRACT

Kibi gold deposit shares similarities with several known gold deposits in Ghana, however, it has not attracted the desired attention from researchers and explorers. Most of the available data and reports produced by these explorers are not well documented. This study sought to unravel the gold mineralization trends of the ill–defined Kibi gold zone at the northern part of the Kibi-Winneba belt in Ghana using litho-structural mapping, geophysical, petrographical and geochemical datasets for effective exploration and exploitation designs. Airborne magnetic, ground resistivity and induced polarization datasets were processed to interpret the geology and estimate the depth to basement of magnetic source in the area. . Thin and polished section petrographic assessment of modal and ore minerals respectively were determined on representative samples. Major and trace element composition of selected representative rock samples were determined by X-ray fluorescence (XRF) and gold contents were determined by fire assay-atomic absorption spectrometry (FA-AAS). The Kibi gold district is underlain by deformed and altered schist, sodic greywacke, andesitic tuff (volcaniclastic rock) and basaltic to alkali basalt which is faulted to form hanging and footwall mafic volcanic rocks. The majorgeological structures observed in the area are lineation, foliations, folds, fractures/joints, faults, shear zones and quartz veins. These structures represent at least three major deformation events, namely D1, D2 and D3. D1 compressional deformation resulted in NNW-SSE oriented sub-horizontal foliations and stretching lineation, as well as E-W trending tight-isoclinal recumbent folds. The D2 compressional event created regionally and locally oriented dextral shear zones trending NE-SW, as well as NE-SW trending asymmetric to upright open folds. Gold mineralization is associated with D2 structures. The linear features in the area generally trend NW-SE, E-W and NE-SW and are occasionally dissected in several sections by NW-SE (T1) and NE-SW (T2) mafic dykes and north-south fractures (F1). D3 represents splays of D2.

Hydrothermal alteration along quartz-carbonate veins varies greatly, typified by strong silicification, sulphidization, carbonatization, albitization, and sericitization. This is also linked to dispersed pyrrhotite, pyrite, and arsenopyrite (+/- sphalerite) as well as patchy to ubiquitous sulphidization. Gold mineralization is both hosted as quartz-bearing veins and disseminations in the metasedimentary rocks with quartz veins or as disseminated in wall rocks without quartz veins. The mineralization is characterized by ore mineral assemblage which consists of pyrite, chalcopyrite, magnetite in veins; magnetite, tourmaline and micron-sized sulphides in metasedimentary rocks. Pyrite is the main pathfinder mineral for gold even though chalcopyrite, sphalerite, rutile, haematite, magnetite, pyrrhotite and molybdenite are good indicators. Gold is associated with 2nd generation pyrite which is fractured and has sieve texture. The main pathfinder elements for gold in the Kibi area are Ag and As. Alteration styles in the area include albitization, carbonatization, sericitization, silicification and sulphidization. The andesitic tuff samples are peraluminous and tholeiitic and the occurrence of calc-alkaline basalt and ocean-floor basalt indicate possible subduction-related magmatism in a volcanic arc environment. Detritus of the sodic greywackes are mafic to intermediate composition and derived from an oceanic island arc provenace. Basaltic to alkali basalts are predominantly metaluminous and derived from volcanic arc-related lavas. The calc-alkaline nature of the hanging wall suggests subsequent metasomatism that resulted in the emplacement of gold. The arc-related signatures suggest a compressive domain, which can be attributed to orogenic events that might have created pathways for the emplacement of the gold. The composition of host rocks, alteration patterns, structural control and ore paragenesis suggested an orogenic metamorphic (transitional mesothermal-epithermal) gold-type mineralization in the Kibi Gold Zone.

# DEDICATION

I dedicate this piece of work to my Dad and Mum and all my lovely siblings. I say thank you.

# ACKNOWLEDGEMENT

First and foremost, I give thanks to the almighty GOD for guiding and giving me the gift of life and strength throughout my project period. My gratitude and appreciation goes to my parents for their infallible financial support, moral training and parental instinct which have made me who I am now. Special thanks go to my supervisors, Prof. P.M. Nude, Prof. F. Nyame and Prof. J. Manu for their continual guidance, encouragement and advice. Again, I thank all the lecturers in my department for imparting knowledge, advice and encouragement.

Finally, to all my coursemates and Christian brothers, I say thank you.

## TABLE OF CONTENTS

# LIST OF TABLES

# TABLE OF FIGURES

# CHAPTER ONE

# INTRODUCTION

## 1.0 Background of the study

Ghana is rated tenth in the world for exportation and production of gold (Koranteng, 2019). It is also the leading producer of gold (4.8 Moz) on the African continent, ahead of South Africa (4.2 Moz), with a volume reserve of 8.74 metric tonnes from 2015 to 2020. South-western Ghana is regarded as one of the most prolific regions for gold exploration, with gold making up 90% of the country's total mineral exports. In 2020, gold production to Ghana's gross domestic product (GDP) was around 6 billion U.S. dollars. However, the highest contribution of gold to GDP recorded in 2018 was approximately 9.5 billion Ghana cedis (Aryee, 2020). The complexity of geological structures hosting this gold boom is linked to the Eburnean orogeny (ca. 2.1-1.9 Ga) (Smith et al., 2016).

Griffis et al. (2002), are of the view that the majority of gold produced in Ghana is from the Birimian in the southern margin and it occurs in three main styles:

i. Alluvial deposits occurring in river valleys.
ii. Shear zone-hosted hydrothermal mineralization.
iii. Granitoid-hosted hydrothermal mineralization.

The alluvial gold deposits occur in most river valleys meanwhile, the main source of gold is accounted for by the larger hydrothermal style of gold mineralization (Kesse, 1985). The shear zone-hosted hydrothermal gold mineralization on regional and local scales is controlled by major deformational structures, with imprints extending from shallower (~5km) to deeper (>15 km) depth on the cratonic scale. Deeper structures, such as faults and shear zones, acted as conduits for auriferous mineralized fluids with high gold concentrations to advect upward to form gold deposits in second and third - order structures or fractured rock units in basins and belts (Masurel et al., 2022). Granitoid-hosted gold mineralization in the Birimian has often been associated with chemical and mineralogical alteration of the host rock. Albitization, carbonatization, sericitization, silicification and sulphidization are major alteration styles resulting from mineralized fluid interactions with host rocks as the fluids migrate through structural conduits in the rock before crystallization (Deksissa and Koeberl, 2004).

Previous workers (Boadi et al., 2022; Yiridomoh, 2001, Barenblitt et al., 2021) are of the view that to meet the gold demand and production for the year 2021 and beyond, a continuous search for new potential gold targets is required. The advanced development in GIS allows for more reliable and cost-effective methods of combining geoscience data sets to map new potential zones. The use of GIS-based geoscience integration to predict possible mineralized zones in Ghana is gaining recognition. In the areas where it has been implemented, the approach was successful, for example in the Ahafo Gold District of the Sefwi greenstone belt, Newmont Ghana applied this principle to define areas that might host lode gold mineralization and that eventually led to the discovery of the Subika super gold pit. The technique employed GIS-based weighted overlay, fuzzy overlay, and weight-of-evidence to integrate evidential layers deduced from digital elevation, geological, and geophysical datasets (Nwazelibe et al., 2023). Newmont Ghana used this approach to successfully delineate potential zones for lode gold mineralization that could act as a roadmap for additional research in the study area. Adopting and implementing cost-effective GIS geoscience integration in Ghana has been very critical in mapping prospective zones for exploration purposes (Kreuzer et al., 2019). The advent of efficient and cost-effective exploration, continuous mining production and government support will not only increase gold production levels but will also make it a long-term sustainable endeavor (McFaul et al., 2013).

Exploration based on conventional methods is crucial, but it should be combined with information from related geological, geochemical, mineralogical, geophysical and structural studies (Dzigbodi-Adjimah, 1993). Historically, gold exploration methods have evolved around simple discovery and findings of eluvial and alluvial gold nuggets on surfaces due to the process of physical weathering activities (Ward, 1966; Addo-Fening, 2013). Traditional approaches to mineral prospecting including soil sampling, stream sediment analysis, conventional geological mapping, and drilling have dominated exploration in Ghana for decades, even though some of them have been less successful in areas where bedrock geology is obscured by tropical vegetation, laterite, and thick saprolite soils. Adopting geophysical mapping (e.g., gravity, magnetic, seismic tomography, and magnetotelluric) will suffice for a thorough assessment of deeper subsurface structural architecture (Lowell, 2014).

Exploration success depends on finding targets at depth to meet the demand for mineral resources in the future. This calls for advancements in the detection and interpretation of geophysical, geological, ore mineralogy, and geochemical data. The integration of aeromagnetic geophysical data, satellite imagery, geological and geochemical techniques has made it possible to explore vast geographic areas and is an effective instrument for researching basement faulting (e.g., Qari, 1989; Abdelsalam and Stern, 1999, Volesky et al., 2003; Zouaghi, 2020; Eldosouky et al., 2021).

Although artisanal mining of alluvial and vein gold continues at the northern margin of the Kibi - Winneba belt (study area Figure 1.1), the exact mineralization style of the deposit has not been well understood and documented. Given the economic interest and the importance of gold in the economy of Ghana, there is a need to explore available gold occurrences and place value on the Kibi gold district. The difficulty in doing so can be related to the inadequate geophysical, geological and geochemical data on the gold deposit. It is in this perspective that this research seeks to use geophysical, geological and geochemical characteristics of the host rocks, their structural conditions for the emplacement of gold and the style of mineralization in the Kibi gold district to characterize the potential gold mineralization and deposit type for effective exploration design.

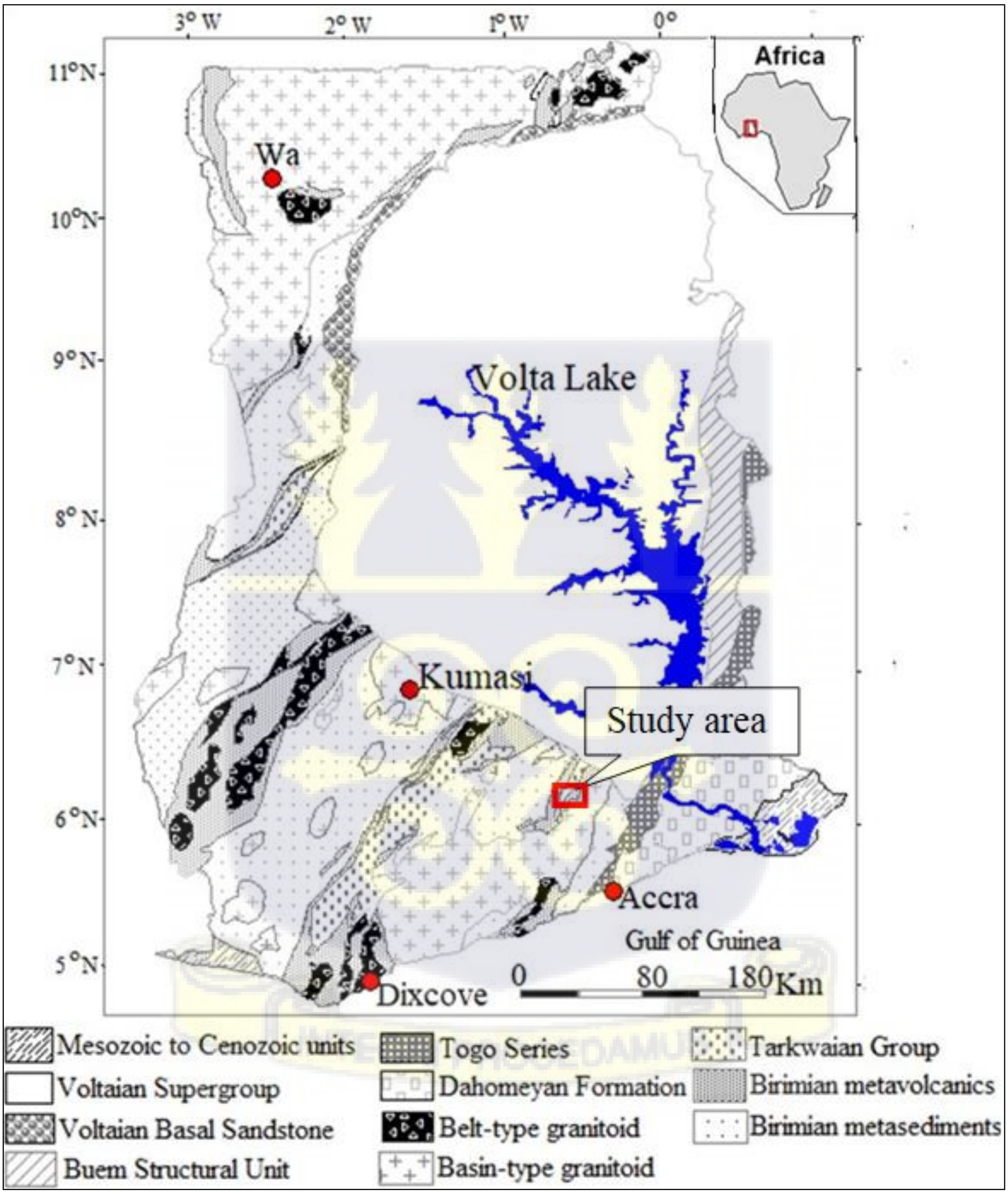

**Figure 1.1: Geological map of Ghana showing the study area (redrawn after Petersson et al., 2018).**

## 1.1. Problem statement

Even though, the Kibi gold deposit shears similarities with several known gold deposits in Ghana such as the: Ayanfuri deposit mined by Perseus Mining Limited, Anyankyerim and Nhyiaso deposits mined by AngloGold Ashanti Ltd., Subika deposit mined by Newmont Mining Limited and Chirano deposit mined by Kinross Gold Corporation (Griffis et al., 2002), it has not attracted much attention from researchers and explorers. Most of the available data and reports of these explorers are poorly documented.

Previous efforts by ancient gold explorers to conventionally exploit the source of the lode gold deposits in the study area were without much discovery success (Technical Report, Xtra Gold Resources Corp, 2012). A London-based junior, Akim Ltd (1928), is known to have carried out some exploration and development work on quartz veins at the Kibi Mine on the outskirts of the town of Kibi, which ended with little economic success. Meanwhile, artisanal miners in the area have been exploiting both alluvial and lode gold deposits for several decades (Technical Report, Xtra Gold Resources Corp, 2012). Previous workers in the Kibi gold district (Boateng et al., 2018; Agyemang et al., 2019; Foli et al., 2020) concentrated on both the alluvial gold deposit and conducted a detailed investigation on the source of the lode gold deposit using conventional and geological methods.

The challenges associated with gold exploration and prospecting in the study area have to deal with the complex geometry of the gold deposit and its narrow nature, subtle mineralogical differences associated with regional and local structures that serve as important markers that may distinguish between barren rock formations and those containing potentially economic ore. Additionally, the geology of the study area is not well understood due to the lack of surface outcrops and the thick vegetation cover of the Atiwa forest (Griffis et al., 1998). These pose a major challenge to the understating of gold mineralization trends and patterns in the area.

Preliminary geological mapping activities conducted in the study area reveal the presence of structurally controlled minor splay-off mineralized features such as dykes and sills of high-grade gold content but sandwiched between major barren faults and shear zones (Technical Report, Xtra Gold Resources Corp, 2012). These structures are difficult to detect by conventional exploration methods. Hence, a multi-stage integral exploration approach using geology, geophysics, geochemistry, and ore mineralogy will lead to a better understanding of the deposit, its structural controls, and the nature of the alteration of host rocks in the study area. According to Kopé et al. (2021), the integration of geological and geophysical gold exploration approaches identified numerous gold-bearing structures in the recent discoveries of the Gara, Kofi, Diambaye I and II, and Fekola gold deposits in western Mali. Also in French Guiana, Combes et al. (2022) employed an integrated approach (geological and geophysical and geochemical studies) in gold exploration and uncovered previously unrecognized target zones within the southern Paramaca Greenstone Belt. Conversely, the complexity of geological structures within the Kibi area might have contributed to the misunderstanding and misclassification of the gold deposit thereby causing huge financial loss to explorers. In light of this, this study seeks to use geophysics, geological, and geochemical exploration surveys to map the gold-bearing structures in the Kibi gold zone and analyze their trends and patterns concerning the various rock types to better understand the deposit. The outcome of this research will help design future exploration programs.

## 1.2. Justification

The benefit of this research will be to provide a well-documented report on the geological structures, geology, and geochemistry of the Kibi gold district, which will help unravel the gold mineralization potential of the area. The results will also provide useful information to mining companies. Airborne geophysics, petrographical, and geochemical exploration surveys can be linked to provide an integrated interpretation that reveals the structural control and hydrothermal alteration of the rocks of mineral deposits. It is evident that most gold mining sites are becoming extinct, hence the need to explore new mineralized zones. The success of this research will also provide a reliable geologic database to improve upon the current geological map of Ghana, add to existing knowledge and create job opportunities that will address sustainable development goals one and nine.

## 1.3. Aim and specific objectives

This research aims to understand the gold mineralization trends and patterns in the Kibi gold district using an integrated approach (geophysical, geological, and geochemical data) for effective exploration and exploitation designs.

The specific objectives are to:

i. Delineate structural lineaments, lithological units and hydrothermal alteration zones within an area.

ii. Determine multi-elemental concentrations and associated alteration patterns in the rock units to identify the possible pathfinder elements associated with gold mineralization in the study area.

iii. Specify the style(s) of gold mineralization in the study area.

iv. Suggest the genesis of the ore-forming fluid in the study area.

v. Propose a genetic model of the mineralization and suggest prospecting guides to circumscribe the primary deposit.

## 1.4. Scope of study

This study primarily elaborates on the structural, lithological and geochemical characteristics of the lode gold deposits in the Kibi gold zone using airborne and ground geophysical data, geological field mapping, petrography, ore mineralogy and whole-rock geochemical datasets. The results from this study will be used to establish the gold mineralization trends and patterns in the Kibi gold zone, Ghana.

## 1.5. Location of the study area and accessibility

The study area covers portions of the Abuakwa South Municipality, Abuakwa North District, Atiwa East District, Kwaebibriem District, Fanteakwa and Fanteakwa South Districts, Denkyembour District, Suhum District and Atiwa West District (Figure 1.2) in the Eastern Region Ghana. It occupies an area of approximately 480 km$^2$, specifically at the northeastern margin of the Kibi – Winneba Belt (Technical Report, Xtra Gold Resources Corp, 2012).

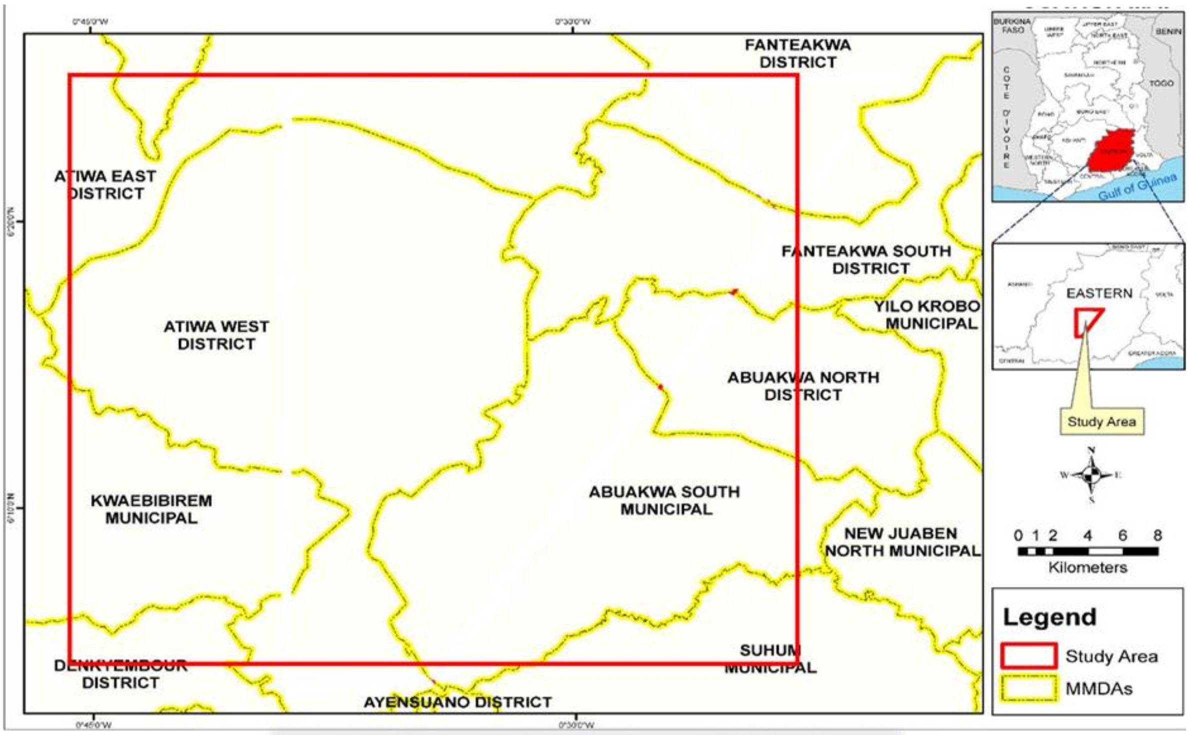

**Figure 1.2: District map of Ghana showing the location of the study area (red rectangle) in the Eastern Region of Ghana (Abuakwa South Municipal Report, 2018).**

Two asphalted secondary highways provide access to the study area from northwest Accra which is the main national highway (Abuakwa South Municipal report, 2018). Moreover, the north-central and south-eastern parts of the Kibi area are linked by a tarred road that branches off of the Accra-Kumasi trunk route about 15 km northeast of Kibi. In contrast, the tarred road servicing the town provides access to the south-western extremity of the study area. During this research, temporary roads were constructed to provide access to the drill sites because of the forested vegetation.

## 1.6. Geomorphology and Vegetation

The topography of the study area is characterized by steep sloping ridges and undulating mountainside hills (Figure 1.3). The NNE-trending Atewa Range, which is about 50 km long and 10-15 km long, also outcrops in the study area. A rich range of high-canopy tropical hardwoods, typical of southwestern Ghana, may be found on the steep slopes, whereas the summit is home to long-hanging vines and other vegetation types. The study area is predominated by relatively mild relief (10–30 m). However, at the base of the Atiwa Range's steep-sided flanks, the relief drastically changes (Technical Report, Xtra Gold Resources Corp, 2012). With a maximum elevation of roughly 780 meters above mean sea level, the Range is significantly higher than the nearby lowlands, which are only 180 to 200 meters above mean sea level. One of the water supplies for the nearby communities is the Birim River, which has its headwaters in the Atiwa Range (Eisenlohr & Hirdes, 1992). Low to thick bushes and deciduous trees with open canopies make up the study area's vegetation. Occasionally, there are pockets of relatively dense primary and secondary forests (Figure 1.3).

**Figure 1.3: Aerial photograph showing the geomorphology and vegetation cover of the Kibi area (study area) (Technical Report, Xtra Gold Resources Corp, 2012).**

## 1.7 Thesis structure

This is how this thesis is organized: Chapter one (1) provides background information on the study and overview of the Kibi – Winneba belt, highlights the problem statement, justification, objectives, scope of work and location of the study area, geomorphology and vegetation of the study area. Chapter two (2) presents information on the literature that was reviewed during this research. Chapter three (3) throws light on the methodology employed for the study and Chapter four (4) presents the results and discussion of the field and laboratory work. Lastly, chapter five (5) indicates the conclusion, recommendations and major findings.

# CHAPTER TWO

# LITERATURE REVIEW

## 2.0. Introduction

This chapter gives an overview of the regional and local geological setting of the study area based on publications. The chapter also looks at the advantages of combining information from geochemistry, petrography, aeromagnetics, and ore mineralogy as a helpful tool for gold mineral prospecting. Several geological, structural, geophysical, geochemical, and mineralogical data must be combined, according to Amer et al. (2012), to explore the upper crust's ore deposits. The chapter goes into more detail about the gold mineralization at the Kibi-Winneba Gold Belt (study area) and goes over important information about Ghana's gold-bearing geological formations.

## 2.1. West African Craton and the Man Shield

The Little Atlas Mountains of Morocco in the north and the Gulf of Guinea in the south make up the West African Craton, which is Archean to Palaeoproterozoic in age. To the west and east, close to Africa's northwest coast, and along the northern portion of the border between Nigeria and Benin, it is bordered by younger mobile belts, respectively. Two supracratonic sedimentary basins are sandwiched between three metamorphic and magmatic shields. The Archean to Palaeoproterozoic Man Shield is in the south, the Palaeoproterozoic Anti-Atlas Belt is in the far north, and the Archean to Palaeoproterozoic Reguibat Shield is in the north (Figure 2.1). According to Ennih and Liégeois (2008), the Taoudeni Basin is situated in the West African Craton's center, whereas the Tindouf Basin is situated in the region's north. The Man Shield is said to be composed of Archean nucleus to the west and Palaeoproterozoic Birimian units in the middle and eastern parts, according to Griffis et al. (2002) and Ennih and Liégeois (2008). The later units, which cover a significant amount of Ghana, Côte d'Ivoire, Burkina

Faso, southern Mali, northern Guinea, and the southwest corner of Niger, are made up of metasediments, metavolcanics, and related intrusive complexes (Griffis et al., 2002).

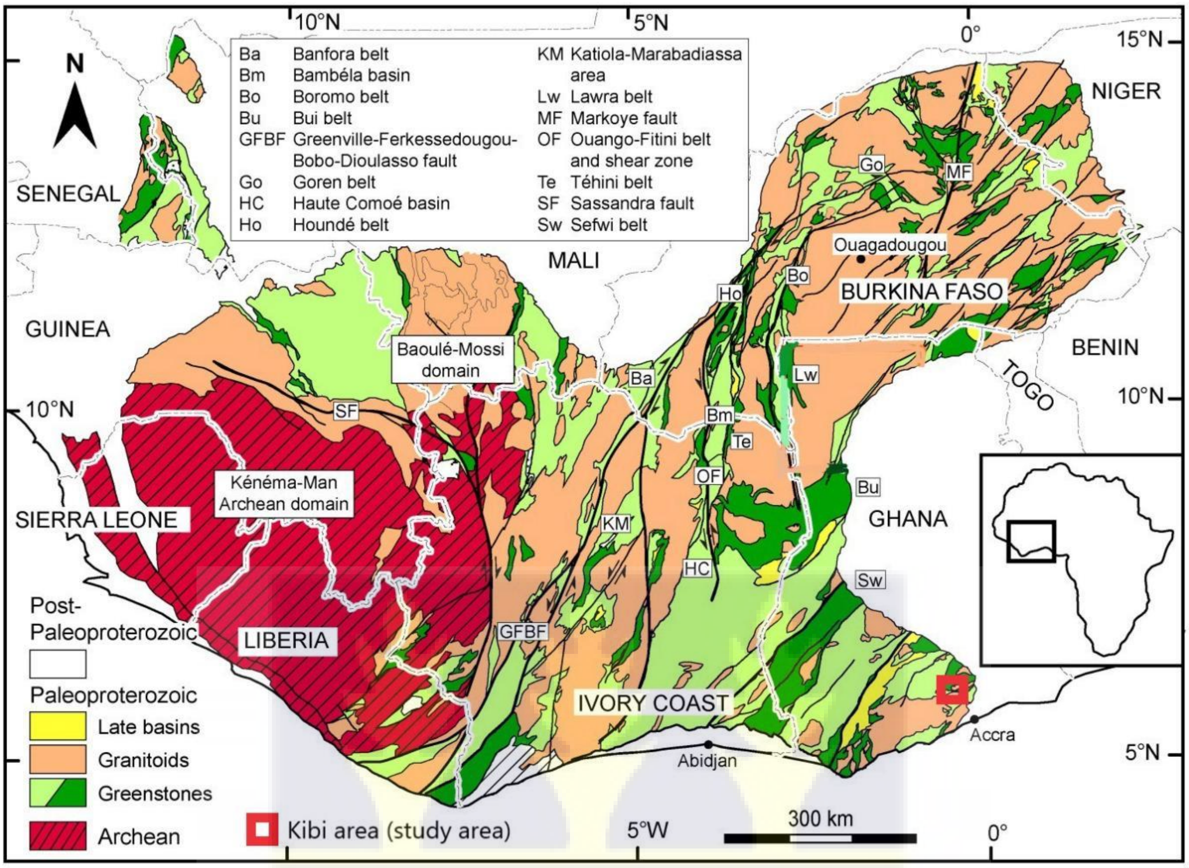

**Figure 2.1: Geological map of the Archean and Paleoproterozoic units of the Leo-Man Shield of the West African Craton (WAC) (after Attoh et al., 2006). Insert (red square) is the Kibi area (study area).**

## 2.2. Regional Geological Setting of Ghana

Metamorphosed clastic sedimentary Tarkwaian Group and volcano-sedimentary Birimian Supergroup rocks from the Palaeoproterozoic (2300-1900 Ma) make up the vast majority of Ghana (Oberthür et al., 1998; Griffis et al., 2002). That makes up the Man Shield (or Leo Shield) in Ghana's West African Craton. The majority of Ghana's gold reserves are located in these units, which will be discussed further. However, some newer geological successions and intrusions are also recognized and briefly addressed, as are various Palaeoproterozoic granitoids, such as mafic intrusions. The Birimian and Tarkwaian units in Ghana have all been metamorphosed to at least lower greenschist facies (Griffis et al., 2002), with local variations in the grade of metamorphism, especially in the presence of granitic intrusions and in higher grade places in some of the northern belts. It has been suggested that in a retrograde assemblage, the metamorphism of the greenschist facies, which was preserved, took place before that of the amphibolite facies (John et al., 1999; Yao & Robb, 2000). Palaeoproterozoic granitoids also have imprinted characteristics such as foliation and mylonitization (John et al., 1999).

### 2.2.1. Birimian Supergroup

Previous scholars had classified the Birimian Supergroup into metasedimentary and metavolcanics groups (Junner 1935, 1940, Griffis et al., 2002; Oberthür et al., 1997). Hundreds of kilometers of greenstone belts (volcanic belts) of the Birimian Supergroup run through the middle of Ghana in a roughly northeasterly direction, while the southern belts reach into the southeast of Burkina Faso and the southwest of Niger. Although the belts are typically 20-70 km wide, they are only 10-20 km wide in northern Ghana (Griffis et al., 2002; Arhin et al., 2015; Nude et al., 2012). Despite the presence of tholeiitic lavas, ultramafic rocks, and andesitic-dacitic, calc-alkaline pyroclastics, the majority of the belt units are composed of dacitic and rhyodacitic lavas (Attoh et al., 2006; Dampare et al., 2008; Berge, 2011). Crossing Ghana from southeast to northwest are the Birimian volcanic bands known as the Kibi-Winneba Belt, the Ashanti Belt, the Manso Nkwanta/Asankrangwa Belt, the Sefwi Belt, the Bui Belt, the Bole-Navrongo Belt, the Wa-Lawra Belt, and the Julie Belt.

Multiple Birimian metasedimentary basins may be found in Ghana, including the Cape Coast Basin in the southeastern corner, the Kumasi and Sunyani Basins in the southwest, and the Maluwe Basin in the west (Figure 2.2). As seen in (Figures. 2.3 and 2.4). South of Ghana, the basins are around 60-70 km broad but shrink as you move north (Griffis et al., 2002). Different lithofacies and depositional settings are found around the margins of the belts and basins. Wacke, turbidite-related facies (lower slopes of volcanic ridges), volcaniclastic/argillite facies (proximal to volcanic ridges), argillite/volcaniclastic facies (distal to volcanic ridges), argillite facies (low energy environments in the central part of the basin), and chemical sediment facies (transition zones between volcanic belts and basins) are all examples.

Birimian volcanic belts likely originated in an oceanic island arc setting (Sylvester & Attoh, 1992; Dampare et al., 2008). To further complicate matters, Feybesse et al. (2006) proposed that plutonic activity and deposition on a continental margin, followed by juvenile basic intrusive and extrusive magmatism, and finally the collision of old continental and juvenile crust, shaped the tectonic environment where the volcanic belts formed. Deposits of Birimian metasediments were thought to have taken place along volcanic ridges and in adjoining basins, and their source has been attributed to nearby volcanic belts (Griffis et al., 2002). Recent work by Brako et al. (2022) proposes that the Birimian metasediments originated from an active continental rift margin, which is consistent with the tectonic setting proposed by Leube et al. (1990). Age constraints from zircons in Birimian Supergroup metavolcanics range from 2162 ± 6 Ma to 2266 ± 2 Ma (Davis et al., 1994; Oberthür et al., 1998; Griffis et al., 2002; Adadey et al., 2009; Loh et al., 2009; Perrouty et al., 2012).

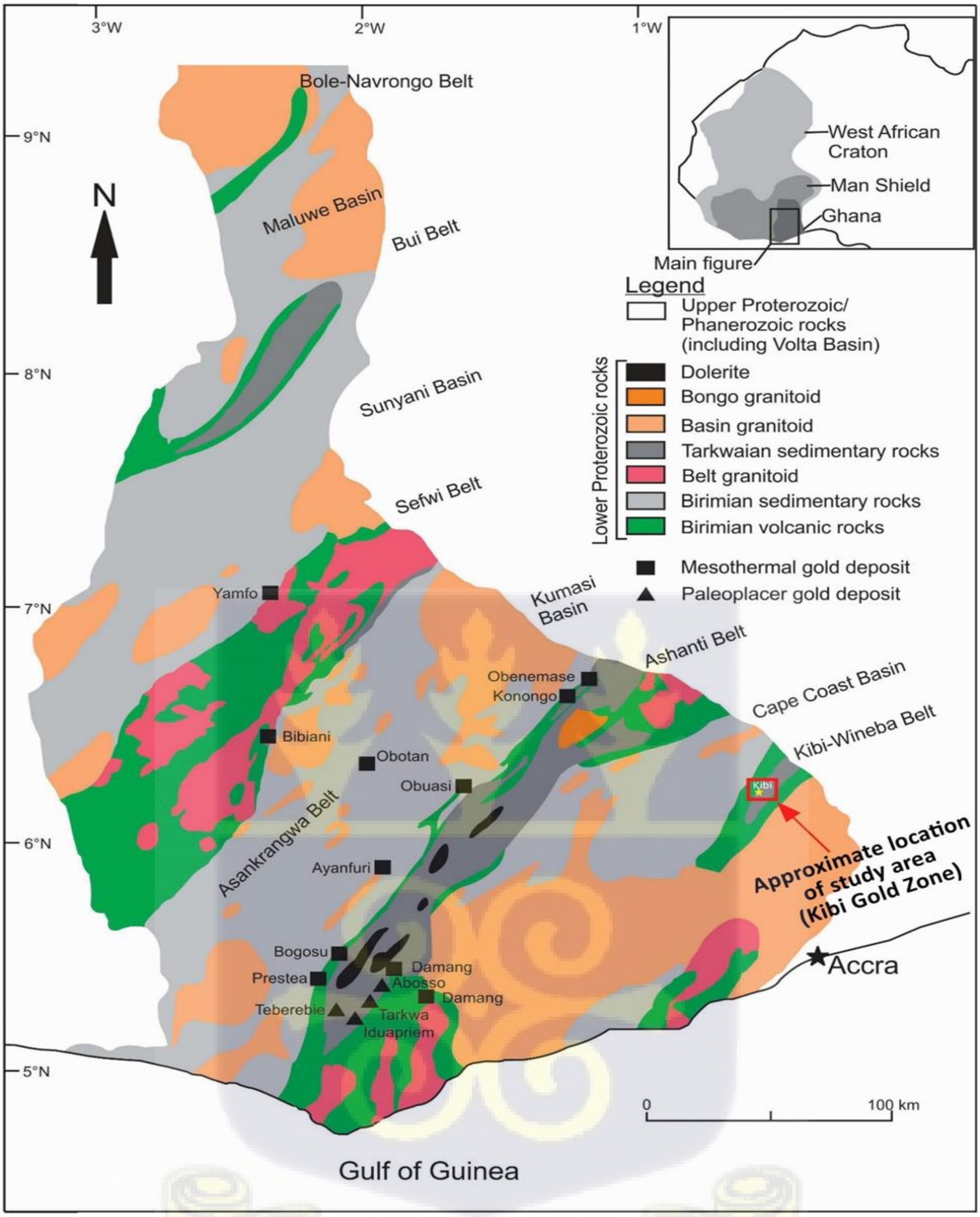

**Figure 2.2: Geological map of southwest Ghana, displaying the gold-bearing belts and the locations of the most famous palaeoplacer and mesothermal gold deposits (after Pigois et al., 2003).**

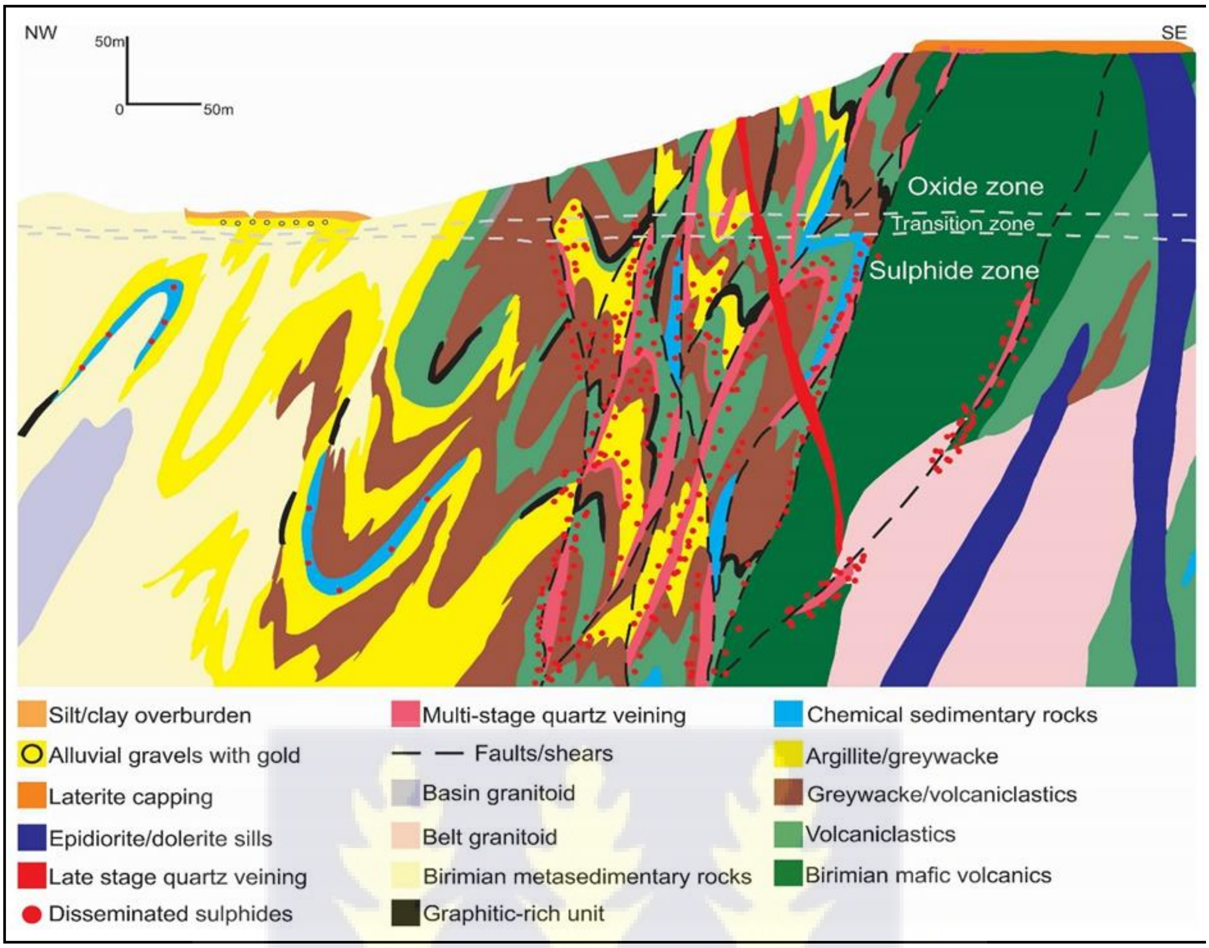

**Figure 2.3: Northwest to southeast schematic cross-section of a typical Ashanti-type, Birimian mesothermal quartz vein and quartz vein-associated sulfide gold deposit (after Griffis et al., 2002).**

### 2.2.2. Tarkwaian Group

Several volcanic belts in West Africa contain sandstones, conglomerates, and argillites similar to those that make up the Tarkwaian Group. In Ghana, the Tarkwaian Group is most advanced in the Ashanti Belt (Figure 2.2), with a thickness of about 2,500 meters, and in the Bui Belt, with a thickness of about 9,000 meters. Furthermore, the Tarkwaian Group is located in the Kibi-Winneba belt, the northern Bole-Nangodi belt and the eastern end of the Sefwi belt (Griffis et al., 2002). Part of the Ashanti belt, the Tarkwaian Group had the form of a long, thin basin with a half-graben at its western fault-bounded contact. Tarkwa phyllite, Banket

Formation, Kawere Formation, and Huni Sandstone are its four major units. The Kawere Group consists of conglomerates and sandstones and has a thickness of 250–700 m. Above it, in the Banket Formation, are interbedded conglomerates and cross-bedded sandstones. The conglomerates are made up of volcanic clasts and quartz pebbles from the Birimian period. The Tarkwa placer gold deposit (a 100 m thick gold zone) is located inside the Banket Formation, which is estimated to have a maximum thickness of 600 m and slopes upward into the Tarkwa Phyllite, which is 400 m thick (Figure 2.4). Kesse (1985), Strogen (1991), Griffis et al. (2002), Pigois et al. (2003), and Perrouty et al. (2012) all describe a series of sandstone that is 1,400 meters thick, interbedded with quartzite and phyllite, and intruded by tiny dolerite sills.

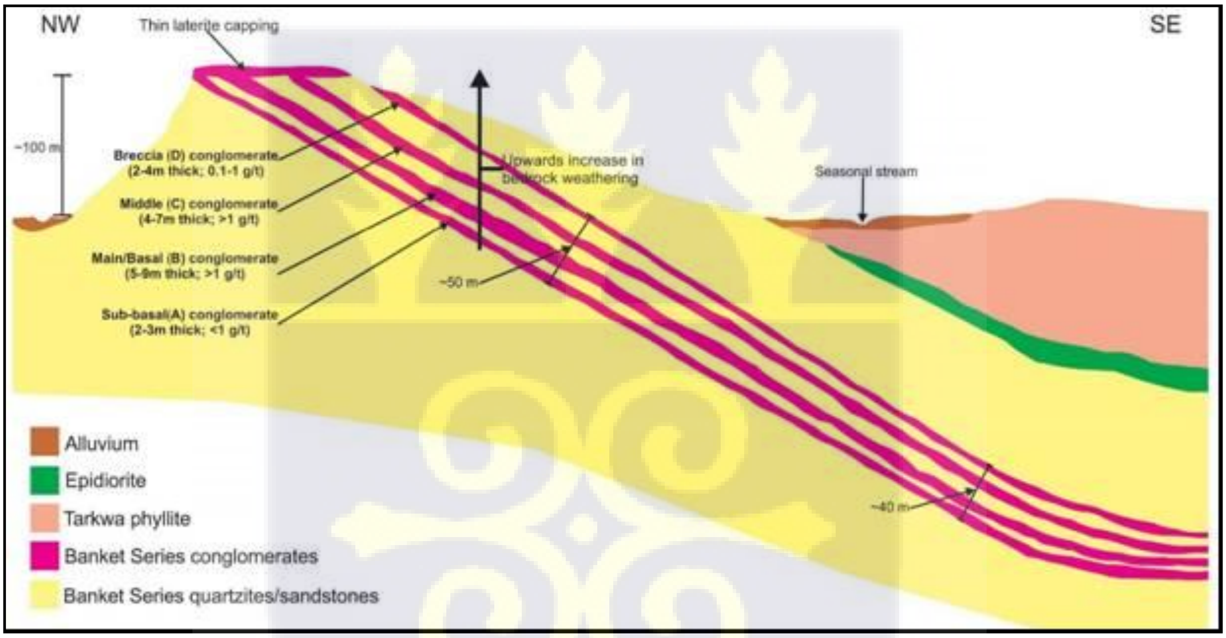

**Figure 2.4: Cross-section of a typical Banket Formation hosted within the Paleoproterozoic Tarkwaian Palaeoplacer gold deposit in the (after Griffis et al., 2002).**

Tarkwaian Group in the Bui Belt includes the Sabiyi cycle, which is about 7,000 meters thick and consists of the Nyanchulo and Tombe Formations, and the Bui cycle, which is about 2,000 meters thick and consists of the Nuapo, Kane, and Mundale Formations, according to Griffis et al. (2002) and Kiessling (1997). Unlike the Sabiyi cycle, which occurs throughout the basin, the Bui cycle is localized to its northern portion. Quartzites form the bedrock in both cycles;

these quartzites coarsen upward to form conglomerates, which are then covered by quartzites that thin upward. The Mundale Formation, composed primarily of siltstone, may be found at the peak of the Bui cycle. The Tarkwaian conglomerates of the Bui Belt are rich in the Palaeoplacer gold mined in Tarkwa (Griffis et al., 2002).

When compared to the underlying Birimian Supergroup sedimentary layers, the depositional setting for the Tarkwaian Group units is strikingly different. As previously discussed, (Sestini, 1973; Kiessling, 1997; Griffis et al., 2002), conglomeratic units from the Tarkwaian Group are hypothesized to have been altered by braided stream channels following their initial deposition in alluvial fans. The latter are speculated to have higher concentrations of fine gold particles within the channel conglomerates. The detrital zircons in the Kawere and Banket Formations (Davis et al., 1994; Hirdes and Nunoo, 1994; Pigois et al., 2003; Perrouty et al., 2012) put a cap on the date at which the Tarkwaian Group may have been deposited. However, based on all available concordant zircon data, Perrouty et al. (2012) determined that deposition may have begun as late as 2107 Ma. Deposition of the Tarkwaian Group is also dated to be between 2102 and 2097 Ma (Adadey et al., 2009; Oberthür et al., 1998; Perrouty et al., 2012) due to the presence of metagabbro sills and granitoids that were pushed into place.

### 2.2.3. Paleoproterozoic intrusions

Ghana is rife with granitoid intrusions that date back to the Paleoproterozoic. There are two recognized types of granitoids: belt-type (also known as Dixcove-type) and basin-type (often known as Cape Coast-type; Yao et al., 2001; Griffis et al., 2002). The belt-type granitoids are I-type granitoids that are fine to medium-grained and older than the basin granitoids (2145-2190 Ma). Volcanic belts are often seen near them. In contrast, the basin-type granitoids intrude into sedimentary basins and can be found in large batholithic complexes (Griffis et al., 2002). These granitoids are younger than the belt-type granitoids (2090-2125 Ma), but they are otherwise similar. Additional traits that differentiate these two granitoids are their distinct mineralogy, geochemistry, contact metamorphism, alterations, and textural features. More information on these features may be found in Yao and Robb (1998) and Griffis et al. (2002). Granitoids can be divided into two economic categories: mineralized and unmineralized (Yao & Robb, 1998; Yao et al., 2001). Paleoproterozoic granitoids have colonized the Birimian volcanic belts and sedimentary basins over northern, western, and southern Ghana (Yao & Robb, 2000).

Mafic intrusives, likely of Paleoproterozoic age, are common in Ghana's volcanic belts, especially the Ashanti and Sefwi Belts (Griffis et al., 2002). They often appear to be younger than the granitoids of the volcanic belt but older than the metamorphism that occurred in the volcanic belt. The two compositional types expected to be most common in places where mafic flows are dominant are later-stage gabbro-dioritic intrusions and sills and feeder dykes with a tholeiitic basalt affinity. Similar mafic intrusions may have occurred in Birimian volcanics and volcaniclastics (Griffis, 1998; Griffis et al., 2002), as well as sills and small dykes intruding Tarkwaian clastic deposits in the Ashanti belt (Griffis, 1998; Griffis et al., 2002). The Mpohor Intrusive Complex, which includes the Mpohor gold mine and is located about 15 kilometers northwest of Takoradi in southwest Ghana, is another example of a bigger complex that combines mafic intrusives. The end of the Eoeburnean magmatic phase has been signaled by the presence of granodioritic, dioritic, and gabbroic compositions in both the Mpohor intrusions and the Ashanti Belt mafic sills (Griffis, 1998; Griffis et al., 2002).

### 2.3. The Pan – African Dahomeyides Belt

South of the Trans-Saharan mobile belt, the Dahomeyides band of Africa stretches for nearly a thousand kilometers from southeast Ghana through Togo, Benin, and Nigeria. There have been two studies on this topic (Attoh, 1998; Attoh & Nude, 2008; Aidoo et al., 2022; Kwayisi et al., 2024). Scientists have hypothesized that the belt is a terrane formed by the Neoproterozoic collision of the West African craton, Congo craton, and Sahara Metacraton continental blocks (Bessoles & Trompette, 1980; Caby, 1987; Affaton et al., 1991; Castaing et al., 1993; Attoh et al., 1997; Liégeois et al., 2003; Nude et al., 2012). As a result of this impact, mega-shear zones developed along the WAC margin. The foreland of the belt, the Volta Basin, is most prominent in Ghana and sticks out from the intersection of the Dahomeyides Belt and the WAC. Dahomeyides belt has a well-organized orogenic architecture (Attoh, 1998; Attoh & Nude, 2008; Castaing et al., 1993) with its primary three litho-structural zones being, from West to East: the Volta Basin; (ii); (iii); (iv); the Suture Zone; and (v); the internal zone, also known as the Benin-Nigerian shield. Interactions with thrust jets separate these regions.

The WAC's deformed edge and the Buem and Atacora units are all consistent with the western outer structural units of the Pan-African Dahomeyides belt. The westernmost unit, the Buem, has been thrust into the Volta Basin. Ancient basement (pre-Neoproterozoic gneisses) and metasedimentary rocks from the WAC passive edge (Affaton, 1990, Attoh et al., 2013) make up both structural units. Mafic volcanics and serpentinized ultramafic rocks, as well as shale, siltstone, arenite, hematitic, and sericite schists, comprise the bulk of the Buem Structural Unit. The metamorphic sediments of the Volta basin, date back to the Neoproterozoic and Proterozoic eons (Attoh, 1998; Attoh & Nude, 2008; Affaton et al., 1991; Castaing et al., 1993; Affaton et al., 1997), are sometimes regarded as the eastern lateral equivalent of these metasediments. Osae et al. (2006) note that the upper and lower parts of the Buem formation are fine-grained quartzite and siltstones, while most of the clastic strata are made up of sandstone and shale. There are two forms of gabbro that form from mafic rocks. The other shows arc symptoms but is sub-alkaline like N-MORB and contains some crustal contamination. In addition to being alkaline, the one has a predilection for OIB/E-MORB

(Attoh et al., 2007; Kwayisi et al., 2022; Nude et al., 2009; Nude et al., 2012; Hammerli et al., 2017). According to Cahen et al. (1984), the average K/Ar age of the volcanic rocks in the Buem structural unit is around 512 Ma. This is similar to the age of 500 Ma discovered in the Dahomeyan basement in the Dahomeyides belt (Grant, 1985; Jones, 1990; Aidoo et al., 2024). Ages of 620 Ma from K/Ar of glauconite and 638 Ma from Rb/Sr of illite (Affaton et al., 1978) and 650 Ma from Rb/Sr of glauconite and 550 Ma from K/Ar of illite (Clauer et al., 1982) are possibly consistent with the age of deposition. Oriented NNE-SSW with an eastward dip, the Atacora Structural Unit consists of metamorphosed greenschist and amphibolite assemblages. The Buem Structural Unit was overthrusted by a sequence of rocks including quartzite and quartzitic sandstone, schists, and phyllite; the sandstones and schists both contain a conglomeratic horizon (Affaton, 1990; Affaton et al., 1991 & 1997; Attoh et al., 1997). The reworked basement complex, dated to 2.1 Ga (Tairou, 2012; Agbossoumondé et al., 2007), is surrounded by the orthogneissic Kara-Niamtougou or Mô Unit, the plutono-metamorphic Palimé-Amlamé and/or Ho Units, and the Sokodé-Kéméni Unit. Radiometric dating of the Atacora rocks only allowed us to establish an age for the Pan-African event. This date is far older than those proposed by Attoh et al. (1997), who suggested that the earliest age of 575 Ma can be linked to the formation of nappes based on 40Ar/39Ar dating of muscovite.

## 2.4. The Voltaian Supergroup

The geological sequence of the Volta Basin is nonconformably located on the southeastern boundary of the WAC. Affaton (1990), Affaton et al. (1991), and Castaing et al. (1993) identified three unconformity-bounded sequences that make up the basin: the Tamale Supergroup, the Oti-Pendjari Supergroup, and the Bombouaka Supergroup. Because the basin stands in for the foreland and the westernmost portion of the belt, the exact lithology of these occurrences is irrelevant to the research. Sandstones and siltstones deposited in deltaic, fluvial, and nearshore or shoreface environments at a depth of 500 meters make up the bottom sequence, also known as the Bombouaka Supergroup (Affaton, 1990; Carney et al., 2010). The Oti-Pendjari Supergroup, which includes the middle series, is composed of wacke-type sandstones and conglomerates, silex, dolomitic limestone, and a series of argillaceous layers (Carney et al., 2010). As it travels about 3-4 kilometers east, this structure thickens and curves forward. According to previous studies (Affaton et al., 1991; Bertrand-Sarfati et al., 1991; Kalsbeek et al., 2008; Carney et al., 2010), the top mega series of the Tamale Supergroup is composed of unusual lithic conglomerates and arenites that were deposited as terrestrial molasse during the terminal stages of uplift in the Dahomeyides belt. The eastern regions of the Bombouaka and Oti-Pendjari supergroups contributed to the Pan-African event by generating rocks in the Meso- to Neoproterozoic (1.1-0.6 Ga) period. The third cluster of rocks was formed between 500 and 300 Ma during the Palaeozoic Era.

## 2.5. Geology of the Kibi-Winneba Belt

Towards the east, the Birimian metavolcanic belts in southern Ghana reach the Kibi-Winneba belt. Many can be found in the prosperous Ashanti Gold Belt, which can be found to the east of Ghana's operational gold mines. Simon et al. (2012) report that the Kibi greenstone belt extends for roughly 60 km and trend northeastward. Its northern extension is covered by younger, flatter layers from the Voltain basin, and its southern end is truncated by huge batholiths of granitoids. The Kibi Belt is composed of a syncline that is heavily folded and slightly inverted, oriented north-northeast (Simon et al., 2012). This syncline comprises a wide range of metavolcanics, mafic intrusions, and metasediments. There appears to be gradual transitions between the Birim River Basin and the Kibi Belt. The majority of the belt's western margin is made up of steeply dipping, heavily deformed, and fractured metasediments with large bands of graphite commonly found (Rae et al., 2006). These feature numerous shallow-level mafic plutons (mainly epidiorites) and are bordered by mafic to intermediate metavolcanic flows, metavolcaniclastics, and metasediments. Lithologies of clastic metasediments, some of which are fairly coarse, are the prominent lithologies in the belt's core, which roughly correlates with the major Birim River valley. Nonetheless, mafic and intermediate to possibly felsic metavolcanic rocks are more abundant and appear to be tilted to the northwest along the peak of the notable Apedwa hills on the eastern side of the belt (Rae et al., 2006).

Well-recognized are the late Eburnean granitoid batholiths that separate the Kibi Gold belt and the Winneba belt into two distinct volcanic belts to the southwest of Cape Coast (Griffis et al., 2002). Due to its limited exposure, poor government survey mapping, and lack of exploration, the geology of the Kibi Gold Belt is less well understood than that of other Birimian greenstone belts in Ghana (Simon et al., 2012). The Atewa Range, which dominates the region's terrain and features high cliffs and a relief of about 500 m with the surrounding valleys and a flat peak that rises to an elevation of roughly 780 m above sea level, is the most prominent physical feature. The Atewa Range is supported by Birimian rocks that trend northeast to southwest (Figure 2.5), and these rocks include greenstones (altered basalts and andesites), phyllites, meta-tuffs, epi-diorite, meta-greywacke, and chert. Thick metasedimentary strata of greywacke, argillite, and phyllite surround large valleys. Birimian metasediments and metavolcanic rocks were first deposited in the far northwest of the Atewa Range (Simon et al., 2012). Regional traverses and airborne geophysical data show that volcaniclastics are widely dispersed, with mafic flows and sills confined to more specific zones. Numerous minor, radiometrically inferred intrusive plutons of the Belt type appear to be scattered across the belt, while numerous northeast-elongated intrusive bodies of the Basin type are inferred inside the metasediments along the belt's western margin.

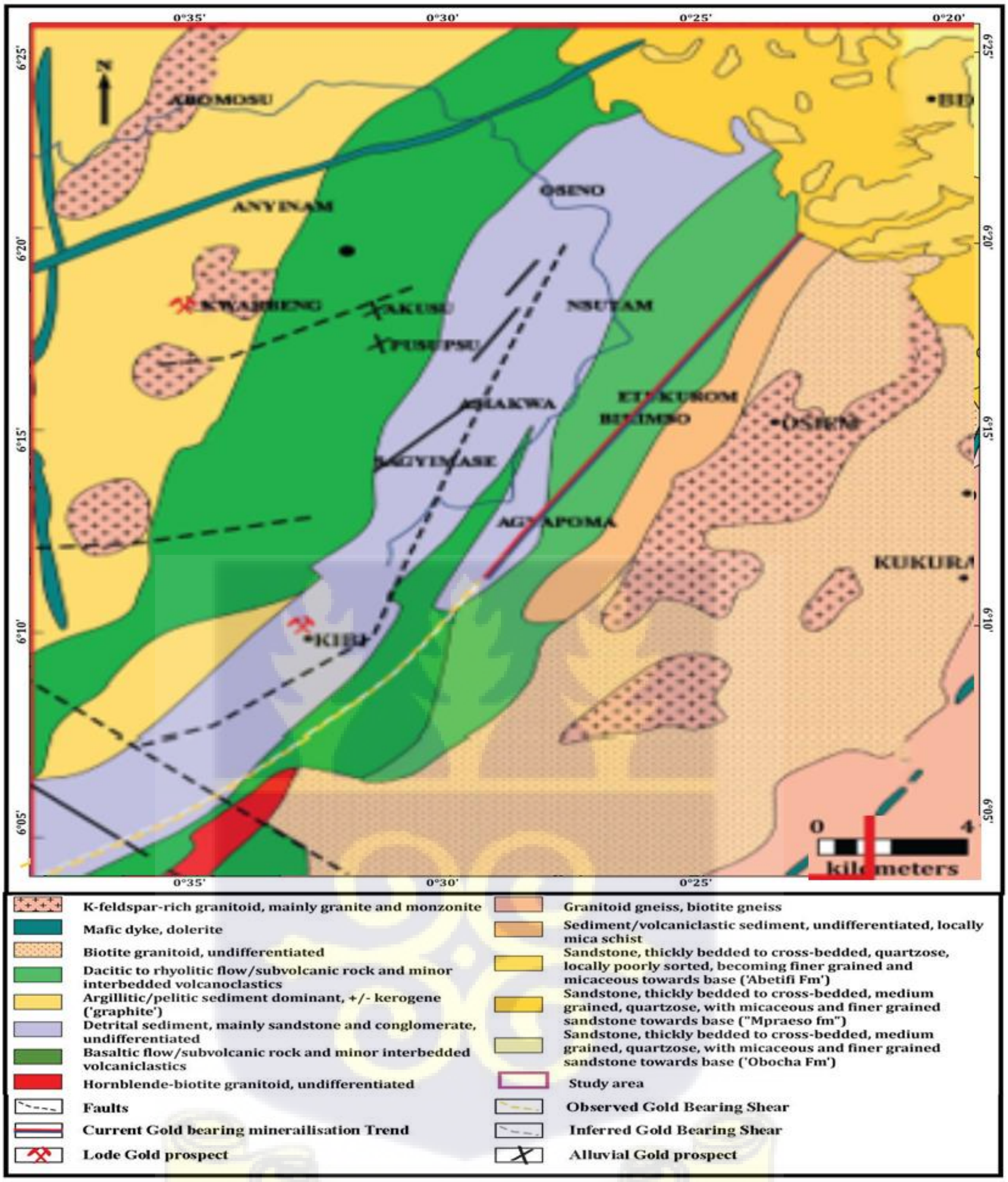

**Figure 2.5. Geological map of the Kibi gold zone of the Kibi-Winneba belt (after Pigois et al., 2003)**

While most Basin-type granitoids are granodioritic to granitic, Belt-type granitoids range from dioritic to granodioritic. Belt-type granitoids, in contrast to the Basin granitoids, were deposited earlier as subvolcanic plutonism (Hirdes et al., 1992). This occurred before the onset of the Eburnian Orogeny, at 2116 Ma. The belt appears to have numerous regional NE-trending structures, as inferred from topographic patterns and aircraft geophysical data. Many of the major valleys on the Atewa Range's flanks are intersected by other geological features. The presence of large alluvial gold deposits in valleys near some of these postulated structures may be indicative of primary lode gold sources. According to models developed by Eisenlohr et al. (1992), the syn-depositional belt is an antiformal structure that has folded in on itself, with a significant reversal fault (dipping northwest) on the eastern side of the range.

### 2.5.1. Deformational history of the Birimian Belts

In Ghana's Birimian belts, the distribution of gold mineralization appears to be largely governed by deformational structures, notably in the case of mesothermal gold mineralization (Griffis et al., 2002). The majority of Ghana's gold deposits are housed by the Birimian Supergroup and Tarkwaian Group, which contain a typical northwest-to-southeast cross-section of a Banket Formation-hosted Tarkwaian Palaeoplacer gold deposit (Griffis et al., 2002). The Eburnean orogeny can be used to explain its various deformational occurrences (Perrouty et al., 2012). This may be seen especially clearly in the southwest Ghanaian Ashanti Region, where six deformational occurrences (marked D1 to D6) have been recorded (Perrouty et al., 2012; 2015):

- Before the Tarkwaian Group's development, the D1 event, also known as the Eoeburnean deformation event, caused regional scale folding in the Sefwi Group's metavolcanics through north-south compression. Also introduced between 2187 and 2158 Ma were D1 synorogenic granitoids.

- The D2 event, an extensional phase, made the Kumasi and Akyem basins accessible, where the Kumasi Group was deposited. On the western border of the Ashanti Belt, the Sefwi and Kumasi Groups converge at the Ashanti Fault.
- The D3, or Eburnean event, is defined by large folds that resulted from northwest-southeast compression within the Birimian and Tarkwaian groups.
- Small-scale shear zones on the western Ashanti Belt that intersect the D3 folds are an indication of the D4 event. It also led to the reactivation of the splays of the Ashanti Fault. A fold at the Wassa gold mine has been identified as being related to the D4 incident. The D3 and D4 events are thought to have happened at the same time as the Eburnean magmatic phase.
- The D5 event is characterized by small-scale (1 cm to 5 m) open to tight, symmetrical recumbent folds with a subhorizontal crenulation cleavage.
- Open folds with a sub-vertical crenulation cleft are what are known as D6 events.

Amponsah et al. (2015) speculated that other gold-bearing belts in Ghana display analogous deformational events even though these deformational events for the Ashanti belt are fully reported. Three deformational events (named DW1-DW3) have been found in the Wa-Lawra Belt in northwest Ghana, for instance. The causes of the DW1 event were north-south crustal compression, the DW2 event was north-south extension and exhumation of high-grade terranes, and the DW3 event was steeply dipping northeast-northeast- and northwest-trending shear zones.

The Julie deposit, a component of the Julie Belt in northwest Ghana, has three deformational events (DJ1-DJ3) as well. The Wa-Lawra belt's DW1 and DW3 events, respectively, equate to DJ1 and DJ2 (Amponsah et al., 2016). Brittle faulting with a northeast to southwest orientation is what defines the DJ3 occurrence (Amponsah et al., 2016).

The Wa-Lawra Belt's DW1 and DW2 events, as well as the Julie Belt's DJ1 events, are likely to correspond to the Ashanti Belt's D1 and D2 events, according to Amponsah et al. (2016). The Wa-Lawra and Julie belts' DW3 and DJ2 events are comparable to the D3 and D4 events of the Ashanti belt. Additionally, the D4 event of the Ashanti Belt can be related to the DJ3 event. Therefore, it would seem that at least the D1 to D4 episodes identified for the Ashanti belt are typical of the gold-bearing Birimian belts in southwestern, western, and northwestern Ghana.

### 2.5.2. Geological setting and description of main gold mineralization types in Ghana

According to Griffis et al. (2002), there are five distinct types of regional gold occurrences in West Africa. For example, there are mesothermal gold-quartz vein deposits, as well as mesothermal auriferous arsenopyrite and quartz vein mineralization (also known as mesothermal quartz vein and quartz vein-associated sulfide type mineralization). In Ghana, the two most important types of gold occurrences are the Tarkwaian Palaeoplacer type, which is located in the Tarkwaian Group levels, and the mesothermal quartz vein and quartz vein-associated sulphide type mineralization, which is located in the Birimian Supergroup units (Figures 2.3 and 2.4). Oberthür et al. (1995) further subdivided the Ashanti Belt's mesothermal quartz veins and the sulphide mineralization associated with them into quartz vein types that are hosted by shear zones and quartz vein types that are coupled with sulphide ore types. Disseminations and stockwork hydrothermal gold mineralization in basement-type granitoids are two examples of novel mineralization types cited by Oberthüret al. (1995). Because of their abundance in the country, this study will concentrate on deposits connected with mesothermal quartz veins and the sulphide, palaeoplacer, and hydrothermal mineralization that occurs in quartz veins associated with granitoid types. The mesothermal quartz vein, quartz vein-associated sulphide type mineralization, and turbidite-hosted deposit types have been hypothesized to share a common ancestor; however, the other three regional varieties for West Africa are rarely observed in Ghana (Berge, 2011). Evidence of supergene alteration of mesothermal vein gold mineralization has been found from the Ashanti Region, as stated by Bowell (1992). Table 2.1 details the important gold occurrences in Ghana, including their locations, mineralization types, typical gold grades, and availability of resources.

### 2.5.3 Mesothermal quartz vein and quartz vein associated sulphide type mineralization

Often referred to as Ashanti shear zone type mineralization, mesothermal quartz vein and quartz vein-associated sulphide mineralization makes up the bulk of Ghana's gold deposits (Figure 2.2). This mineralization style has its type site at Obuasi, the largest gold mine in the area. Bepkong, Bibiani, Bogosu, Damang, Konongo, Prestea, Wassa, and the Yamfo district are a few examples of other deposits in Ghana (Figure 2.1; Table 2.1) that also feature this mineralization style. Previous studies have found that mesothermal quartz vein and quartz vein-associated sulphide-type mineralization is typically confined to tectonic corridors up to more than 50 km long and several km wide that trend NNE to NE (Milési et al., 1991; Mumin et al., 1994; Oberthür et al., 1997; Yao et al., 2001; Griffis et al., 2002; Allibone et., 2002). There is a theory that the "greenstone" belts of Ghana, also known as the Birimian belts, are composed of metasediments and metavolcanics from the Birimian Supergroup, along with younger siliciclastics from the Tarkwaian Group. Mineralization appears to be linked to geological features like faults and folds in the surrounding area. Fougerouse et al. (2015) discovered that gold mineralization at Obuasi is exclusively found along the northeast-trending Ashanti fault zone, where the Ashanti thrust fault is divided into mineralized splay faults composed of graphitic shears.

**Table 2.1: The location, type of gold mineralization, average grade and estimated resources of known gold deposits in Ghana. The mesothermal vein type mineralization listed in the table is short for the mesothermal quartz vein and quartz vein-associated sulphide type or Ashanti-type mineralization (Smith et al., 2016).**

| Name of deposit | Location | Mineralization types | Average grades | Total resource estimates (recent and/or past) | References |
|---|---|---|---|---|---|
| | **Kibi-WinnebaBelt** | | | | |
| Atewa Range | Southeastern Ghana, near the town of Kibi | Mesothermal vein type | NA | NA | Griffis *et al.* (2002) |
| Winneba-Mumford Area | Southern extension of Kibi-Winneba Belt | Mesothermal vein type; Palaeoplacer type | ~0.5-1.0g/t | NA | Griffis *et al.* (2002) |
| | Ashanti Belt/Kumasi Basin | | | | |
| Abosso | Southern Ashanti Belt, ~20km north-east of Tarkwa, south of Damang | Mesothermal vein type; Palaeoplacer type | ~7g/t | ~0.6Moz Au | Griffis *et al.* (2002) |
| Anwia | 15km northwest of Axim,1km north of Nkroful, Kumasi Basin | Mesothermal vein type | ~1.3g/t | ~0.15Moz | Griffis *et al.* (2002) |
| Ayanfuri | Central Ashanti Belt, 16km west of Dunkwa-on-Ofin | Mesothermal vein type; Granitoid type | ~1.5g/t | 0.2Moz Au | Griffis *et al.* (2002) |
| Benso | Eastern limb of Ashanti Belt, ~38km southwest of Wassa deposit | Mesothermal vein type | NA | NA | Parra-Avila *et al.* (2015) |
| Besease | 7km west of Nkawkaw, northeast cover of Ashanti Belt | Mesothermalveint ype, alluvial | ~4.7g/t | ~0.2Moz | Griffis *et al.* (2002) |
| Bogosu | South western Ghana, 60-90km northeast of Atlantic coastline | Mesothermal vein type | ~2.0-5.3g/t | >2.5MozAu | Mumin *et al.* (1994);Oberthür*et al.*(1997); Griffis *et al.* (2002);Allibone *et al.* (2002) |
| Dabokrom | 15km northwest of Tokaradi | Mafic-hosted mineralization | ~3-15g/t | ~0.7Moz | Griffis *et al.* (2002) |
| Damang | Southern Ashanti Belt, ~20km northeast of Tarkwa. | Mesothermal vein type; Palaeoplacer type | ~1.3-2.2g/t | ~5Moz Au | Griffis *et al.* (2002); Pigois *et al.* (2003); Tunks *et al.* (2004) |
| Golden Ridge | 130 km northwest of Accra, northeastern margin of Ashanti Belt | Mesothermal vein type | NA | NA | Griffis *et al.* (2002) |

**Table 2.1 continued: The location, type of gold mineralization, average grade and estimated resources of known gold deposits in Ghana. The mesothermal vein type mineralization listed in the table is short for the mesothermal quartz vein and quartz vein-associated sulphide type or Ashanti-type mineralization (Smith et al., 2016).**

| Name of deposit | Location | Mineralization types | Average grades | Total resource estimates (recent and/or past) | References |
|---|---|---|---|---|---|
| Iduapriem | Southern end of Tarkwa district,southern hill of Tarkwa syncline | Palaeoplacer type | ~1.2-1.7g/t | ~2Moz Au | Griffis *et al.* (2002) |
| Konongo | Northeastern extremity of Ashanti Belt, ~70km northeast of Obuasi | Mesothermal vein type | ~1.1-3.9g/t | ~0.9Moz | Oberthür *et al.* (1997); Griffis *et al.* (2002) |
| Kubi | WesternmarginofAshantiBelt,6 km northeast of Dunkwa | Mesothermal vein type | ~6g/t | ~0.8Moz | Griffis *et al.* (2002) |
| Mampon-Aboronye | 20kmsouthwestofDunkwa, western flank of Ashanti Belt | Mesothermal vein type | ~5.5g/t | ~0.4Moz | Griffis *et al.* (2002) |
| NkranHill | 40 km west-northwest of Obuasi | Mesothermal vein type; Granitoid type | ~2.2g/t | >2.5Moz Au | Griffis *et al.* (2002) |
| Nkroful | 15km northwest of Axim, west of Ashanti Belt, Kumasi Basin | Mesothermal vein type, alluvial | <4g/t | NA | Griffis *et al.* (2002) |
| Obuasi | Ashanti Region, 60 km south of Kumasi,160km northwest of Accra | Mesothermalvein type; Granitoid type | ~2.6-10.1g/t | >60Moz | Bowell *et al.* (1990); Oberthür *et al.*(1997); Osae *et al.* (1999); Yao and Robb (2000); Fougerouse *et al.* (2015) |
| Prestea | Southwestern Ghana, 60-90km northeast of Atlantic coastline | Mesothermal vein type | ~3.4g/t | >7.2MozAu | Mumin *et al.* (1994); Oberthür *et al.*(1997) |
| Salman | 15km north of Axim, the western boundary of Ashanti Belt | Mesothermal vein type | ~1.6-2.3g/t | ~1.2Moz | Griffis *et al.* (2002) |
| Tarkwa | Southwestern Ashanti Belt, from Bonsa River in south to Damang in north | Palaeoplacer type | ~1.2-2.4g/t | >40Moz | Griffis *et al.* (2002); Pigois *et al.*(2003); |
| Teberebie | Western ridge of Tarkwa syncline | Palaeoplacer type | ~2.0-2.4g/t | ~2MozAu | Griffis *et al.* (2002) |
| Wassa | Southern Ashanti Belt, ~40km northeast of Tarkwa | Mesothermal vein type | ~2.4g/t | ~4 Moz Au (possibly up to 10 Moz) | Parra-Avila *et al.* (2015);<br>Perroutyet *al.* (2015) |

**Table 2.1 continued: The location, type of gold mineralization, average grade and estimated resources of known gold deposits in Ghana. The mesothermal vein type mineralization listed in the table is short for the mesothermal quartz vein and quartz vein-associated sulphide type or Ashanti-type mineralization (Smith et al., 2016).**

| Name of deposit | Location | Mineralization types | Average grade | Total resource estimates (recent and/or past) | References |
|---|---|---|---|---|---|
|  | **Asankrangwa Belt** |  |  |  |  |
| Abore North | 45km southwest of Kumasi; Asankrangwa Belt | Mesothermal vein type; Granitoid type | ~2g/t | ~0.3Moz | Griffis *et al.* (2002) |
| Mpeasem | Western side of Ofin River, Asankrangwa Belt | Mesothermal vein type | ~2.5g/t | ~0.8Moz | Griffis *et al.* (2002) |
|  | **Sefwi Belt** |  |  |  |  |
| Bibiani | Eastern margin of Sefwi Belt,<br>80 km west southwest of Bibiani | Mesothermal vein type | ~2.6g/t | ~1.8MozAu | Griffis *et al.* (2002) |
| Chirano | 90 km southwest of Kumasi,<br>Central western margin of Sefwi Belt | Mesothermal vein type; Granitoid type | ~2.2g/t | ~1.4Moz | Griffis *et al.* (2002) |
| Ntotoroso | 30 km south of Sunyani, Sefwi Belt | Mesothermal vein type; Granitoid type | ~2.3g/t | ~1.4Moz | Griffis *et al.* (2002) |
| Yamfo-Kenyase | South of Sunyani, Sefwi Belt | Mesothermal vein type; Granitoid type | ~3g/t | ~6.2Moz | Griffis *et al.* (2002) |
|  | **Bui Belt** |  |  |  |  |
| Brohani | Central western Ghana | Palaeoplacer type | >1g/t | NA | Griffis *et al.* (2002) |
|  | **Bole-Navrongo Belt** |  |  |  |  |
| Dokrupe | Southern margin of Bole -Navrongo Belt | Mesothermal vein type | ~2.8g/t | ~0.18Moz | Griffis *et al.* (2002) |
|  | **Wa-Lawra Belt** |  |  |  |  |
| Bepkong | Northwestern Ghana, Wa-Lawra Belt | Mesothermal vein type | ~1.8g/t | ~0.1Moz | Amponsah *et al.* (2015) |
|  | **Julie Belt** |  |  |  |  |
| Julie | North western Ghana, Julie Belt | Granitoid type | ~1.5g/t | ~0.8Moz | Amponsah *et al.* (2016) |

Large, steeply dipping vein systems are characteristic of the first category of mesothermal quartz vein and quartz vein-related sulphide type deposits: quartz vein gold deposits. Vein networks can be as thin as 2 meters (m) and as thick as 20 to 55 meters (m) in the case of Prestea, and anywhere in between. Gold mineralization in quartz veins has been proven to be related to the regional ductile to brittle D3 deformational event of northwest-to-southeast compression in Bepkong, Bogoso, Damang, Obuasi, and Wassa. Quartz vein-hosted gold mineralization was first discovered in the Wassa area in the early 2000s (Griffis et al., 2002; Allibone et al., 2002; Tunks et al., 2004; Amponsah et al., 2015; Fougerouse et al., 2015; Perrouty et al., 2015).

The second kind of Ashanti-type mineralization is characterized by the presence of quartz vein networks. Quartz vein-associated sulphide mineralization is characterized by widely spaced sulfide zones in the host rocks that can extend as deep as 100 m (for example, in Prestea) into the host rock. In addition, the gold mineralization in the dispersed sulphide zones is unproductive or refractory (Griffis et al., 2002). Nonetheless, it accounts for a majority of the mineral deposits in Obuasi (Fougerouse et al., 2013). Earlier stages of gold mineralization for the dispersed sulphides are indicated by the zones' resemblance to pods of varying sizes and the prevalence of quartz vein networks within them (Figure 2.2; Griffis et al., 2002). The quartz vein is associated with the D3 event, and its mineralization may have happened at the same time as the sulphide mineralization (Fougerouse et al., 2013; 2015).

Griffis et al. (2002) state that metasediments are typically found near graphitic/carbonaceous, siliceous, or manganiferous chemical sedimentary rocks, mafic volcanic rocks, and belt intrusions, and that these metasediments are the host rocks for mesothermal quartz vein and quartz vein-associated sulphide mineralization.

Birimian gold orebodies are either of the disseminated sulphide (DST) or quartz vein (QVT) kinds (Leube et al., 1990). The two forms of DST are:

i. lithofacies controlled subtype which is regional in extent and syngenetic, and

ii. the structurally controlled subtype which occurs at the selvages of the QVT and is epigenetic as well as the QVT (Leube et al., 1990).

Milési et al. (1992) took a different tack and argued that the DST and QVT, both of which were deposited during the final phase of D2 deformation, were epigenetic. Quartz ore bodies can be any color from transparent white to black, and can have varying densities, shear strengths, and fracture patterns. Both sides of the quartz orebody show evidence of rock alteration along the ore channels. In addition to carbonate, sericite, silica, and graphite, pyrite is one of the most prominent alteration minerals.

In contrast to metavolcanic rocks, metasedimentary rocks often contain less carbonate (Adjimah et al., 1994). Pyrite, arsenopyrite, pyrrhotite, chalcopyrite, sphalerite, galena, cubanite, alabandite, covellite, marcasite, rutile, titanite, and leucoxene are all present in the DST ore, along with submicroscopic traces of gold in sulphides. According to Adjimah et al. (1993), the DST ore mined in Bogoso consists of galena, tetrahedrite, marcasite, arsenopyrite, sphalerite, chalcopyrite, and primary and secondary pyrite. Mined oxidized DST gold ores from Konongo, AngloGold-Ashanti, contain a variety of alteration minerals including as graphite, sericite, silica, and sulfides. Appiah et al. (1991) postulated that the Prestea gold deposit underwent a similar ore mineral paragenesis, with chalcopyrite exsolutions in sphalerite. According to Milési et al. (1992), mesothermal dispersed arsenopyrite and gold-bearing quartz veins emerge along tectonic corridors, making the Anglogold-Ashanti, (Obuasi), Bogoso, Prestea, and Konongo gold deposits late orogenic. Quartz and arsenopyrite (with gold in its lattices) are the two most common paragenetic minerals in gold-arsenopyrite dispersed ores. The minerals found in the QVT include gold, pyrite, pyrrhotite, tetrahedrite, sphalerite and graphite. Although the DST is often of low grade, Milési et al. (1992) report that it accounts for around 60% of AngloGold Ashanti's gold production.

For the origin of the Birimian gold, numerous theories have been proposed.

i. Junner (1932), and Cooper (1934) postulated that gold ore and the orebody form as an end product of through-going magmatic-hydrothermal solution originating from sub-epexing granitic plutons at depth and associated this with the Dixcove granite.
ii. Ntiamoah-Agyakwa (1979) postulated a metamorphic mobilization of previous syngenetic protore and concentrated it laterally into dilatant fissures and fault zones.

These theories have a few shortcomings. Dzigbodi-Adjimah asserts that the magmatic-hydrothermal theory disregards the possibility of orebodies and ore from different generations (1993). Furthermore, fluid cannot move laterally across formations with steeply dipping foliations and cleavages, which casts doubt on the idea of metamorphic mobilization. Thus, the following resolution was suggested:

i. Geosynclinal deposition in Early Proterozoic followed by folding and fracturing.
ii. Introduction of quartz veins along weak zones
iii. Tectonism causes shearing and fracturing of the quartz
iv. Movement of gold-bearing fluid along fractures
v. Emplacement of late untectonised compact quartz.

Groves and Philips (1987) postulated that the circulation of the ore fluid might be explained by the metamorphic remobilized fluid created by the devolatilization of lower portions of the lithologic pile into low-pressure cracked zones, as shown in Figure 2.6.

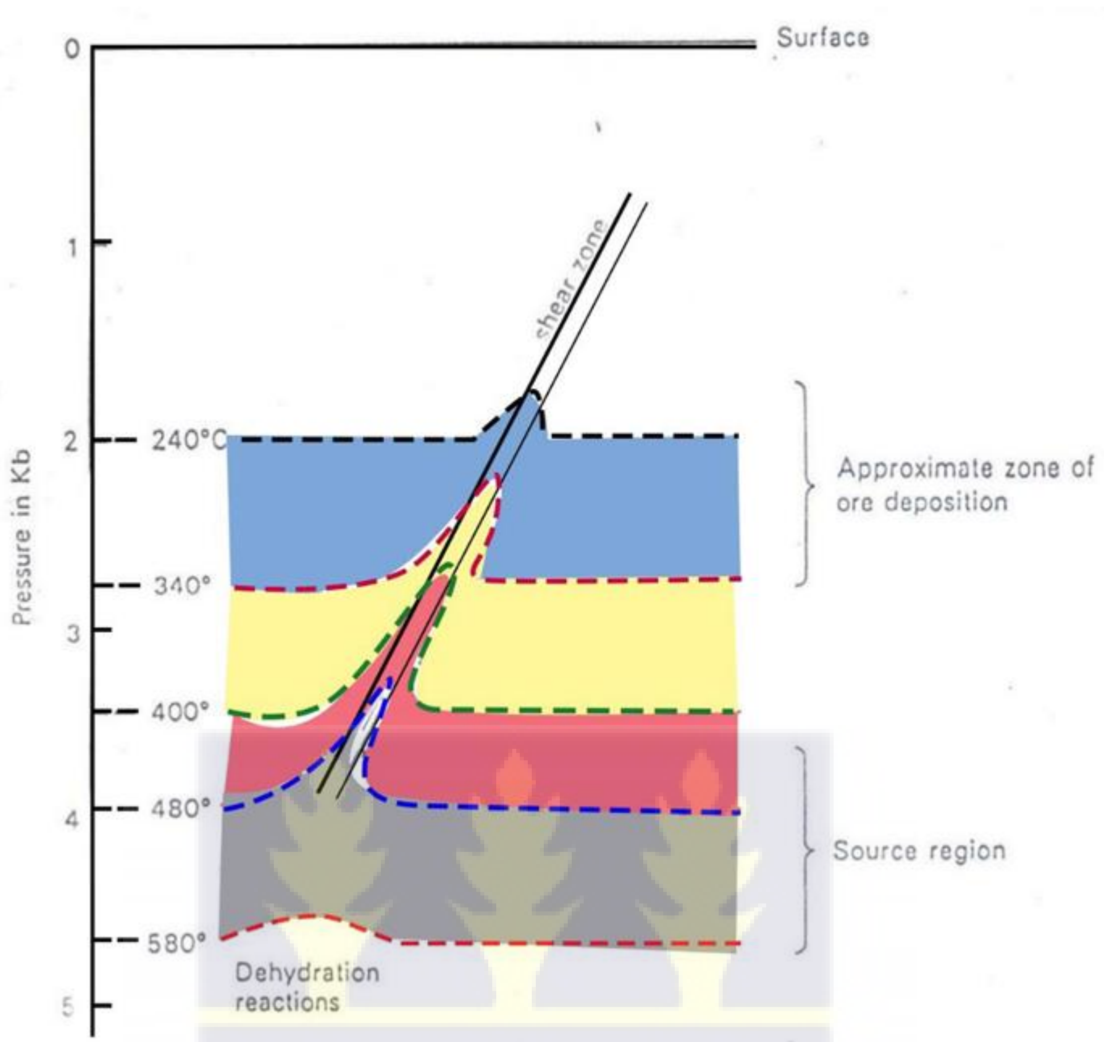

**Figure 2.6: Diagram of a shear zone showing metamorphic water rising from a large volume of rock at depth to higher level (Fyfe and Henley, 1976)**

## 2.6. Gold in the Kibi Belt

The contact point for the satellite lode gold deposits in the Kibi Belt, according to Rae et al. (2006), is where the Birimian granitoids, metasedimentary and metavolcanic rocks are in contact. The base of the mineralization is defined by a near-planar graphitic-dominated fault zone. However, according to Simon et al. (2012), gold mineralization is only found in three lithological units (graphitic shear, feldspar porphyry and meta-volcanic deposits).

## 2. 7. Geophysical surveys in mineral exploration

Many rocks include iron-bearing mineral components that can be used as miniature magnets. There are a few minerals that can only be formed while lava or magma cools. Since the molten rocks haven't completely hardened yet, the magnetic minerals that are still in suspension follow the direction of the magnetic field. The rock's final development is accompanied by the absorption of the magnetic field by these minerals. Sedimentary rocks, as reported by Reeves et al. (1997), also include magnetic records. Iron-rich sedimentary minerals spontaneously align with the magnetic field when they settle out of the water column. Variations in the magnetic mineral concentration of rocks near the surface cause localized changes in the primary field. Magnetite and pyrrhotite are the most common magnetic minerals responsible for creating magnetic anomalies in rocks. Telford et al.'s eternal field theory from 1990 proposes a system for classifying chemicals according to their behavior in this setting.

All of the electron shells are full of diamagnetic materials, hence there are no unpaired electrons. Due to the electrons' orbital angular momentum, they generate a magnetic field perpendicular to the applied field, resulting in a small negative susceptibility (Telford et al., 1990). Diamagnetic earth consists primarily of graphite, marble, quartz, and salt (Reeves et al., 1998). In paramagnetic materials, the presence of unpaired electrons results in asymmetry in the spin magnetic moment and weak magnetic interactions between atoms. According to the Curie-Weiss Law, weak positive susceptibilities for paramagnetic materials drop in an anti-clockwise direction as the absolute temperature rises, while ferromagnetism decreases with rising temperature and disappears totally at the Curie temperature (Reeves et al., 1997). A few naturally occurring examples of ferromagnetic materials with a parallel alignment of moments are cobalt, nickel, and iron. Magnetite, titanomagnetite, and ilmenite are all iron-containing minerals with anti-parallel and/or uneven sub-lattices. Magnetization occurs spontaneously in ferrimagnetic minerals like pyrrhotite and the materials have a high susceptibility (Telford et al., 1990). As stated by Reeves et al. (1997), the majority of magnetic minerals found in nature display ferrimagnetic or weakly anti-ferromagnetic properties.

### 2.7.1. Aeromagnetic Survey

Aeromagnetic surveys, which employ an on-board or towed magnetometer, are common in the field of geophysics. The idea is the same as a magnetic survey with a handheld magnetometer, but with this method, much more ground may be covered in a shorter amount of time, making it ideal for regional monitoring. The data resolution is determined by the height, line spacing, and survey cost per unit area as the plane flies in a grid pattern.

According to research by Telford et al. (1990), the airplane's magnetometer may pick up on minute shifts in the magnetic field's strength as it travels through the air. Temporal effects, which fluctuate continuously, are brought on by the regional magnetic field, whereas spatial changes are caused by both the regional magnetic field and the local effects of magnetic minerals in the earth's crust. When solar and regional effects are taken into account, an aeromagnetic map emerges, showing the location and abundance of magnetic minerals in the upper crust. These materials are usually the iron oxide mineral magnetite. Since magnetic minerals are distributed differently between rock types (faults and folds), a magnetic map can be used to infer geological features of the upper crust at depth, such as the spatial geometry of rock bodies and the presence of structures. When bedrock is buried behind layers of soil, water, or other substances, this is an invaluable tool. Mineral exploration often makes use of aeromagnetic surveys, and these surveys also aid in the creation of geological maps.

### 2.7.2. Data Enhancement Techniques

Enhancements of magnetic field data are processing operations that are intended to favorably emphasize the expression of a selected magnetization at the expense of others, according to previous researchers' suggestions (Milligan & Gunn, 1997). By increasing anomalies brought about by a particular group of geological sources in contrast to abnormalities brought about by other groups of geological sources, many linear and non-linear filtering methods can be employed to enhance airborne geophysical data. In addition to mathematical enhancement methods, a range of imaging algorithms that can be configured to visually enhance the effects of specific geological sources are available. According to Telford et al. (1990), Fourier transforms are particularly useful when transitioning from the frequency domain to the wave number domain and when calculating derivatives. On the other hand, some data augmentation procedures change the data, therefore care must be taken to avoid erroneous applications of improved data.

### 2.7.3. Horizontal derivative

A phase transformation and an increase in high frequencies are also parts of the horizontal derivative, according to Milligan and Gunn (1997). The sharpening of anomaly peaks, which are frequently generated by phase transformation and roughly positioned around the borders of vast bodies, improves the delineation of the body edges. Only when traveling ahead (or backward) down the profile can the horizontal derivative be determined. Gridded data can be used to determine the derivative in any azimuth between 0 and 360°. Some interpreters use this characteristic of the horizontal derivatives to map body contours. Although the process becomes quite unclear for thin bodies, it is challenging to see how horizontal derivatives are superior to vertical derivatives, which offer peaks over the tops of sources and disclose the outlines of sources through strong gradients and inflections (Milligan & Gunn, 1997).

### 2.7.4. Vertical derivative

Vertical gradient (or derivative) filters amplify shorter-wavelength field components more strongly than longer-wavelength field components (Foss, 2011). Fast Fourier Transform (FFT) filters are frequently employed for applying vertical derivative filters on gridded data. The proponents asserted that the amplitude spectrum of the magnetic field could be multiplied by a formula of the following shape to determine a number of vertical derivatives of the magnetic field (Equation 1):

$$\frac{1}{n}\left[\left(u^2+v^2\right)^{\frac{1}{2}}\right]^n$$

……………..Equation 1

Where n is the order of the vertical derivative, *(u, v)* is the wavenumber corresponding to the (x, y) directions respectively. The first vertical derivative, also referred to as the vertical gradient, is the physical outcome of subtracting the data, dividing the result by the vertical distance between the measurement places, and simultaneously measuring the magnetic field at two points that are vertically above one another. The next vertical derivative is the vertical gradient of the previous one, and so on. This feature serves as the foundation for the derivative technique, which balances the effects of nearby anomalies while removing long-wavelength regional effects. In comparison to low frequencies, high frequencies are boosted by these processes, according to the frequency response formula. For projects involving magnetic interpretation, first vertical derivative data are currently practically necessary, according to Adewumi et al. (2018). This derivative of the anomaly gives the anomaly more detail in terms of the depth of the source. When computing the first vertical derivative for an aeromagnetic survey, the advantages of boosting shallow sources, suppressing deeper ones, and improving source resolution are identical to those of directly monitoring the vertical gradient with a magnetic gradiometer. Gunn et al. (1997) claim that the second vertical derivative has even greater resolving power than the first vertical derivative, but to utilize it, high-quality data is required because it amplifies noise at higher frequencies than the first vertical derivative does. Rarely are higher orders of derivatives used in the production of interpretive products.

### 2.7.5. Reduction to pole (RTP)

Luo et al. (2010) asserted that the reduction to the pole (RTP) is a fundamental feature of the magnetic data processing approach, particularly for large-scale mapping. Any source that produces a magnetic anomaly can be made to create the same anomaly if it were placed at the pole and magnetized only by induction by using RTP operation. By eliminating magnetic latitude's impact on the anomalies, which is crucial for anomalies brought on by the crust, RTP can further aid in the understanding of magnetic data. A magnetic field cannot be lowered to the pole by simply moving from a magnetic latitude, where the earth's field is inclined, to a magnetic pole, where the inducing field is vertical (Luo et al., 2010). According to Milligan and Gunn (1997), induced magnetic anomalies have asymmetrical connections to their sources when the earth's field is inclined, but when the inducing field is vertical, the induced anomalies are immediately over their sources. Through the use of the Fourier transform, RTP is transformed from the space domain to the wavenumber domain. In the domain of wave numbers, the RTP operation is expressed (Equation 2) as follows:

$$A_p(u,v) = \frac{A_c A_p(u,v)}{\left(sinI + icosIcos\left(D - \theta\right)\right)^2}$$

…………..Equation 2

where $A_p$ ($u$,$v$) is the Fourier Transform of these observed magnetic data, $A_c$ ($u$,$v$ ) is the Fourier Transform of the vertical magnetic field, $I$ and $D$ are the inclination and declination of the core field, ($u$,$v$) is the wavenumber corresponding to the (x, y) directions respectively (Luo et al., 2010).

### 2.7.6. Radiometric survey

The distribution of particular soils and rocks can be determined using radiometrics, also known as gamma-ray spectrometry, a measurement of the ambient radiation on the earth's surface. Geologists and geophysicists regularly use it to discriminate between different types of rocks as a geological mapping tool. Radiometric analysis is useful for both geomorphology and soil studies, according to Gregory & Horwood (1961). Using radiometric analysis, the spatial distribution of three radioactive elements in the first 30-45 cm of the earth's crust is assessed (potassium-K, thorium-Th, and uranium-U). Using gamma rays generated during their radioactive disintegration, the abundances of K, Th, and U are calculated. The primary objective of radiometric surveys is to determine the 50 absolute or relative concentrations of U, Th, and K in the rocks and soils on the surface. Since changes in the concentration of the three radioelements U, Th, and K correlate with the bulk of important changes in lithology, the method can be applied as a reconnaissance geologic mapping tool in many locations (Wilford et al., 1997). Aerial gamma-ray spectrometry data have been used to identify a variety of characteristics on a regional scale, including fold belts, sedimentary basins, the boundaries of geologic provinces, shear zones, and overprinted structural trends, according to Direen et al. (2001).

### 2.8 Basic Radioactivity

Gunn et al. (1997) defined radioactivity as the process by which an unstable atom transforms into a stable one by disintegrating or nucleon decay. The three types of energy released during decay are alpha, beta, and gamma radiation. Gamma rays are electromagnetic radiation particles, whereas beta radiation consists of electrons, which can move up to a meter in air. Alpha radiation, or helium nuclei, is absorbed by a few centimeters of air (similar to visible light). Gamma rays, according to their supporters, can travel up to 300 meters through air before being stopped by molecules like water and those in soil and rock. The energy of each gamma ray is specific to the radioactive substance it originated from. They have shorter wavelengths than the majority of other electromagnetic radiation. As gamma rays can penetrate up to 30 cm of rock and several hundred meters of air, they are the only choice for remotely monitoring terrestrial radioactivity (Gunn et al., 1997).

### 2.8.1. Geochemistry of the Radioelements (K, U &Th)

Fertl (1983) asserts that K is consequently somewhat high in felsic rocks (granites, etc.), low in mafic basalts, and extremely low in dunites and peridotites. Shale typically has a greater potassium level than carbonates or sandstones, even though the potassium concentration in sedimentary rocks can vary widely (Dickson & Scott, 1997). The behavior of the K-bearing minerals during weathering affects how much radioactive material is present in weathered rocks and soils. During weathering, the principal K hosts will deteriorate in the following order: feldspar, muscovite, biotite, and K. The potassium released during weathering can, given the correct conditions, be absorbed in the formation of potassium-bearing minerals like illite or adsorbed in minute amounts into other clays, such as montmorillonite. Due to clays' efficient uptake of K, saltwater only contains 380 ppm of potassium (Dickson & Scott, 1997). In a gamma-ray survey, potassium is found by detecting the 1.46 MeV gamma-ray released by the disintegration of 40K. This isotope, which makes up 0.02 percent of natural K, can be used to test the K content of the ground directly.

### 2.8.2 Thorium (Th)

Allanite, monazite, xenotime, and zircon can contain thorium in quantities of 52 > 1000 ppm or in trace amounts in other rock-forming minerals (Dickson & Scott, 1997). The two main minerals that include Th are monazite and zircon, both of which can accumulate in heavy mineral sand deposits and remain stable after weathering. When minerals break down during weathering, thorium that is released may be trapped in clays, Fe or Ti oxides-hydroxides, or even both. Th may be transported and adsorbed on colloidal clays and iron oxides, just like U. Th is the source of a decay series with a stable endpoint.$^{208}$Pb, however unlike U, it does not release gamma rays during its decay (Dickson & Scott, 1997).

### 2.8.3 Uranium (U)

Uranium is a minor component of the earth's crust (~3 ppm). Its chemistry is dominated by two valence states $U^{4+}$ and $U^{6+}$. The more reduced form, $U^{4+}$, is generally contained in insoluble minerals. Dickson & Scott, (1997) suggested that uranium may exist in rocks as the oxide and silicate minerals uraninite and uranothorite; in significant U-bearing minerals like monazite, xenotime, and zircon; as trace amounts in other minerals that comprise rocks; or in beside grain boundaries, perhaps as U oxides or silicates. The proponents believe that only monazite and zircon, two of the main U-bearing minerals, remain stable over weathering. A decay cycle originating from uranium culminates in stable $^{206}$Pb. The daughter isotopes of uranium do not release any gamma-rays throughout their decay; instead, the most powerful gamma-rays are released by $^{214}$Bi, which is the final decay product.

### 2.8.4. Disequilibrium

Disequilibrium in the U decay series severely increases the likelihood of mistakes in gamma-ray spectrometric surveying. When radioactive decay results in an unstable daughter product whose half-life is shorter than that of the parent, it will eventually happen that the daughter product is decaying as quickly as it is being formed. A decay series is considered to be in secular equilibrium when all of the daughters experience a decline in activity at the same rate as their original father. Since the relevant half-lives must be taken into account when determining the relative concentration of members of a decay series, identical activity under equilibrium conditions does not necessarily imply equal concentration. Depending on the half-lives of the radioisotopes involved, the time it takes for the system to return to equilibrium when one or more decay products are added to or removed from it can range from days to millions of years. According to Minty (1997), there are no problems with disequilibrium because K only exhibits a single photo-peak and thorium rarely deviates from equilibrium in nature. However, disequilibrium in the environment usually happens in the U decay series.

For precise estimates of U using gamma-ray spectrometry, we rely on the abundance of isotopes like 214Bi and 214Pb that occur far down in the radioactive decay chain, thus we have to assume equilibrium circumstances, which are typically missing. Since equilibrium conditions are necessary for these predictions to be accurate, they are typically expressed as "equivalent uranium" (eU), which serves as a reminder. Even though the Th decay series is virtually always in equilibrium, Minty (1997) hypothesized that the term "equivalent thorium" (eTh) is also frequently used to refer to thorium.

## 2.9. Geophysics of Kibi Belt

Over the Kibi Gold Project, a versatile time domain electromagnetic (VTEM) survey evaluated the ground's elevation, radiometrics, magnetic field, and electromagnetism (resistivity). After data interpretation, a regional interpretative pseudo-geology map was produced. Simon et al. found that these various geophysical units were related to various geological units (2012). The report identified target areas for further ground research in conjunction with other exploratory strategies. Targets were divided into two groups:

i. Resistive-type:

   The interpreted conductive graphitic shear zones and the interpreted conductive graphitic sediment units have been found to contain areas of low conductance/susceptibility, in accordance with the silicification concept for gold mineralization.

ii. Granitoids-type:

Shear/fracture zones identified in basin-type granitoids in the survey region show evidence of sub-economic to economic gold mineralization. Target locations are thus those where interpreted fractures join interpreted basin-type granitoids.

In addition to identifying gaps in the search for gold mineralization, occurrence, and style in the Kibi area, the literature review offered helpful information. In-depth knowledge of ore mineralization trends, patterns, and the basic geology of the Kibi Belt must be obtained through more research.

## 2.10 Geochemistry of the Kibi – Winneba Belt

Previous work by Anum et al. (2015) on the granitoids intruding the Kibi- Winneba belt, indicated that the granitoids are distinguished by their highly fractionated REE, LILE enrichments, and Nb, Ta, and Sr depletion. However, within single bodies, the chemistry of REEs and trace elements reveals differences in the composition of the source rocks. The enrichment of the LREE and LILE suggests the influence of subduction-related fluids during the melting process in a volcanic arc region. In contrast, the depletion of LREE indicates sources without fluid enrichment, a typical feature of within-plate regions. Therefore, the granitoids were most likely derived from an evolved magma or partial melting of the depleted mantle. The granitoids from the Kibi-Winneba area are typically tholeiitic to calc-alkaline, enriched in LILEs such as Cs, K, Rb, U and Th concerning the HFSEs, especially Nb and Ti. Magmas with such chemical characteristics are indicative of subduction-related environments.

Again, the granitoids exhibit variable Sr - and Eu-anomalies which may imply varying extents of plagioclase fractionation since plagioclase has exceptionally high positive Sr and Eu anomalies but depleted in all other REEs and Y (McKay et al., 1994). Likewise, positive Ba, strong negative Nb–Ta, P, and Ti anomalies, and variable Sr anomalies displayed by the studied rocks suggest that the sources of the granitoids may be more depleted in HFSE than typical orogenic granitoids.

# CHAPTER THREE

# METHODOLOGY

## 3.0. Introduction

To concentrate on the target mineral, a modern exploration program should be completely integrated by taking into consideration all relevant geoscientific data sets (Robert *et al*., 2007; Kuma *et al*., 2010; Magalhães and Filho, 2012). This chapter gives an outline of the various integrated methods and processes that were employed in this study. The methodology employed in this study includes: geophysical data acquisition and analysis, geological field mapping and sampling and geochemical analysis (including multivariate statistics). The data has been integrated and interpreted to address the specific objectives of this study.

## 3.1. Aeromagnetic geophysical survey of the Kibi gold zone

### 3.1.1. Data Acquisition

Airborne magnetic maps covering parts of Field Sheets 0601A4, 0601B3, 0601C2, 0601C4, 0601D1 and 0601D3 located in the Kibi gold zone were obtained from the Geological Survey Authority, Ghana. The aeromagnetic data for the study area was extracted from the Volta Basin data flown by Fugro Airborne Surveys in 2006, the Aerodat data flown in 1992 and High Sense A3 flown by High Sense Geophysical Surveys of Canada in 1999-2000.

With a flight line and tie-line spacing of two kilometers and twenty kilometers, respectively, the nominal flying altitude above the ground was 500 feet or roughly 152 meters. However, the flight and tie line directions were 150˚/330˚ and 60˚/240˚ respectively. The International Geomagnetic Reference Field (GRF) served as the basis for the regional adjustment of the magnetic data. The image obtained on December 17, 2010, using Landsat 5TM with seven bands, is part of a scene that has path number 188 and row number 56. To the National Center for Remote Sensing (NCRS), Jos, EROSEDC developed and sent the dataset in the National

Data Format (NDF) for the new National Landsat Archive Production System (NLAPS). The same data is shown in seven bands using raster format and band sequential organization (BSQ) of the image. Radiometric correction was also applied to each scene. Four mosaic image sceneries were first adjusted for tonal differences and then subsisted to match the study area's locations.

### 3.2.2 Data Processing

Using an enhancement approach, a gridding routine, and removing the earth's background magnetic field were done to filter the aerial data used in this study. However, the contractors at the Geological Survey of Finland made some corrections, such as background correction (aircraft, radon, and cosmic), micro-leveling, stripping, eliminating diurnal variations in the earth's magnetic field, aircraft heading, instrument variation, the lag error between the aircraft and the sensor, and anomalies between flight lines and tie lines. The Universal Transverse Mercator Coordinate System, zone 31 of the Northern Hemisphere, is where the dataset is co-registered.

Geosoft® (Oasis Montaj) and Discover 12 were the primary software for processing and improving the aerial geophysical data. In order to integrate the interpreted results, a GIS environment was created using ArcGIS. The two distinct geophysical aerial datasets (magnetic and radiometric) were acquired, databases (projects) were constructed, data processing and interpretation were performed.

### 3.2.3 Gridding

According to Foss (2011), gridding produces a new, fundamentally distinct data construct by interpolating data from measurement points to nodes of a regular mesh. However, the dataset was gridded to a 100 m interval using Briggs' minimal curvature method (1974). Once a grid had been created, it was shown as an image. Both the magnetic and radiometric data were griddled using the minimal curvature method. The survey data was randomly distributed, and then the minimum curvature method interpolated it onto a standard grid. After that the images were created using the Geosoft® software program, and they were exported in the GeoTIF format together with any accompanying files that may have contained spatial reference data. Since the images were spatially referenced, they could be presented in a GIS environment and viewed with any image-viewing software. Since filters need evenly spaced data points, gridding the data made it possible to apply filters.

## 3.3 Enhancement of Aeromagnetic Dataset

Numerous linear and non-linear filtering strategies can improve the airborne magnetic dataset Using mathematical enhancement approaches, various imaging algorithms can be specified to visually increase the impacts of specific geologic sources (Milligan and Gunn, 1997). The results of a few enhancing strategies are described in the discussion that follows. To boost high frequencies and delineate body borders in the aeromagnetic data, high-pass and horizontal gradient were applied because some mineral deposits are susceptible to high-frequency magnetic responses. Generally, all the enhancing approaches were carried out with Geosoft® (Oasis Montaj 7.3) and MapInfo-Discover 2012 software.

The MagMap module in Geosoft®, which provides several tools for processing magnetic data, was employed to process and apply filters to the absolute international geomagnetic reference field minus the overall field intensity is the magnetic-anomaly grid. The Grid and Image tool was used to present it as an image once the requisite filters had been applied. Reduction to the Pole, Downward and Upward Derivative, First Vertical and Analytic Signal and Horizontal Derivatives were the two-dimensional fast Fourier transform filters employed to improve the data quality. The grid was expanded along both coordinates to imitate periodicity in the preprocessing stage. With dummy values, the algorithm fills in the grid's borders. To provide enough room for maintaining regular periodicity, the grid was extended. The filled grid is periodic along both locations since the dummy area was interpolated.

### 3.3.1 Reduction to the Pole (RTP)

The geomagnetic anomalies were filtered using the reduction to pole (RTP) filter for low geomagnetic latitudes (Remnant Magnetic Intensity: RMI). The method reduces directional noise brought on by the low geomagnetic latitude by using an azimuthal filter in the frequency domain (Philips, 1997). Using this post-processing method, the asymmetry in the RMI data that results from the earth's magnetic field's non-vertical inclination is eliminated from the gridded data. This makes the images simpler and superimposes geomagnetic anomalies from vertical sources over the corresponding geologic body, instead of causing them to be distorted and offset to one side.

### 3.3.2 First Vertical and Horizontal Derivatives

Data from the RTP grid was processed using the first vertical derivative (1VD) filter. Usually, small and large amplitude responses are more evenly reflected by this filter. The grayscale 1VD grid improved the linear features in the region. Applying the first horizontal gradient or derivative (1HD) to the RTP grid also improves it, which is important when attempting to map linear structures such as dikes and/or faults from the geomagnetic dataset. These filters offer greater accuracy and resolution at greater intervals. Identification of the geologic boundaries of formations in the research area was facilitated by the horizontal derivative. Higher derivative images using various filters, including 2VD and 2HD, generated interesting results, however, many distortions were observed in the images as a result of the process's increase in the noise level that was injected into the data. Since they were utilized as a guide, these images were not employed to interpret the first derivative images. This post-processing method estimates the rate of change of the magnetic field spatially in the vertical direction using the gridded data. It makes the high-frequency anomalies stronger than the low-frequency abnormalities.

### 3.4 Downward and Upward Continuation (DC and UC)

By using the magnetic intensities of geologic structures buried deep within the crust, the impacts of shallow anomalies were suppressed by using the UC filter (Pašteka et al., 2018). To see more intense signs emanating from more substantial structures, the RMI grid was extended to depths of 100, 200, 400, and 800 m. As a result, high-frequency abnormalities were smoothed out in relation to low-frequency anomalies. If the source is shifted closer to the measurement plane, the DC filters improve responses from shallow-depth sources (Zhang et al., 2018). On the other hand, the continuation shows short wavelength disturbances in the data, which seem to be signals from very shallow sources. To avoid short-wavelength noise and large amplitude during data processing, the short-wavelength signal must be removed, which is usually associated with shallow sources. In order to accomplish this, the Butterworth filter (a low-pass filter), was used to filter out short-wavelength noise (as determined by the radially averaged energy spectrum), before employing the downward continuation filter. The *MagMap's* energy spectrum was useful for figuring out how deep the data might be extended downward.

#### 3.4.1 Analytical Signal Amplitude

The residual magnetic field was used to calculate the analytical signal amplitude, which was then gridded to show the distribution of the magnetic signature regardless of the magnetization's orientation. The amplitude of the analytical signal is proportional to the amplitude of magnetization and is independent of the source's magnetization direction. High analytical signal amplitudes are connected with the highest concentrations of mineral deposits in this region (Silva et al., 2003).

### 3.4.2 Depth to Basement

The depth to basement of the magnetic body understudy was calculated using the Geosoft Oasis Montaj depth to basement extension, which calculates the direction of dip (orientation), intensity (susceptibility) and position (along the profile and depth) of magnetic source bodies on a magnetic profile (Florio, 2020). The Werner deconvolution function, which computes the depth to the magnetic anomaly's basement using the horizontal and vertical derivatives, was used. Utilizing the vertical and horizontal derivatives in the computation of the magnetic anomaly's basement depth, the Werner deconvolution function was used. The selected anomaly profile was perpendicular to the geological formation that gave rise to the field. In an array of sliding windows along the profile, the Werner Deconvolution function uses a least-squares technique to calculate the characteristics of the source body, considering the source bodies to be dikes or contacts with infinite depth extension (Ku & Sharp, 1983). The terms "Contact" and "Dike" refer to solutions derived from the horizontal gradient and the full field profile, respectively.

For each window, the calculation on individual Werner Deconvolutions produces a single solution, which is a section of the anomaly profile that it operates on. In order to provide the desired result, several dialog settings that regulate how many solutions the Werner deconvolution generates were precisely configured. 500 was chosen as the value for the window expansion increment, which defines the size and number of steps taken between the minimum and maximum lengths. The movement of the Werner operator down the profile between calculations was set to 200 in order to reduce the number of generated solutions. Setting an amplitude threshold for the anomalies allowed us to reject solutions brought on by input profile noise (setting the "Residual cut-off" to 0.1). The computed solutions can be shown in profiles or 2D charts because they are recorded in an Oasis Montaj database (GDB).

### 3.4.3 Airborne Radiometric Data

### 3.4.4 Total Count (TC), Potassium (K), Thorium (Th) and Uranium (U) Channels

After micro-leveling the full data set to get rid of any apparent residual errors, the total count image was made using the Grid and Image tool in the Geosoft® software. Since the data was gathered in a gridded window with the varying grid based on the instruments, exploration cost and kind of plane utilized during the survey, these images were produced by using mini-curvature gridding. The trends, patterns, and geological units present were then connected with the images.

### 3.4.5 Ternary Images and Ratio Maps

Potassium, thorium, and uranium were assigned to the red, green, and blue color, respectively, because the blue tends to reduce the poorest signal-to-noise ratio of the uranium channel. The resulting visuals, which will be discussed in more detail later, are composed of colors that reflect minute differences in the three band ratios and are produced by the relative intensities of the three components. The distinction among the individual histograms of K, Th, and U was improved to provide the optimum color variation utilizing a histogram equalization.

In order to obtain much information from the individual methods, separate interpretations were made for magnetic and radiometric data. During the interpretation process, various groupings with distinct signatures (e.g., high magnetic, high K) were identified and allocated to distinct layers within the ArcGIS environment. This arrangement allowed for the combination of various layers in the interpretation system.

## 3.5 Ground Geophysics

### 3.5.1 Grid lines setting and line cutting

This section uses IP and resistivity techniques to map the structural controls that affect the mineralization of gold in the research area. These are among the most effective geophysical methods for delineating lithological units within mineralized and unmineralized faults/shear zones for gold exploration based on the contrast in electrical properties of the various lithologies (Echague et al., 2024). This study employed IP and resistivity survey techniques as groundproof on the structural control targets identified by the aeromagnetic survey to corroborate the underlying rock types, hydrothermal alteration zones and structural lineaments within the study area.

In the northwest-southeast trends, systematic grid lines were placed on the baseline at intervals of about 15 km, parallel to the contacts of the underlying rock groups. Over the 45km route chosen for this investigation, five (5) cross lines in total were placed. The cross lines seek to confirm important lithological connections and boundaries in the auriferous zones where artisanal miners are mining lode gold. The artisanal lode gold mining locations studied were Kibi, Pano, Asikam, Agyapoma, Ettukrom, Ankaase, Kwabeng, and Akrofufu.

### 3.5.2 Data Acquisition

ABEM Terrameter LS2 which was secured from the Geological Survey Authority, Ghana was used in this study. Data was acquired with the maiden ABEM Terrameter LS 2resistivity meter. The transmitter and receiver are included with the device as a single unit to facilitate speedier data collection. A twin 2 x 21 cable system with 21 electrodes removed from either end held the ABEM Terrameter L2 in place. The two 2 x 21 cables had 41 non-polarizable electrodes connected to each takeout, and measurements were made along 9 survey lines. Data was exported to a computer to be processed. Measurements are automatically taken by the device and saved in the Terrameter LS2. Depending on the ground conditions, a depth between 18 and 25 percent of the overall survey length can be attained using the electrical approach for the dipole-dipole array (Neyamadpour, 2010). The dipole array was selected for the fourteen-tire survey due to the protocol's exceptional resolution. A survey length of 2 km was conducted with electrodes spaced 50 m apart to reach the greatest depth of interest. The majority of the survey lines reached a depth of 500 meters.

### 3.5.3 Data Quality

Best data collection practices were ensured throughout the survey. The process of ensuring data quality started from data acquisition to data processing. The electrical approach is frequently accompanied by issues with contact electrodes and highly resistant materials, which can hamper data gathering and lower the quality of the data. Every survey began with contact electrode inspections to make sure that free current was being injected into the ground. A salt solution was utilized to boost conductivity and lower contact resistance in the case of high-contact electrodes with a resistance of more than 1.0 KOhm. Before data processing and inversion, Negative apparent resistivity and chargeability values which are less typical of an electric survey were removed to reduce the errors associated with the inversion process.

### 3.5.4 Data Processing

The software Res2Dinv from Arhus Geotomo was used to invert field data. For appropriate data models, the software employs the smoothness constraint algorithm. Based on the smoothness constraint, the RES2DINV modeling software offers a highly quick quasi-Newton technique (deGroot-Hedlin & Constable, 1990; Sasaki, 1992; Loke & Barker, 1996). Using the finite difference or finite element method, the program determines the model blocks' apparent resistivity values and compares them to the data collected in the field.

### 3.5.5 Data Processing and Interpretation

Aeromagnetic data interpretation involves both quantitative and qualitative approaches. The qualitative approach involves the delineation of magnetic zones of the contour map based on the character and intensity of the anomalies, and magnetic texture; analyzing the magnetic zones by studying the amplitude and shape of the magnetic profiles over the bodies, and interpreting those shapes. Making measurements and using the results of calculations to derive conclusions are both parts of quantitative interpretation. The subsequent slope techniques — Peters' Hannel's, and Tiburg's—as well as 2-D spectrum analysis—were used to determine the depth to magnetic anomalous bodies to do this.

### 3.6. Geological field mapping and sample collection

Geological mapping is an important tool in the location of ore bodies and a direct method to detect and reveal the 3- dimensional distribution of rock types and their associated structures in a selected area. The mapping was carried out in northwest-southeast (NW-SE) grid lines through ten (10) traverses across strike lengths of the different rocks in the area. The base map (topographical map) of the Kibi-Winneba belt was used as a basic guide during the mapping process. A total of hundred and fifty (150) rocks and quartz vein samples were purposefully collected from outcrops at irregular intervals using a hammer. Important features such as boundaries of rocks, ancient erosion surfaces (unconformities), bedding planes, faults and the edges of igneous intrusive contacts were mapped. The details of these features were recorded in the field notebooks. Areas mapped include Kibi, Asikam, Agyapoma, Ettukrom, Saamang, Kwabeng and Akrofufu. The field locations of this structure were noted using the Global

Positioning System (GPS). Illuminated loupe Lense was used to examine mineral textures in the hand specimens of rock that contain nuggets obtained from lode gold mineralized quartz veins at Akrofufu, Kwabeng, Etukrom, Afiasa, Agyapoma and Kibi East (Habitat) where artisanal gold mining activities are currently being operated. The compass and hands lens aided in the prospective study of the lithologies using the right-hand rule.

Major secondary geological structures observed in the Kibi gold zone include fractures, folds, and foliations. The trend and dip of mineralized quartz veins and structures (e.g., foliation, lineation, folds, faults, and shear) occurring within outcrops were measured using Brunton compass. The measured structures were processed using rosettes and stereographic projections for their statistical interpretations.

Structural data measured on the field were processed using the Geo-Orient software to build rosettes and stereographic projections for kinematic and dynamic studies of structures. Geophysical data were processed using Envi and ArcGIS software. These images were processed to identify and correlate the structural features that could serve as channels for ore-forming fluids and gold deposition. Geo-analytical and statistical software were used for the interpretation of the results obtained from the various analyses. The results were also compared to other previous works.

### 3.6.1. Thin section preparation and analysis

Thin and polished sections were prepared and analyzed to identify mineral constituents, their texture, microstructures and alteration phases to classify the rocks properly, determine their paragenesis and relationships. Overall, seventy (70) rock samples (made up of 10 greywackes, 10 hanging wall basalt, 10 footwall basalt, 10 volcaniclastics and 30 schists) collected from the Kibi gold zone were cut into thin slices, placed on the hot plate and mounted on a glass slide with epoxy resin, allowed to cure, ground to 30 µm thickness and covered with a cover slide.

The prepared thin sections were examined using the petrographic microscope at the Geological Engineering laboratory, University of Mines and Technology (UMaT), Tarkwa. The procedure followed for the preparation of thin section followed after Grundmann and Scholz (2015).

### 3.6.2. Preparation of polished sections

For the polish section, the remaining "twin" surface slab rock samples were labeled on the other side with a permanent marker and trimmed to a suitable size to fit the chosen mould (ring). The best face to be polished was lapped on a cast iron rotating plate with successive abrasives lurries of 60, 80, 100, 120, 400 and 600 to make it flat and remove severe surface deformations. A suitable reusable mould was selected and the top end to be level with the specimen was abraded with 120 abrasive paper to make the surface edges flat. The inside was smeared with vaseline to make the ring removable and reusable. The flat-lapped face of the specimen was placed down on a plastic sheet smeared with vaseline on a stable working table and a mould or ring was placed around the specimen. The mould (ring) diameter was such that the distance between the inner walls of the ring and the specimen was at least 1mm to ease good coverage of the specimen with the moulding medium. Epoxy resin (resin+catalyst,1:1) was prepared in a suitable container, well stirred and allowed to bubble for about 10 minutes and poured into the mould to cover the specimen completely and allowed to cure overnight. Fine lapping, rough polishing and polishing were subsequently done and finally buffed up in MgO on billiard cloth and thus ready for microscopic observation. In all, forty (40) polished sections were examined under the Leica 2700DP reflected light microscope at the Department of Geological Engineering, University of Mine and Technology (UMaT).

### 3.7 Whole-rock geochemical analysis

The application of major element chemistry to rock classification and nomenclature is widely used in igneous rocks but is also useful in sedimentary rocks (Rollinson, 1993). Major elements are also reflective of the mineralogy of the rock sample. XRF analytical method was employed to study the major element contents of the rocks understudy. This is because XRF has long carborundum as an excellent technique for the analysis of the major elements, but precise analyses are obtained for a relatively small number of trace elements (Norman et al., 1989). Since minor, trace and REEs compositions help in differentiating between rock types, the ICP-MS analytical method was used to determine the minor, trace and REEs concentrations of the various rock types. The reason for using the ICP-MS analytical method is because of its low detection limits and can analyze most elements on the periodic table (over 80 elements). This technique has been employed by most workers in conducting whole-rock geochemical analyses (Sakyi et al., 2019; Anani et al., 2019; Asiedu et al., 2019; Brako et al., 2022).

### 3.7.1 Sample preparation for whole-rock geochemical analysis

After careful examination of hand specimens and the prepared thin sections, a total of seventy-eight (78) representative fresh rock samples comprising: greywacke (18), volcaniclastic rock (20), hanging wall mafic volcanic (20) and footwall mafic volcanic (20) were selected for whole-rock geochemical analysis using XRF analytical method. These selected samples were cut into blocks (8x6) cm, cleaned with distilled water, dried and transported to Australian Laboratory Services (ALS) Vancouver-Canada through their representatives in Brofredu-Kumasi, Ghana. At the laboratory, standard procedures were followed during the preparation of samples for whole-rock geochemical analyses. The samples were weighed and crushed to about 70% below 2 mm and subsequently split using the riffle splitter and pulverized and split to 85% to pass through <75µm. Powdered samples were obtained by mechanical crushing and pulverization using an agate mortar. Six (6) duplicate samples were added to check the precision of the laboratory results.

### 3.7.2 Major elements analysis using XRF

Whole-rock major element analysis for seventy-eight (78) fresh and representative rock samples was performed on fused discs by automated XRF-06 at the Australian Laboratory Services, Canada. The pellets were prepared using 50% lithium tetraborate ($Li_2B_4O_7$) and 50% lithium borate ($LiBO_2$). 9.0 g of lithium borate flux (50% - 50% $Li_2B_4O_7$ - LiBO2) was combined with 0.9 g of calcined or burned material, thoroughly mixed, and fused in an auto fluxer at 1050 °C. The resultant melt was used to create a flat molten glass disc. After then, X-ray fluorescence spectroscopy (XRF) was used to examine this disc. The upper detection limit is 100% and the lower detection limit is 0.01%.

Loss on Ignition (LOI) was designed to measure moisture or impurities content lost when a rock sample was ignited under controlled conditions. The muffle furnace was heated for about one hour at 1000$^{o}$C before igniting the pulverized samples. 1g (Weight A) of the accurately weighed pulverized rock sample was placed in an already weighed crucible (Weight crucible). The weighed sample (1g) was ignited at 1100°C in the muffle furnace for at least 12 hours allowing volatile substances (hydrates and hydroxyl-compounds) and carbon dioxide from carbonates to escape until mass ceases to change. The process was repeated to ensure that the mass change was complete. After ignition, the samples were made to cool in a desiccator and weighed accurately (Weight B). The weight of the sample before heating was recorded (equation 1):

$$LOI = \frac{Weight\ A - Weight\ B}{Weight\ A - Weight\ crucible} * 100\% \qquad \text{........................ Equation 1}$$

### 3.7.3 Trace elements analysis using ICP-MS

ICP-MS was used to examine the 76 samples for trace multi-element concentrations, including rare earth elements (REEs). In a closed Teflon bomb heated to about 140 $^{o}$C on a hot plate, around 100 mg of pulverized whole rock was dissolved in 2 ml HF and 1 ml $HNO_3$. The bomb was then opened and dried to remove silica. The Teflon bomb was then filled with 1.5 ml of HF, 1.5 ml of $HNO_3$, and 10 ml of $HClO_4$. To dissolve the sample, the bomb was placed within a steel jacket and baked at 190 degrees celsius for five days.

After dry down, concentrated $HNO_3$ was added to create nitrates, and then the process was finished with evaporation. Once again, the Teflon bomb was placed inside the jacket and heated to 150$^o$C for a full day after which 2 milliliters of 50% $HNO_3$ was added to it. A 500-fold dilution was then applied to the solution after 0.5g of rhodium (1 ppm) was added as an internal standard. ICP-MS was used to evaluate the solutions after that. Most of the time, ICP-MS analysis precisions were better than 5%. For elements present in concentrations more than 1%, analytical uncertainties were 1-3%, and for elements present in concentrations less than 1wt%, they were roughly 10%. Chu et al. (2009) provided a detailed overview of this analytical process. Precision was generally less than 10%.

### 3.7.4 Fire Assay-Atomic Absorption Spectrometry (FA-AAS)

Twenty (20) samples of each of the selected rock types (greywacke, volcaniclastic rocks and mafic volcanic rocks) were analyzed for gold by conventional fire assay-atomic absorption spectrometry (FA-AAS) (Delaney and Fletcher, 1999) at Australian Laboratory Services (ALS). FA-AAS is widely recognized for its dependability and pulverized to P90 - 75 µm. A 50g charge was fused at 1100°C in a graphite furnace after being dissolved in a molten flux. At 950°C, cupellation was used to extract the produced lead button. Following the digestion of the resulting gold prill using an aqua regia mixture, the solution was examined using a Varian 55B atomic absorption spectrometer. This device was equipped with an air acetylene burner, a 4-mA lamp current and a detection limit set at b5 ppb. Using a 10% HCl matrix and a 1000 ppm stock solution, gold standards were produced. Analytical precision and relative errors were estimated using replicate analyses of standards and field-split duplicates following ALS quality control protocols. Based on earlier research conducted in the savannah regions of northern Ghana and southwest Ghana, gold concentrations of 0.4 ppm or higher were deemed unusual (Griffis et al., 2002).

### 3.7.6 Multivariate statistics

#### 3.7.6.1 Hierarchical cluster analysis

According to Bouguettaya et al. (2015), cluster analysis offers a wide range of techniques for categorizing variables and instances according to their similarities and differences. The three main categories of cluster analysis include approaches that allow for overlapping clusters, partitioning methods, and hierarchical methods (agglomerative or divisive). There are numerous specialized techniques and algorithms within each type of method. The agglomerative hierarchical cluster analysis may be the most used type of analysis. Additionally, the advocates claimed that the cluster for this particular group of approaches is each of the n subjects. Step 1 involves joining the two subjects that are the most related to create one cluster that includes all n-1 clusters. In Step 2, the two clusters that are the most similar are combined to form one cluster, resulting in all n-2 clusters. Each subject is placed in the same cluster that forms at Step n-1 until the process is repeated. The outcome is a hierarchical classification tree (dendrogram). In data analytics, hierarchical clustering is crucial, especially given the exponential rise of real-world data. Instead of relying on distance metrics or measures of association, Ward's Method, according to Murtagh & Legendre (2011), treats cluster analysis as an analysis of variance issues. This approach uses an agglomerative clustering algorithm that starts with the leaves, moves through the branches, and ultimately reaches the trunk. The distance between variables is thought to be measured using the squared Euclidean distance. Additionally, the data is vertically oriented, and the standardized converted value is the z-score. According to Schonlau (2004), a phenon line should be drawn across the dendrogram to distinguish the different clusters of interest to make it simple to identify the individual cluster members.

### 3.7.5 Bivariate statistics

To evaluate the strength of the links between various elements in the data sets, a correlation matrix was created in SPSS using Pearson's correlation coefficient. As indicated in Table 3.1, the correlation coefficients were categorized based on the classification.

**Table 3.1: Interpretation of the size of a correlation coefficient (r) (Hinkle et al., 2003)**

| Size of correlation (±) | Interpretation of correlation |
|---|---|
| 0.90-1.00 | Very high |
| 0.70-0.90 | High |
| 0.50-0.70 | Moderate |
| 0.30-0.50 | Low |
| 0.00-0.30 | Negligible |

# CHAPTER FOUR

# RESULTS AND DISCUSSION

## 4.0 Introduction

This chapter elaborates on the results and interpretation of the geophysical, petrographical and geochemical datasets collected from the Kibi gold district. Data collected from each methodology was interpreted appropriately supported by tables and figures. The interpreted data was discussed to provide a detailed understanding of the lithology, structural hosts, pathfinders and overall gold mineralization trends and patterns in the Kibi gold zone. The geophysical survey measured ground elevation, radiometric, magnetic field, resistivity and induced polarization. The data interpretation produced an interpretive pseudo-geology map of the region. Numerous geological units and distinct geophysical units can be connected.

## 4.1 Airborne geophysical surveys

### 4.1.1 Magnetic anomalies in the study area

The structural trends and pattern of the study area, principal elongated structures, as well as, folded structures and faults are represented as several short discontinuous lineaments (Figure 4.1a). The visual and manual interpretations were applied to identify different structures. From these interpretations, structural diversity and the major NE-SW shear zone that crosses the study area are visible (Figure 4.1a). Six Target areas are defined and recommended in this thesis for further ground truthing. Two kinds of structural trends were identified:

- NE-SW Resistive-type: following the silicification model for gold mineralization, areas of low conductance/susceptibility have been targeted within the interpreted conductive graphitic shear zones (Afiasa, Gold Mountain and Adukrom-Segyemase satellite gold deposits) and the interpreted conductive graphitic sediment units (Figure 4.1b)

- NE-SW granitoid-type: shear/ fracture zones in basin-type granitoids are known to exhibit sub-economic to economic gold mineralization in the study area. Due to the predominant shearing and fracturing, rock types underlying the Agyapoma and Cobra Creek areas are highly deformed. These targets have been identified and delineated for further exploration targets where the trends and patterns of the interpreted fractures intersect the interpreted basin-type granitoids as shown in (Figure 4.1b).

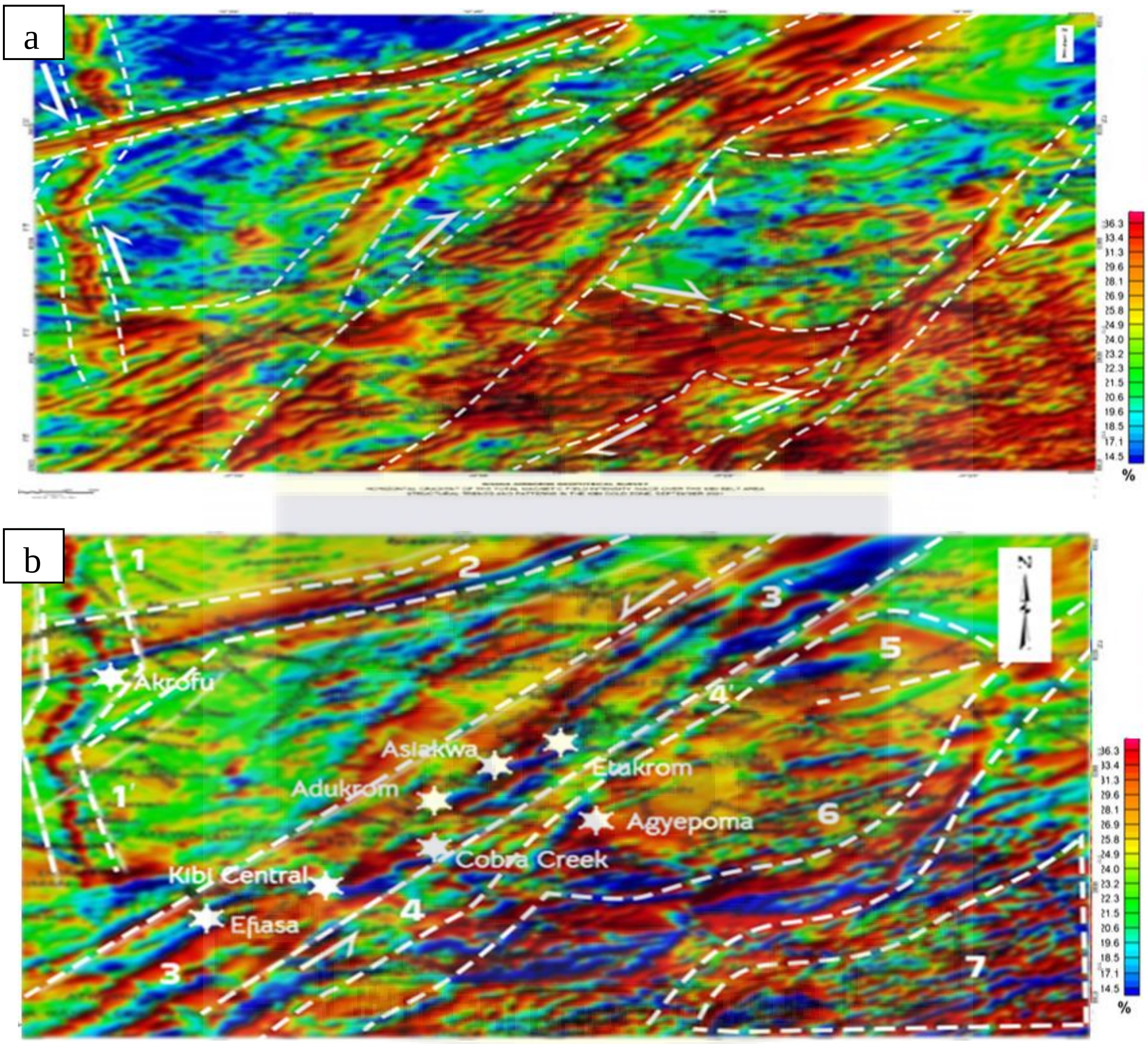

**Figure 4.1: a) Magnetic intensity map showing structural trends and deformational patterns in the study area b) Location of satellite lode gold deposits on the magnetic intensity map**

Magnetic anomaly peaks were superimposed on the geology of the study area. The total magnetic field's analytical signal transforms magnetic data into anomalies whose shapes can be utilized to infer the depths of the margins of magnetic bodies. These anomalies' maxima mark the boundaries of magnetic bodies. The airborne geophysical data suggest that the Kibi gold belt tapers to a spot about 43 km beneath the Volta River Basin. It is truncated by NW-SE faults (T1 and T2) and wider westwards than the geologically established margin with two major NE- SW mafic dykes MD1 and MD2, which also mark a major fault (Figure 4.2). Eastwards on the study area over the undifferentiated granitoid, the magnetization level is low (shown in red) and characterized by a high relief pattern (Figure 4.2).

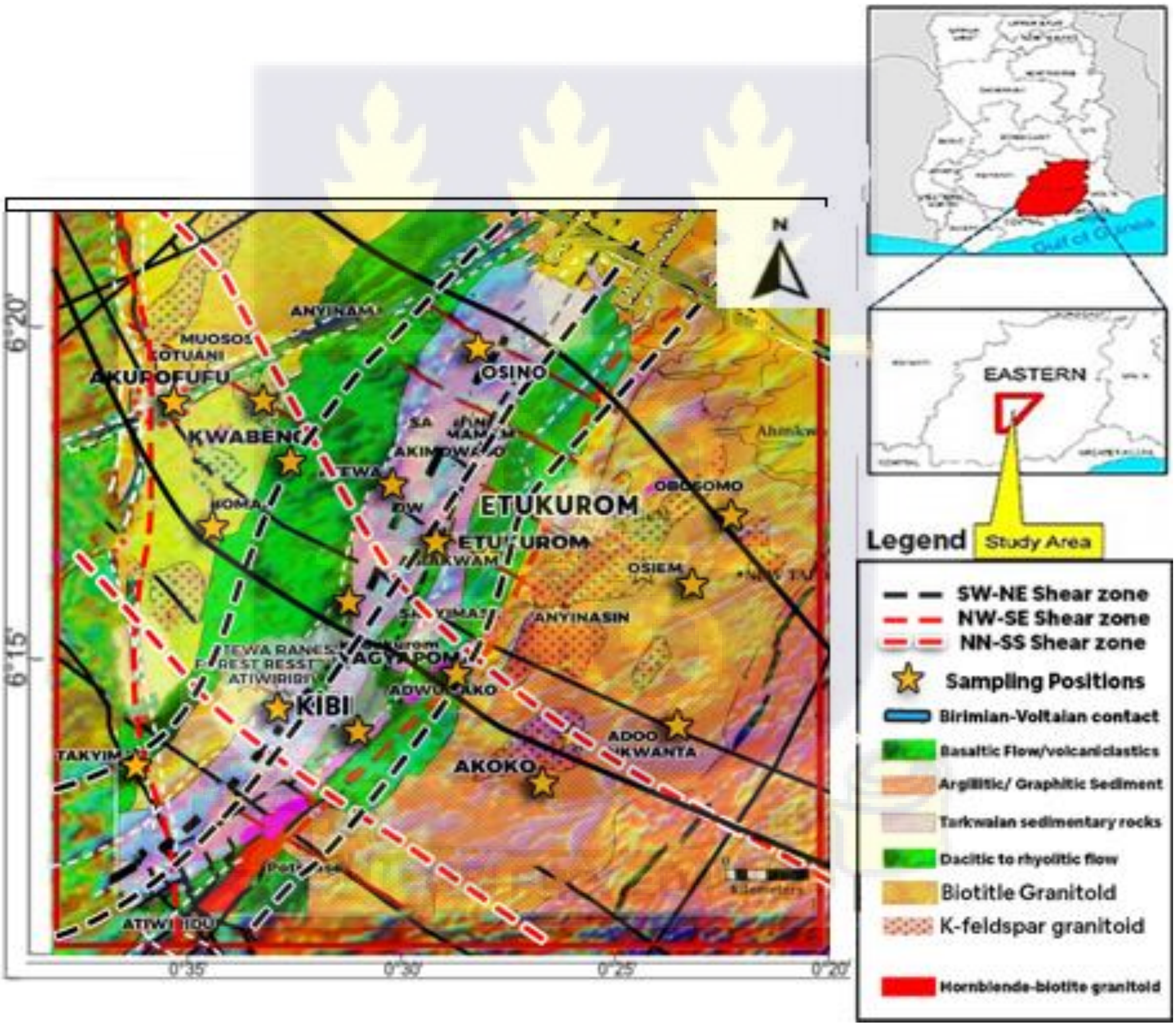

**Figure 4.2: The total magnetic field intensity showing major structures and magnetic zones in the study area, boundary shown in the red rectangle.**

Linear magnetic anomaly features (dykes, fractures, geologic contacts) sometimes show displacements and sharp amplitude changes that indicate faulting (Figure 4.3). The main fault trends NE-SW and approximately coincides with the regional shear zone of the Kibi – Winneba Belt. Major NW-SE fault lines (T1 and T2) truncate the shear zone; being displaced in several sections by minor NE- SW, north-south and east-west faults and dykes.

Several long-range NW-SE quartz veins associated dykes dissect the Kibi - Winneba Belt westwards. A major N-S fracture, filled with quartz veins, occurs in this study area (Figure 4.3). It extends from south to north (F1) within the magnetic image. It is older than the NE-SW dyke that extends beneath the southwestern parts of the Volta River Basin since its orientation changes direction in several sections and dislocated west of Kwabeng and Anyinam at the Akurofufu locality by late-stage tectonic events. The undifferentiated detrital sediments, mainly sandstone and conglomerates of the Tarkwaian Group show relative irregular and low magnetization patterns in Kibi, Pano, Segyimase, Asiakwa and Osino (Figure 4.3). These rocks are in contact with the basaltic, subvolcanic rocks and minor volcaniclastics of the Birimian Super-group at Kibi East, Agyapoma, Ajomoku and Etukrom exhibit high magnetization levels with moderate to irregular patterns.

The horizontal gradient of the magnetic field is useful in delineating geologic contacts between the various rock units and potential areas for gold and base metal mineralization (Gobashy et al., 2023). Anomalous gold and other base metals can be found in Akoko, Kibi, Kwabeng, Osino, Ettukrom, and Anyinasin (Figure 4.4). This first vertical derivative of magnetic field intensity maps lithology and major structural features, which are important in locating mineralization. The magnetic pattern (Figure 4.4) reveals that the whole area has high relief with magnetic lineation similar to the NE-SW trending Sefwi Belt. The trend (E-W, NE-SW, and NW-SE) of these dykes and fractures, as well as the folding, shearing, and displacements of some of these linear features have been more clearly defined. A north-south lineament (fracture) having a relatively low magnetic level occurs at the western parts of the map. It shows a significant displacement at the Akurofufu locality in the NW-SE direction as well as in several places that indicate faulting and also that it is older than the mafic dykes and faults existing in the area.

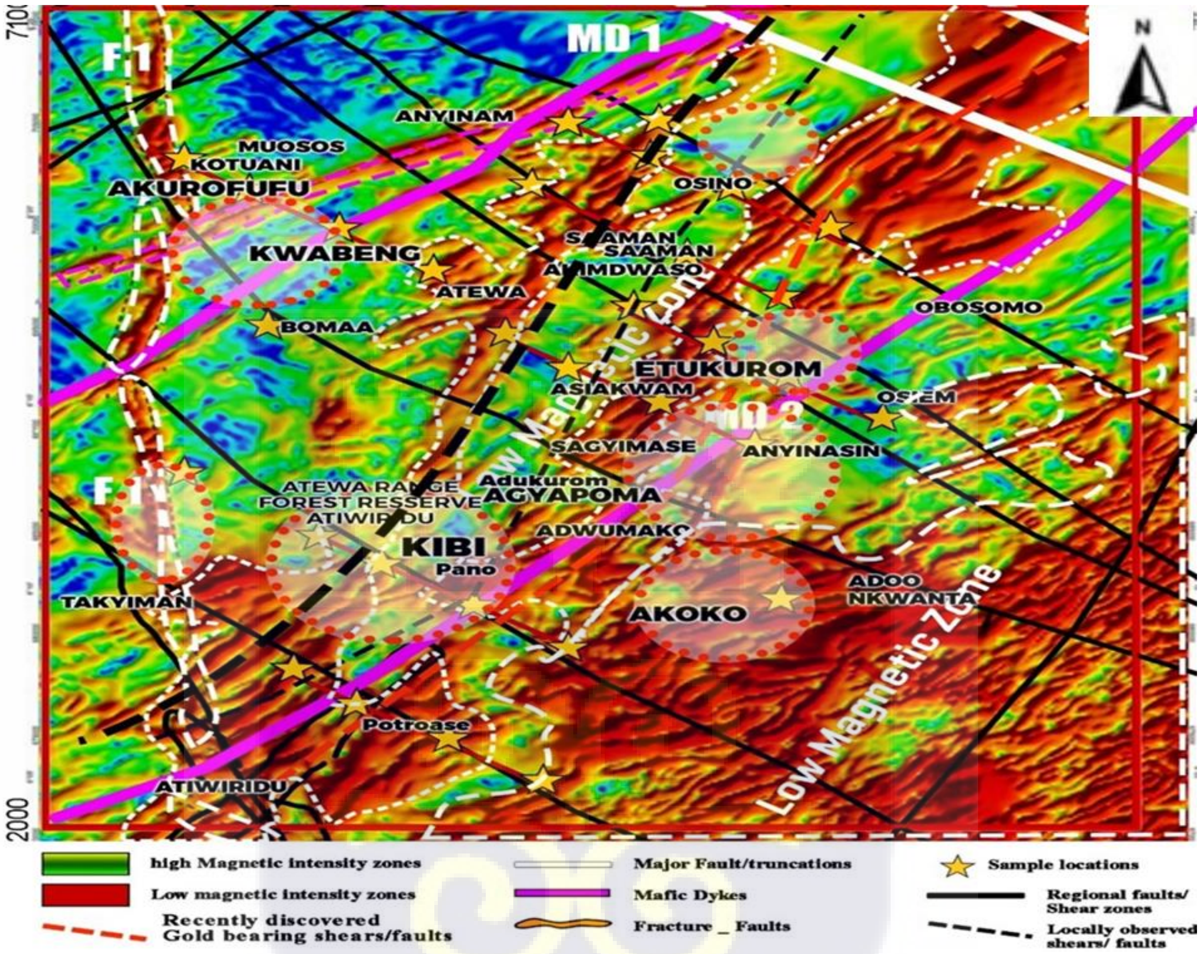

**Figure 4.3: Magnetic intensity map showing potential areas for gold and base metal mineralization (indicated by red short dashes circle).**

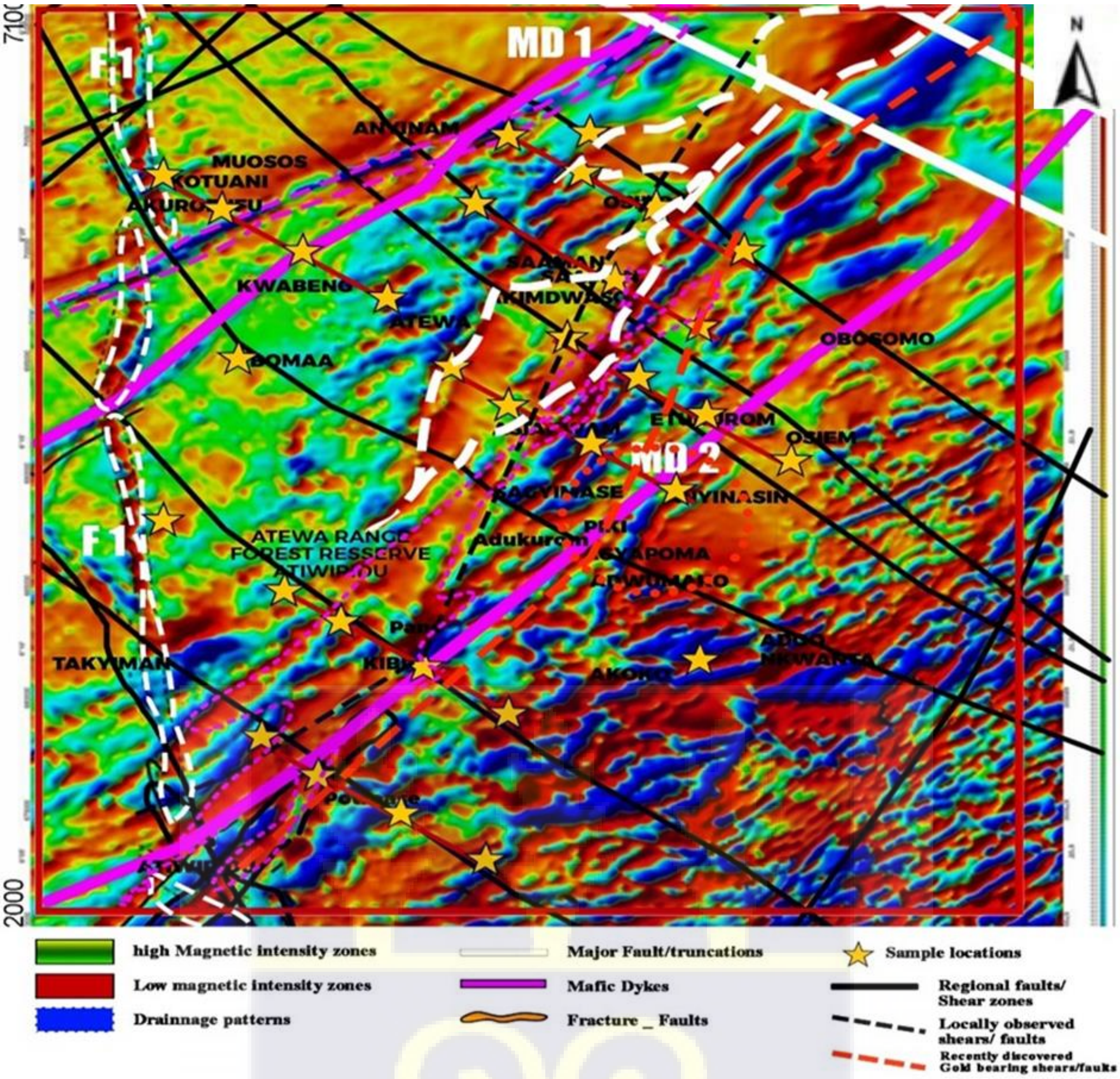

**Figure 4.4: This component of the magnetic field intensity (First Vertical Derivative) reveals the whole area has high relief with magnetic lineation similar to the NE-SW trending Sefwi Belt.**

The Birimian Supergroup, which is comprised of dacitic and rhyolite rocks to the east, depicts a high magnetization level and high relief magnetic pattern. Biotite and muscovite, undifferentiated, granitoids in this part of the study area illustrate similar magnetic nature in the map. These structural features (mafic dykes, fractures, faults, shearing and dislocations) as revealed in the total as well as the first vertical derivative (Figure 4.4) of the total magnetic field, are important tectonic structures in focusing mineralization (eg. the bauxite deposits, principal alluvial gold deposits and manganese occurrences found in this study area).

Generally, both Birimian and Tarkwaian rock units in the study area are intruded by mafic dykes that trend NNW, east-west and north-south (Figure 4.5). The Kibi gold district lies over high magnetic levels within the Kibi-Winneba Belt shear zone with most of these dykes and faults criss-crossing it. These structures are potential areas for gold and base metal mineralization. Structurally, the northwestern portion of the study area occupies a local antithetic, dextrally-sheared domain (Figure 4.3), within an overall sinisterly-sheared and transposed Kibi- Winneba Belt.

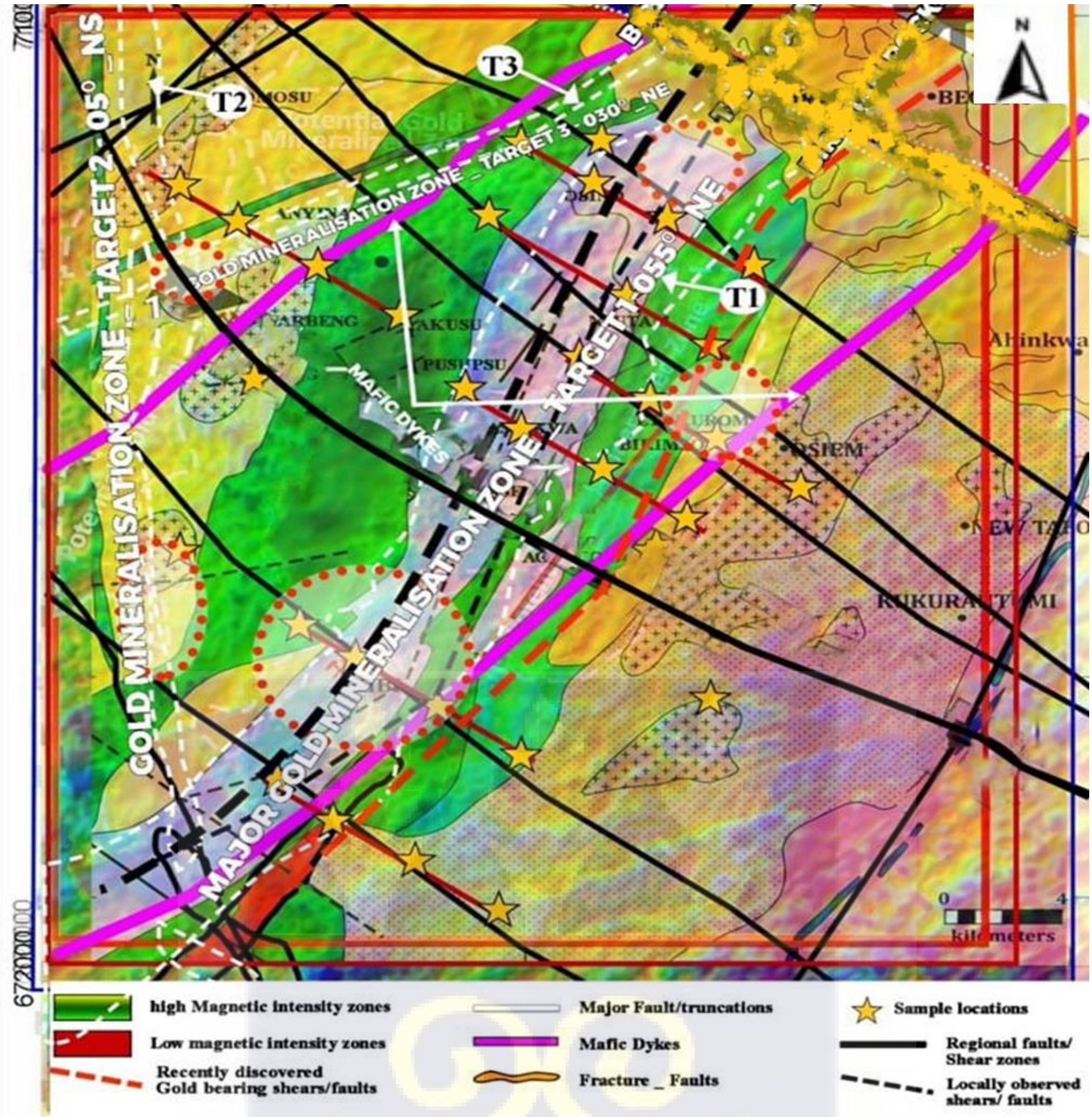

**Figure 4.5: Geology superimposed on integral maps of total magnetic field intensity, horizontal gradient, first derivative and analytic signal of the study area.**

### 4.2 Gamma-ray spectrometry (Radiometric) and its implication for gold mineralization in the study area

The ratios of radioelement concentrations (Th/K, U/Th, U/K) are useful indicators of magmatic to hydrothermal processes relating to mineralization (Abdel-Hakeem et al., 2023). High potassium (K) levels correlating with low Thorium or low Th/K ratios are usually noted in gold areas. The Th/K ratio anomaly defines the mineralized structures. The study area is marked by two distinct light - coloured areas that indicate high Potassium (Figure 4.6), Thorium (Figure

4.7) and Uranium (Figure 4.8) as delineated potential gold mineralization zones. The central portion of the ternary map in the study area depicts a northeast-southwest trend covering areas such as Kibi, Pano, Asiakwa, Agyapoma, Ettukrom, Osino and Ankaase. The northwest portion of the ternary map shows moderate to high concentrations of Potassium, Thorium and Uranium covering areas such as Kwabeng, Akrofufu, Muoso, Asuom, Abomosu, Takyiman and Bomaa (Figures 4.6, 4.7 and 4.8).

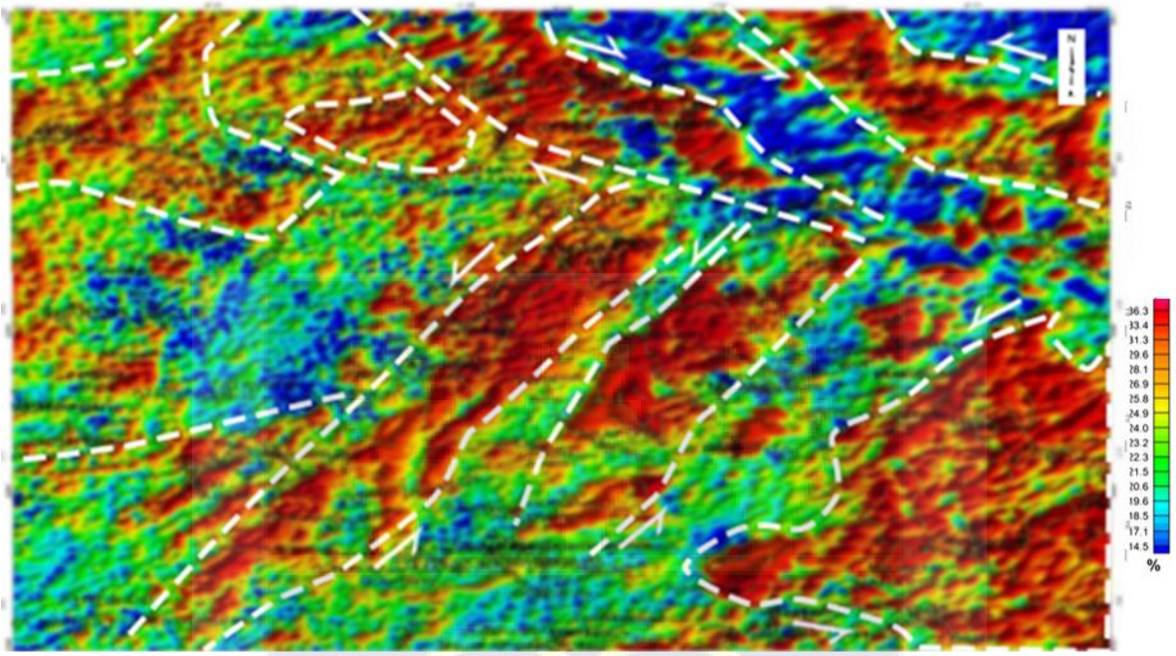

**Figure 4.6: Thorium concentration map for the Kibi gold zone.**

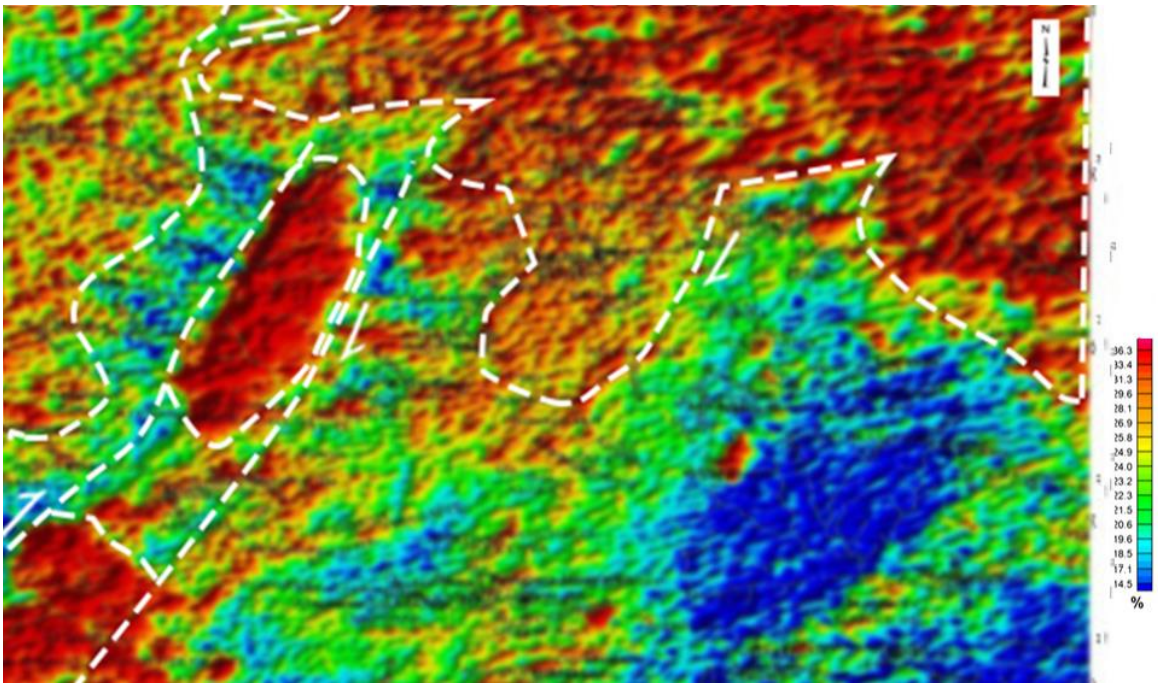

**Figure 4.7: Potassium concentration map for the Kibi gold zone.**

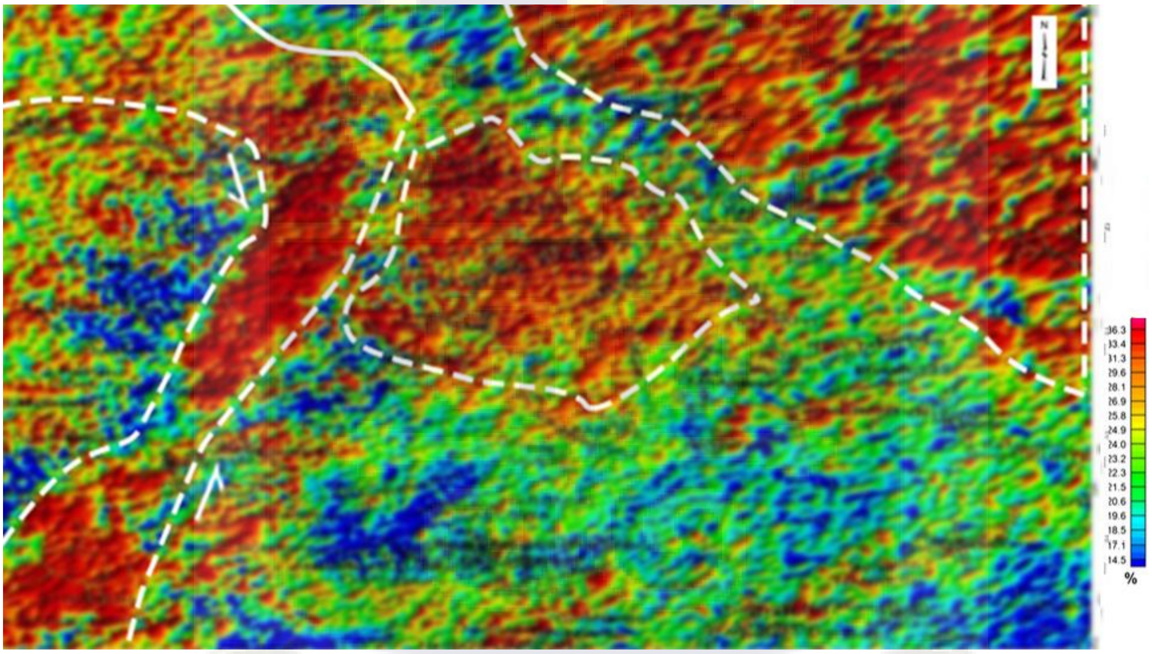

**Figure 4.8: Uranium concentration map for the Kibi gold zone.**

The Birimian-type granitoids in the Kibi gold zone are distinguishable on the ternary map (Figure 4.9). They appear to be of varying composition with some minor potassium-rich mineralization. Red depicts the highest K concentration; that is areas characterized by exposed granitic bodies. Green shows the highest Th concentration; that is various ferruginous materials at the surface. Blue illustrates the highest U concentration; that is calcareous sediments, soils and calcrete. Black to brown: low in all K, Th, and U: duricrusts and exposed bedrock (mainly greenstones). White to yellowish: highest in all three components (K, Th, U), which correspond to geomorphologically active areas with exposed weathered granite and sediments derived from granite. This ternary image of potassium, thorium and uranium radiated concentration marks the location and outer margins of the bauxite deposit Atewa range of hills with enrichment of thorium on the hilltop and enrichment of potassium down the slope at their rims. Radiometric measurements are essentially outcrop and surface mapping techniques. The data show clearly a tectonic break at the southern parts of the hill range, where two lines dip in the radiation hues, which coincide with the location of fault lines. Figure 4.10 is an integral map of a ternary image over the total magnetic field intensity and geological map of the Kibi gold zone. This composite map aligns continuously with the ternary image and confirms the fault zones, structural controls and possible fluid pathways in the study area.

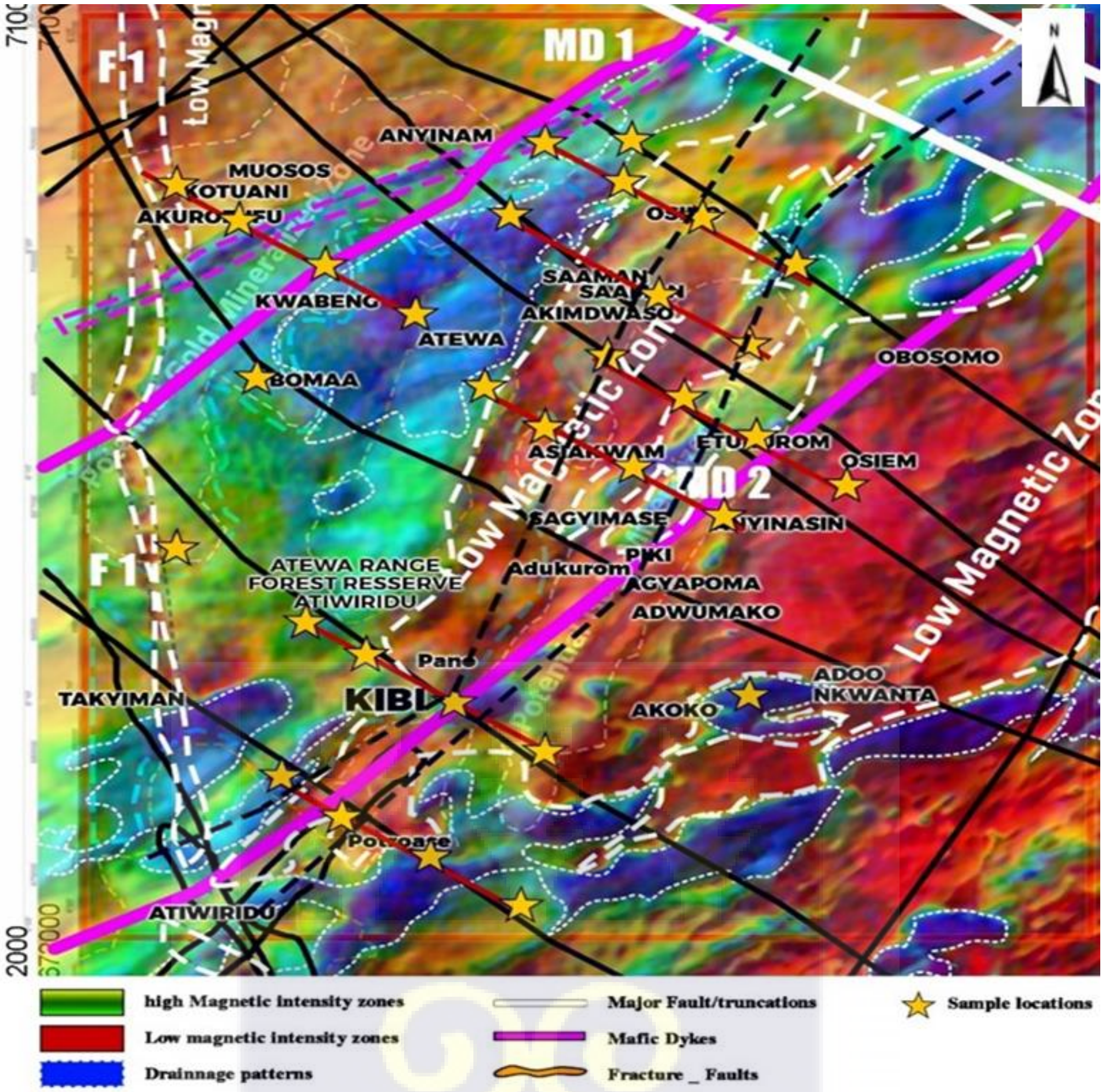

**Figure 4.9: Total magnetic field intensity over a ternary image (K, Th, U). The black straight lines are the regional faults and shear zones while the black short dashes are the locally observed shear and fault.**

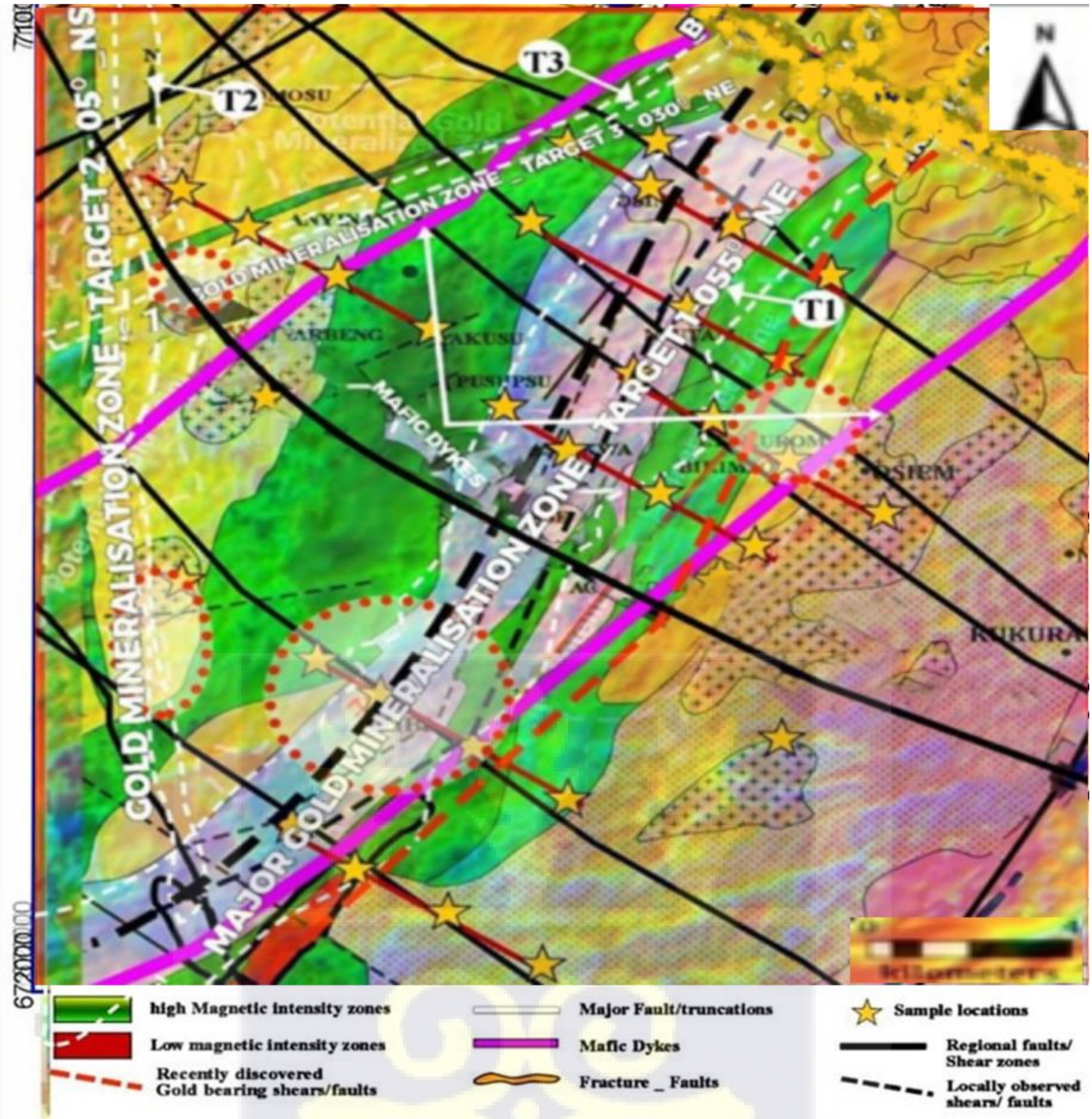

**Figure 4.10: Superimposed map of geology, the total magnetic field intensity, Potassium (K), Thorium (Th) and Uranium (U) images of the Kibi gold zone.**

## 4.3 Ground Geophysical Resistivity and Induced Polarization

### 4.3.1 Ground magnetic survey

The ground magnetic survey was conducted in the study area to help define the lithological and structural patterns of the mineralized trend, and prioritized trench/drill targets in the study area. A soil geochemical grid, totaling approximately 180 line- kilometers with station readings every 12.5m along the lines was employed in this study. The survey identified the satellite lode gold deposits with the magnetic susceptibility domains reflecting local lithological units and a possible structural deformation corridor. The south-western portion of the grid is underlain by rocks exhibiting relatively high magnetic.

A NE-trending, low magnetic susceptibility area situated between two moderately magnetic units defines the northeastern quarter of the grid. The induced polarization (IP) scan discovered a highly charged and conductive corridor that is spatially associated with this linear, non-magnetic area. This association may be connected to the host rock's magnetite breakdown caused by structure/alteration. The corridor's low magnetic susceptibilities may also be related to the heavy clays and graphite present.

### 4.3.2 Ground IP/resistivity survey

In order to identify trench/drill targets and describe the lithological and structural pattern of the mineralized trend, a portion of the study area (about 64-line kilometers) was gridded using IP/Resistivity survey. Using a Pole - Dipole Array with a dipole length of 50m and dipole separations of n = 1 to 6, the approximately 64 line-kilometer IP/Resistivity (Time Domain) survey covered the entire magnetic survey gold-in-soil trend at 200 m spacing, with about 100 m detail sections centered on known gold showings (38 survey lines). At n = 6, this survey design produced an estimated depth of investigation of between 175 and 200 meters.

The IP/Resistivity survey identified 2 main resistive domains exhibiting a close spatial relationship with the main five (5) gold-in-soil anomalies of the Kibi Gold (Zones) as follows;

- The Kibi Central Gold Mountain
- The Etukrom Gold Zone
- The Agyapomaa Gold Zone
- The Akoko Gold Zone
- The Adukrom – Asiakwa areaGold Zone

## 4.4 Resistivity and induced polarization (IP) models for the study area

### 4.4.1 Resistivity and induced polarization (IP) model of line 1 (Etukrom area)

The inverse model obtained from the profile (line 1) shows high resistivity anomalous body on an average depth between 120 to 140m which indicates the present of schist, basalt and granitic rocks as observed during the field mapping (Figure 4.11a). The discontinuity at 240 m has been interpreted as a possible fault and may serve as a spot for mineral accumulation. The thin conductive layer at the surface may represent clay materials that are present on line 1. There is a high chargeability anomaly that extends from about 330m to 1020m. A chargeability value as high as 260 msec could be further investigated. High chargeability is closely related to sulphide accumulation which can usually hold gold. The depth of this anomalous body according to the inversion model may be about 100m to 170m. The geophysical line 1 that was surveyed at Etukrom may hold a prospect and could be investigated and possibly drilled at point A (960m) in Figure 4.11b.

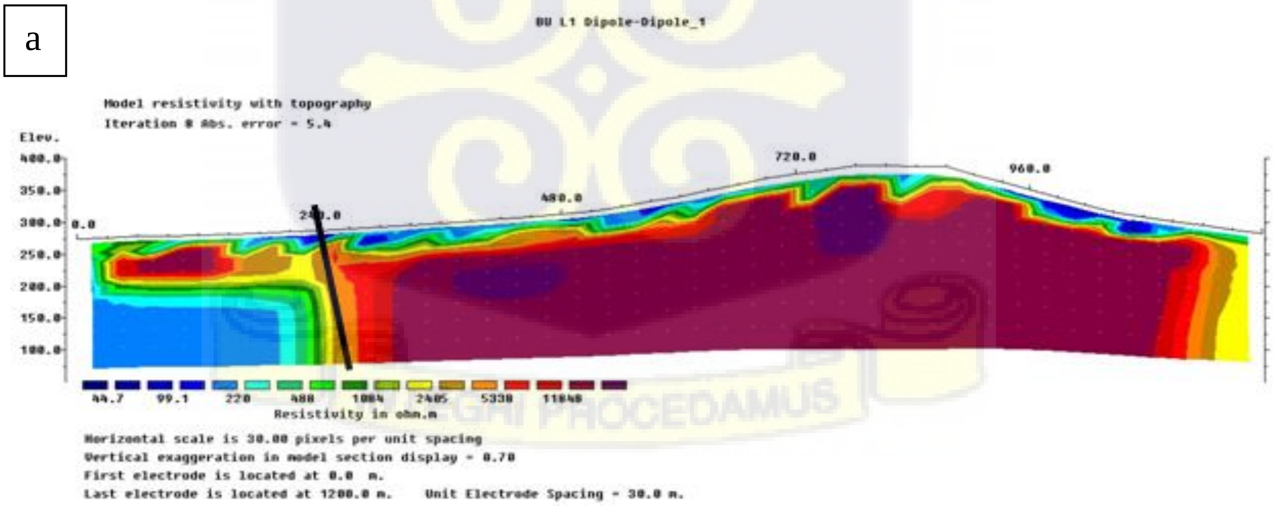

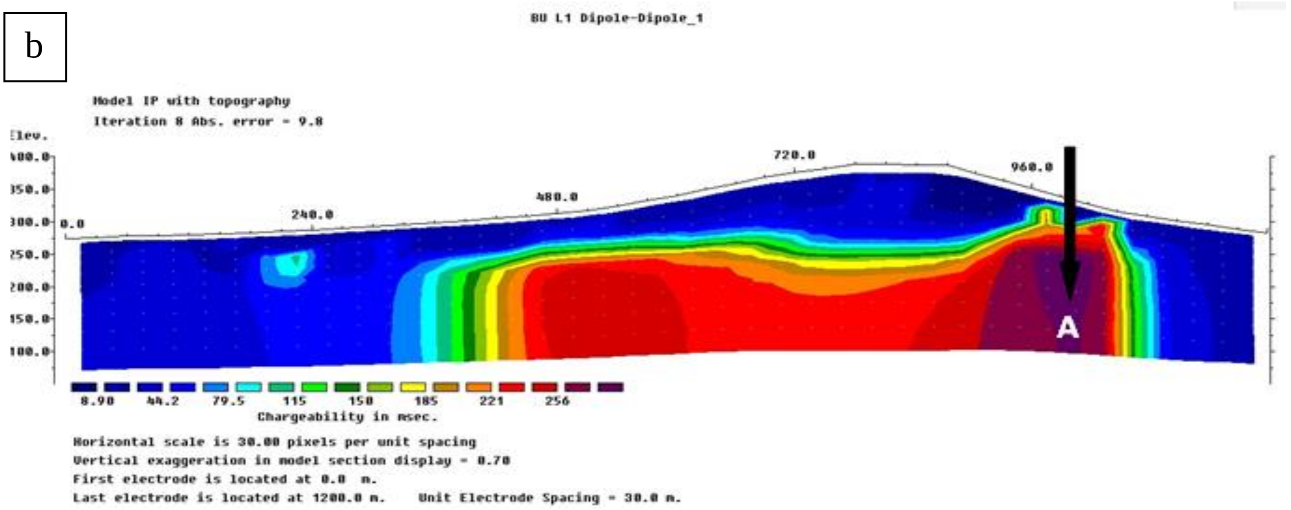

**Figure 4.11: Pseudosections of a) resistivity and b) IP for line 1 in the Etukrom area**

### 4.4.2. Resistivity and IP models of line 2 (Agyapoma area)

A low resistivity anomaly at 480m is sandwiched between high resistivity anomalies. This may represent a fracture filled with saturated geologic material, possibly clay or water. Figure 4.12a is the inversion model of line 2. Line 2 is at the southern part of line 1 and a high chargeability anomalous body was mapped here as well. The chargeability value (200 msec) indicates a possible sulphide body that suggests possible mineralization. Rock types such as graphitic phyllite, greywackes, carbonate schist and silicified quartz feldspar porphyries were the dominant outcrops observed during the mapping exercise. A high chargeability (200 msec) anomalous body extends from 0m and peaks at about 480m. This high chargeability anomaly at point A (680m) (Figure 4.12b) needs further investigation. The estimated depth of this anomaly is about 120m to 200m.

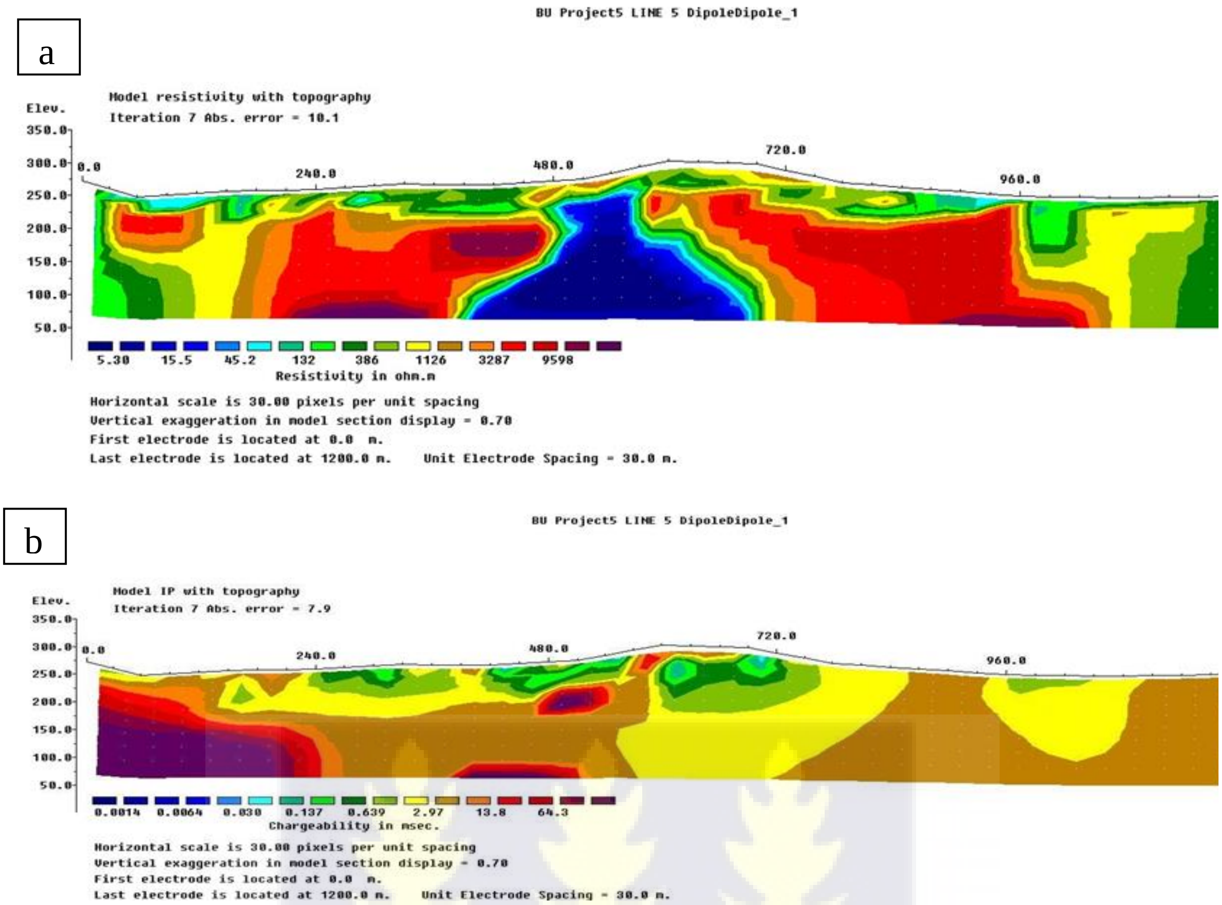

**Figure 4.12: Pseudosections of a) resistivity and b) IP model for line 2 in the Agyapoma area**

### 4.4.3. Resistivity and IP model of line 3 (Kibi area)

Figure 4.13a also reveals a resistive anomaly from the resistivity distribution on line 3. This anomaly is within an average depth of about 75 to 120m. Thin conductive clay material is also represented with a resistivity of about 150 Ohm.m. A relatively high chargeability anomalous body was also mapped at a depth of about 120 to 170m on this survey line. The chargeability (15.0 msec) of line 3 (Figure 4.13b) was not as high as the previous lines (Lines 1 and 2). This could be attributed to the presence of granitoids, sandstone, conglomerate and shale in the area. Notwithstanding, further investigation could be conducted around 720m at point A (Figure 4.13b).

a

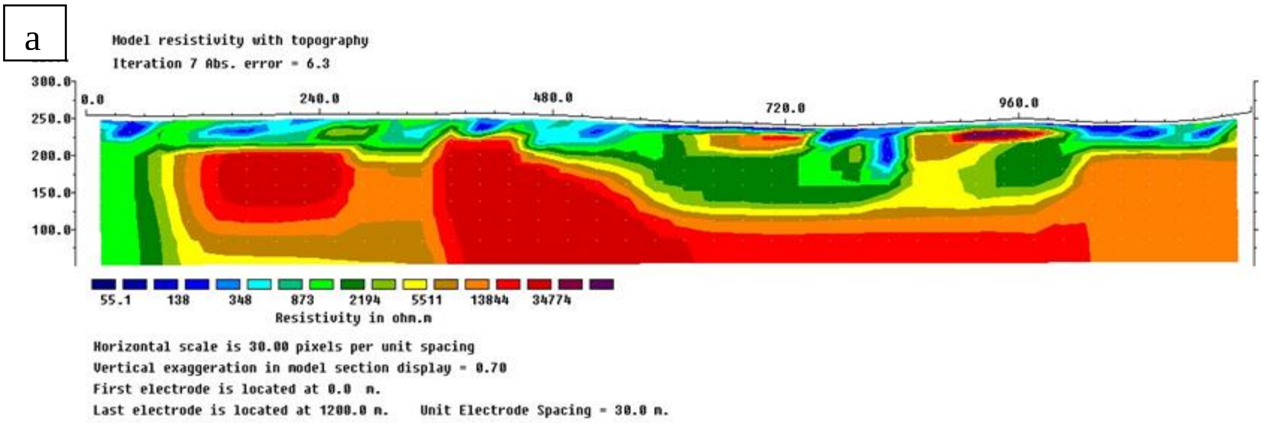

b

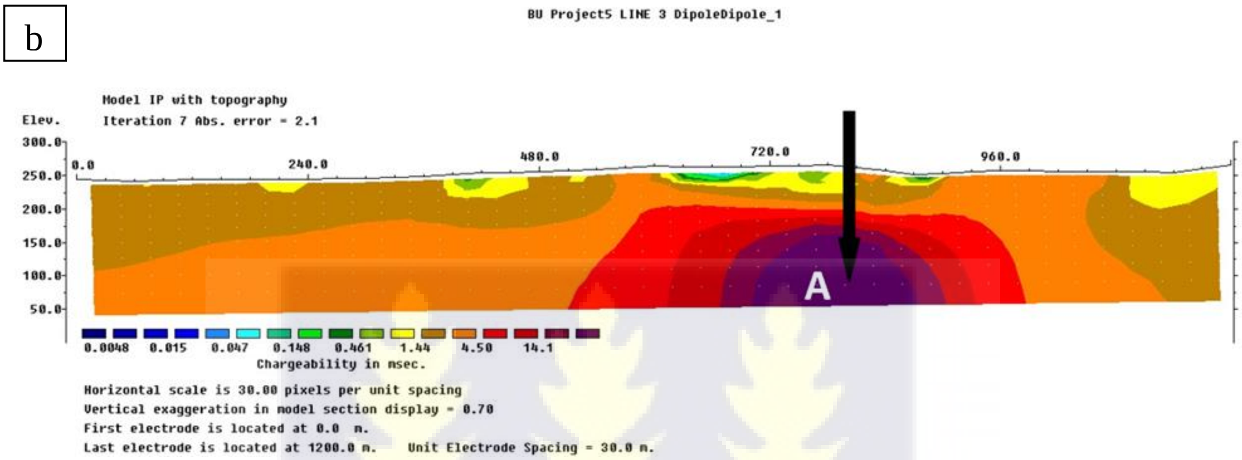

### 4.4.4. Resistivity and IP models of line 4 in the Hemang area

Figure 4.14a shows the inversion model from resistivity distribution on line 4 at Hemang in the northmost of the survey area. A very large resistivity anomalous body occurs between 120m and 450m. Beyond 450m a less resistive anomaly is present which may indicate a different geologic body. This is consistent with the high geologic bodies that are buried on the other survey lines according to inversion models. High chargeability anomalous bodies were delineated at around 240m and 930m (Figure 4.14b). At a depth of about 175m, a relatively high chargeability anomaly is also present. These signatures suggest the Hemang area might be mineralized.

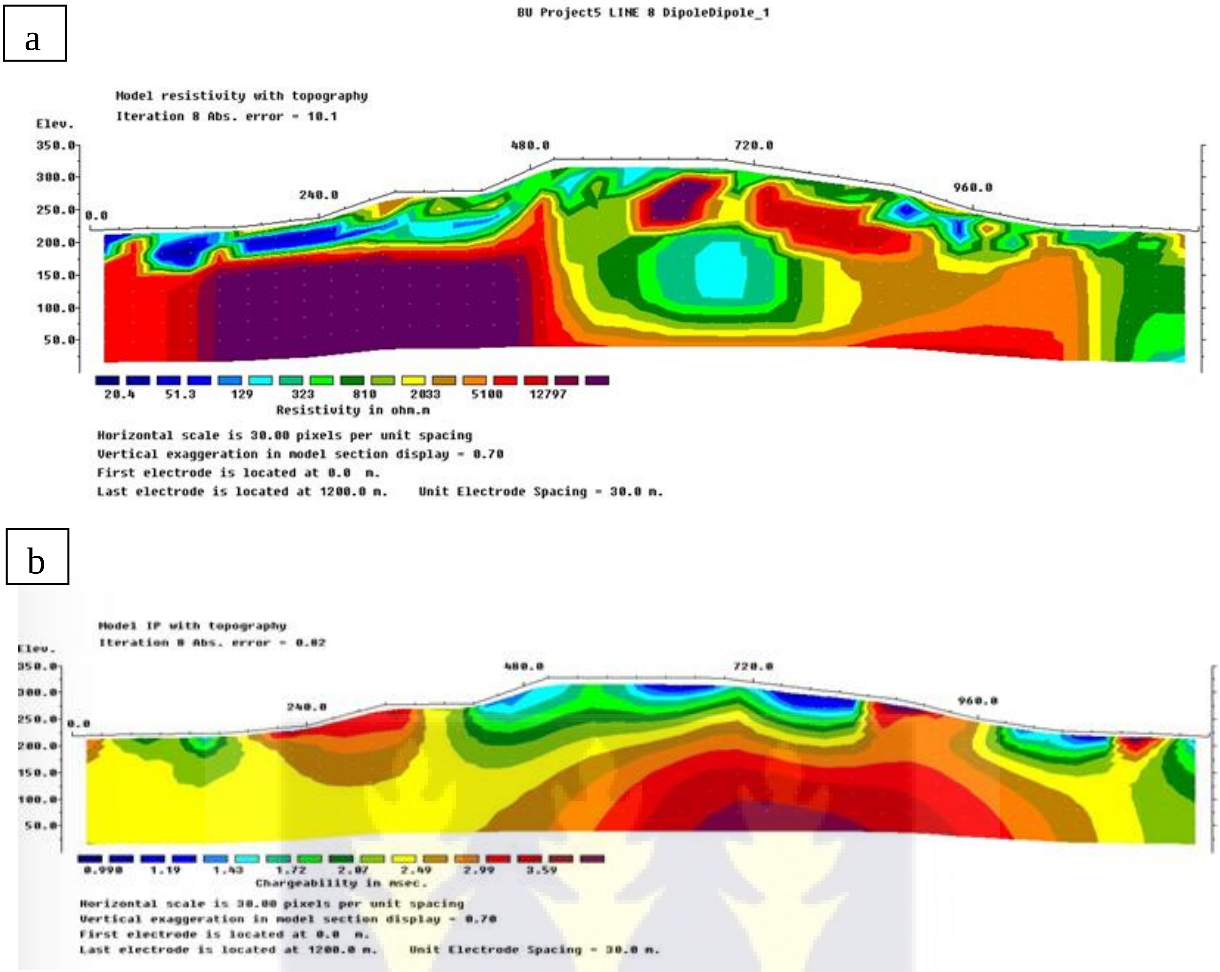

**Figure 4.14: Pseudosections of a) resistivity and b) IP for line 4 in the Hemang area.**

### 4.4.5. Resistivity and IP models of line 5 (Adukrom - Asiakwa)

Large resistivity anomalies occur between 240m and 480m and truncate between 570m and reappear around 840m. This discontinuity may represent a fault or a weathered-away geologic material. The top layers have a low resistivity value which represents the clay material that is predominant at the surface. Figure 4.15a represents the inversion model of survey line 5. Figure 4.15b represents the chargeability tomography of Line 5 surveyed around Adukrom and Asiakwa areas. Relatively high chargeability anomalous bodies occurring between 480m and 930m can be attributed to the underlying rock types such as granite, quartz, basalt and schist. This area should be area could be investigated. The resistive domains are interpreted to reflect the granitoids and/or carbonate-silica alteration associated with the known gold mineralization. The significant NE trending center corridor with high conductivity and high chargeability, which probably belongs to a graphitic shear zone was identified by the survey. IP anomalies could be indicators of dispersed sulfurides connected to gold mineralization. Quoting Hobbs et al. (1976), structural geology is the study of "how rocks respond to the application of deforming forces, and with the structures that result from deformation." This covers the evaluation and interpretation of geophysical aerial photographs. In geology, "structure" refers more broadly to the 3-D geometry of all rock units within an area as well as the processes that have formed that geometry over time. Figure 4.16, illustrates detailed structural delineations from aeromagnetic data in the Kibi Gold Zone. An essential tool for comprehending structural controls and defining and interpreting the kinematics of gold mineralization in the study area is the intrinsic capacity of magnetic rock bodies to "see" in three dimensions. Ground elevation, radiometric, magnetic field, and electromagnetism (resistivity) were all measured during the survey. There is a correlation between distinct geological units and different geophysical units.

The structures represented in the lineament map comprise regional foliations, folds, fractures and shear zones. A few morphological lineaments were present around the river channels with structural controls and the lithologic border. Straight sections of river channels, which are often supposed to curve, show that these morphological lineaments appear to have a structural origin. From this study, three orientations of lineaments can be distinguished:

- NE-SW, which is the predominant orientation (first-order structures),
- NW-SE, which is the secondary orientation (second-order structures)
- N-S, which is the least abundant in the Kibigold zone. The N-S trending lineaments are few and are identified in the northwest to the SW part of the study area (Figure 4.16).

Generally, the central to the south-east margins of the study area are strongly deformed and folded indicating a host ductile rock unit mainly the greywackes. The southwestern region of the study area is moderately deformed and folded.

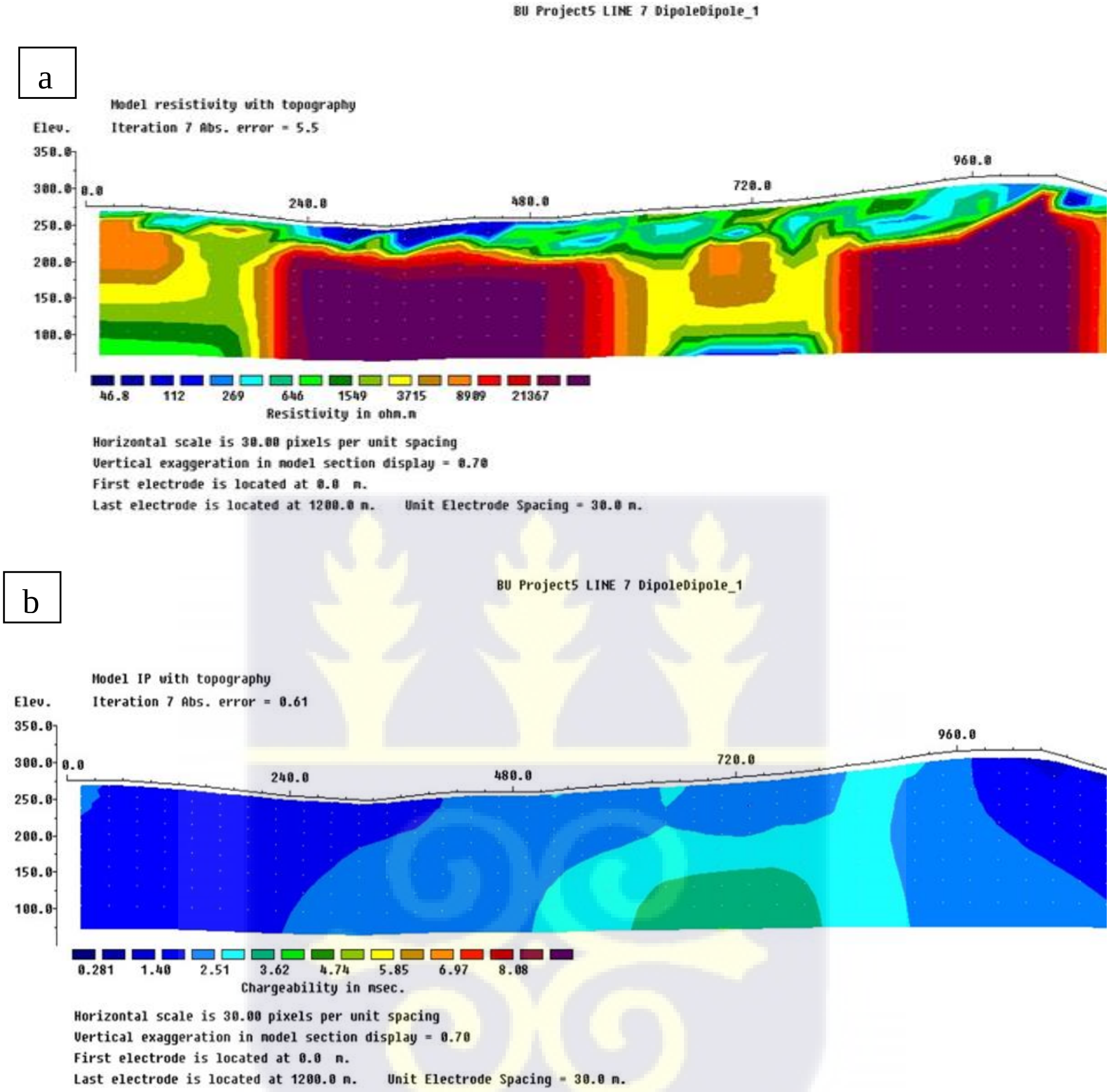

**Figure 4.15: Pseudosections for a) resistivity and b) IP for line 6 (Adukrom – Asiakwa area) within the metasediments (greywacke and epiclastic rocks).**

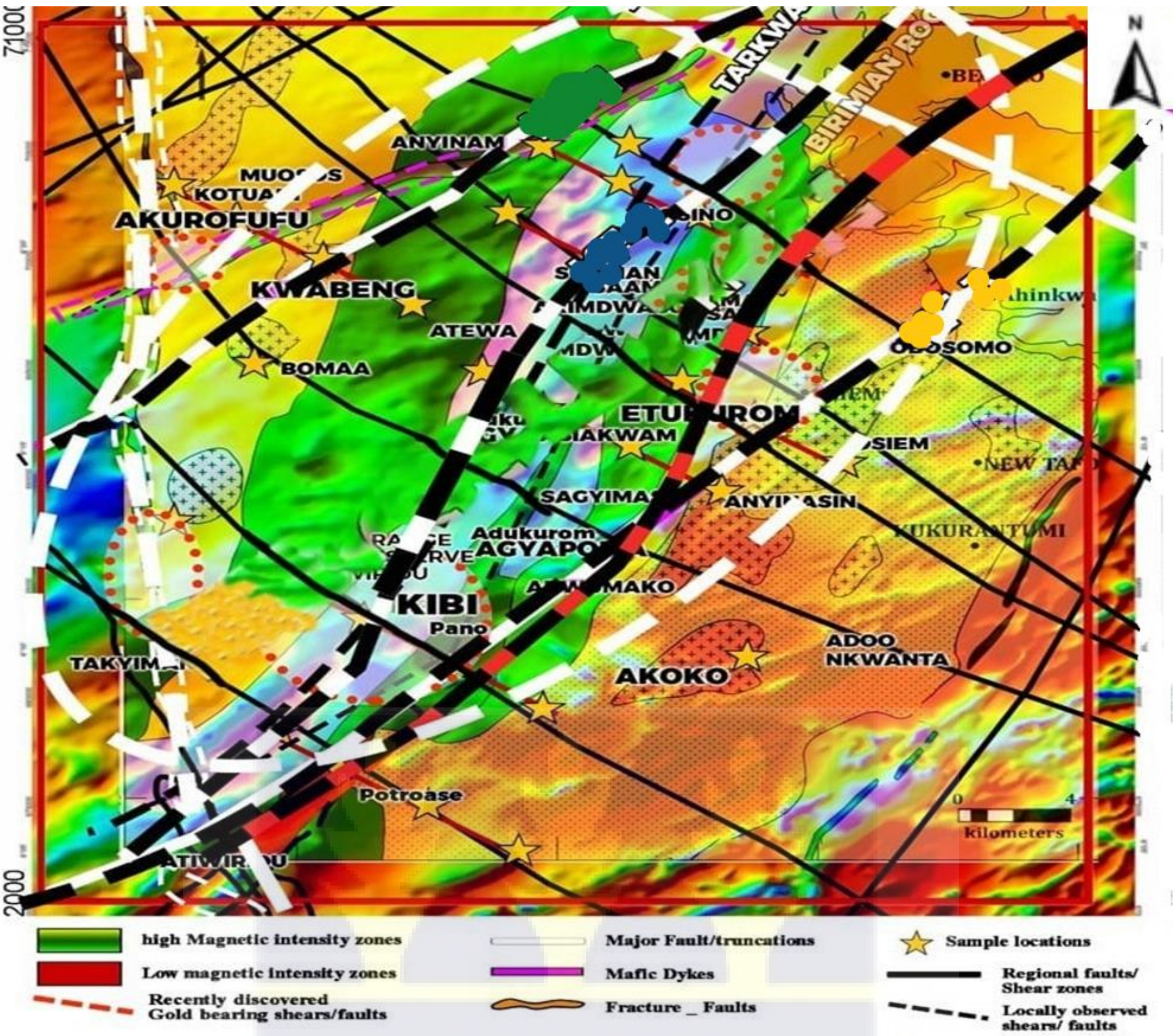

**Figure 4.16: An integrated structural map showing structural trends, sampling locations, geology and deformational patterns in the study area.**

## 4.5 Rock distribution in the study area

Generally, the study area (Figure 4.17) is overlain by surface deposits of sand or gravel, or more commonly, angular or subangular quartz pebbles, derived doubtless from the vast numbers of quartz veins that intrude the rocks of these parts. These surface deposits are often, either in whole or in part, laterised, and yield a red soil which may overlie sandstones and quartzites of the Tarkwaian Group.

Metavolcanic and metasedimentary rocks underly the Kwabeng, Anyinam and Tachiman communities of the study area. The metavolcanics are made up of basaltic and andesitic rocks while the metasediments are sodic greywackes, schist (carbonate chlorite schist, quartz-carbonate schist and mylonitic quartz chlorite schist) and epiclastic rocks. The granitic bodies present are encased in amphibole schists and are very often porphyritic with predominant alkali feldspars. Aplitic varieties of the granite occur Akrofufu, and in the weathered state are sometimes quite difficult to distinguish from quartzites. Generally, these granitic bodies are slightly foliated due to the alignment of mica and feldspar phenocrysts in a northeasterly direction.

Detrital sediments, sandstone and conglomerates were observed in artisanal mining pits in Akyem Apapam, Afiasa, Kibi, Sagyemase, Asiakwa and Osino areas. The contact of the detrital sediments and the subvolcanic rocks is well exposed at Potroase and Adukrom. This contact is characterised by an NNE-SSW mineralized shear zone which is well exposed at Agyapoma and Etukrom where lode gold artisanal mining is prominent. Generally, the area is moderately deformed owing to the presence of fractures, foliation, lineation, folds, dykes, shear zones and faults (Figure 4.17).

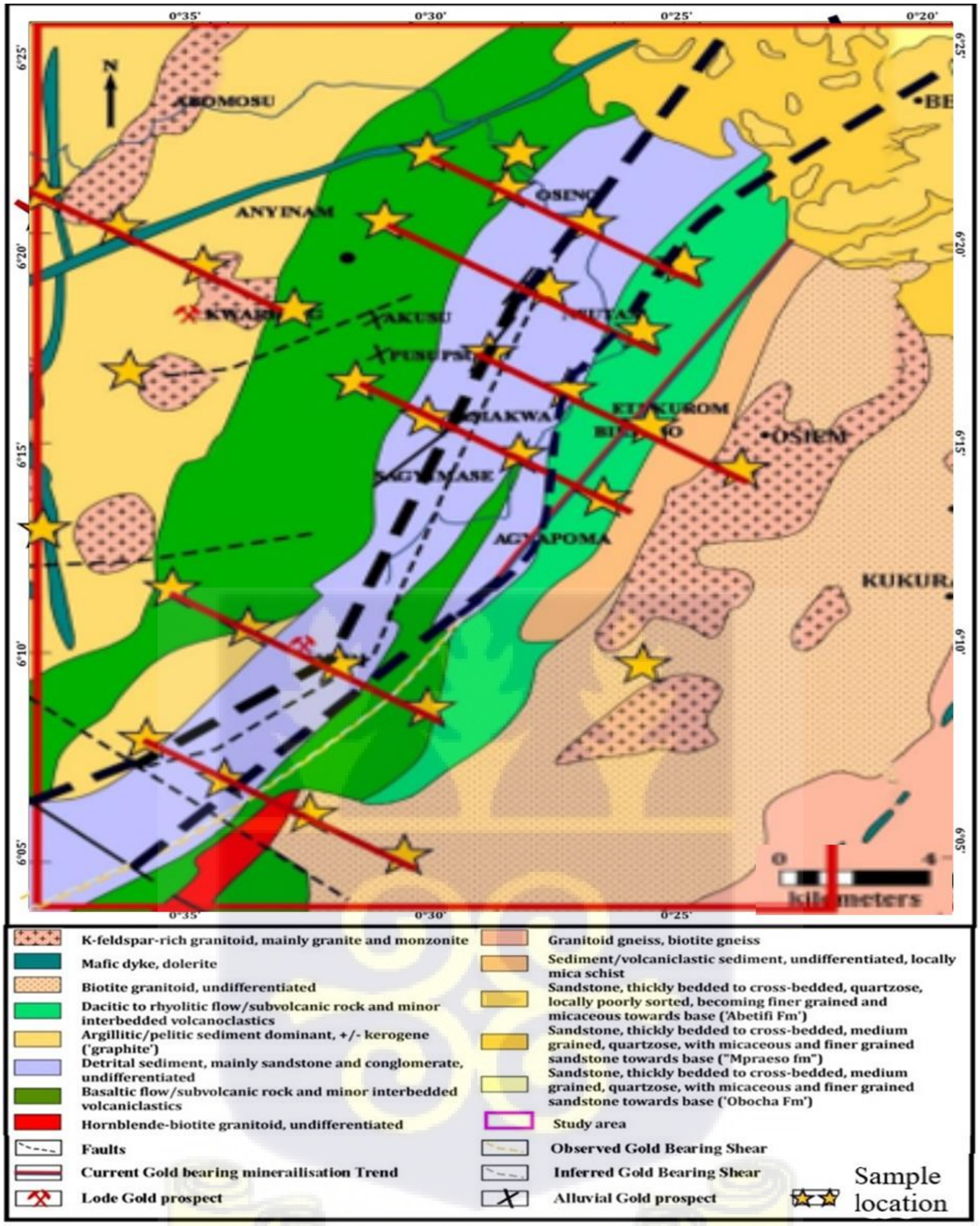

**Figure 4.17: Geological map showing the approximate positions where rock samples were collected (yellow stars) in the study area.**

### 4.5.1 The metasedimentary rocks in the study area

The metasedimentary rocks underlying the study area are schist, quartz-carbonate schist, and quartz chlorite schist which is often mylonitic.

### 4.5.2 Schists

Outcrops of schist occur on top of the Etukrom hill located at north easting part of the study area. The schist is greenish grey when fresh but dark grey when weathered and predominantly fine-grained, strongly indurated even though strongly deformed. The rock is sandwiched between volcanoclastic rock (andesitic tuff) and feldspathic greywacke (Figure 4.18a). In the field, the rock is highly deformed probably due to compressive forces, heat, and hydrothermal activities. The exposed contact observed (Figure 4.18b) is characterized by intense deformation with slicking sides, brecciated weak zones, and associated quartz-carbonate alterations which have strong indications of mineral fluid pathway and fluid emplacements. Again, the schist shows significant deformation with abundant deformed medium-grained disseminated sulfides visible in hand specimen (Figure 4.18c). It appears to have undergone solid-state and ductile – deformation, with quartz and carbonate infiltrations and significant opaque and sulfide mineralization. The rock appears to have undergone polyphase deformation.

Some significant geological structures observed in this area are faults, fold fractures and various generations of quartz stringers, veins and veinlets which occasion crosscut others (Figure 4.18d). Due to the intense deformation, the schist in the study area can be subdivided into three categories namely: carbonate chlorite schist, quartz-carbonate schist and mylonitic quartz chlorite schist based on mineralogy.

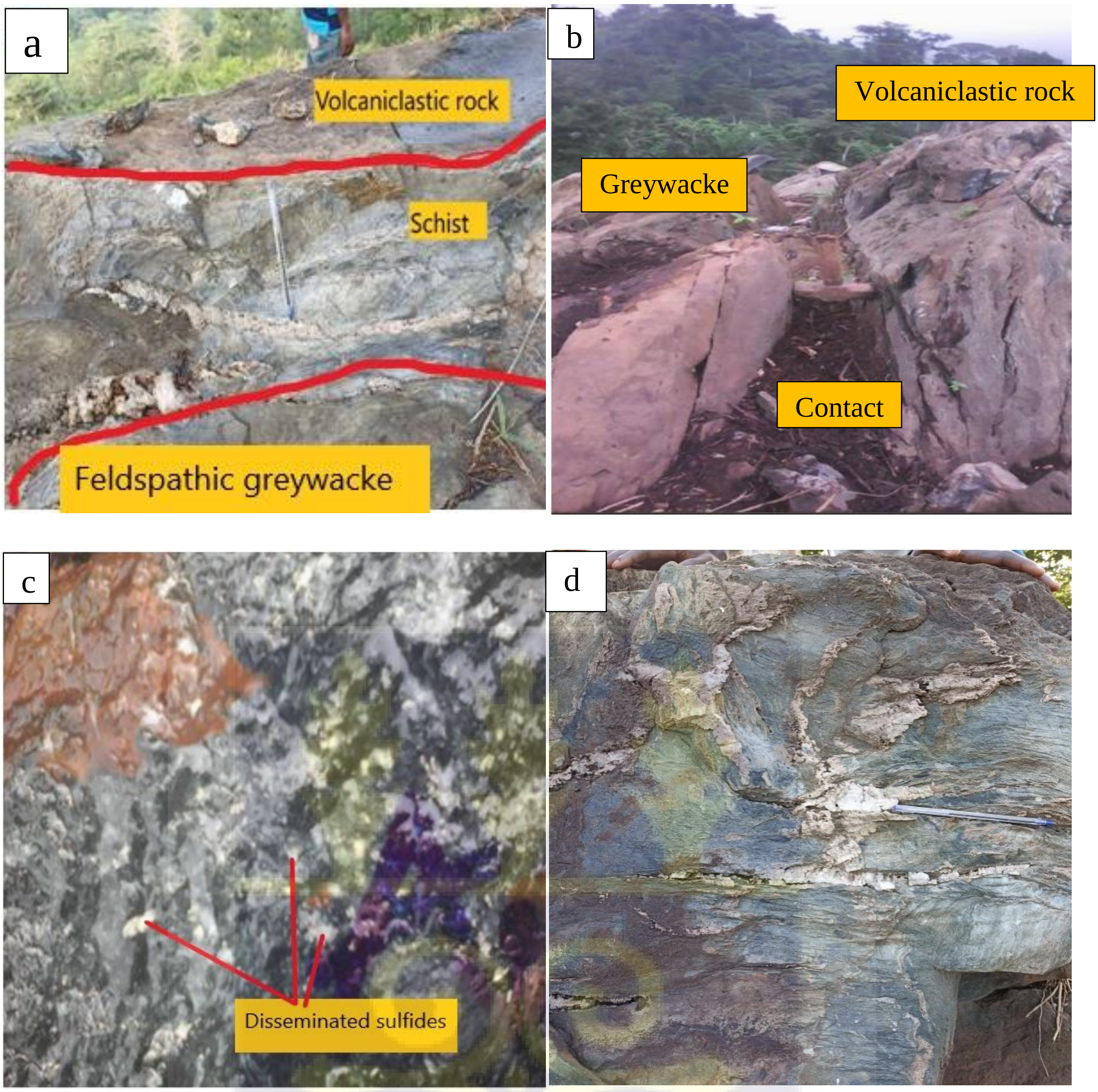

**Figure 4.18: Field photographs of the schist, feldspathic greywacke and volcaniclastic rocks (andesitic tuff) occurring in the study area showing a) contact between the schist and the volcaniclastic rocks b) contact between the schist and the greywackes c) disseminated sulphides within the schist occurring in the Etukrom area d) several generations of quartz stringers, veins and veinlets which occasion crosscut others**

Microscopically, the carbonate chlorite schist is dominated by opaque minerals and chlorite (Figures 4.19a and b). The opaque minerals appear to be ferromagnesian-derived, most likely amphibole. Shear textures are shown by the strong preferred orientation of constituent minerals, with an S1 schistosity overprinted by S2 in a somewhat anastomosing texture (Figure

4.19b). This assemblage is impregnated by significant quartz and carbonate minerals. In polished section, the sulfide minerals occur as amorphous isolated grains (Figure 4.19c) and occasionally as aggregates in preferred oriented and within alteration zones (Figure 4.19d). The mineral compositions and their respective modal contents by point counting are indicated in Table 4.1.

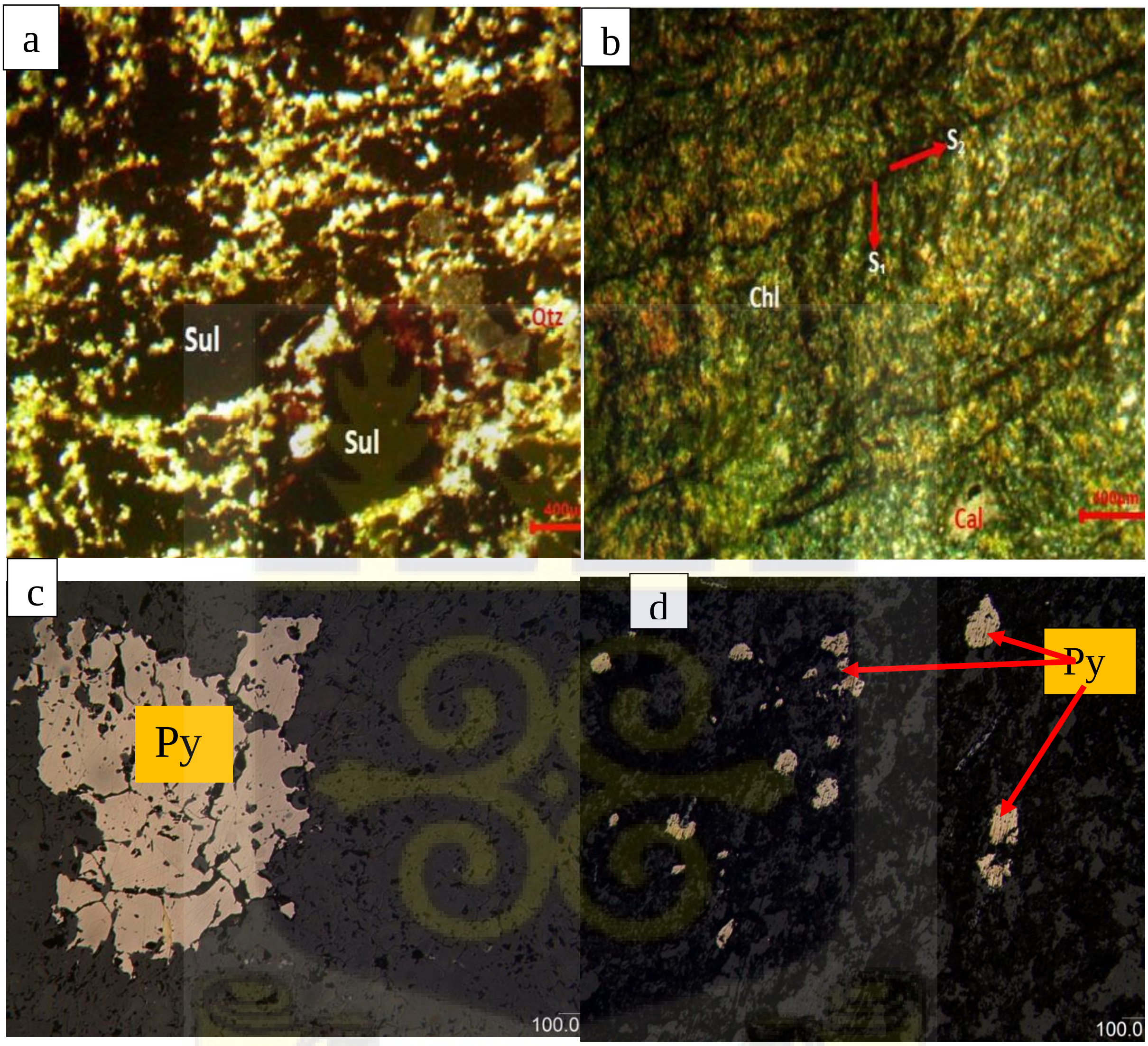

**Figure 4.19: Photomicrographs of the carbonate chlorite schist occurring in the Kibi area a) microtexture with overprints (sulphide and opaque) b) microtexture with S1 and S2 fabric c) polished section showing amorphous pyrite d) polished section showing aggregates of scattered pyrite.**

### 4.5.3 Quartz carbonate schist

The quartz-carbonate schist is carbonate-mineralized, strongly foliated and significantly silicified with predominance of disseminated sulfide. The rock appears to be of a volcanic origin of mafic protolith abundant in opaque minerals. Hand specimen examination shows the mafic minerals have been chloritized, and infiltrated by calcite and quartz. The rock has a prominent shear fabric (Figures 4.20a and b) and produces effervescence when dilute HCl is sprayed on it which suggests the presence of carbonate minerals.

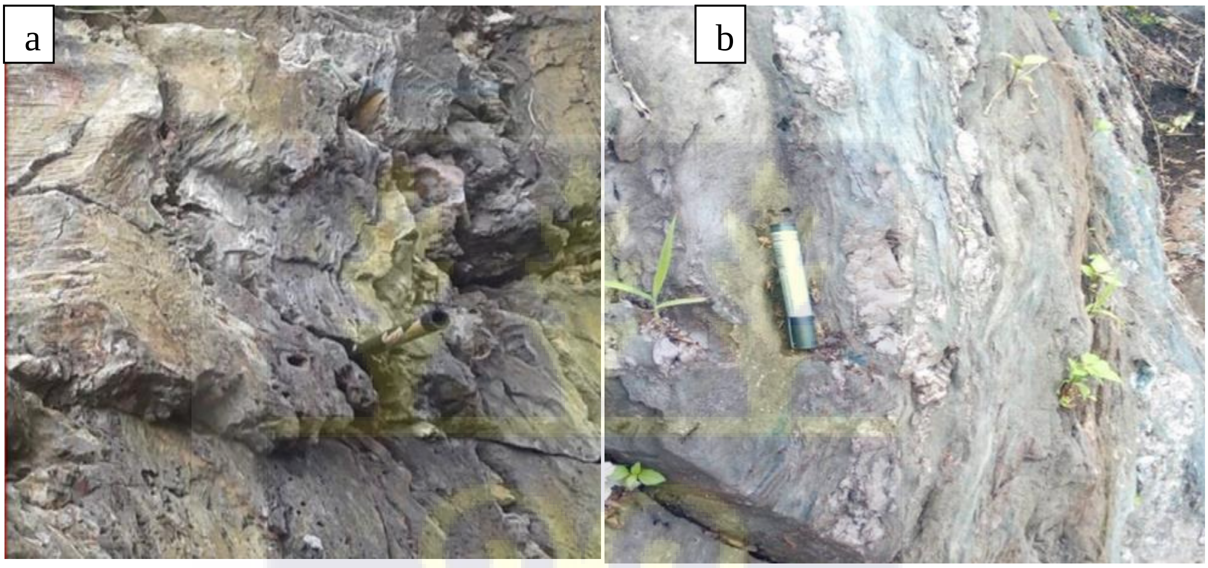

**Figure 4.20: Field photographs showing a) highly foliated and deformed quartz-carbonate schist b) different generations of quartz veins.**

In thin section, the rock is significantly altered and now dominated by chlorite, carbonate and quartz along the shear fabric (Figures 4.21a and b). The assemblage is cut at places by a network of veinlets filled with quartz and carbonate minerals (Figure 4.21b). In alteration haloes, and also in some of the veins are cubic, sub-cubic deformed sulfide minerals. Chlorite is fibrous (Figure 4.21b); quartz is recrystallized and occurs as veins or impregnations (Figures 4.21a and b). Calcite is coarse and associated with quartz (Figure 4.21a). Remnants of amphibole are found as pseudomorphs in alteration haloes. In polished section, pyrite grains range from euhedral to anhedral (Figure 4.21c). Occasionally, euhedral porphyroblast of pyrite engulfs chalcopyrite and sphalerite in contact zones (Figure 4.21d). The mineral compositions of the quartz-carbonate schist and their respective modal contents by point counting are indicated in Table 4.1.

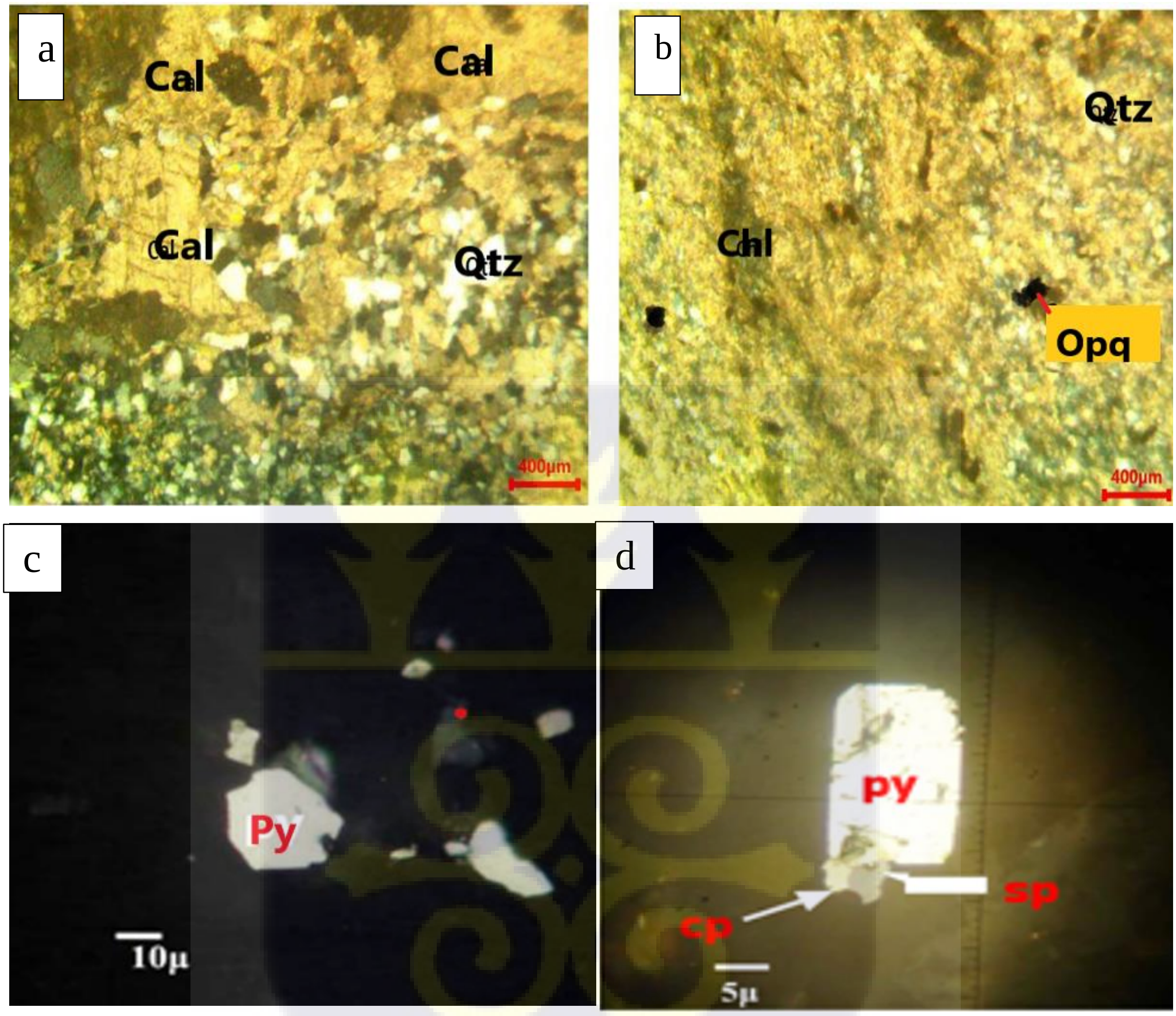

**Figure 4.21: Photomicrographs of the quartz-carbonate schist occurring in the Kibi area showing a) sheared fabric b) preferred orientation of the minerals c) euhedral to anhedral pyrite grains (polished section) d) euhedral (py) porphyroblast engulfing chalcopyrite (py) and sphalerite (sp) in contact (polished section).**

### 4.5.4 The mylonitized quartz chlorite schist

In hand specimen, the mylonitized quartz chlorite schist was strongly mylonitized and silicified, massive, cherty and poly-deformed. It appears to have suffered contact metamorphism and is rich in opaque minerals. In thin section, the rock is fine-grained and partly foliated (Figures 4.22a and b). It is composed of elongated and fibrous chlorite-sericite microtexture that has been cut by coarse-grained quartz and overgrown by opaque minerals. Quartz is strained and occurs as recrystallized aggregates and individual crystals (Figures 4.22a and b) along cracks or weak zones of the rock. The whole assemblage has a preferred orientation, defined by prominent elongated chlorite and opaques. The mineral compositions of the mylonitized quartz chlorite schist and their respective modal estimations by point counting are indicated in Table 4.1.

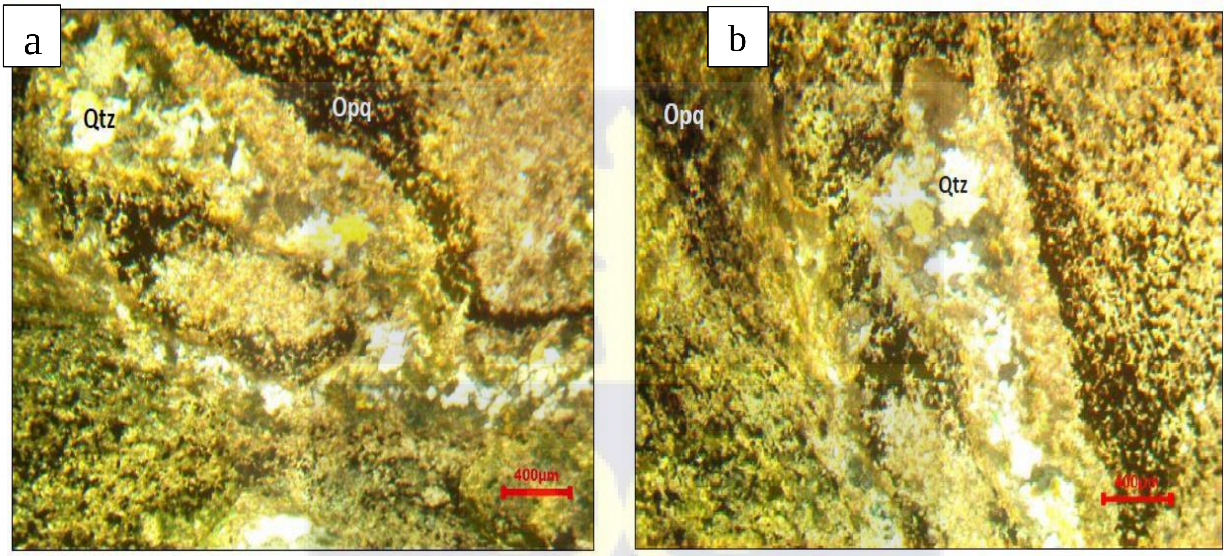

**Figure 4.22: Photomicrograph of the mylonitized quartz chlorite schist a) showing characteristic chlorite-sericite shear fabric b) bands of opaque minerals occurring along and quartz veins.**

**Table 4.1. The modal compositions of the schist in the Kibi area (vol %) by point counting.**

| Rock type | | Quartz | Chlorite | Sericite | Calcite | Opaque minerals | Sulfide minerals |
|---|---|---|---|---|---|---|---|
| Carbonate chlorite Schist | CCS001 | 15 | 49 | 1 | 5 | 20 | 10 |
| | CCS002 | 16 | 50 | 3 | 3 | 21 | 7 |
| | CCS003 | 15 | 51 | 1 | 6 | 18 | 9 |
| | CCS004 | 17 | 47 | 1 | 4 | 21 | 10 |
| | CCS005 | 16 | 49 | 2 | 5 | 20 | 8 |
| | CCS006 | 15 | 49 | 1 | 5 | 19 | 11 |
| | CCS007 | 15 | 50 | 2 | 6 | 18 | 9 |
| | CCS008 | 16 | 48 | 2 | 6 | 21 | 7 |
| | CCS009 | 17 | 50 | 1 | 4 | 19 | 9 |
| | CCS010 | 15 | 51 | 3 | 4 | 20 | 7 |
| Quartz carbonate schist | QCS001 | 20 | 43 | | 30 | 5 | 2 |
| | QCS002 | 21 | 46 | | 28 | 4 | 1 |
| | QCS003 | 22 | 43 | | 28 | 6 | 1 |
| | QCS004 | 20 | 45 | | 30 | 5 | 1 |
| | QCS005 | 21 | 46 | | 26 | 5 | 2 |
| | QCS006 | 20 | 45 | | 30 | 4 | 1 |
| | QCS007 | 22 | 44 | | 28 | 3 | 3 |
| | QCS008 | 19 | 46 | | 27 | 6 | 2 |
| | QCS009 | 21 | 45 | | 28 | 4 | 2 |
| | QCS010 | 22 | 43 | | 29 | 5 | 1 |
| Mylonitized quartz chlorite schist | MQS001 | 30 | 40 | 8 | | 20 | 2 |
| | MQS002 | 28 | 38 | 11 | | 22 | 1 |
| | MQS003 | 31 | 37 | 8 | | 21 | 3 |
| | MQS004 | 31 | 38 | 10 | | 20 | 1 |
| | MQS005 | 29 | 40 | 9 | | 21 | 1 |
| | MQS006 | 30 | 41 | 8 | | 19 | 2 |
| | MQS007 | 29 | 39 | 11 | | 18 | 3 |
| | MQS008 | 32 | 40 | 8 | | 19 | 1 |
| | MQS009 | 30 | 38 | 10 | | 20 | 2 |
| | MQS010 | 33 | 38 | 11 | | 17 | 1 |

### 4.5.5 Greywacke (GW)

The greywacke is foliated, brownish or greenish grey when fresh, and becomes darker as it weathers (Figure 4.23a). It is fine to medium-grained and highly indurated with sporadic occurrences of mafic bands running through some of them. Occasionally, there are inclusions of angular to subrounded fragments of greenstone and quartzite within the greywackes. The greywacke samples produce effervescences when dilute HCl is sprayed on them indicating the presence of carbonate minerals. Structurally, the greywacke is highly deformed with characteristic joints/fractures (Figure 4.23a). Quartz veins are usually discordant but sometimes concordant (Figure 4.23b). Few outcrops display characteristic cross-bedding structures while others display characteristic reverse bedding. The general strike of the greywacke is NE-SW and the average dip direction is NW, however, there are local variations in their orientations.

In thin section, the rock is composed of quartz, chlorite, feldspar and carbonate minerals forming a well–defined fabric of segregated bands (Figure 4.23c). The quartz and feldspar grains are stretched (Figure 4.23c). The quartz sometimes occurs as phenoclast (Figure 4.23d) and occasionally shows wavy extinction. The carbonate in the rocks was classified using the criteria of Adjimah (1988), that the ankerite is cloudy and the calcite clear with polysynthetic twinning. The carbonate is mainly ankerite and is locally segregated in some areas. The preferred alignment of the minerals gives the rock a schistose texture. Schistosity is enhanced by the parallel alignment of thin laminations of sericite and chlorite and the flattening of elongated quartz (Figure 4.23c). The dominant laminations comprise quartz with abundant coarser grains of plagioclase. The plagioclase often contains inclusions of fine-grained sericite.

Thin laminations of sericite and chlorite occur between the quartzo-feldspathic bands with calcitic carbonate occurring throughout the rock and mostly in the interstices of quartz and feldspar. Coarser-grained pods or veins of calcitic carbonate, quartz, and feldspar occur sporadically in some thin sections. The mineral compositions of the greywacke and their respective modal estimations by point counting are indicated in Table 4.2. Based on the contents of quartz (Q), Feldspar (F) and rock fragments (L) predominantly chert, the greywackes samples were plotted on the QFL ternary diagram (Figure 4.24) by Pettijohn (1987). On the QFL plot (Figure 4.24), the studied siliciclastic samples classify as feldspathic greywackes.

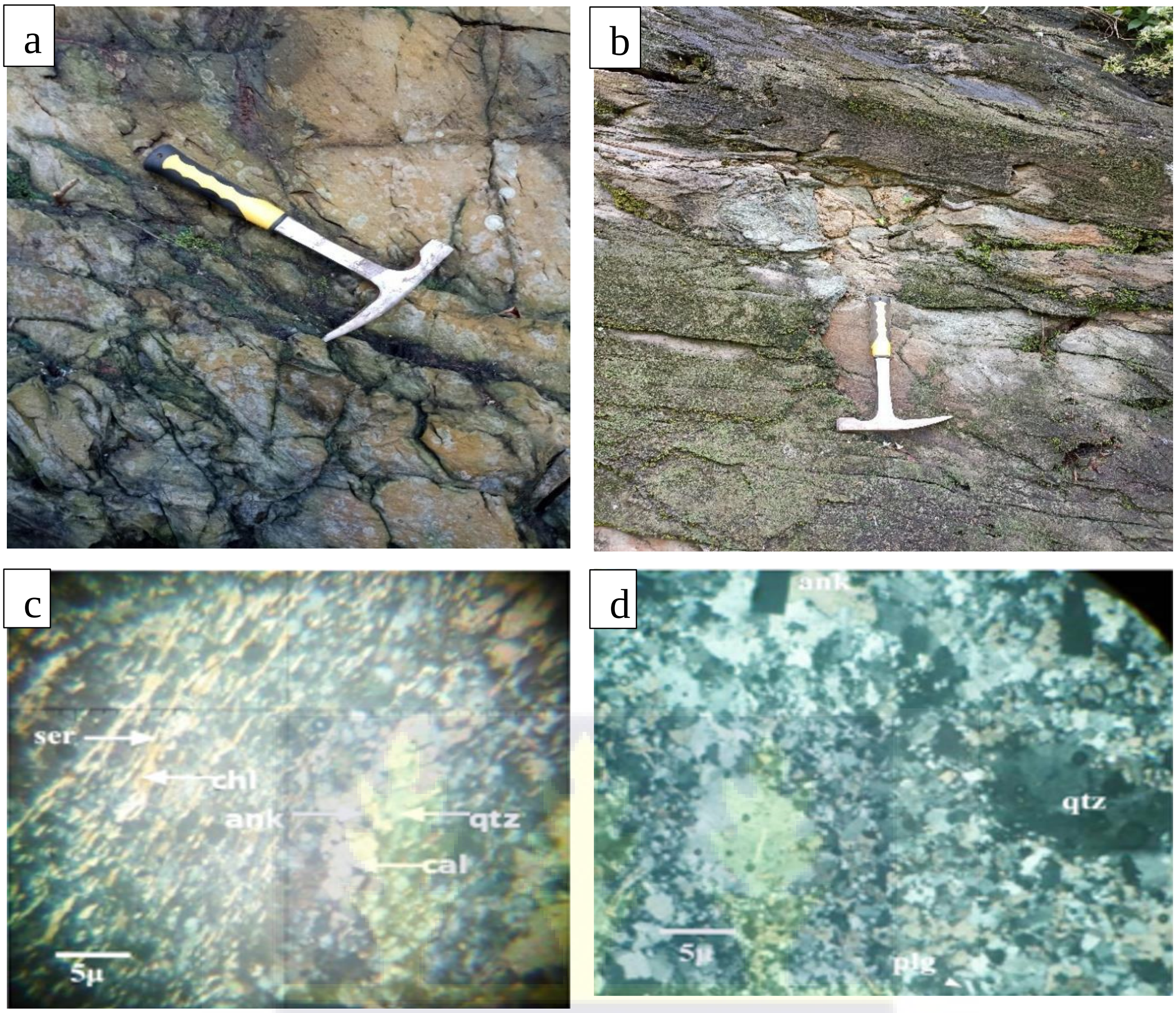

**Figure 4.23: Field photographs and photomicrographs of the greywacke in the Kibi area a) field photograph of highly fractured greywacke b) field photograph of highly deformed greywacke with a concordal quartz vien d) Photomicrograph showing the alternate alignment of quartz, chlorite, ankerite and sericite bands (GW01) under crossed-polars. c) Photomicrograph showing phenoblast of quartz within a fine to medium-grained matrix (GW01).**

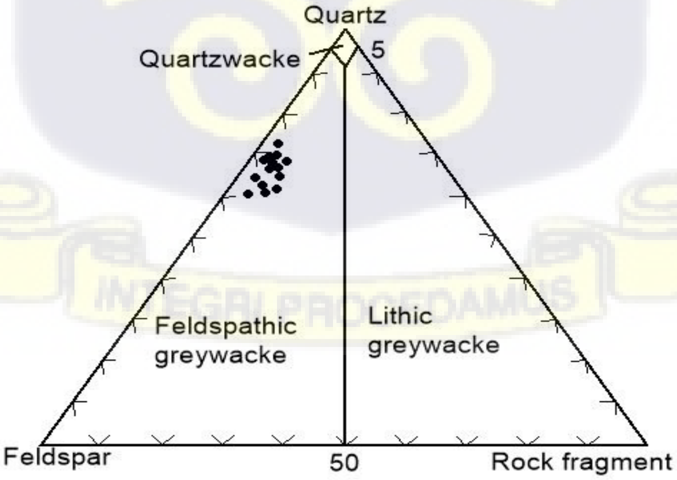

**Figure 4.24: Ternary diagram for greywacke composition based quartz, feldspar and lithic fragments proposed by Pettijohn (1975).**

### 4.5.6 Ore Mineralization in the greywacke

Figure 7a is a polished section photomicrograph of the feldspathic greywacke showing two types of sulfides. In Figure 4.25a, pyrite and chalcopyrite are in contact, and both are corroded and xenomorphic. Figure 4.25b shows corroded anhedral pyrite grains. A grain of chalcopyrite close to the shattered pyrite is also corroded. Similarly, Figure 4.25c shows shattered corroded pyrite and euhedral pyrite porphyroblasts with undigested rock inclusions. In Figure 4.25d, the pyrite is fractured, invaded and corroded by silica. In Figure 4.25e (magnified Figure 4.25d), the shattered pyrite contains chalcopyrite inclusions and is also invaded and corroded by silica. Pyrite and chalcopyrite are observed to be in contact (Figure 4.25f) with the pyrite replacing the chalcopyrite. The pyrite is subhedral and contains undigested rock material while the chalcopyrite is corroded. Undisturbed euhedral pyrite porphyroblasts with undigested rock also occurs within the same sample (Figure 4.25g). Figure 4.24h shows subhedral pyrite porphyroblasts with interconnected fractures.

Figure 4.25i is an enlarged portion of Figure 4.25h showing some of the interconnected fractures filled with chalcopyrite. A gold grain is seen within a fracture of a pyrite in Figure 4.25k. Corroded chalcopyrite and sphalerite are in contact, and a part of the chalcopyrite is engulfed by a euhedral pyrite (Figure 4.25l). Tiny grains of rutile and haematite occur in the greywacke, (Figures 4.25k and l respectively). These are mostly small anhedral grains but there are also a few subhedral to euhedral grains as seen in Figure 4.25k and Figure 4.25l.

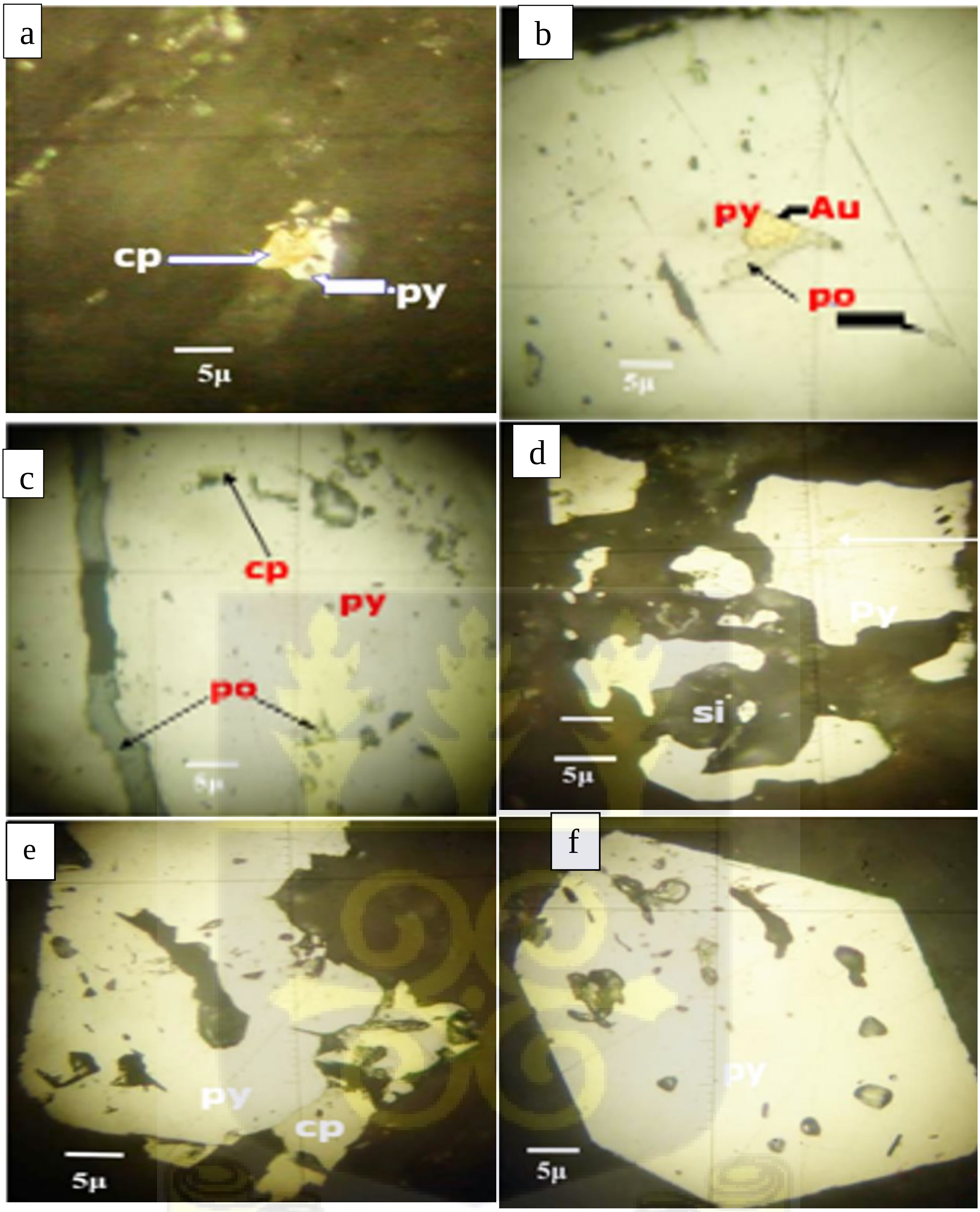

**Figure 4.25 (a-f): Polished section photomicrograph of greywacke (sample GW01) showing a) paragenesis of anhedral pyrite and chalcopyrite b) sheared greywacke (sample GW02) showing a grain of chalcopyrite and a shattered grain of pyrite. The pyrite is corroded and the fractures are filled with younger silica c) two generations of pyrite: a tectonised corroded pyrite and a euhedral sieve textured pyrite d) shattered and corroded grain of pyrite with inclusions of chalcopyrite e) pyrite with sieve textures replacing chalcopyrite f) euhedral sieve textured pyrite porphyroblast.**

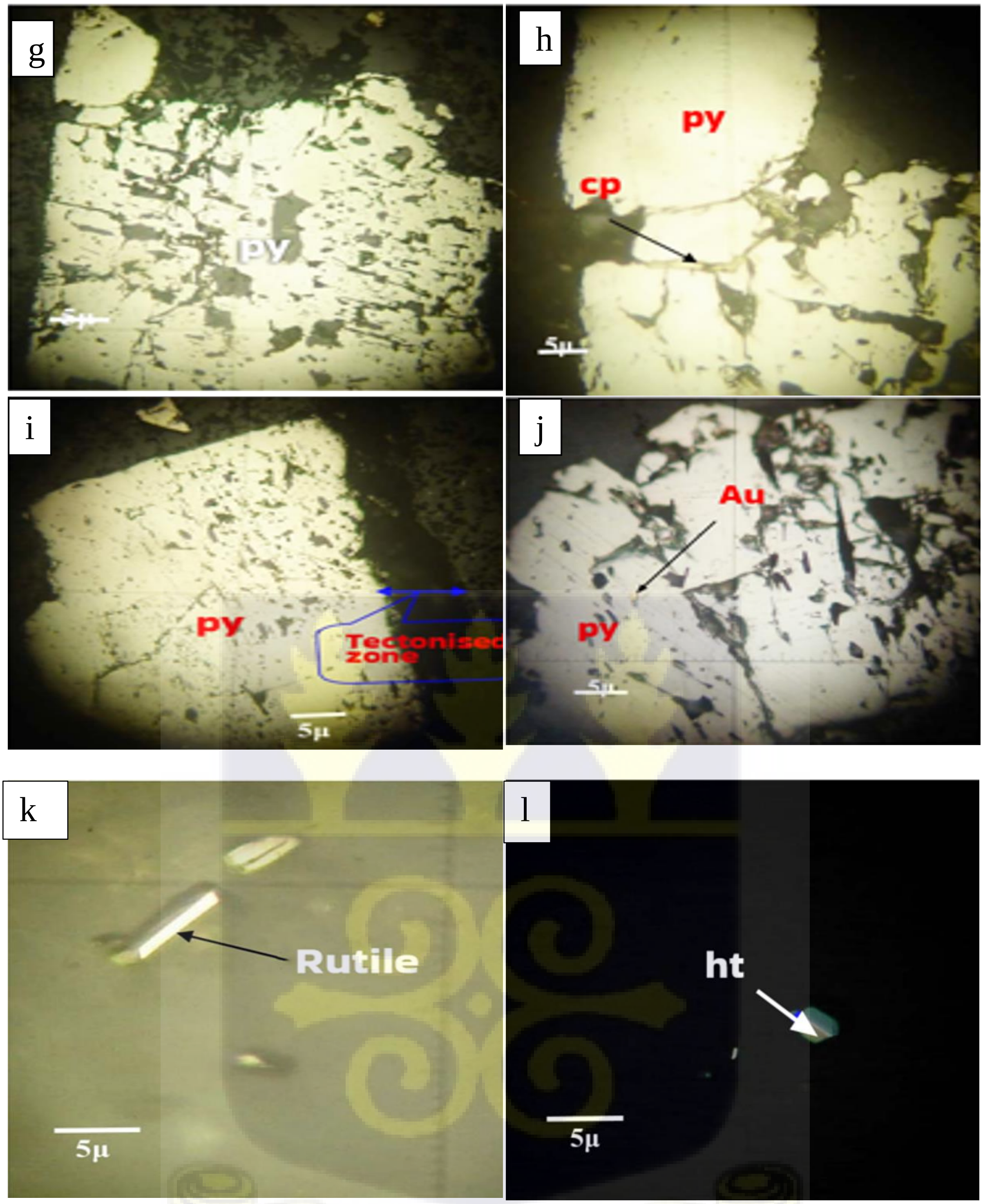

**Figure 4.25 continued: Polished section photomicrograph of the greywackes occurring in the Kibi area showing g) fractured pyrite porphyroblast with undigested rock h) a photomicrograph of greywacke showing fractured pyrite with chalcopyrite filling the fractures (GW03) i) subhedral pyrite porphyroblast lying along a tectonised zone with a post crystallization fracture j) a tectonised pyrite grain with Au speck in a fracture k) rutile grain (GW02) l) haematite grain under crossed-polars (GW02).**

### 4.5.7 Volcaniclastic rock (VE) (Andesitic tuff)

In hand specimen, the rock is siliceous and sheared. It has visible quartz clasts and quartz-carbonate veinlets and contains visible disseminated sulphides. In thin section, this rock is made up of recrystallized or annealed quartz clasts and albite grains. There are thin laminations of chlorite, sericite and some opaque minerals, anastomosing the porphyroblasts. Schistosity is defined by the preferred alignment of sericite and chlorite and the flattening and elongation of quartz grains (Figure 4.26a). Segregated laminations also exist with quartz-albite dominant laminations and sericite-chlorite dominant laminations. Chlorite is unevenly distributed, and it usually occurs with sericite. Chlorite is locally recrystallized and is coarser-grained (Figure 4.26a). Ankerite in the rock occurs mostly in quartz-albite laminations (Figure 4.26b).

The altered specimen is made up essentially of quartz and ankeritic carbonate with minor feldspar, chlorite and sericite interlocked together. A weak fabric is defined by the alignment of quartz, sericite and carbonate showing folding in some places (Figure 4.26c). Subhedral feldspar is occasionally seen interspersed within the quartz-ankeritic carbonate-sericite matrix (Figure 4.26c). The alteration minerals are quartz, sericite, feldspar and carbonate (Figure 4.26d). The mineral compositions of the volcaniclastic rock and their respective modal contents by point counting are indicated in Table 4.2.

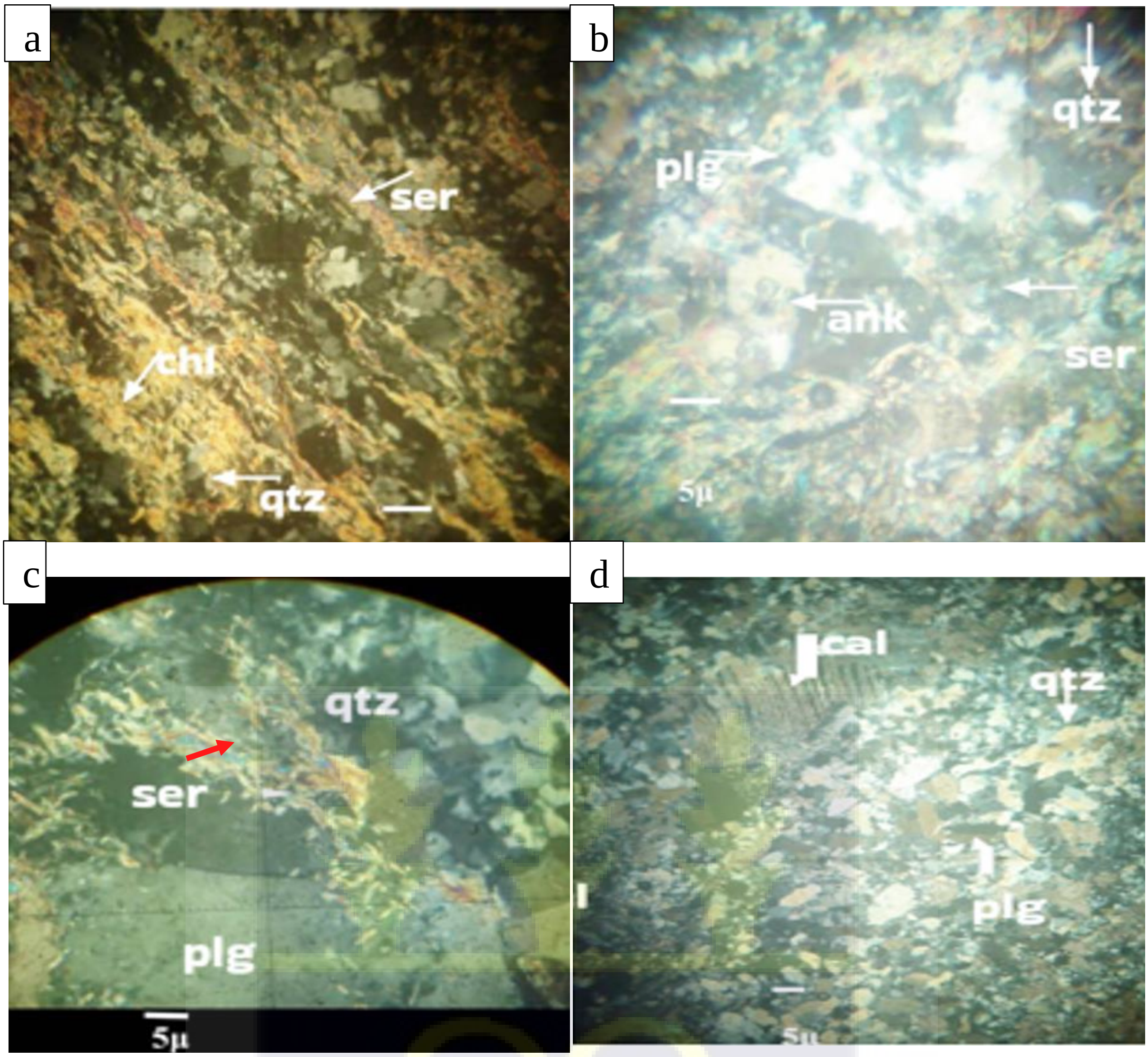

**Figure 4.26 (a-d): Photomicrograph of the volcaniclastic rock occurring in the Kibi area showing a) segregated bands of chlorite-sericite with quartz "eyes" (VE16) b) interlocking grains of quartz, plagioclase and carbonate weakly aligned (VE04) c) euhedral plagioclase undergoing sericitization (VE04) d) phenoblast of calcite surrounded by fine to medium grained quartz. Quartz =qtz, calcite = cal, plagioclase = plg, sericite = ser, chlorite = chl and ankarite = ank.**

### 4.5.8. Ore Mineralization in the volcaniclastic rock (Andesitic tuff)

Pyrite is the most dominant mineral in the unaltered volcaniclastic rock. It exists as either anhedral, fractured, or corroded grain. Locally, pyrite is observed replacing magnetite, (Figure 4.27a). Pyrrhotite is the second dominant mineral, and all the grains observed are anhedral and have corroded edges. Sparse fine-grained chalcopyrite is disseminated in the sample.

In the altered volcaniclastic rock, the most dominant sulphide is pyrite which is mostly subhedral with some having sieve textures and fractured. Other sulphide types like pyrrhotite and chalcopyrite occur mostly in cavities of fractured pyrites. Figure 4.27b shows a shattered pyrite containing chalcopyrite inclusion in one of the fragments. The fragments are invaded and corroded by a silica-bearing fluid. Chalcopyrite occurs as either individual tiny grains or in the fractures of pyrite. A gold grain in contact with pyrrhotite is contained within a fractured and subhedral pyrite (Figure 4.27c). The pyrrhotite was likely part of the fluid that deposited the gold. Few grains of pyrrhotite are also observed either filling cavities or fractures in pyrite (Figure 4.27d).

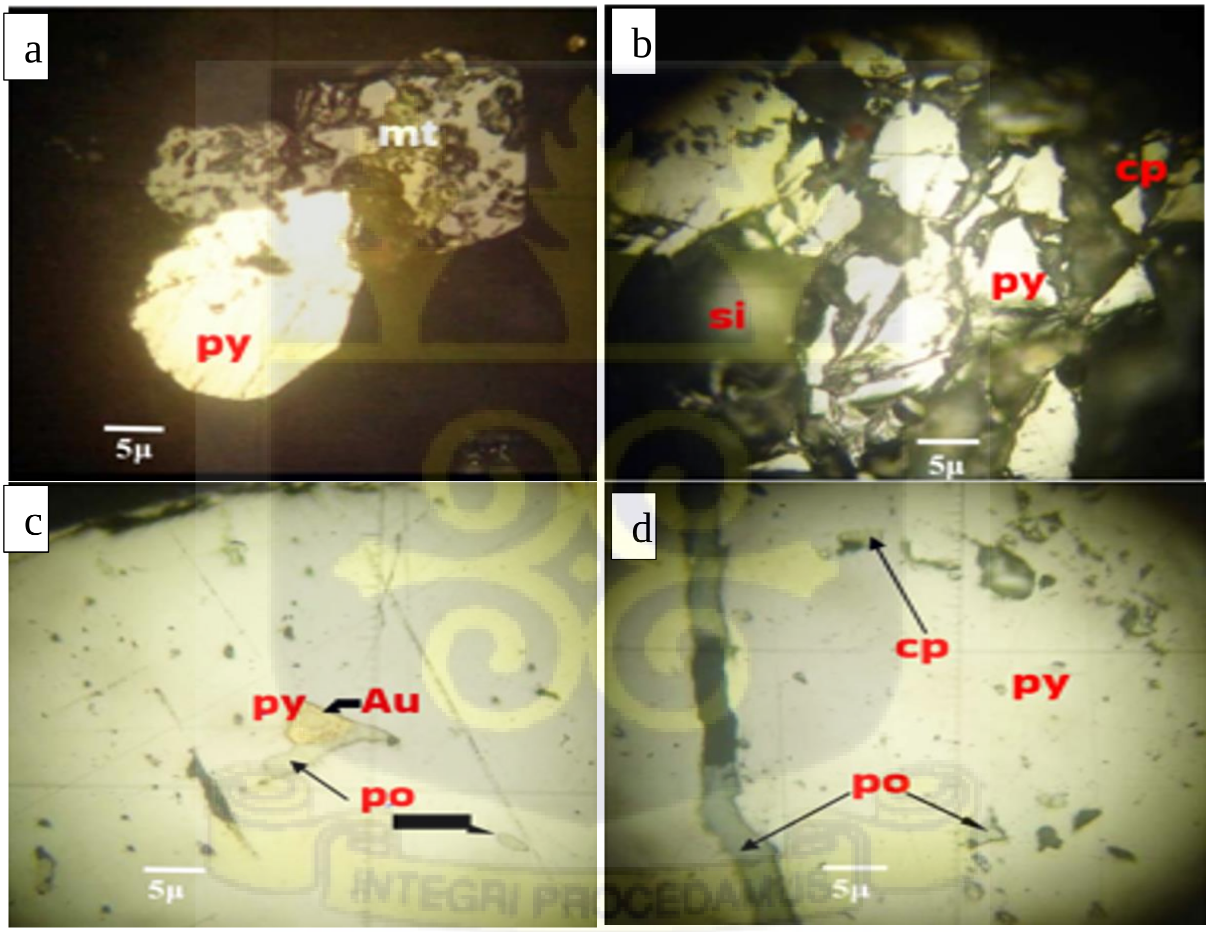

**Figure 4.27: Polished section photomicrograph of the volcaniclastic rock showing a) pyrite replacing magnetite b) pyrite with silica filling the spaces in between. Chalcopyrite is included in one pyrite grain (VE04) c) Au and pyrrhotite in contact and filling a cavity in pyrite (VE04) d) chalcopyrite occupying a cavity and pyrrhotite forming a vein in pyrite (VE05).**

**Table 4: The mineral compositions of the greywacke and volcaniclastic rock samples and their respective modal contents (vol %) by point counting.**

| Rock type | Sample ID | Quartz | Plagioclase | Chlorite | Sericite | Calcite | Ankerite | Opaque minerals | Sulphide minerals | Chert |
|---|---|---|---|---|---|---|---|---|---|---|
| Greywacke | GW 01 | 30 | 10 | 21 | 13 | 11 | | 3 | 10 | 2 |
| | GW02 | 33 | 10 | 20 | 14 | 12 | | 4 | 5 | 2 |
| | GW 03 | 35 | 12 | 23 | 11 | 11 | | 3 | 2 | 3 |
| | GW04 | 25 | 12 | 24 | 13 | 12 | | 2 | 10 | 2 |
| | GW05 | 31 | 15 | 22 | 12 | 10 | | 3 | 4 | 3 |
| | GW06 | 30 | 17 | 22 | 10 | 14 | | 1 | 4 | 2 |
| | GW07 | 32 | 13 | 24 | 12 | 12 | | 4 | 2 | 1 |
| | GW08 | 30 | 16 | 24 | 14 | 10 | | 3 | 2 | 1 |
| | GW09 | 35 | 15 | 20 | 12 | 10 | | 1 | 4 | 3 |
| | GW10 | 35 | 12 | 23 | 12 | 12 | | 1 | 3 | 2 |
| Volcaniclastic rock | VE 01 | 32 | 26 | 10 | 15 | 8 | 2 | 1 | 6 | |
| | VE 02 | 30 | 29 | 10 | 16 | 9 | 2 | 2 | 2 | |
| | VE 03 | 31 | 33 | 11 | 13 | 6 | 1 | 1 | 4 | |
| | VE 04 | 35 | 28 | 9 | 14 | 9 | 2 | 2 | 1 | |
| | VE 05 | 33 | 33 | 10 | 10 | 7 | 1 | 1 | 5 | |
| | VE 06 | 32 | 30 | 9 | 17 | 6 | 3 | 1 | 2 | |
| | VE 07 | 30 | 30 | 10 | 12 | 7 | 1 | 2 | 8 | |
| | VE 08 | 30 | 30 | 11 | 14 | 9 | 3 | 1 | 2 | |
| | VE 09 | 32 | 31 | 10 | 12 | 8 | 1 | 2 | 4 | |
| | VE 10 | 31 | 30 | 9 | 15 | 9 | 3 | 1 | 2 | |

### 4.5.9 Hanging wall Mafic Volcanic Rock (HW)

In the field, massive, concave down outcrops of the mafic volcanic rocks occur predominantly at Etukrom and its environments in the central portion of the study area. The rock is fine to medium-grained and highly deformed owing to the presence of fractures, folds, faults and shear zones. The NE-SW trending fault aided in the separation of mafic volcanic rock into hanging wall and foot wall which are compositionally different. Evidence of faulting is sometimes observed in outcrops of the mafic volcanic rocks (Figure 4.28a), even though the main fault core along the trace is not well exposed on the surface. The hanging wall mafic volcanic rock appears highly sheared and silicified probably due to subsequent hydrothermal interaction compared to the footwall (Figure 4.28b). The contact between the hanging wall and the shear zone appears densely welded and devitrified (Figure 4.28c). Sulphides are sparsely distributed within the hanging wall mafic rock.

In hand specimen, the hanging wall mafic volcanic rock is weakly foliated, chloritized and often grey with quartz-calcite veinlets parallel to foliation. The rock is essentially fine-grained with a schistosity defined by chlorite and sericite alignment. It has pods or lenses made of quartz and calcitic carbonate (Figure 4.28a). A set of quartz-calcitic veins is observed parallel to the general schistosity and cross-cutting the schistosity (Figure 4.28a). The unaltered rock is very fine-grained, and the various minerals are not easily discernible (Figure 4.28b).

The altered rock in hand specimen appears fine-grained, brecciated, silicified and contains quartz-carbonate veinlets and sulphides. Under the microscope, the rock is composed mainly of quartz and feldspar and minor ankeritic carbonate forming a weak preferred orientation (Figure 4.28b). The quartz grains have serrated boundaries. There are also areas of segregated sericite in the quartz-carbonate-feldspar interstices. Both quartz and feldspar porphyroblasts occur in the sample. Some quartz porphyroblasts exhibit undulose extinction. Table 4.3 lists the mineral compositions of the hanging wall mafic volcanic rock together with the corresponding modal estimations derived from point counting.

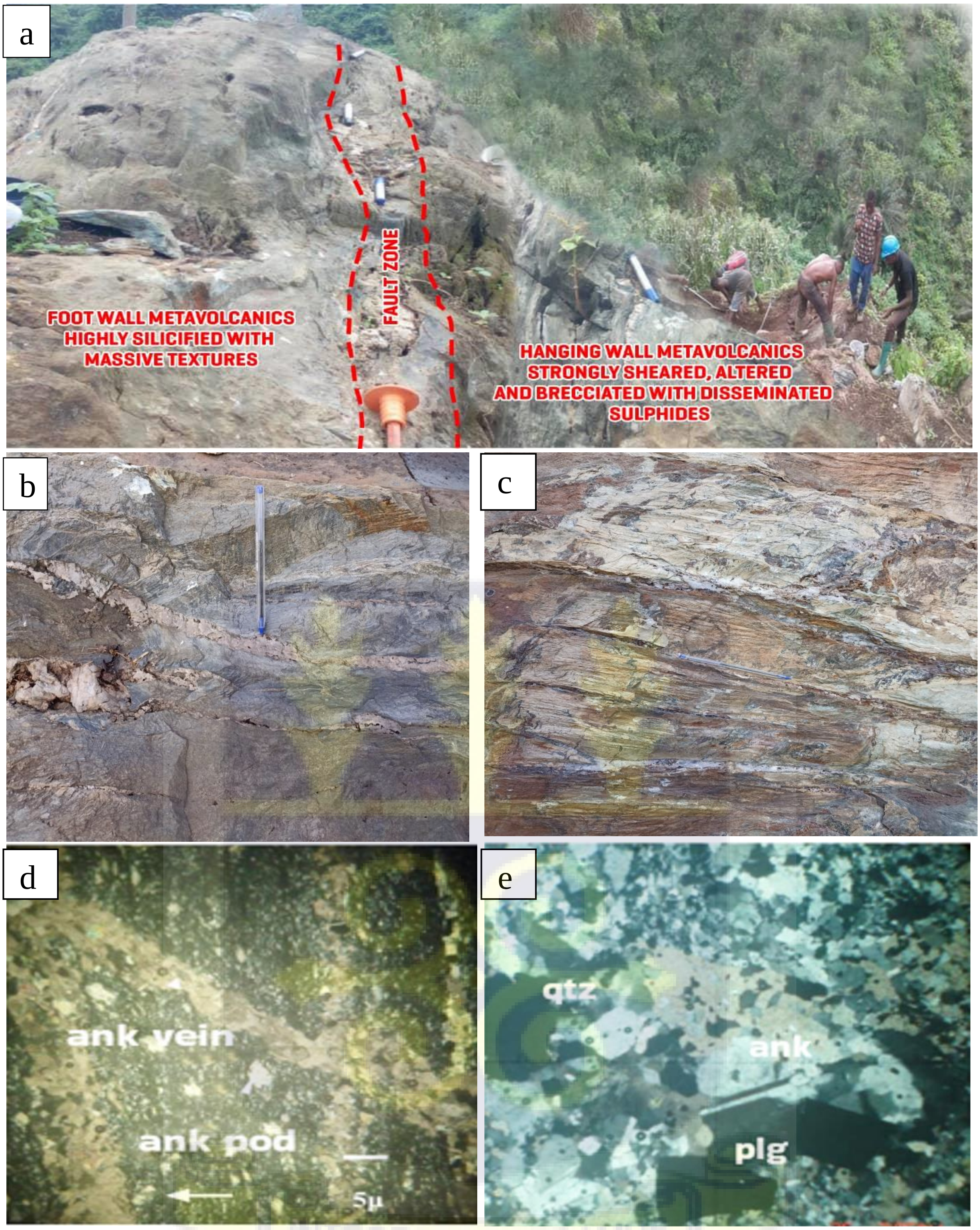

**Figure 4.28: Field photographs of the mafic volcanic rocks ( a-c) and photomicrographs of the hanging wall mafic volcanic rocks (d and e) occurring within the Kibi area showing a) the fault zone within the concave down mafic volcanic rock b) slightly deformed foot wall mafic volcanic rock c) welded and devitrified surface of the hanging wall mafic volcanic rock d) fine texture and carbonate pods and cross veins (HW06) e) interlocking grains of quartz (qtz), plagioclase (plg) and carbonate (ank).**

### 4.5.10 Gold mineralization in the hanging wall mafic volcanic rocks

Sulphides are sparsely distributed in the hanging wall mafic rock. However, the most dominant sulphide is chalcopyrite occurring as fine corroded grains. One pyrite grain is in contact with chalcopyrite with both of them having corroded edges (Figure 4.29a). Some parts of the country rock have abundant disseminated magnetite which are visible in the hand specimen. A sample taken from a zone with alternating thin bands of altered and unaltered rock shows that magnetite only occurs in the zones of no alteration or incipient alteration but is completely absent in the altered (ore) zones. The magnetite grains are mostly subhedral to euhedral with cavities filled with substances deposited by invading fluid. Pyrite is locally observed filling fractures in magnetite (Figure 4.29b). Subhedhedral pyrites are often seen replacing magnetite (Figure 4.29c) or have inclusions of sieve-textured magnetite. Few chalcopyrite grains also occur as inclusions in anhedral pyrite. Sparse haematite grains also occur among the minerals in the altered zones. A grain of chalcopyrite also occurs in contact with and between two grains of pyrite with mutual surfaces. Tiny grains of pyrrhotite also occur in the sample.

Polished sections from the ore zone under reflected light show that pyrite occurs in many textural forms, (anhedral, subhedral and euhedral) with some having fractured and sieve textures (Figures 4.29 a, b, c and d) thus giving a clue to the tectonic history and ore paragenesis. Pyrite occurs as either individual grains or in association with other minerals. In Figure 4.29e, pyrite is in mutual contact with sphalerite, with chalcopyrite almost at their joint but in contact with the pyrite. All three minerals are corroded. Chalcopyrite is in mutual contact with pyrite (Figure 4.29f and Figure 4.29g).

Gangue “islands” as indicated by p1 and p2 in Figures 4.29f and p3 in Figure 4.29g suggest that they are not undigested rock material (which would have been older) but rather caused by fluid infiltration through openings caused by tectonic activity. It is observed at these points (p, p2 and p3) that the said “islands” cut across the mutual boundaries between the pyrite and chalcopyrite. A few fine grains of chalcopyrite inclusions are also found in the fractures of some pyrite. In Figure 4.29h, chalcopyrite is filling a cavity and a fracture in pyrite. Other minerals also identified include tiny grains of haematite and rutile, some of which occur in fractures in pyrite (Figure 4.29i and Figure 4.29j). Few pyrrhotite crystallites areal so distributed within the sample with some occurring very close to the anhedral pyrites (Figure 4.29k). Locally, a pyrrhotite grain is seen filling a fracture interconnected to another fracture filled partly by gold in a pyrite grain (Figure 4.29d). Gold grains are observed filling fractures in pyrites (Figures 4.29c and 4.29d). Up to four gold specks are observed in fractures in one big pyrite porphyroblast (Figure 4.29g). Another gold grain is also in contact with chalcopyrite in a cavity (Figure 4.29h). In Figure 4.29n, a tiny gold grain occurs close to sphalerite sandwiched between two pyrite grains. Free gold is also observed very close to a subhedral fractured and corroded pyrite (Figure 4.29m).

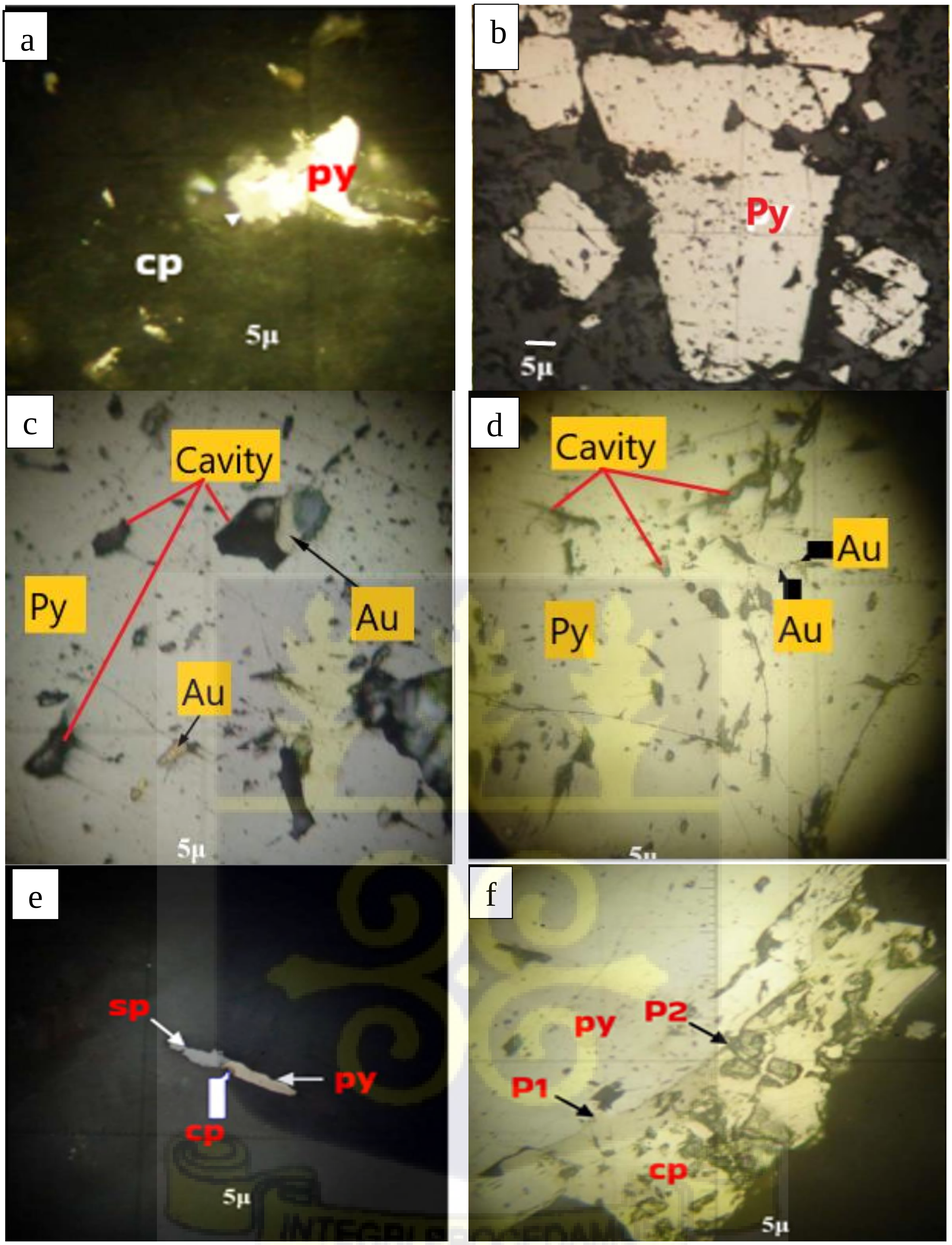

**Figure 4.29: Polished section photomicrographs of hanging wall mafic volcanic rock (sample HW06) showing chalcopyrite replacing pyrite. Both grains appear corroded, (HW06) b) two generations of pyrite c) Au grain in cavities within a sieve textured and fractured pyrite d) Au filling a cavity in a fractured pyrite grain. Also, pyrrhotite is seen filling a crack in the pyrite e) sphalerite, pyrite and chalcopyrite paragenesis, all appear corroded f) the paragenesis of pyrite and chalcopyrite.**

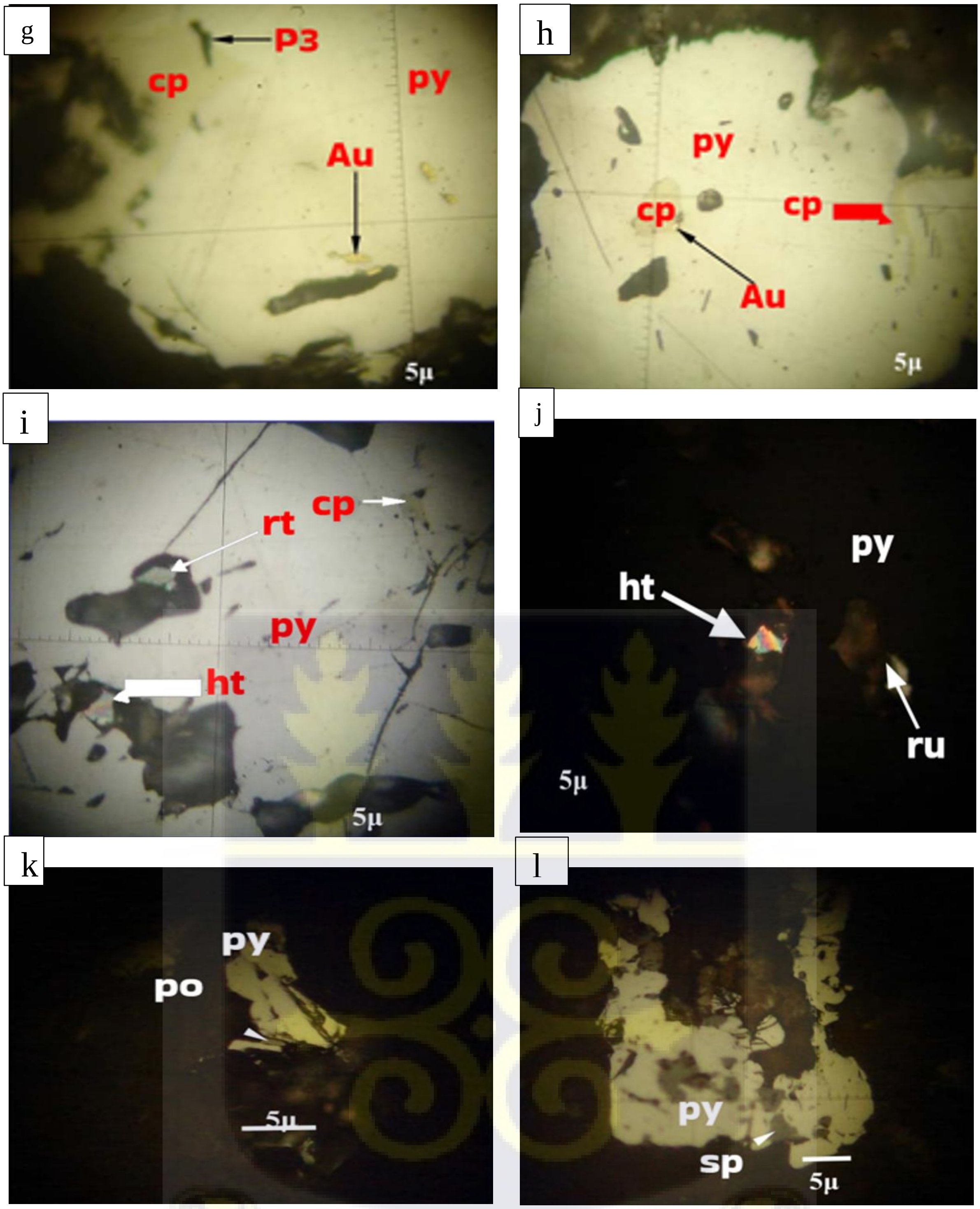

**Figure 4.29 continued: Polished section photomicrographs of hanging wall mafic volcanic rock (HW06) showing g) part of fractured pyrite in contact with chalcopyrite and four Au grains in cavities h) chalcopyrite and Augrainsin a cavity. Chalcopyrite is also filling a gap in the pyrite i) grains of haematite, rutile and chalcopyrite in cavities within pyrite j) a crystallite of pyrrhotite sandwiched between pyrite grains k) a subhedral corroded pyrite and sphalerite grains.**

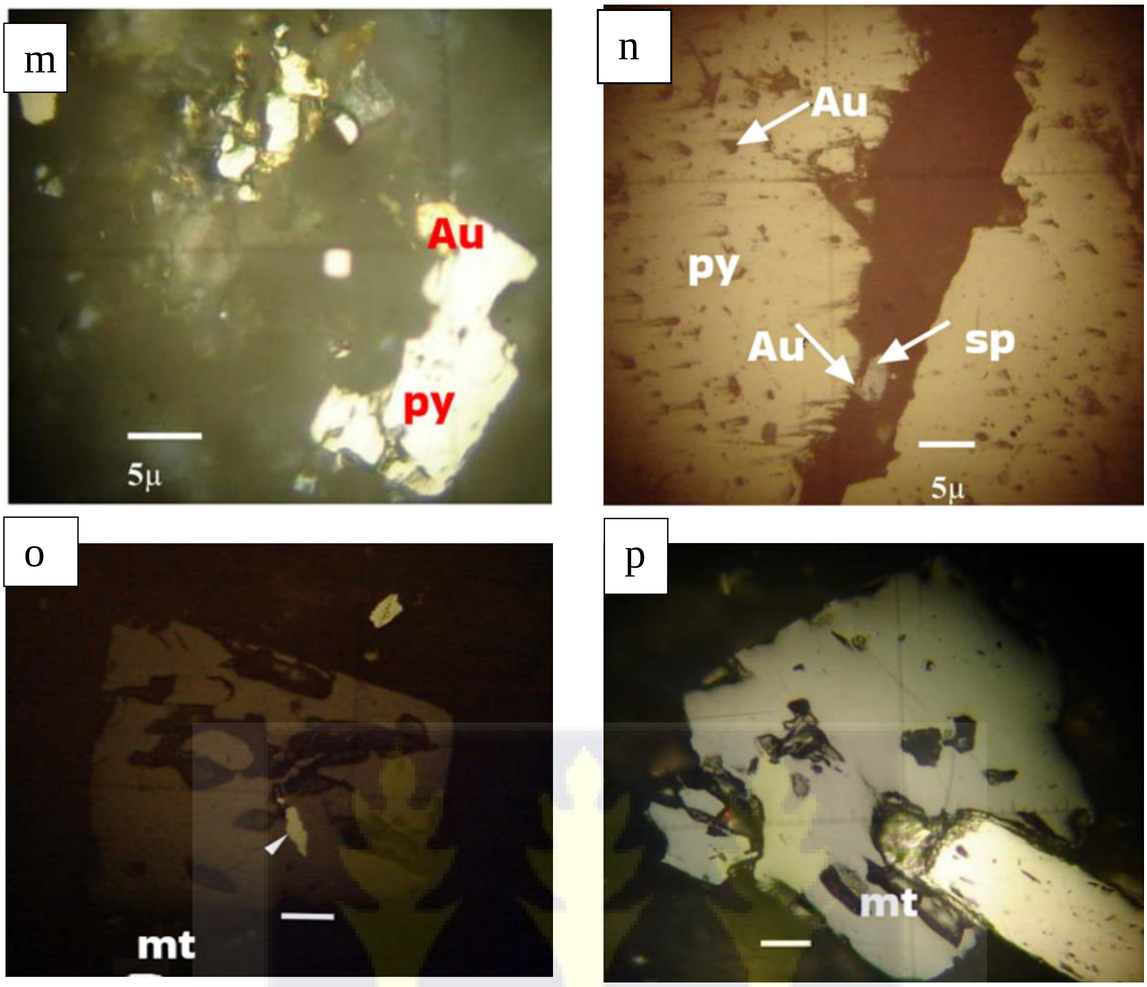

**Figure 4.29 continued: Polished section photomicrographs of hanging wall mafic volcanic rock (HW09) showing m) free Au lying alongside subhedral fractured and corroded pyrite n) Au grains in fractures o) subhedral magnetite with sieve textures and pyrite in a cavity p) magnetite being replaced by pyrite.**

### 4.5.11 Footwall mafic volcanic rock

The footwall mafic volcanic rock is sheared, fine-grained, chloritized and underlies the graphitic shear zone. In thin section, the rock is composed mostly of fine-grained chlorite and epidote (Figure 4.30a). Recrystallized quartz, plagioclase, sericite and carbonate (Figure 4.30b) are also present usually in a fine-grained matrix made up of chlorite and epidote. The mineral compositions of the footwall mafic volcanic rock and their respective modal estimations by point counting are indicated in Table 4.3.

There are also minor ankeritic and calcitic carbonates. Quartz and carbonate also exist together with chlorite and epidote. This sample contains fractured pyrite with chalcopyrite inclusions in its fragments. Chalcopyrite is the abundant sulphide in this sample occurring as anhedral grains with corroded edges (Figure 4.31a). Figure 4.31b, shows corroded grains of chalcopyrite. Corroded anhedral pyrite grains occur together with sphalerite which is also corroded (Figure 4.31c). Their contact boundary appears to be mutual. Figure 4.31d shows subhedral undisturbed pyrite grains occurring along and within a tectonic zone. Molybdenite and haematite grains are observed in the quartz vein sample, HW05, Figure 4.31e and Figure 4.31f, respectively.

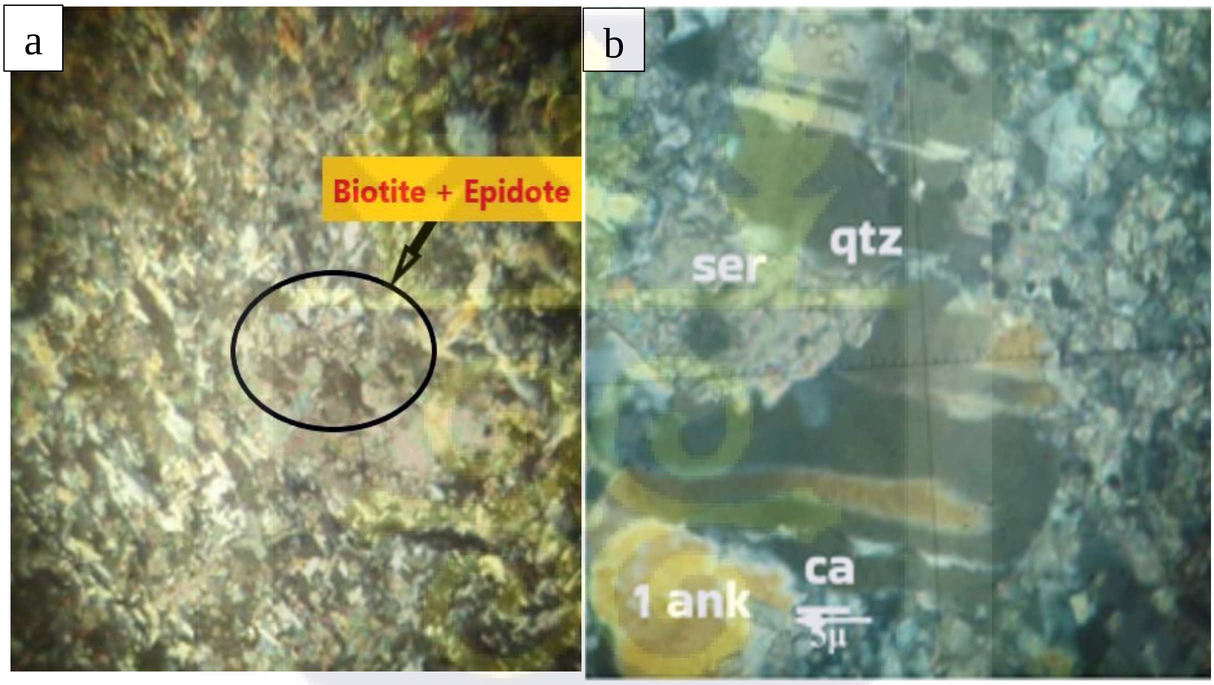

**Figure 4.30: Photomicrographs of footwall mafic volcanic rock (FW03) showing a) recrystallized quartz, plagioclase, sericite and carbonate (FW10) b) fine grains of chlorite and epidote in a very fine groundmass (FW03).**

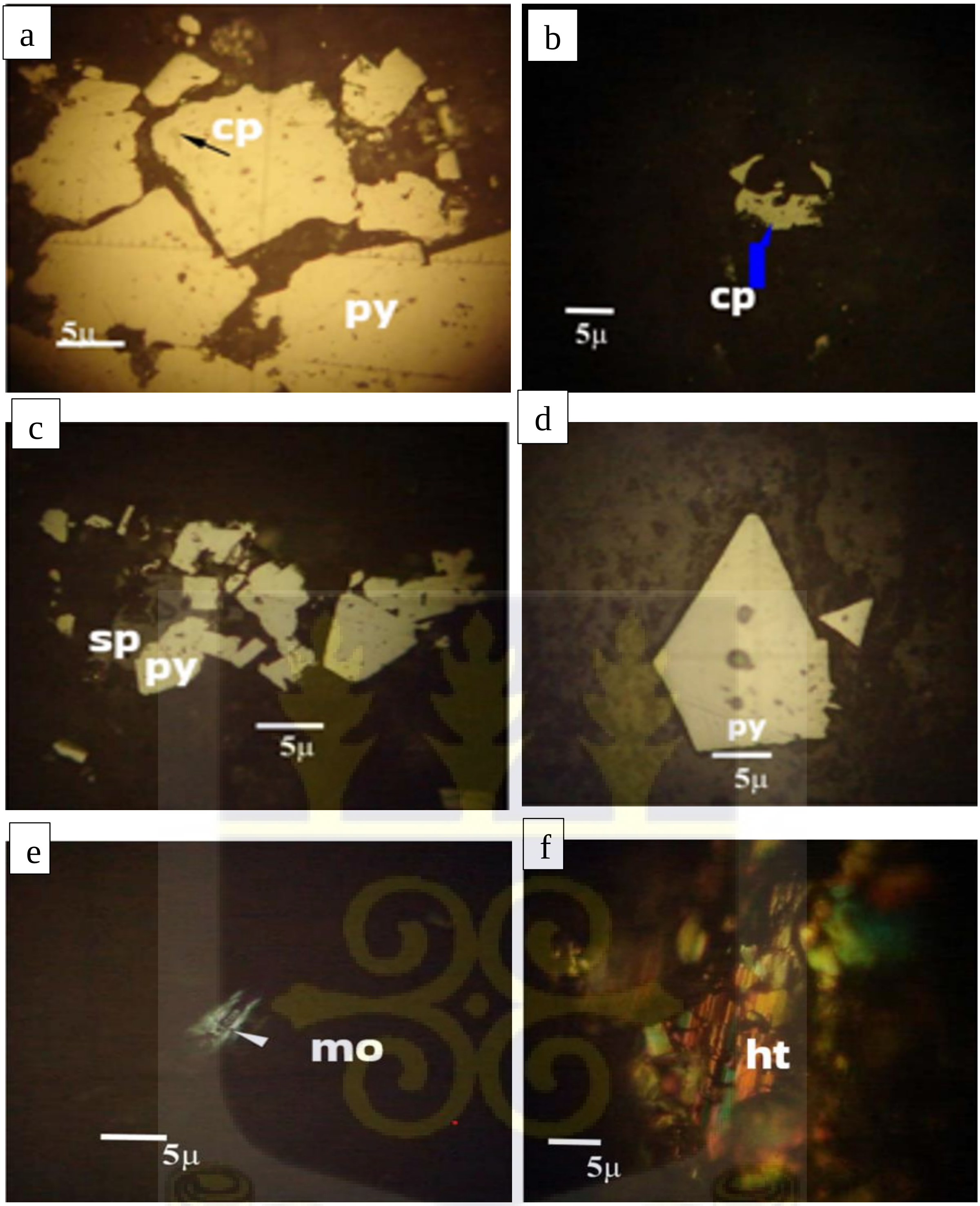

**Figure 4.31: Polished section photomicrographs of footwall mafic volcanic rock (FW13) showing a) tectonised pyrite (py) with chalcopyrite (cp) inclusions b) corroded grains of chalcopyrite c) corroded grains of sphalerite (sp) and pyrite d) undisturbed subhedral pyrite grains e) molybdenite (mo) grain f) haematite (ht) grain.**

**Table 4.3. Mineral compositions of the hanging wall mafic volcanic rock and their respective modal contents by point counting**

| Rock type | Sample | Quartz | Plagioclase | Chlorite | Sericite | Epidote | Calcite | Ankerite | Opaque minerals |
|---|---|---|---|---|---|---|---|---|---|
| Hanging wall (volcanic) | HW01 | 29 | 20 | 23 | 2 | | 4 | 21 | 1 |
| | HW 02 | 30 | 17 | 24 | 4 | | 4 | 20 | 1 |
| | HW 03 | 28 | 23 | 22 | 3 | | 4 | 18 | 2 |
| | HW 04 | 25 | 24 | 19 | 5 | | 5 | 21 | 1 |
| | HW 05 | 33 | 19 | 18 | 3 | | 4 | 21 | 2 |
| | HW 06 | 31 | 18 | 24 | 2 | | 4 | 20 | 1 |
| | HW 07 | 29 | 20 | 21 | 5 | | 5 | 19 | 1 |
| | HW 08 | 27 | 21 | 22 | 3 | | 4 | 22 | 1 |
| | HW 09 | 30 | 16 | 24 | 5 | | 5 | 18 | 2 |
| | HW 10 | 27 | 20 | 21 | 5 | | 4 | 22 | 1 |
| Footwall (volcanic) | FW 01 | 24 | 21 | 35 | | 10 | 2 | 6 | 2 |
| | FW 02 | 23 | 19 | 36 | | 12 | 3 | 6 | 1 |
| | FW 03 | 22 | 21 | 38 | | 7 | 2 | 8 | 2 |
| | FW 04 | 21 | 20 | 37 | | 12 | 3 | 6 | 1 |
| | FW 05 | 20 | 22 | 35 | | 11 | 3 | 7 | 2 |
| | FW 06 | 22 | 18 | 37 | | 12 | 3 | 7 | 1 |
| | FW 07 | 19 | 23 | 36 | | 13 | 2 | 6 | 1 |
| | FW 08 | 21 | 21 | 35 | | 12 | 3 | 6 | 2 |
| | FW 09 | 20 | 19 | 38 | | 11 | 2 | 8 | 2 |
| | FW 10 | 21 | 20 | 37 | | 13 | 3 | 5 | 1 |

A similar metamorphic mineral assemblage of quartz, chlorite, sericite, carbonate, and feldspar occurs in the greywacke, quartz epiclastic rock and the hanging wall mafic volcanic rock. Also, chlorite and epidote occur in the footwall mafic volcanic rock. The presence of these minerals suggests greenschist facies metamorphism. Allibone et al. (2002), puts the general metamorphism in the Ashanti volcanic belt at greenschist to upper greenschist facies. Thus, these rocks could be assigned “meta” to their field names for example; greywacke, meta-quartz epiclastic and metavolcanic rocks. Due to the extremely fine nature of the mafic volcanic rocks, these are further classified with the help of the whole rock geochemical data.

## 4.6 Major structures in the Kibi gold zone

Generally, the study area is underlain by intensely deformed rocks. A distinct D1 (S1) and D2 (S2) deformational event has been distinguished from the aeromagnetic and radiometric dataset which was confirmed by geological field mapping. D1 - and D2 are associated with feature recognition and the resolution of the regional-scale geophysical interpretations, down to a target- or outcrop-scale, is often difficult, although general trends and patterns of gold mineralization in the study area are evident. The complexity of folds (tight to isoclinal) and shears that define the target-scale structural settings of the Kibi study area, often result in regional-scale and geophysically-interpreted shears/contacts/lineaments being a challenge (Koegelenberg et al., 2021).

Generally, shear zones (Figure 4.32a and b), fractures, folds (Figure 4.32c) and faults (Figure 4.32d) are the predominant structures in the study area. Most fractures are veined with brecciated minerals which can be attributed to shearing (Figure 4.32c). The predominant structural event in the Kibi – Winneba Belt is thrusting which gave rise to a fault that extends 10km. Four events have been recognized notably D1, D2, D3 and D4, (Davis and Stephens, 2005). D1 (S1) bedding, (S0) - parallel foliation and associated F1 isoclinal folds. Regional to license-scale S1 foliations may be assumed to be sub-parallel to lithological contacts, which otherwise provide sufficient contrast on geophysical surveys. Associated features, including F1 isoclinal folds (viz. shear-folds) that show fold widths varying from centimeter-scale up to 200m, are only observed on a target scale. D1 is consistently and readily correlated with the regionally-defined D1, as described by Perrouty et al. (2012).

D 2 (S 2) - Regional- to license-scale NNE- to NE-trending S 2 foliations are consistently observed and characterized as a pervasive and penetrative axial-planar cleavage to tight- to isoclinal F 2 folds. S 2 cleavages are particularly well-defined in the metasediments, which are prone to preferential cleavage development, compared to more rheologically competent, interlayered metavolcanics and intrusions. S 2 and associated F 2 folds locally transpose and refold S 1 and F 1 foliations and folds. Moreover, regional - to licence -scale shears, that otherwise constrain, internally dissect, segment and locally transpose relict D 1 domains defining the Kibi Belt are assigned to D 2. In this context, D 2, may be compared/associated with regionally-defined D3-4 reverse-sinistral kinematics, as described by Perrouty et al. (2012).

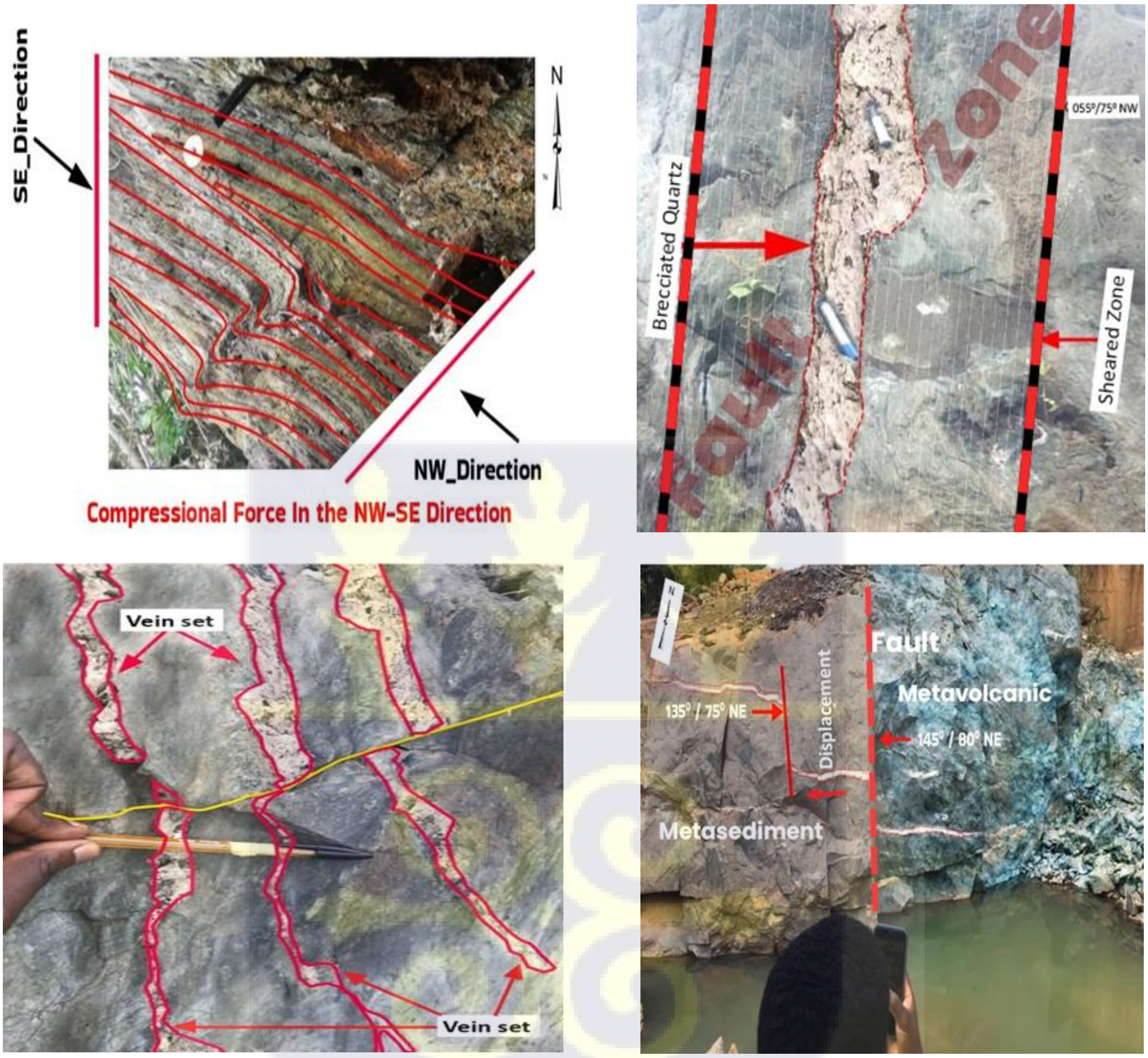

**Figure 4.32: Geological structures in the Kibi area a) folded metasedimentary beds in the Ettukrom gold zone b) brecciated quartz vein within a sheared metasedimentary rock in the Agyapoma gold zone. c) set of veins in metavolcanic rocks d) fault zone resulting in the displacement of a vein intruding both metavolcanic and metasedimentary rocks in the Kibi gold zone**

## 4.7 Mineralization style(s) and deposits

Gold mineralization in the study area is associated with the metasedimentary and metavolcanic rock units. The average gold grades of the outcrop samples are 2.56 g/t at Ettukrom, 4.8g/t at Agyapoma,16.5g/t at Cobra Creek, 1.4g/t at Adukrom - Segyemase, 1.7g/t at the gold mountain and 1.2g/t at Afiasa (Independent Technical Report of Kibi Gold Project by Xtra Gold Resources Corp, 2012). Gold mineralization in the study area is characterized by auriferous quartz-carbonate (Figure 4.33a), tensional vein, arrays or stockworks (Figure 4.33b) hosted in the quartz-feldspar porphyry as observed Cobra Creek and Agyapoma satellite lode gold deposit as against mafic to intermediate metavolcanic layers or undifferentiated and sills/dykes, and graphitic mineralized shear zones as recorded in Afiasa, gold mountain and Adukrom-Segyemase. Gold mineralization in the study area is geologically analogous to other intrusive or metavolcanic-hosted gold deposits of Ghana. This includes nearby deposits such as Newmont Akyem mines at Nkawkaw, Akroma mines at Nkawkaw, and Oware mine at Konongo in the Ashanti belt. It can also be compared to Kinross Goldfields Chirano and Newmont Mining Subika deposits in the Sefwi Belt. These tensional vein arrays are generated where the above-mentioned competent host lithologies undergo preferential strain, leading to fracturing and auriferous mineralization. Such sites are typically localized along host-metasediment contacts that define sheared fold limbs, fold hinges or apparent flexures. Auriferous vein arrays are penetrative into metasediments but to a very limited extent. Hydrothermal alteration adjacent to quartz-carbonate veins is highly variable, but in heavily veined (stockworks) granitoid the assemblage is characterized by moderate to strong quartz, carbonate, chlorite and sericite alteration. This is also associated with patchy to pervasive sulphidization in the form of disseminated pyrrhotite, pyrite and arsenopyrite (+/- sphalerite).

**Figure 4.33: a) Auriferous quartz-carbonate rock b) Stockworks hosted by the quartz-feldspar porphyry as observed Cobra Creek and Agyapoma satellite lode gold deposit.**

Typically, they are connected to regional structures that trend NNE to NE and are underlain by argillites, greywackes and volcaniclastics. Even though, intermediate and mafic granitic intrusions occurring in the volcanic belt are also important host rocks (Ahafo Mineral Resource / Reserve Report, 2006).

The stereonet (Figure 4.34) was employed as a means of understanding and interpreting the stereographical projection of three-dimensional information of the study area onto a two-dimensional plane. The attitudes of the various geologic structures such as lineaments, foliations, shear zones and faults in the study area were plotted to understand the trends and patterns of gold mineralization. Three major structural trends were observed in the study area. Northwest-southeast (NW-SE) 320$^{o}$ trending that resulted in most regional faults (DO1). This was observed in most unmineralized joints (Figure 4.35), lineaments, faults, shear zones and isoclinal folds at Takyiman, Potroase, Bomaa, Addo Nkwanta, Anyinam and Osiem.

Two late local tectonic events resulted in parallel northeast-southwest trending NE-SW ($055^0$) gold mineralized shear zones. These faults run through the metasedimentary Tarkwaian rocks at Kibi, Pano, Asiakwa, Agyapoma, Ettukrom, Osino and Ankaase where lode gold artisanal mining is effectively being exploited.

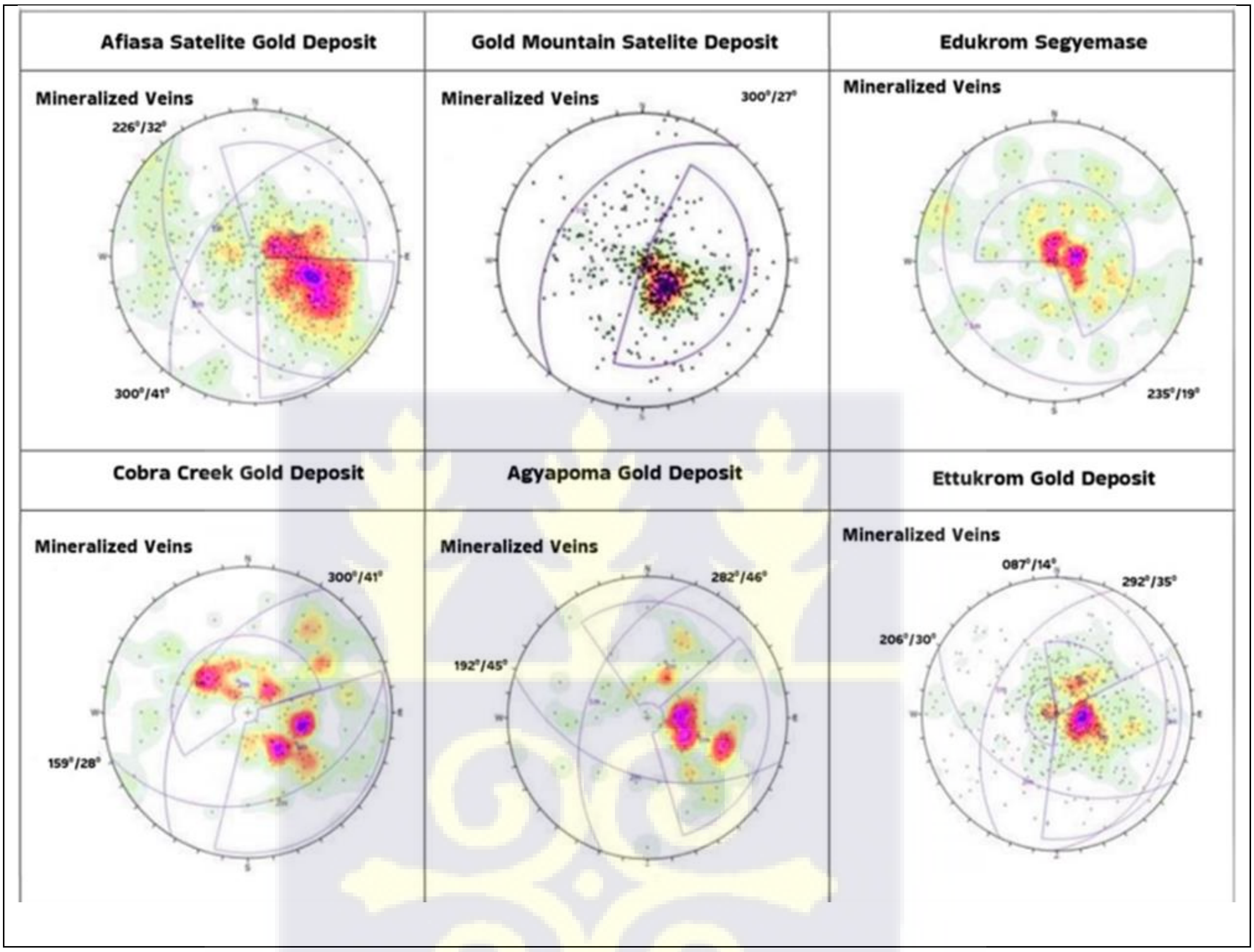

**Figure 4.34: Stereographic plots of mineralized veins in the Kibi gold zone.**

This type of deposit is generally associated with composite quartz-vein arrays which are usually related to the disseminated sulphides (Kesse, 1985). The mineralized shear zones are characterized by strong carbonate, chlorite and sericite alterations which are intensely silicified. The outcrops are strongly faulted, magnetic and mylonitic as shown in Figure 4.32.

Also, field observation from Kibi, Pano, Asiakwa, Agyapoma, Ettukrom, Osino and Ankaase mapping exercise, revealed meso and micro-structural analysis suggesting that two local deformational episodes (named DO1 and DO2) occurred in the Kibi gold zone. NW-SE compression produced tight isoclinal F1 folds with NE-SW striking axial planes, sub-vertical S1 metamorphic foliation and NW-SE plunging L1 lineations during the first episode (DO1). The development of this NE-SW S1 foliation, which is categorized as either strongly strained or low strained, is closely correlated with the occurrence of this early deformation event (Eisenlohr and Hirdes, 1992). The D2 event observed at Obuasi is correlated with the tight isoclinal F1 folds with NE-SW striking axial planes and steep dipping (Allibone et al., 2002). These NW-SE folds and shears zones in the Tarkwaian rock unit hold extensional veins striking $055^0$ and moderately dipping to the southwest correlated with high gold grades of quartz veins of the outcrop samples.

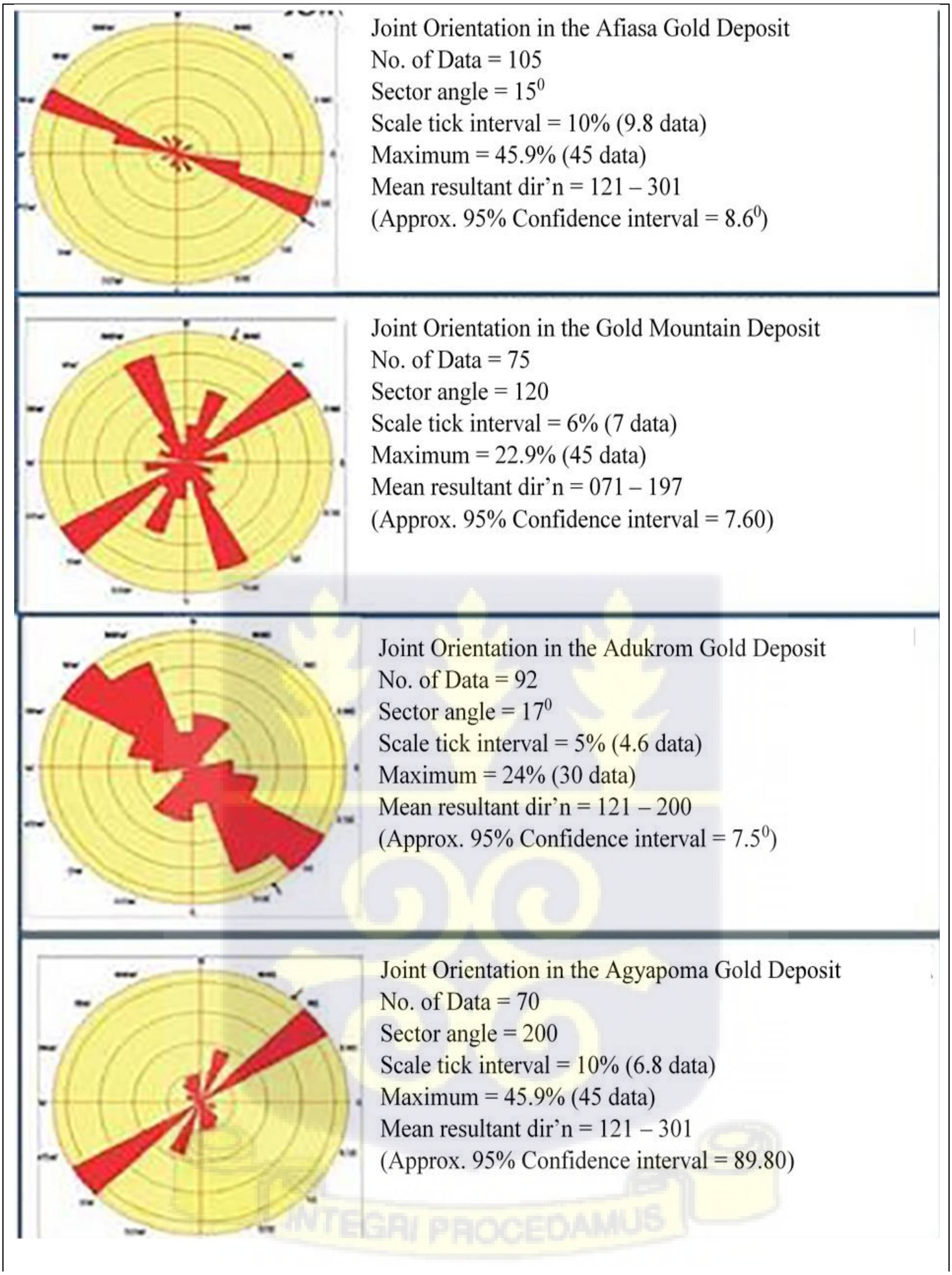

Joint Orientation in the Afiasa Gold Deposit
No. of Data = 105
Sector angle = $15^0$
Scale tick interval = 10% (9.8 data)
Maximum = 45.9% (45 data)
Mean resultant dir'n = 121 – 301
(Approx. 95% Confidence interval = $8.6^0$)

Joint Orientation in the Gold Mountain Deposit
No. of Data = 75
Sector angle = 120
Scale tick interval = 6% (7 data)
Maximum = 22.9% (45 data)
Mean resultant dir'n = 071 – 197
(Approx. 95% Confidence interval = 7.60)

Joint Orientation in the Adukrom Gold Deposit
No. of Data = 92
Sector angle = $17^0$
Scale tick interval = 5% (4.6 data)
Maximum = 24% (30 data)
Mean resultant dir'n = 121 – 200
(Approx. 95% Confidence interval = $7.5^0$)

Joint Orientation in the Agyapoma Gold Deposit
No. of Data = 70
Sector angle = 200
Scale tick interval = 10% (6.8 data)
Maximum = 45.9% (45 data)
Mean resultant dir'n = 121 – 301
(Approx. 95% Confidence interval = 89.80)

**Figure 4.35: Stereographic plots of the joints in the various satellite lode gold deposit**

## 4.8. Interpretation of Ore Textures

The ore minerals encountered in the study area may be grouped into three generations, namely, generation 1 (the oldest), generation 2 (intermediate) and generation 3 (the youngest). Pyrite occurs throughout the three generations as discussed below.

i. Pyrite (1) is anhedral and corroded (Figure 4.25a)

ii. Pyrite (2) is fractured and corroded (Figure 4.25b)

iii. Pyrite (3) is euhedral with or without inclusions (Figure 4.25d).

These generations as shown in Figure 4.29 occur in the hanging wall mafic volcanic rocks while those in Figure 4.31 also occur in the footwall mafic volcanic rocks. Chalcopyrite occurs in the first (1) (Figure 4.29a) and second (2) generations (Figure 4.31f) and partly overlaps the third generation because the exact timing of the filling in fractures and cavities (Figures 4.29j and 4.31b respectively) in second-generation pyrite is not known. Rutile and haematite exist in both generations 1 and 2 (Figure 4.29h and Figure 4.31j). Sphalerite and magnetite are only present in the first generation. Gold only occurs in the second generation and is associated with pyrite 2 which is fractured and has sieve textures (Figures 4.29k and 4.31c). The association of pyrrhotite with gold in a pyrite cavity (Figure 4.31c) suggests that the pyrrhotite was probably crystallized out from the same mineralizing fluid as that which deposited the gold. Pyrrhotite is of hydrothermal source and occurs as corroded anhedral grains usually in unmineralized rocks (HW and VE) and probably of a magmatic source. It is well known that, in metamorphic settings, pyrite can undergo desulphidation reactions and become pyrrhotite (Toulmin and Barton 1964). However, two generations of pyrrhotite are inferred, an earlier magmatic and a later hydrothermal pyrrhotite. Adjimah (1988) reported primary and hydrothermal pyrrhotite in the metavolcanic rocks of Prestea. Molybdenite exists in a mineralized quartz vein and was probably crystallized out from the same mineralizing fluid. The presence of both pyrrhotite and molybdenite in the mineralizing fluid suggests a high-temperature source. The existence of rutile in the cavities of generation 2 pyrite and within the invaded fluid suggests a deep-seated magmatic source of the mineralizing fluid. A summary of the paragenetic sequences with time is shown in Table 4.4.

**Table 4.4. Summary of mineral generations with time**

| Mineral | Mineral generations based on pyrite morphology | | |
|---|---|---|---|
| | 1 (anhedral pyrite) | 2 (fractured pyrite) | 3 (euhedral with or without inclusions) |
| Pyrite | ▬ | ▬ | ▬ |
| Chalcopyrite | ▬ | ▬ ▬ | |
| Sphalerite | ▬ | | |
| Rutile | ▬ | ▬ | |
| Haemattite | ▬ | ▬ | |
| Magnetite | ▬ | | |
| Gold | | ▬ | |
| Molybdenite | | ▬ | |
| Pyrrhotite | ▬ | ▬ | |

The presence of both magnetite and haematite gives a clue to the reduction/oxidation (redox) condition that existed. The magnetite grains were invaded by some fluid and also replaced by pyrite, and the presence of haematite grains gives some supporting evidence that the mineralizing environment was possibly oxidizing and can be shown by the following equation (Equation 3) (Guilbert and Park, 1986):

$$\underset{\text{Magnetite}}{Fe_3O_4} \rightleftarrows \underset{\text{Haematite}}{Fe_2O_3} \quad \text{Oxidizing reduction} \quad \text{……….. Equation 3}$$

## 4.9 Geochemical characteristics of the greywackes

### 4.9.1 Major element contents

According to Armstrong-Altrin et al. (2018), the major element content of rocks often defines their mineralogy. Table 4.5 presents variable concentrations of the major elements in weight percent (wt.%) for the eighteen (18) greywacke samples collected form the Kibi gold zone. From the XRF analysis, $SiO_2$ ranges from 37.87- 64.51wt.%, $TiO_2$ (0.22 - 0.80) wt.%, $Al_2O_3$ (7.93-17.51) wt.%, MnO (0.06 - 0.16) wt.%, $K_2O$ (0.2 – 3.6) wt.%, $Fe_2O_3$ (3.97-9.13) wt.%, $P_2O_5$ (0.12 – 0.38) wt.%, MgO (3.06 - 7.59) wt.%, $Na_2O$ (2.18 – 7.18) wt.%, and CaO (1.24 - 10.16) wt.%. The majority of the $SiO_2$ may have come from detrital quartz, given the low to moderate $SiO_2$ level. The average $SiO_2/Al_2O_3$ ratio of 4 indicates low sediment maturity probably associated with intermediate igneous rocks (Roser et al. 1996). However, the ratios of $Al_2O_3/Na_2O$, $Al_2O_3/K_2O$, $K_2O/Na_2O$ and $Al_2O_3/TiO_2$ in the greywacke samples are 3.6, 11.2, 0.5 and 28.2 respectively (Table 4.5). A slightly reduced $K_2O/Na_2O$ ratio indicates that the rock type understudy is mineralogically immature and that Na-rich plagioclase predominates (Osae et al., 2006) as seen in petrography. The greywacke samples might have intermediate igneous provenance, based on the high $Al_2O_3/TiO_2$ ratio (28.2). From the Harker plot for the greywacke samples collected from the Kibi gold zone (Figure 4.36), all elements exhibit scattered trends except $TiO_2$, which shows a high negative correlation with $SiO_2$.

From Table 4.6, all the major oxides (CaO (r=-0.71), $TiO_2$ (r=-0.62), $Al_2O_3$ (r=-0.62), $Fe_2O_3$ (r=-0.56), MnO (r= -0.74), MgO (r=-0.80) and $P_2O_5$ (r=-0.073)) correlate negatively with $SiO_2$ barring $Na_2O$ and $K_2O$ which display negligible correlation (r =0.29 and -0.09). The negligible contents of $K_2O$ and $Na_2O$ in the greywacke samples maybe attributed to their susceptibility to alteration and hence their diffused patterns. This indicates that the majority of $SiO_2$ in the greywacke samples are present as quartz grains, with traces of biotite, amphiboles, K-feldspar and plagioclase. The moderate positive correlation (r = 0.55) between $K_2O$ and $Al_2O_3$ suggests reasonable contributions from K-bearing minerals especially K-feldspar (McLennan et al. 1983; Ji'an and Lianhua 1994) which is evident in the petrography.

Additionally, the moderately negative correlation (r = -0.71) between $SiO_2$ and CaO indicates the presence of carbonates, likely as secondary minerals or as an alteration product of calcic plagioclase, while the weak positive correlation (r = 0.15) between $Al_2O_3$ and MgO may imply a minimal contribution of chlorite in the source rock (Feng and Kerrich 1990). The potential contribution of ferromagnesian minerals, such as magnetite, epidote, and biotite, is suggested by the positive association between MnO-$TiO_2$ and $Fe_2O_3$-$TiO_2$. In the greywackes, loss on ignition (LOI) values vary from 0.00 to 18.4. The high LOI contents associated with the greywacke samples may be attributed to the carbonate content (Figure 4.23c) and subsequent hydrothermal alteration that affected the rocks.

## Table 4. 5 Whole-rock major-element compositions of greywackes from the Kibi area

| Sample | GW01 | GW02 | GW03 | GW04 | GW05 | GW06 | GW07 | GW08 | GW09 | GW10 | GW11 | GW12 | GW13 | GW14 | GW15 | GW01 | GW17 | GW18 |
|---|---|---|---|---|---|---|---|---|---|---|---|---|---|---|---|---|---|---|
| $SiO_2$ | 51.8 | 59.9 | 51.6 | 53.6 | 37.9 | 48.5 | 64.0 | 51.5 | 54.3 | 64.5 | 52.8 | 55.4 | 51.9 | 50.0 | 62.2 | 57.2 | 57.8 | 41.0 |
| $TiO_2$ | 0.6 | 0.5 | 0.4 | 0.6 | 0.8 | 0.7 | 0.5 | 0.5 | 0.5 | 0.2 | 0.7 | 0.5 | 0.6 | 0.7 | 0.4 | 0.4 | 0.5 | 0.4 |
| $Al2O_3$ | 16.7 | 15.5 | 15.0 | 16.2 | 11.7 | 13.1 | 12.2 | 12.3 | 16.8 | 7.9 | 17.5 | 16.0 | 16.3 | 15.2 | 17.0 | 12.3 | 11.9 | 10.7 |
| $Fe_2O_3$ | 6.7 | 6.1 | 4.2 | 6.6 | 9.0 | 9.1 | 5.9 | 6.9 | 6.8 | 4.0 | 8.1 | 6.4 | 7.1 | 7.2 | 5.0 | 5.3 | 5.5 | 5.2 |
| MnO | 0.1 | 0.1 | 0.1 | 0.1 | 0.2 | 0.1 | 0.1 | 0.1 | 0.1 | 0.1 | 0.1 | 0.1 | 0.1 | 0.1 | 0.1 | 0.1 | 0.1 | 0.2 |
| MgO | 4.2 | 3.7 | 3.8 | 4.0 | 7.6 | 5.9 | 3.4 | 5.2 | 4.4 | 4.5 | 3.6 | 3.7 | 3.7 | 4.4 | 3.1 | 3.6 | 3.6 | 6.0 |
| CaO | 3.2 | 2.6 | 5.5 | 3.7 | 10.2 | 4.4 | 4.2 | 6.8 | 3.9 | 5.4 | 2.6 | 2.5 | 3.4 | 5.1 | 1.2 | 3.7 | 4.6 | 9.6 |
| $Na_2O$ | 2.8 | 6.1 | 7.2 | 3.4 | 2.8 | 4.3 | 5.5 | 3.2 | 3.5 | 5.6 | 2.2 | 5.4 | 4.9 | 2.6 | 4.1 | 6.5 | 6.0 | 6.4 |
| $K_2O$ | 2.7 | 1.2 | 1.1 | 2.4 | 1.7 | 1.2 | 0.9 | 2.1 | 2.7 | 0.2 | 3.6 | 2.0 | 2.4 | 3.1 | 3.3 | 1.0 | 0.6 | 0.5 |
| $P_2O_5$ | 0.1 | 0.2 | 0.2 | 0.1 | 0.2 | 0.2 | 0.2 | 0.2 | 0.2 | 0.1 | 0.2 | 0.2 | 0.1 | 0.2 | 0.1 | 0.3 | 0.4 | 0.2 |
| LOI | 10.2 | 2.1 | 9.3 | 8.6 | 17.0 | 12.5 | 0.0 | 10.4 | 6.9 | 6.2 | 8.7 | 7.0 | 9.0 | 11.0 | 3.2 | 9.1 | 6.8 | 18.4 |
| $SiO_2/Al_2O_3$ | 3.1 | 3.9 | 3.4 | 3.3 | 3.2 | 3.7 | 5.3 | 4.2 | 3.2 | 8.1 | 3.0 | 3.5 | 3.2 | 3.3 | 3.7 | 4.7 | 4.9 | 3.8 |
| $Al_2O_3/Na_2O$ | 6.0 | 2.5 | 2.1 | 4.7 | 4.2 | 3.0 | 2.2 | 3.8 | 4.8 | 1.4 | 8.0 | 3.0 | 3.3 | 5.9 | 4.2 | 1.9 | 2.0 | 1.7 |
| $Al_2O_3/K_2O$ | 6.2 | 12.6 | 14.1 | 6.9 | 6.9 | 10.6 | 12.9 | 5.8 | 6.2 | 36.0 | 4.9 | 8.0 | 6.9 | 4.9 | 5.2 | 12.9 | 20.1 | 21.3 |
| $K_2O/Na_2O$ | 1.0 | 0.2 | 0.1 | 0.7 | 0.6 | 0.3 | 0.2 | 0.7 | 0.8 | 0.0 | 1.7 | 0.4 | 0.5 | 1.2 | 0.8 | 0.1 | 0.1 | 0.1 |
| $Al_2O_3/TiO_2$ | 30.3 | 31.0 | 40.6 | 29.4 | 14.6 | 17.9 | 25.9 | 24.2 | 32.3 | 36.0 | 24.7 | 31.5 | 27.7 | 21.1 | 40.4 | 29.3 | 25.8 | 24.2 |
| CIA | 69.0 | 57.6 | 53.7 | 66.3 | 64.5 | 60.9 | 54.9 | 61.9 | 66.0 | 45.7 | 70.0 | 59.1 | 60.6 | 66.6 | 62.4 | 51.3 | 53.1 | 49.1 |
| MIA | 37.9 | 15.2 | 7.4 | 32.6 | 29.0 | 21.7 | 9.7 | 23.8 | 31.9 | 8.7 | 40.1 | 18.2 | 21.2 | 33.2 | 24.7 | 2.6 | 6.1 | 1.8 |
| PIA | 75.0 | 58.5 | 54.0 | 70.6 | 68.1 | 62.4 | 55.4 | 65.5 | 70.8 | 45.5 | 79.1 | 60.9 | 63.1 | 73.5 | 66.7 | 51.4 | 53.2 | 49.0 |

**Table 4. 6: Correlation matrix for the major elements in the greywacke samples from the Kibi area**

| | $SiO_2$ | $TiO_2$ | $Al_2O_3$ | $Fe_2O_3$ | MnO | MgO | CaO | $Na_2O$ | $K_2O$ | $P_2O_5$ |
|---|---|---|---|---|---|---|---|---|---|---|
| $SiO_2$ | 1 | | | | | | | | | |
| $TiO_2$ | -0.621 | 1 | | | | | | | | |
| $Al_2O_3$ | -0.639 | .562 | 1 | | | | | | | |
| $Fe_2O_3$ | -0.562 | .949 | .464 | 1 | | | | | | |
| MnO | -.741 | .310 | .134 | .328 | 1 | | | | | |
| MgO | -.801 | .453 | .158 | .513 | .789 | 1 | | | | |
| CaO | -.711 | .142 | .086 | .127 | .800 | .847 | 1 | | | |
| $Na_2O$ | .296 | -.684 | -.413 | -.699 | -.110 | -.260 | .032 | 1 | | |
| $K_2O$ | -.090 | .511 | 0.552 | .442 | -.231 | -.205 | -.429 | -.789 | 1 | |
| $P_2O_5$ | -.075 | -.032 | -.099 | -.109 | .324 | -.042 | .113 | .407 | -.398 | 1 |

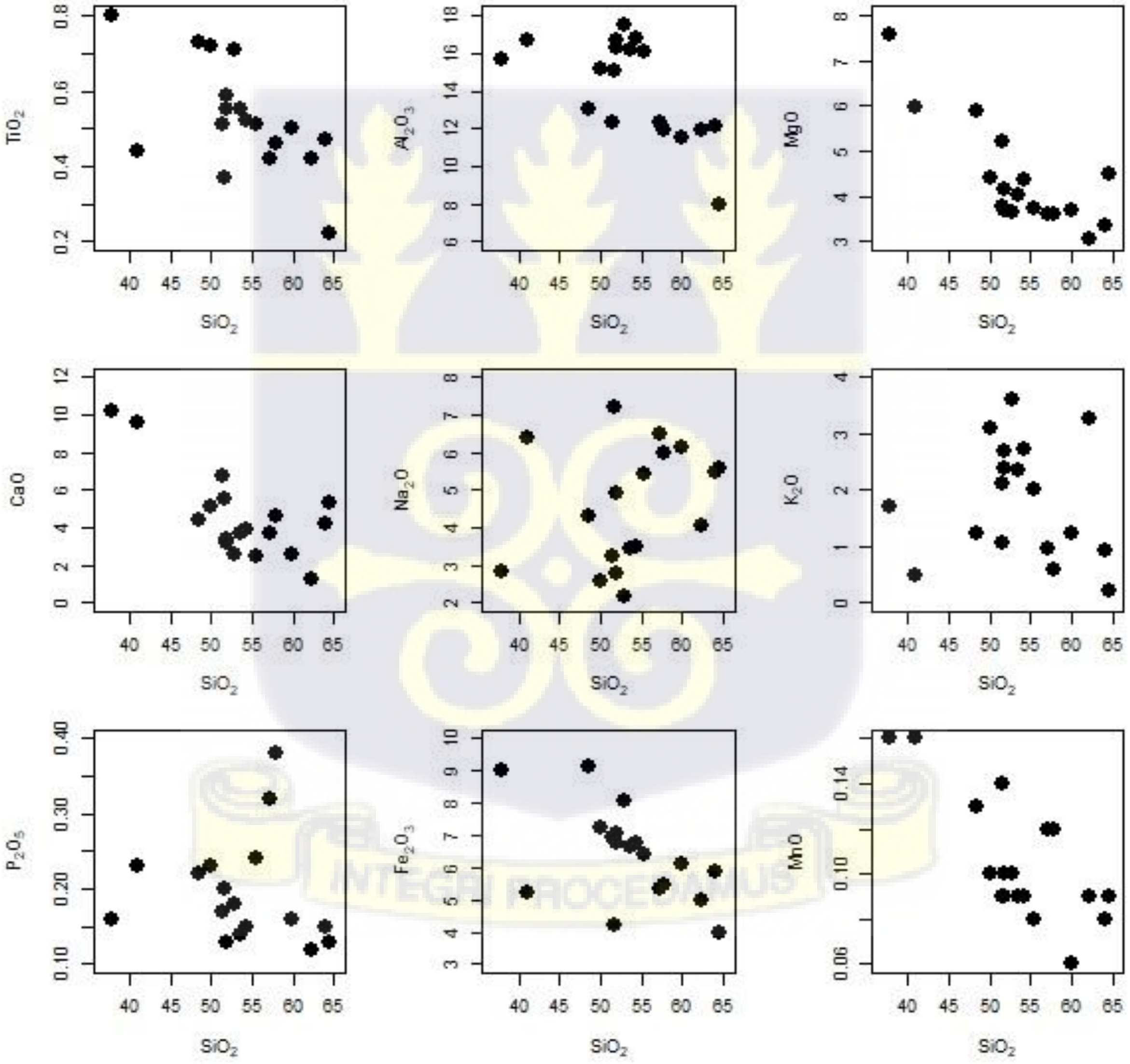

Figure 4.36: Harker diagram for the greywacke samples in the Kibi gold zone

### 4.9.2 Trace element contents in the greywacke samples

Trace element geochemistry has been widely used in understanding the evolution of the earth (White, 2013) and has been grouped into large ion lithophile elements (LILE) (Rb, Ba, Sr, Cs and U), high field strength elements (HFSE) (Y, Zr, Nb, Ta, Th and Hf) and transitional elements (V, Cr, Co, Cu, Ni and Sc). The study of high field strength elements (HFSE) can give helpful details regarding the source rocks because they are least altered by metamorphism, alteration and other geochemical processes like chemical weathering (McLennan, 1989). The trace element contents within the graywacke samples understudy were normalized against the Upper Continental Crust (UCC) and Post Archean Australian Shales (PASS) values proposed by Taylor and McLennan (1985). This is because rocks with enriched LILEs coupled with slightly depleted HFSEs and transitional elements display signatures of UCC (Figure 4.37a) and PAAS (Figure 4.37b).

Concentrations of selected LILEs have been presented in Table 4.7. In greywacke samples, the average values of Rb, Ba, Sr, Cs, and U are 41.19 ppm, 777.22 ppm, 570 ppm, 2.85 ppm, and 4.57 ppm, in that order. The high Ba and Sr levels in the greywacke samples compared to the average UCC contents indicate their predominance in the source rocks, or perhaps because of high feldspar content, synsedimentary precipitation of barite, or effect from later metamorphism (Gale and Roberts 1974). Generally, the enrichment of the LILEs (Ba, Sr, U, Rb and Cs) on the UCC normalized spider diagram (Figures 4.37a and b) suggest the influence of crustal materials, as proposed by Allibone et al. (2009).

The average contents of HFSEs **(**Y, Zr, Nb, Th and Hf) in the greywacke samples are 17.38, 95.83, 5.27, 5.11 and 10.18 ppm, respectively (Table 1). In comparison to UCC, low Y and Zr levels indicate extensive reworking during sediment transit, which may have resulted in the loss of heavy minerals, especially zircon (Asiedu et al. 2000). The Nb content is less than the mean UCC value of 10.70 ppm, indicating the potential impact of minerals from the continental crust (McLennan 1989). Since Nb is stationary throughout sedimentary processes, Hofmann (1988) suggests that the depletion of Nb indicates its fractionation from the parent rock. Hf concentration is almost the same as the average UCC value of 5.8 ppm (Taylor and McLennan 1995) which suggests different levels of mafic minerals and the depletion of heavy minerals especially zircon (Cullers, 1988). The average Zr/Hf ratio of 9.94 suggests that zircon predominates in the greywacke samples.

For the transitional elements in Table 4.7, the average contents of Cr and V in the greywacke samples are 147 ppm and 129.0 ppm respectively. V and Cr concentrations in all the samples are higher compared to their average UCC values for V and Cr are 107 ppm and 85 ppm respectively (Taylor and McLennan, 1995), which suggest a mafic source rock and the possible mica depletion (Wilson 1989; Cox and Lowe 1995; Wang et al. 2013). Also, the low Co (38.04 ppm) and Ni (35.08 ppm) contents compared to the average UCC values (Co = 44 ppm and Ni = 17 ppm) may indicate the slight influence of matrix materials as well argillaceous debris (Pettijohn 1963) in the greywackes understudy. The average Cr/Ni ratio for the selected greywacke is 4.45 which indicates the presence of mafic materials such as magnetite and chlorite as seen in the thin section. The average Cu content 31 which is slightly higher than the average UCC values of Cu (25 ppm) the presence of ferromagnesian minerals as supported by Sawyer (1986). Au concentration in the greywacke samples collected from the Kibi gold zone ranges from 1.2 to 5.2 ppm.

**Table 4. 7 Whole-rock trace-element (ppm) compositions of greywackes from the Kibi – Winneba Gold Belt of Ghana**

| | GW01 | GW02 | GW03 | GW04 | GW05 | GW06 | GW07 | GW08 | GW09 | GW10 | GW11 | GW12 | GW13 | GW14 | GW15 | GW16 | GW17 | GW18 |
|---|---|---|---|---|---|---|---|---|---|---|---|---|---|---|---|---|---|---|
| V | 131 | 129 | 84 | 131 | 263 | 193 | 110 | 127 | 150 | 43 | 140 | 140 | 223 | 170 | 87 | 97 | 56 | 48 |
| Cr | 129 | 137 | 91 | 162 | 289 | 251 | 162 | 166 | 176 | 91 | 199 | 126 | 170 | 288 | 39 | 29 | 37 | 119 |
| Co | 32.7 | 43.7 | 38.2 | 46.8 | 47.4 | 49.5 | 39.5 | 42.7 | 40.4 | 24.8 | 46.6 | 31.8 | 43.1 | 47.8 | 24.3 | 25 | 34.3 | 26.2 |
| Ni | 30.4 | 37.8 | 17.1 | 32.6 | 68.4 | 54.2 | 26.6 | 41.8 | 43.4 | 19.5 | 66.7 | 33 | 39.1 | 73.9 | 13 | 6.2 | 6 | 21.8 |
| Cu | 23.3 | 25.3 | 14.9 | 22.2 | 61.9 | 51.6 | 26.8 | 20.5 | 27.9 | 20.1 | 38 | 40.9 | 45.5 | 59 | 20.1 | 32 | 31.9 | 8.8 |
| Zn | 84.2 | 79.6 | 55 | 83 | 102.1 | 99.2 | 44.6 | 65.5 | 79.6 | 41 | 89.5 | 77.8 | 82.5 | 74.1 | 72.9 | 75.6 | 48.9 | 73.4 |
| Ga | 17.6 | 19.1 | 20.6 | 16.3 | 17.6 | 17.3 | 20.1 | 14.8 | 18.7 | 11.6 | 19 | 18.7 | 20.4 | 16 | 16.9 | 15.3 | 13.8 | 15.8 |
| As | 15.3 | 13.5 | 3 | 18.9 | 7.4 | 3.6 | 6 | 2.2 | 22.8 | 1.2 | 42.9 | 1.4 | 1.1 | < 0.8 | 1.4 | 3.4 | 6.5 | 0.9 |
| Rb | 61.5 | 27.2 | 23.8 | 51.2 | 36.6 | 29 | 20.8 | 46.2 | 63.3 | 7 | 87.7 | 50.9 | 54.7 | 65.1 | 70.9 | 18.4 | 13.9 | 13.3 |
| Sr | 410 | 433 | 1451 | 394 | 474 | 440 | 743 | 453 | 417 | 709 | 471 | 303 | 483 | 361 | 167 | 475 | 578 | 1498 |
| Y | 14.3 | 13.5 | 10.2 | 13.8 | 15.5 | 19.9 | 8.7 | 15 | 16.6 | 10.7 | 17.7 | 19.2 | 18.9 | 18 | 30.5 | 23.9 | 26.9 | 19.5 |
| Zr | 98 | 97 | 76 | 86 | 62 | 123 | 74 | 83 | 97 | 41 | 124 | 115 | 118 | 105 | 202 | 75 | 88 | 61 |
| Nb | 5.4 | 5.6 | 4.1 | 4.6 | 3.9 | 6.1 | 4.3 | 4.9 | 5.6 | 3.5 | 6.5 | 6.2 | 5.6 | 5.1 | 8.8 | 4.1 | 4.7 | 5.4 |
| Mo | 0.9 | 2.1 | 29.4 | 0.8 | 3.6 | 0.9 | 4.3 | 1.9 | 0.9 | 25.8 | 1.2 | 9.7 | 3.2 | 1.9 | < 1.0 | 1.3 | 2.3 | 16.6 |
| Sb | 4.2 | 7.6 | 7.8 | 5.4 | 8.4 | 5.3 | 8.4 | 5 | 7 | 6.6 | 32.9 | 11.5 | 11.1 | 9.3 | 13.6 | 12.2 | 13.6 | 10.6 |
| Cs | 1.3 | 5.1 | 3.3 | 2.5 | 1.6 | 1.2 | 3.8 | 1.8 | 2.9 | 1 | 6.2 | 2.2 | 5.7 | 3.9 | 3.7 | 2.7 | 1.4 | 1 |
| Ba | 759 | 338 | 1260 | 610 | 575 | 329 | 1640 | 403 | 662 | 134 | 1293 | 514 | 1225 | 942 | 872 | 873 | 509 | 1052 |
| La | 10.7 | 13.7 | 9 | 13.5 | 1.5 | 15.2 | 7.9 | 8.6 | 10.7 | 5.9 | 16.5 | 10.9 | 8.5 | 10.7 | 17.4 | 11.2 | 11.7 | 6.3 |
| Ce | 26.8 | 24.2 | 5.5 | 12.1 | 5.8 | 25.4 | 7.8 | 14.9 | 19.7 | 7.7 | 24.8 | 21.1 | 10.3 | 16.8 | 29.3 | 11.7 | 18.2 | 12.9 |
| Au | 2.11 | 1.46 | 1.25 | 2.32 | 1.22 | 1.4 | 1.28 | 1.64 | 2.54 | 4.84 | 1.82 | 2.34 | 2.53 | 2.58 | 2.42 | 5.22 | 2.93 | 1.99 |
| Ag | 0.08 | 0.05 | 0.09 | 0.77 | 0.07 | 0.07 | 0.08 | 0.23 | 0.01 | 0.05 | 0.04 | 0.25 | 0.12 | 0.03 | 0.03 | 0.08 | 0.6 | 0.7 |
| As | 52.8 | 27.6 | 1410 | 2420 | 669 | 1065 | 465 | 637 | 51.4 | 0.6 | 900 | 504 | 1902 | 39.8 | 45.4 | 53.8 | 1023 | 774 |
| Hf | 6.9 | 16.9 | 14.6 | 15.7 | 6 | 10.8 | 12.1 | 7.9 | 7.7 | 5.7 | 12.3 | 8.1 | 11.6 | 11.9 | 9.9 | 8.2 | 9 | 8 |
| Ta | 7.9 | 14.7 | 10 | 20.5 | < 6.7 | 11.5 | 9.7 | 6.6 | 7.5 | 7.4 | 14.3 | 6.6 | 15.2 | 13 | 8.4 | 5 | 6 | 6.7 |
| Pb | 9.6 | 25.9 | 16.9 | 15.1 | 10 | 10.4 | 30.2 | 12.5 | 10.7 | 17.3 | 12.8 | 11.8 | 12.9 | 24.1 | 8 | 8.4 | 16.5 | 17.7 |
| Bi | 2.3 | 8.2 | 6.9 | 8.4 | 2.3 | 5 | 6.1 | 4 | 2.9 | 2.5 | 5.9 | 3 | 5.4 | 5.9 | 2.5 | 3.4 | 3.4 | 5.2 |
| Th | 4.8 | 3.8 | 1,5 | 6.9 | 1.4 | 8.4 | 1.5 | 6.1 | 6.9 | 4.4 | 5.1 | 7.8 | 4 | 3.8 | 9.2 | 4.9 | 5 | 2.9 |
| U | 4 | 2.4 | 1.6 | 7.1 | 1.8 | 7.9 | 1.8 | 6.1 | 7.9 | 3.1 | 2.1 | 7.1 | 1.9 | 1 | 8.2 | 6 | 7.1 | 5.1 |

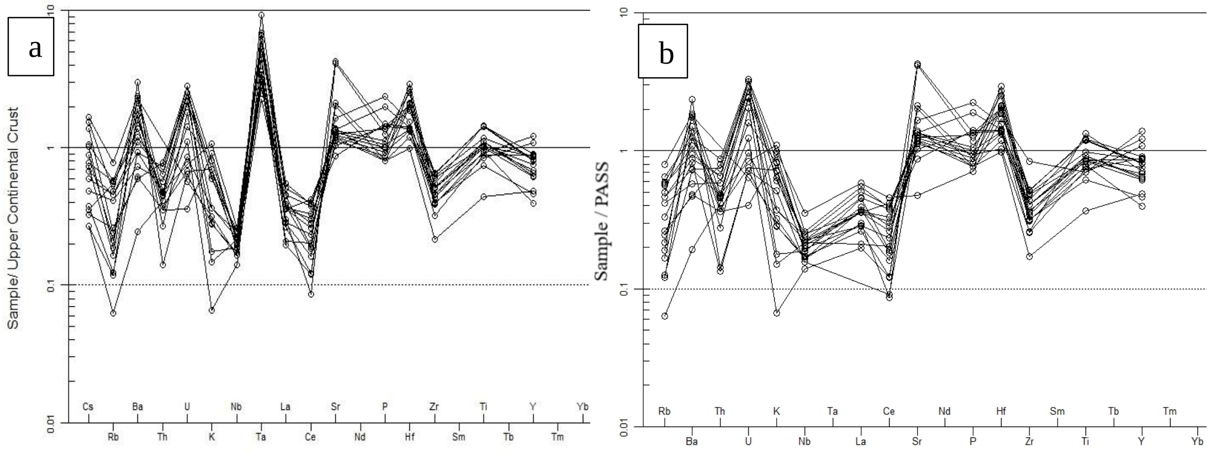

Figure 4.37: Trace element contents of the greywacke samples collected from the Kibi gold zone normalized against average a) UCC b) PAAS. The normalizing values are from Taylor and McLennan (1985).

### 4.9.3 Geochemical Classification of the greywacke

While the $SiO_2/Al_2O_3$ ratio identifies the amount of feldspar, quartz and clay components as well as distinguishes between mature and immature sediments, the $Na_2O/K_2O$ ratio discriminates among sandstones, arkose, and greywackes (Pettijohn 1972; Potter 1978). Pettijohn (1972) suggested that siliciclastic sedimentary rocks be divided into six fields, such as quartz arenite, litharenite, and greywacke, by comparing log ($SiO_2/Al_2O_3$) to log ($Na_2O/K_2O$). The investigated rock samples plot as greywackes on the log (($SiO_2/Al_2O_3$) against the log ($Na_2O/K_2O$) classification plot (Figure 4.38a). Furthermore, the samples were specifically plotted as sodic sediments (Figure 4.38b) on the $Fe_2O_3$+MgO, $Na_2O$, and $K_2O$ ternary diagram (Marston 1978), which is in line with the petrographic investigations.

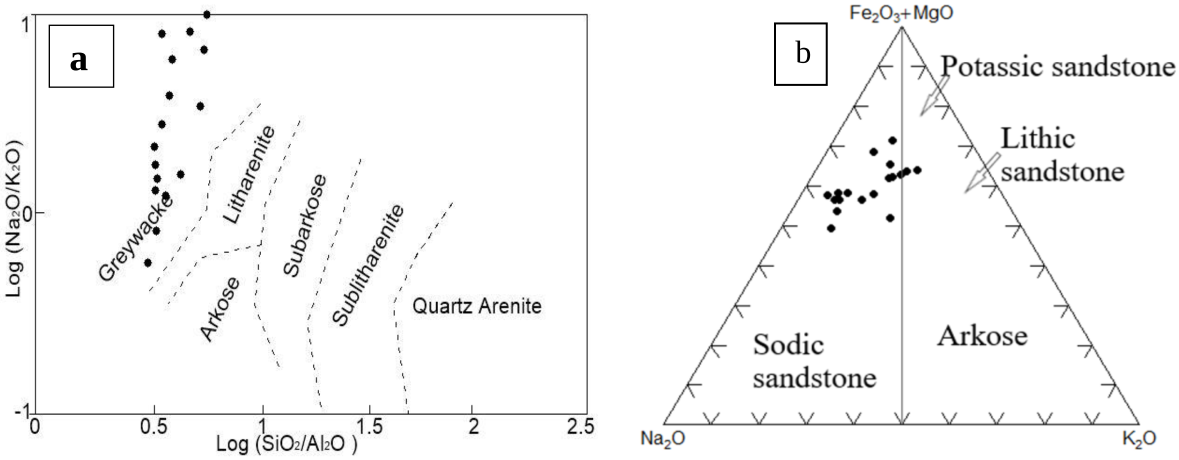

**Figure 4.38: Geochemical classification of the greywacke samples in the Kibi gold zone (a) Log ($SiO_2/Al_2O_3$) versus log ($Na_2O/K_2O$) (after Pettijohn 1972) (b) Trilinear plot of $Fe_2O_3$+MgO-$Na_2O$-$K_2O$ (after Marston 1978).**

### 4.9.4 Source rock composition

The varying ratios of plagioclase and K-feldspar in the metamorphosed greywackes point to either differential stability in the earth's surface conditions or their respective predominance in the metamorphic and igneous source rocks. Greywackes derived from sodium-rich volcanic or associated with feldspar albitization during diagenesis or low-grade metamorphism are typically characterized by a high plagioclase content (Pettijohn et al., 2012). The presence of chert in the metagreywacke may also suggest the influence of earlier sedimentary source rocks. A near-source derivation of debris, rapid deposition, and limited reworking are suggested by the presence of angular to subrounded clasts, moderately altered feldspars, and poor sorting in the greywackes (Basu, 1976; Blair & McPherson, 1994).

According to earlier workers (Wang et al., 2013; Cullers & Podkovyrov, 2000; Cullers, 2000; Wronkiewicz & Condie, 1990; Taylor & McLennan, 1985), the trace element ratios (La/Co = 0.29, Th/Cr = 0.05, Th/Co = 0.14, and Cr/Th = 60.66) are essential markers of provenance. The greywacke samples plot between basalt and UCC source rocks on Taylor and McLennan's

(1985) La/Co versus Th/Co binary diagram (Figure 4.39a). The greywackes' trace element ratios (Table 4.8) somewhat agree with data from mafic source rocks (Cullers 1994, 2000). In the discriminant function, 1 and 2 diagram (Figure 4.39b) by Roser and Korsch (1988), detritus of the greywackes have mafic to intermediate igneous provenances with two samples plotting in the field of felsic provenance.

**Table 4.8: Trace element ratios of the greywacke samples collected form the Kibi gold zone compared with felsic (Cullers et al. 1988), mafic (Cullers 2000, 1994) and Neoproterozoic UCC sources (Condie 1990).**

| Ratio | greywackes | Sediments from felsic sources | Sediments from mafic sources | Mean Neoproterozoic UCC values |
|---|---|---|---|---|
| La/Co | 0.29 | 1.80-13.8 | 0.14-0.38 | 1.79 |
| Th/Co | 0.14 | 0.67-19.4 | 0.04-1.40 | 0.72 |
| Cr/Th | 44.27 | 4.0-15.0 | 25-500 | 4.46 |

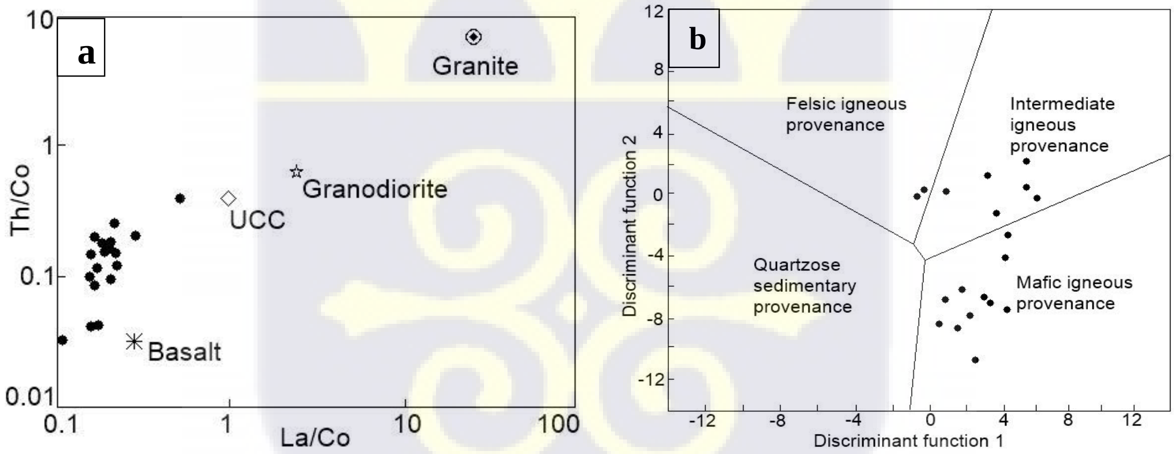

**Figure 4.39: (a) La/Co vrs Th/Co plot (b) Major element Discriminant Function diagram for sedimentary provenance determination by Roser and Korsch (1988). The discriminant functions are: Discriminant Function 1= (−1.773 $TiO_2$) + (0.607 $Al_2O_3$) + (0.760 $Fe_2O_3$) + (−1.500 MgO) + (0.616 CaO) + (0.509 $Na_2O$) + (−1.224 $K_2O$) + (−9.090); Discriminant Function 2= (0.445 $TiO_2$) +(0.070 $Al_2O_3$) + (−0.250 $Fe_2O_3$) + (−1.142 MgO) + (0.438 CaO) + (1.475 $Na_2O$) + (−1.426 $K_2O$) + (−6.861).**

#### 4.9.4.1 Sediment maturity

From the petrographic study, the greywacke samples in the Kibi gold zone are fine to medium-grained, compositionally immature, and poorly sorted with an average modal composition of quartz (68) % - feldspar (28)% and rock fragment (4)%. Roser et al. (1996) reported that quartz dominates over feldspar, mafics, and rock fragments as sediment maturity increases. The $SiO_2/Al_2O_3$ ratio (which is 4) for the greywacke (Table 4.9) is indicative of low maturity. Additionally, a $K_2O/Na_2O$ ratio of 0.5 indicates that Na-rich plagioclase predominates (Table 4.9), indicating that the rocks are mineralogically immature. To establish the composition of the source rocks, Cox et al. (1995) suggested using the non-quartzose composition of the sedimentary rocks and their index of compositional variability (ICV) (ICV= $(Fe_2O_3 + K_2O + Na_2O + CaO + MgO + MnO + TiO_2)/Al_2O_3$). ICV values greater than one show a low concentration of clay minerals combined with a higher concentration of minerals such as pyroxenes, K-feldspar, plagioclase, amphiboles, and pieces of rock (Cox et al. 1995). In a tectonically active margin, siliciclastic rocks with ICV values >1 are associated with first-cycle sediments and are compositionally immature (Perri et al. 2012). The greywackes in the Kibi gold zone have an average ICV value of 1.6, suggesting minimal recycling and immature composition.

### 4.9.5 Weathering history

The chemistry of a siliciclastic rock is mainly dependent on the composition as well as the pedogenetic processes present (Boggs, 2009). Previous workers (Nesbitt et al., 1982, Cox et al., 1995) have used chemical index of alteration (CIA = $(Al_2O_3/ [Al_2O_3+CaO^*+Na_2O+K_2O]) * 100$), chemical index of weathering (CIW= molar $(Al_2O_3/ (Al_2O_3+ CaO^*+ Na_2O)) * 100$) and plagioclase index of alteration (PIA= $(Al_2O_3-K_2O)/(Al_2O_3+ CaO + Na_2O-K_2O)) * 100)$) to deduce the weathering and alteration conditions of the source rock. The main difference between the CIA and CIW is the omission of $K_2O$ in the equation of the CIW. Generally speaking, values of 50 indicate an unweathered upper continental crust value (UCC), while values of 100 and beyond are thought to be extensively weathered. In this study, CIA was calculated followed after Nesttbit et al. (1982).

The concentration of CaO incorporated in the silicate fraction is denoted by CaO*, and the major oxides that have been selected are given in molar proportions based on the CIA equation. Under the assumption that the Ca/Na ratios of the silicate material are appropriate, McLennan (1993) proposed an indirect approach for estimating the CaO content of the silicate fraction. As part of the procedure for quantifying the CaO concentration (CaO*) of the silicate fraction, the molar percentage of $P_2O_5$ is subtracted from the molar proportion of total CaO. The "remaining number of moles" after subtraction is regarded as the molar proportion of CaO of the silicate fraction if it is smaller than the molar proportion of $Na_2O$. When the molar proportion of $Na_2O$ is more than the "remaining number of moles," it is referred to as the molar proportion of CaO of the silicate fraction (CaO*). Therefore, CIA for the greywackes can be calculated (Equation 4) as:

$$CIA = \left( \frac{\left(\frac{14.18}{101.96}\right)}{\left(\frac{14.18}{101.96}\right)+\left(\frac{4.58}{56.08}\right)+\left(\frac{4.58}{61.98}\right)+\left(\frac{1.82}{94.19}\right)} \right) * 100 = 59.7\ \% \text{ ..................Equation 4}$$

The average CIA value for the sampled greywacke is 59.7 % (Table 4.7). Also, the average CIW value for the greywacke is 65.5%. Based on the CIA and CIW values, the greywackes are slightly weathered.

### 4.9.6 Mineralogical index of alteration

Utilizing the mineralogical index of alteration (MIA= 2*(CIA-50)) as suggested by Voicu et al. (1997), the rocks under investigation were classified according to the level of chemical alteration they expressed. MIA values between 0 and 20% are typically categorized as incipient, between 20% and 40% as weak, between 40% and 60% as moderate, and between 60% and 100% as intense to excessive degree of alteration (Voicu et al., 2002). For the greywackes, the average MIA value (Table 4.7) is 19.3%, indicating incipient alteration.

### 4.9.7 Plagioclase index of alteration (PIA)

The degree of chemical alteration can affect the chemistry of the parent rock. Fedo et al. (1995) proposed that altered plagioclase will have a PIA ((PIA = ($Al_2O_3$ -$K_2O$)/ ($Al_2O_3$+ CaO + $Na_2O$-$K_2O$)) * 100)) value of 50 whilst the Phanerozoic shale will have a value of 79. The average PIA value of the greywackes is 62.3 % (Table 4.7) which indicates the presence of weak to moderately altered plagioclase from the source rocks. The $Al_2O_3$-CaO*$Na_2O$ - $K_2O$ (A-CN-K) ternary diagram after Nesbitt and Young (1982) was employed to graphically display the degree of PIA. On the A-CN-K ternary diagram (Figure 4.40), all the rocks show a linear trend from plagioclase toward illite. The greywackes are in the region of plagioclase indicating a low degree of plagioclase alteration in the direction of muscovite.

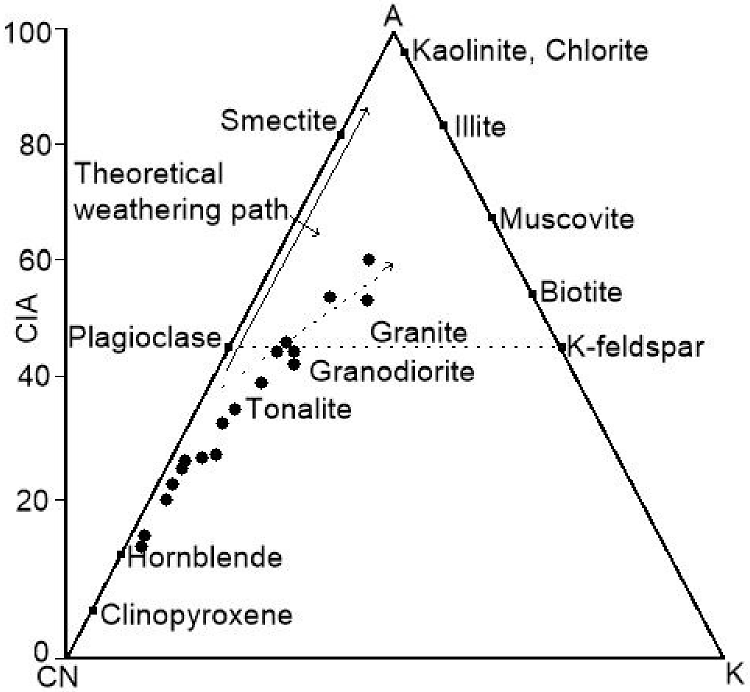

**Figure 4.40: A–CN–K ternary plot (after Nesbitt and Young 1982) showing the weathering trend of the greywacke samples collected from the Kibi gold zone.**

### 4.9.8 Tectonic setting

Low to middle-rank metamorphic source rocks are responsible for the elevated proportion of undulose quartz and the prevalence of polycrystalline grains with more than three crystal units per grain (Basu et al. 1975) in the greywacke samples collected from the Kibi gold zone. The rocks under study may have undergone metamorphism that resulted in the remobilization of some elements, such as major elements and LILEs, rendering them ineffective in determining the appropriate tectonic setting. Rather, in this study, more resistant HFSEs (such as Y, Zr, Nb, Th, and Hf) were utilized since they can provide reliable information on tectonic settings. Nonetheless, Table 4.7 indicates that the rock samples under investigation have a very low $TiO_2$ (<2.0 wt.%) concentration, which points to the influence of igneous rocks deposited in a magmatic arc (Pearce 2014). The geochemical signatures of the greywacke samples (Figure 4.37) show positive peaks at Sr and Ba and negative peaks at Nb,Ta, Zr, and Hf. These signatures indicate that the rocks formed in an arc setting, most likely due to subduction (Fitton et al., 1988; Saunders et al., 1988).

To distinguish between the tectonic setting of Precambrian metasedimentary rocks, Bhatia & Crook (1986) used immobile elements (such as La – Th – Sc and Co – Th – Zr/10). The majority of the examined samples in the Co – Th – Zr/10 ternary diagram (Figure 4.41a) came from an oceanic island arc. Additionally, Verma and Armstrong-Altrin (2013) postulated 2 multi-dimensional function major element diagrams for discriminating 3 main tectonic settings (island or continental arc, continental rift and collision) of sedimentary rocks based on their $SiO_2$ contents [high-silica ($63\% < SiO_2 < 95\%$) and low-silica ($35\% < SiO_2 < 63\%$)]. On the high silica content multi-dimensional function diagram (Figure 4.41b), 51% of the studied greywacke samples plotted in the continental rift margin while 49% plotted within the continental or island arc field. This provides convincing evidence about the source area which is consistent with the tectonic setting of the Birimian terrain in Ghana as proposed by (Leube et al. 1990).

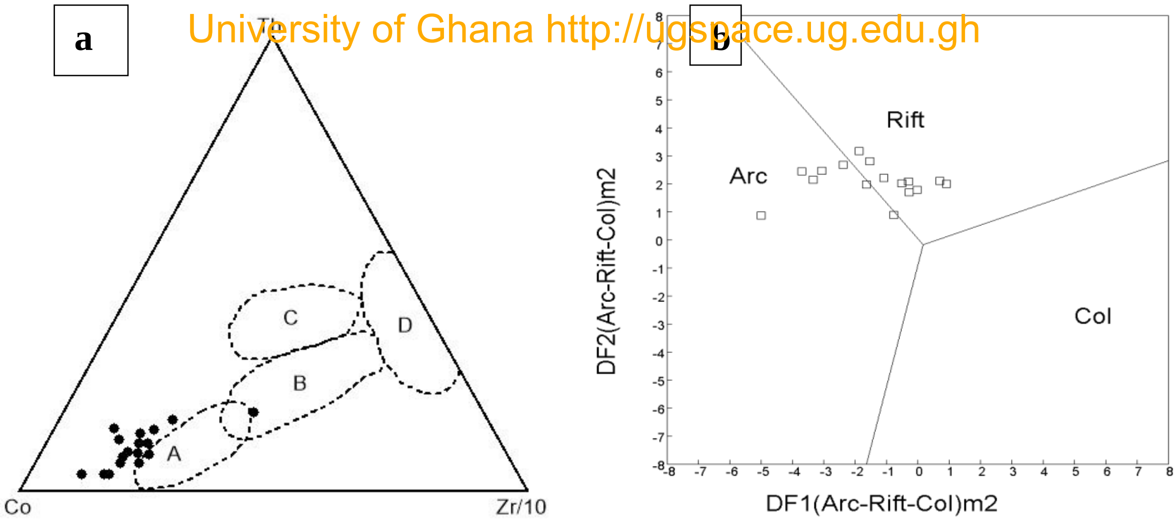

**Figure 4.41: (a) Th – Co – Zr/10 ternary plot for discriminating against tectonic setting of greywackes in in the Kibi area (after Bhatia & Crook, 1986). A, Oceanic Island Arc; B, Continental Island Arc; C, Active Continental Margin; D, Passive Continental Margin. (b) Multidimensional function major element diagram proposed by Verma and Armstrong-Altrin (2013) for high-silica clastic sediments. The discriminant function equations are as follows: DF1(Arc-Rift-Col) m1 = (–0.263 × In($TiO_2$/$SiO_2$)adj) + (0.604 × In ($Al_2O_3$/$SiO_2$)adj) + (–1.725 × In($Fe_2O_3$t/$SiO_2$)adj) + (0.660 × In(MnO/$SiO_2$)adj) + (2.191 × In(MgO/$SiO_2$)adj) + (0.144 × In(CaO/$SiO_2$)adj) +(–1.304 × In($Na_2O$/$SiO_2$)adj) + (0.054 × In($K_2O$/$SiO_2$)adj) + (–0.330× In($P_2O_5$/$SiO_2$)adj) + 1.588. DF2(Arc-Rift-Col) m1 = (–1.196 × In($TiO_2$/$SiO_2$)adj) + (1.604 × In ($Al_2O_3$/$SiO_2$)adj) + (0.303 × In($Fe_2O_3$t/$SiO_2$)adj) + (0.436 × In(MnO/$SiO_2$)adj) + (0.838 × In(MgO/$SiO_2$)adj) + (–0.407 × In(CaO/$SiO_2$)adj) + (1.021 × In($Na_2O$/$SiO_2$)adj) +(–1.706 × In($K_2O$/$SiO_2$)adj) + (–0.126 × In($P_2O_5$/$SiO_2$)adj) – 1.068.**

### 4.10 Geochemical characteristics of the volcaniclastic rocks

Due to the low content of clast (Figure 4.26) in the volcaniclastic rocks samples, they were modeled as volcanic rocks. Table 4.9 exhibits variable concentrations of the major elements in weight percent (wt. %) for the twenty (20) selected volcaniclastic rock samples. From the XRF analysis, the volcaniclastic from the Agyapoma area demonstrates a range of $SiO_2$ (59.07 - 61.99) wt.%, $TiO_2$ (0.5 - 0.89) wt.%, $Fe_2O_3$ (7.43-8.967) wt.%, MnO (0.581- 0.2146) wt.% and $Na_2O$ (1.04 – 2.85) wt.%. The high $Al_2O_3$ (16.77-19.79) wt.%, content can be attributed to the feldspars as observed in the petrography. $K_2O$ is also quite high (2.2-4.082) wt.% which may suggest the progressive concentration of $K_2O$ during magmatic fractionation or hydrothermal alteration of the source rocks. $P_2O_5$ is generally low varying from 0.05 to 0.26 wt. % which is consistent with intermediate rocks reflecting the fractionation of apatite. In Figure 4.42**,** $TiO_2$,

$Al_2O_3$, MgO, $Na_2O$, $K_2O$ and $Fe_2O_3$ exhibit decreasing trends with $SiO_2$ while MnO, $P_2O_5$ and CaO show scattered trends. Fractional crystallization of the ferromagnesian minerals like plagioclase and pyroxene from the source rocks is indicated by a decrease in the concentrations of CaO, $F_{e2}O3$, MgO, and $TiO_2$ relative to $SiO_2$.

**Table 4. 9: Whole-rock major-element concentrations (wt.%) of volcaniclastic rocks from the Kibi Gold Belt of Ghana**

| Sample | $SiO_2$ | $TiO_2$ | $Al_2O_3$ | $Fe_2O_3$ | MnO | MgO | CaO | $Na_2O$ | $K_2O$ | $P_2O_5$ | $SO_3$ | FeO | $Fe_2O_{3T}$ | $Fe_2O_{3T}$+MgO | $Na_2O$+$K_2O$ |
|---|---|---|---|---|---|---|---|---|---|---|---|---|---|---|---|
| VE01 | 61.07 | 0.78 | 17.80 | 8.26 | 0.18 | 1.95 | 2.16 | 1.80 | 3.53 | 0.16 | 0.97 | 8.07 | 16.23 | 17.73 | 5.33 |
| VE02 | 61.55 | 0.51 | 17.18 | 7.76 | 0.16 | 1.75 | 4.27 | 1.86 | 3.61 | 0.12 | 0.55 | 8.44 | 16.97 | 18.72 | 5.47 |
| VE03 | 59.87 | 0.78 | 18.88 | 8.97 | 0.10 | 2.60 | 3.74 | 2.56 | 3.26 | 0.12 | 1.00 | 9.41 | 18.92 | 20.54 | 5.82 |
| VE06 | 61.87 | 0.56 | 16.77 | 7.81 | 0.12 | 2.00 | 4.29 | 1.64 | 2.84 | 0.13 | 0.76 | 9.79 | 19.69 | 21.89 | 4.48 |
| VE07 | 60.59 | 0.65 | 18.81 | 8.28 | 0.13 | 2.47 | 3.20 | 1.24 | 3.35 | 0.13 | 0.80 | 6.31 | 12.69 | 14.46 | 4.59 |
| VE08 | 59.07 | 0.75 | 19.19 | 8.88 | 0.13 | 2.52 | 4.06 | 2.54 | 4.02 | 0.16 | 0.69 | 8.20 | 16.49 | 18.21 | 5.06 |
| VE09 | 59.23 | 0.84 | 19.78 | 8.47 | 0.09 | 2.50 | 3.54 | 2.30 | 3.34 | 0.13 | 0.40 | 7.18 | 14.45 | 16.25 | 5.64 |
| VE10 | 61.02 | 0.71 | 18.64 | 8.31 | 0.15 | 1.83 | 4.38 | 2.08 | 2.78 | 0.26 | 0.91 | 6.61 | 13.30 | 15.13 | 4.86 |
| VE11 | 60.22 | 0.73 | 18.85 | 8.31 | 0.13 | 2.55 | 2.21 | 1.85 | 4.08 | 0.21 | 1.02 | 8.12 | 16.28 | 17.78 | 5.93 |
| VE12 | 61.60 | 0.66 | 17.23 | 7.65 | 0.21 | 1.80 | 4.32 | 1.61 | 3.30 | 0.17 | 0.60 | 8.49 | 17.02 | 18.77 | 4.91 |
| VE13 | 60.92 | 0.72 | 18.14 | 8.17 | 0.15 | 1.67 | 3.79 | 1.91 | 3.41 | 0.17 | 1.05 | 9.46 | 18.97 | 20.59 | 5.32 |
| VE14 | 59.92 | 0.87 | 18.22 | 8.86 | 0.17 | 2.25 | 4.34 | 2.43 | 3.43 | 0.18 | 0.81 | 9.84 | 19.74 | 21.94 | 5.86 |
| VE15 | 60.64 | 0.60 | 18.36 | 8.23 | 0.18 | 1.82 | 3.25 | 1.29 | 3.33 | 0.18 | 0.85 | 6.36 | 12.74 | 14.51 | 4.62 |
| VE16 | 61.99 | 0.50 | 17.64 | 7.43 | 0.18 | 1.77 | 4.11 | 1.64 | 2.27 | 0.21 | 0.74 | 8.25 | 16.54 | 18.26 | 3.91 |
| VE17 | 59.15 | 0.89 | 18.83 | 8.72 | 0.14 | 2.85 | 3.59 | 2.85 | 3.08 | 0.07 | 0.48 | 7.23 | 14.50 | 16.30 | 5.93 |
| VE18 | 61.00 | 0.71 | 17.73 | 7.95 | 0.10 | 1.88 | 2.09 | 1.93 | 3.62 | 0.09 | 0.90 | 8.00 | 16.16 | 17.66 | 5.55 |
| VE19 | 61.48 | 0.74 | 17.11 | 7.53 | 0.09 | 1.60 | 4.20 | 1.79 | 3.54 | 0.05 | 0.48 | 8.37 | 16.90 | 18.65 | 5.33 |
| VE20 | 60.80 | 0.89 | 19.02 | 8.40 | 0.07 | 1.85 | 3.67 | 2.29 | 3.19 | 0.05 | 0.93 | 9.34 | 18.85 | 20.47 | 5.48 |
| VE21 | 59.80 | 0.79 | 18.70 | 8.74 | 0.11 | 2.22 | 4.22 | 2.07 | 3.29 | 0.06 | 0.49 | 9.72 | 19.62 | 21.82 | 5.36 |
| VE22 | 60.52 | 0.88 | 19.24 | 7.99 | 0.06 | 2.30 | 3.13 | 2.17 | 3.28 | 0.06 | 0.73 | 6.24 | 12.62 | 14.39 | 5.45 |

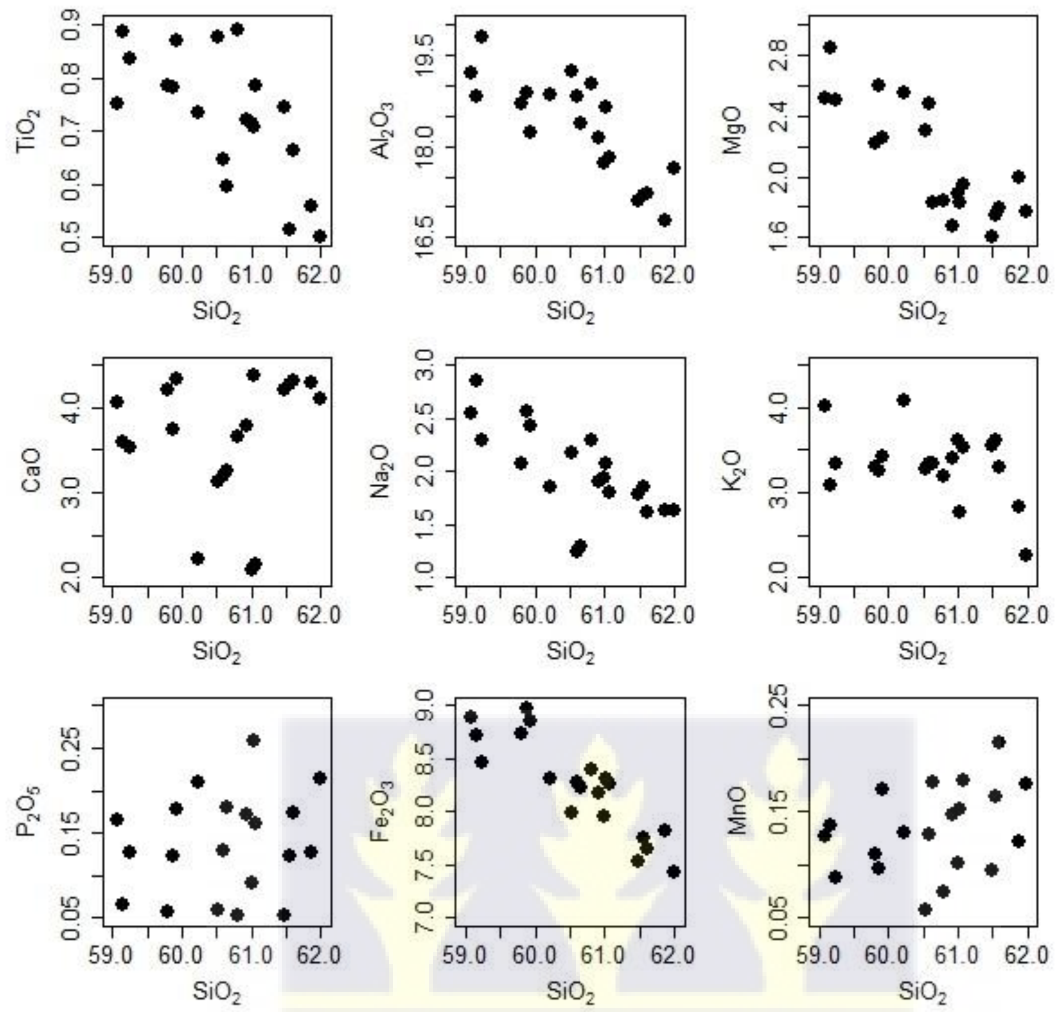

**Figure 4.42: Harker diagram for the volcaniclastic rock samples in the Kibi area.**

### 4.10.1 Trace elements

#### 4.10.1.1 Large ion lithophile elements (LILE) (Rb, Sr and U)

Concentrations of selected trace elements in the volcaniclastic rocks have been presented in Table 4.10. The mean contents of Rb, Sr and U in the rocks are 173.80 ppm, 742.85 ppm and 3.15 ppm respectively. The high Sr content can be attributed to the high feldspar content and also the effect of subsequent metamorphism (Gale and Roberts 1974). Cox and Lowe (1995) postulated that Ba is usually hosted in K-feldspar. The average Rb (122 ppm) and Sr (350 ppm) contents in the volcaniclastic rock samples understudy are higher than the contents in basaltic lava (Rb= 1.00 ppm and Sr = 136 ppm). Since Sr is typically linked to plagioclase (Rollinson, 1993), the plagioclase content in the rock samples under investigation can be the reason for the high Sr level.

#### 4.10.1.2 High field strength elements (HFSE) (Y, Zr, Nb and Th)

The contents of high field strength elements (HFSEs) (Y, Zr, Nb and Th) are controlled chiefly by the chemistry of the source rock as well as the melt processes at the time of rock evolution, as a result, they are not easily altered by agents such as metamorphism and chemical weathering (Rollinson, 1993; McLennan, 1989). Y is usually incorporated into garnet and amphiboles. In this study, the average Y content in the volcaniclastic rock is 13.00 ppm. The low Y content suggests a minimal contribution of accessory minerals such as sphene or apatite in the source rock. The average Zr content (175.85 ppm) in the rock type understudy is less than the average concentration of Zr in the basaltic lava (88 ppm) (Sun, 1980). Generally, the high Zr contents in all the rocks are indicative of the enrichment of heavy minerals, particularly zircon. Again, the average contents of Nb (4.55ppm), Th (12.60 ppm) and U (3.15ppm) in the volcaniclastic samples are higher than their concentration in basaltic lava (Nb=2.5 ppm, Th = 0.20 ppm and U = 0.10 ppm). According to Hofmann (1987), the enrichment of Nb can be attributed to the fractionation of Nb in the source rock. According to Pettijohn (1963), rocks with high zircon and monazite contents usually have high Th and U contents. McLennan, (1989) is of the view that the abundance of Th can be related to continental crust materials.

### 4.10.1.3 Transitional elements

Average V, Cr, Cu and Ni contents are 123.80ppm, 213.80ppm, 32.45ppm and 38.05ppm respectively. Au in the volcaniclastic samples range from 0.01 to 6.12 ppm. Wrafter and Graham (1989) cautioned that a high Cr/Ni ratio is a good indicator of mafic rocks, hence the Cr/Ni ratio (6.7) of the rocks understudy proves that they are intermediate.

**Table 4. 10: Whole-rock trace-element concentrations (ppm) of volcaniclastic rocks from the Kibi area.**

| Sample | V | Cr | Ni | Cu | Zn | Rb | Sr | Y | Zr | Nb | W | Pb | Th | U | Tm | Yb | Au | Ag | As |
|---|---|---|---|---|---|---|---|---|---|---|---|---|---|---|---|---|---|---|---|
| VE01 | 164.0 | 219.0 | 27.0 | 9.0 | 46.0 | 81.0 | 877.0 | 10.0 | 135.0 | 3.0 | 14.0 | 6.0 | 12.0 | 3.0 | 0.3 | 2.5 | 1.5 | 1.1 | 1.7 |
| VE02 | 127.0 | 230.0 | 25.8 | 16.0 | 66.0 | 65.0 | 777.0 | 17.0 | 205.0 | 4.0 | 2.1 | 6.0 | 16.0 | 3.0 | 0.4 | 2.0 | 1.1 | 1.3 | 1.4 |
| VE03 | 102.0 | 197.0 | 31.1 | 41.0 | 64.0 | 70.0 | 755.0 | 12.0 | 181.0 | 5.0 | 9.0 | 6.0 | 13.0 | 4.0 | 0.4 | 1.5 | 0.5 | 1.0 | 3.1 |
| VE06 | 89.0 | 230.0 | 22.1 | 94.0 | 60.0 | 57.0 | 807.0 | 12.0 | 144.0 | 4.0 | 1.9 | 8.0 | 14.0 | 3.0 | 0.5 | 2.0 | 0.4 | 0.1 | 3.4 |
| VE07 | 145.0 | 227.0 | 27.3 | 35.0 | 64.0 | 81.0 | 728.0 | 14.0 | 202.0 | 6.0 | 14.0 | 6.0 | 10.0 | 3.0 | 0.6 | 3.0 | 0.7 | 1.2 | 2.8 |
| VE08 | 64.0 | 170.3 | 34.1 | 12.0 | 78.0 | 47.0 | 650.0 | 9.8 | 155.0 | 4.0 | 1.5 | 5.0 | 11.0 | 4.0 | 0.6 | 3.7 | 0.1 | 1.2 | 3.0 |
| VE09 | 193.0 | 170.0 | 36.0 | 10.0 | 68.0 | 64.0 | 664.0 | 10.0 | 218.0 | 6.0 | 23.0 | 8.0 | 11.0 | 3.0 | 0.7 | 4.4 | 0.9 | 1.1 | 2.7 |
| VE10 | 81.0 | 241.0 | 34.0 | 20.0 | 66.0 | 58.0 | 959.0 | 13.0 | 170.0 | 5.0 | 2.0 | 5.0 | 17.6 | 4.0 | 0.4 | 4.1 | 0.1 | 0.6 | 2.8 |
| VE11 | 164.0 | 219.2 | 27.2 | 9.3 | 46.7 | 71.5 | 887.0 | 10.0 | 136.0 | 3.6 | 14.0 | 6.0 | 12.5 | 3.2 | 0.5 | 3.8 | 1.7 | 2.0 | 1.7 |
| VE12 | 127.4 | 230.3 | 25.1 | 16.2 | 66.1 | 65.3 | 777.1 | 17.4 | 205.1 | 4.2 | 2.1 | 6.8 | 16.0 | 2.1 | 0.5 | 4.3 | 0.8 | 1.3 | 0.2 |
| VE13 | 102.2 | 197.2 | 31.1 | 41.3 | 64.0 | 70.5 | 755.4 | 12.3 | 181.7 | 5.7 | 9.1 | 4.3 | 13.1 | 4.0 | 0.3 | 1.7 | 0.7 | 0.3 | 2.2 |
| VE14 | 89.0 | 165.9 | 34.1 | 94.0 | 60.4 | 57.5 | 807.1 | 12.2 | 144.3 | 4.3 | 1.9 | 8.1 | 14.0 | 3.0 | 0.4 | 2.2 | 1.0 | 1.0 | 2.5 |
| VE15 | 146.0 | 227.7 | 27.1 | 35.1 | 64.9 | 81.7 | 728.1 | 14.5 | 202.1 | 6.0 | 14.1 | 6.1 | 10.2 | 3.0 | 0.4 | 3.2 | 1.0 | 1.5 | 2.3 |
| VE16 | 64.2 | 227.2 | 29.1 | 12.4 | 78.6 | 47.4 | 1029.0 | 12.8 | 155.2 | 4.2 | 1.6 | 5.0 | 17.2 | 4.1 | 0.5 | 3.9 | 1.1 | 1.7 | 2.0 |
| VE17 | 193.1 | 178.2 | 36.1 | 10.1 | 68.0 | 74.1 | 664.0 | 9.2 | 218.8 | 6.5 | 23.1 | 7.1 | 11.0 | 3.2 | 0.5 | 4.6 | 1.2 | 3.0 | 2.3 |
| VE18 | 163.1 | 218.9 | 26.1 | 8.9 | 45.5 | 90.2 | 876.9 | 9.9 | 134.2 | 2.5 | 13.9 | 5.6 | 11.1 | 2.9 | 0.5 | 3.3 | 1.1 | 0.9 | 3.2 |
| VE19 | 126.3 | 229.4 | 24.8 | 15.9 | 65.2 | 64.6 | 736.9 | 16.0 | 204.4 | 3.9 | 2.0 | 5.0 | 15.5 | 2.5 | 0.6 | 4.0 | 0.5 | 0.7 | 2.7 |
| VE20 | 101.7 | 196.4 | 30.1 | 40.9 | 63.9 | 69.3 | 754.2 | 11.5 | 180.2 | 4.1 | 8.9 | 5.4 | 12.2 | 3.9 | 0.7 | 3.5 | 1.8 | 1.0 | 2.2 |
| VE21 | 88.9 | 164.3 | 31.2 | 93.9 | 59.9 | 56.1 | 806.2 | 11.9 | 143.9 | 3.6 | 1.8 | 7.2 | 13.3 | 2.8 | 0.7 | 1.9 | 1.6 | 1.7 | 2.2 |
| VE22 | 144.6 | 226.9 | 26.3 | 34.9 | 63.2 | 80.0 | 727.2 | 13.2 | 201.9 | 5.2 | 13.3 | 5.5 | 10.9 | 2.4 | 0.5 | 2.4 | 0.1 | 1.2 | 0.2 |

### 4.10.2 Classification of the volcaniclastic rock samples

The $SiO_2$ content (59.07 to 61.99) wt.% of the greywacke samples show that they are typically intermediate rocks which is consistent with the Total Alkali-Silica (TAS) diagram (Cox et al., 1979) (Figure 4.43a). According to Hastie et al. (2007), geochemical classification based on major elements may not be suitable for altered rocks, hence the $Zr/TiO_2$ versus Nb/Y diagram by Winchester and Floyd, (1977) was used to confirm this accession. On the $Zr/TiO_2$ versus Nb/Y diagram (Figure 4.43b) the rocks understudy cluster in the field of andesite and basaltic andesite field with one sample plotting as rhyodacite. Based on these classification schemes the rocks understudy can be referred to as andesitic tuffs.

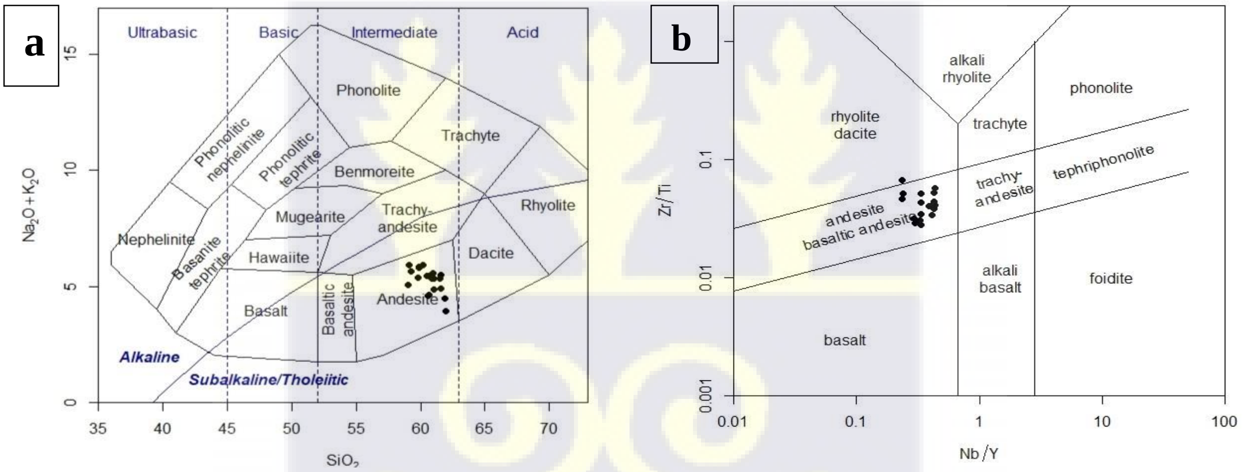

**Figure 4.43: a) $SiO_2$ versus $Na_2O + K_2O$ plot (after Cox et al., 1979) for the volcaniclastic rock samples from the Kibi gold zone b) Zr/Ti versus Nb/Y plot (after Pearce, 1996)**

### 4.10.3 Petrogenesis of the volcaniclastic rocks

The magma differentiation process was further investigated with the AFM ($A=Na_2O + K_2O$, $F=Fe_2O_3$, $M=MgO$) diagram (Figure 4.44a) which shows that the rock samples understudy have a tholeiitic affinity. The studied samples also plot as peraluminous rocks on the $Al_2O_3/CaO+Na_2O+K_2O$ (A/CNK) versus $Al_2O_3/Na_2O+K_2O$ (ANK) binary plot (Figure 4.44b). Also, the negative trends defined by decreasing CaO, $Fe_2O_3$ and MgO with increasing It can be challenging to distinguish between the signatures of partial melting and fractional crystallization based on the composition of primary magma. But processes that occurred during magma evolution can be inferred from the plots of compatible and incompatible elements (Dampare et al., 2008). $SiO_2$ content suggests that during the magma's evolution, plagioclase, olivine, and/or pyroxene were most likely the main phases that crystallized out (Yücel et al., 2017). According to Dampare et al. (2008), the fractionation of ferromagnesian minerals such as pyroxene and olivine decreases the concentrations of compatible elements and increases the concentration of incompatible elements in the liquids.

On the Cr, Ni, Rb, Sr and Th versus $SiO_2$ binary plot (Figure 4.45), there is a decrease in Ni and a slight increase in Th with increasing $SiO_2$ content which suggest that the volcaniclastic rocks underwent minor fractional crystallization during their evolution (Dampare et al., 2008). The decrease in Ni content with increasing $SiO_2$ content may imply that olivine was probably the primary phase that fractionated out of the melt (Yücel et al. 2017). The examined rocks exhibit significant major element abundances that fluctuate along continuous decreasing trends of $Al_2O_3$, MgO, $Fe_2O_3$, $P_2O_5$, and $TiO_2$ against $SiO_2$ and increasing $Na_2O$ with increasing $SiO_2$, making fractional crystallization plausible. However, magma mingling or mixing must be taken into account in addition to contamination and fractionation when analyzing the evolution of magma. When the evolved felsic magma above the continental crust combines with the hot basaltic melt from the magma chambers below, the mixing process takes place and the magma composition becomes more intermediate.

The volcaniclastic rock may represent a more primitive material hence, a majority have also evolved compositions as a sign of fractional crystallization and crustal contamination. The Primitive mantle normalized spider diagram established by McDonough and Sun (1995) (Figure 4.46), was used to discriminate the extent of crustal contamination as well as the environment of magma generation, if any, in the melt, leading to the crystallization of the studied volcaniclastic rocks. In the normalized primitive mantle spider diagram proposed by McDonough and Sun (1995) (Figure 4.46), most of the samples show similar distribution patterns. Generally, the volcaniclastic rocks understudy demonstrate enrichment in the LILEs such as Rb, Ba, Sr, Th and Pb and troughs in HFSEs (Rb, Nb, P and Ti) which can be attributed to the presence of an inherited subduction material in the mantle source or crustal contamination as postulated by Zheng (2019), Fitton et al. (1988) and Saunders et al. (1988). In contrast to the suggested plume-generated setting (Abouchami et al., 1990), the results of this study are compatible with an island-arc setting (Sylvester & Attoh, 1992; Béziat et al. 2000; Attoh et al. 2006; Dampare et al. 2008) for the Palaeoproterozoic rocks of West Africa.

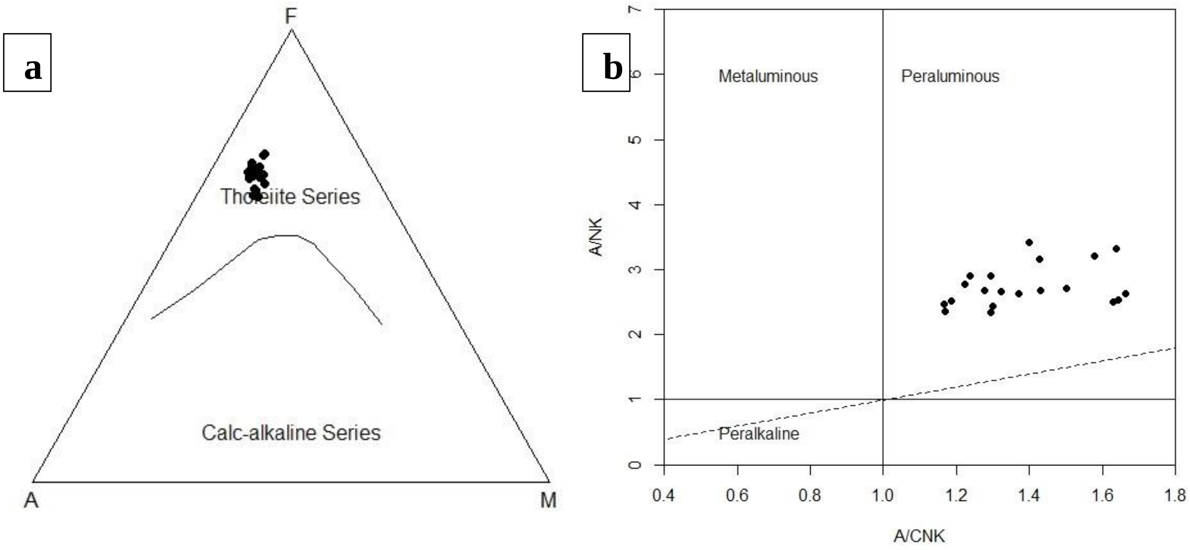

**Figure 4.44: a) AFM (A=$Na_2O + K_2O$), F=$Fe_2O_3$, M=MgO) diagram, showing a tholeiitic affinity for the volcaniclastic rocks. The Calc-alkaline and tholeiitic series differentiation line (Irvine and Barager, 1971). b) $Al_2O_3$/CaO+$Na_2O$+$K_2O$ (A/CNK) verse $Al_2O_3$/$Na_2O$+$K_2O$ (ANK) plot showing the peraluminous nature of the volcaniclastic rocks understudy (Maniar and Piccoli, 1989; Chappell and White, 1974).**

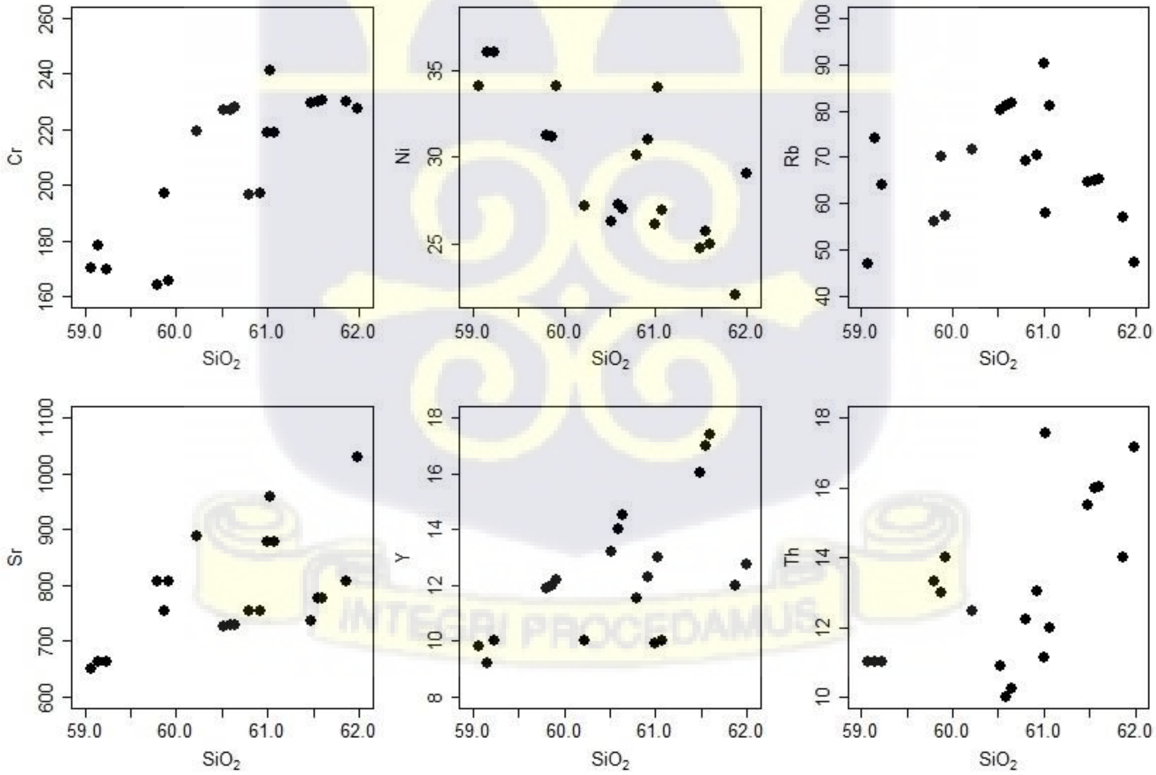

**Figure 4.45: Some selected compatible and incompatible elements versus $SiO_2$.**

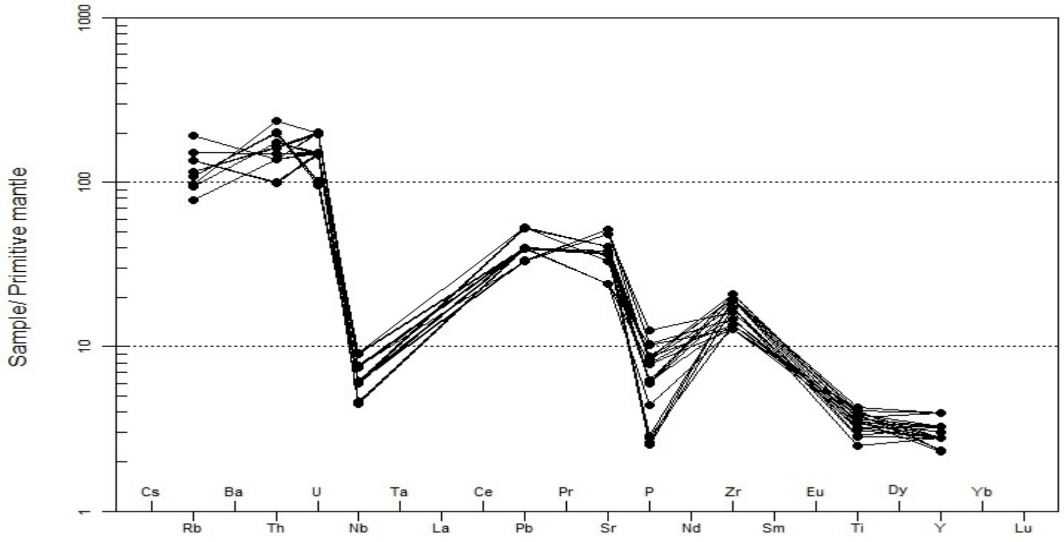

**Figure 4.46: Primitive mantle-normalized multi-element spider plot (after McDonough and Sun, 1995) explaining the magma source of the volcaniclastic rocks in the Kibi area.**

### 4.10.4 Tectonic setting of the volcaniclastic rocks

It has been suggested that the entire Birimian crust formed in an island arc environment (Beziat et al. 2000; Sylvester & Attoh 1992), an intra-cratonic rift to oceanic spreading and accretion (Leube et al. 1990), or an intracontinental trans-tensional back-arc basin (Vidal & Alric 1994). The volcaniclastic rocks under study display volcanic arc-like geochemical signatures, owing to the low concentration of Nb and Ti coupled with the enrichment of LILEs relative to HFSEs. Elevated $Al_2O_3$ (16.77-19.79 wt%) and $K_2O$ (2.2-4.082) wt% contents are typical for continental arcs materials (Condie 1997) which are progressively enriched during magmatic fractionation. Zr - Ti plot by Pearce (1982) has been used to discriminate arc lavas from within plate lavas (WPL) and MORBs. Compared to Nb and Th, for instance, the Zr/Ti ratio is less significantly impacted by calc-alkalinity and alkalinity. This is because Ti is incompatible at the time of basalt fractionation and as a result, the ratio increases with increasing fractionation. The studied volcaniclastic rocks cluster mainly in the Island arc lava field (Figure 4.47a) materials.

Wood's (1980) tectonic discrimination diagram (Th-Zr/117- Nb/16) was also used to study the tectonic context of the volcaniclastic. Plotting of the samples in the calc-alkaline basalt (CAB) field on this diagram suggests that they originated from an arc environment (Figure 4.47b). Shervais (1982) postulated the use of a relative ratio of V to Ti to distinguish between different types of basaltic rocks in terms of their tectonic environments. On Figure 4.47c, the samples have Ti/V ratios between 20 and 100 and hence fall within the fields of calc-alkaline basalt (CAB) and Ocean-floor basalt (OFB) indicating possible subduction-related magmatism in a volcanic arc environment as displayed in Figure 4.47d.

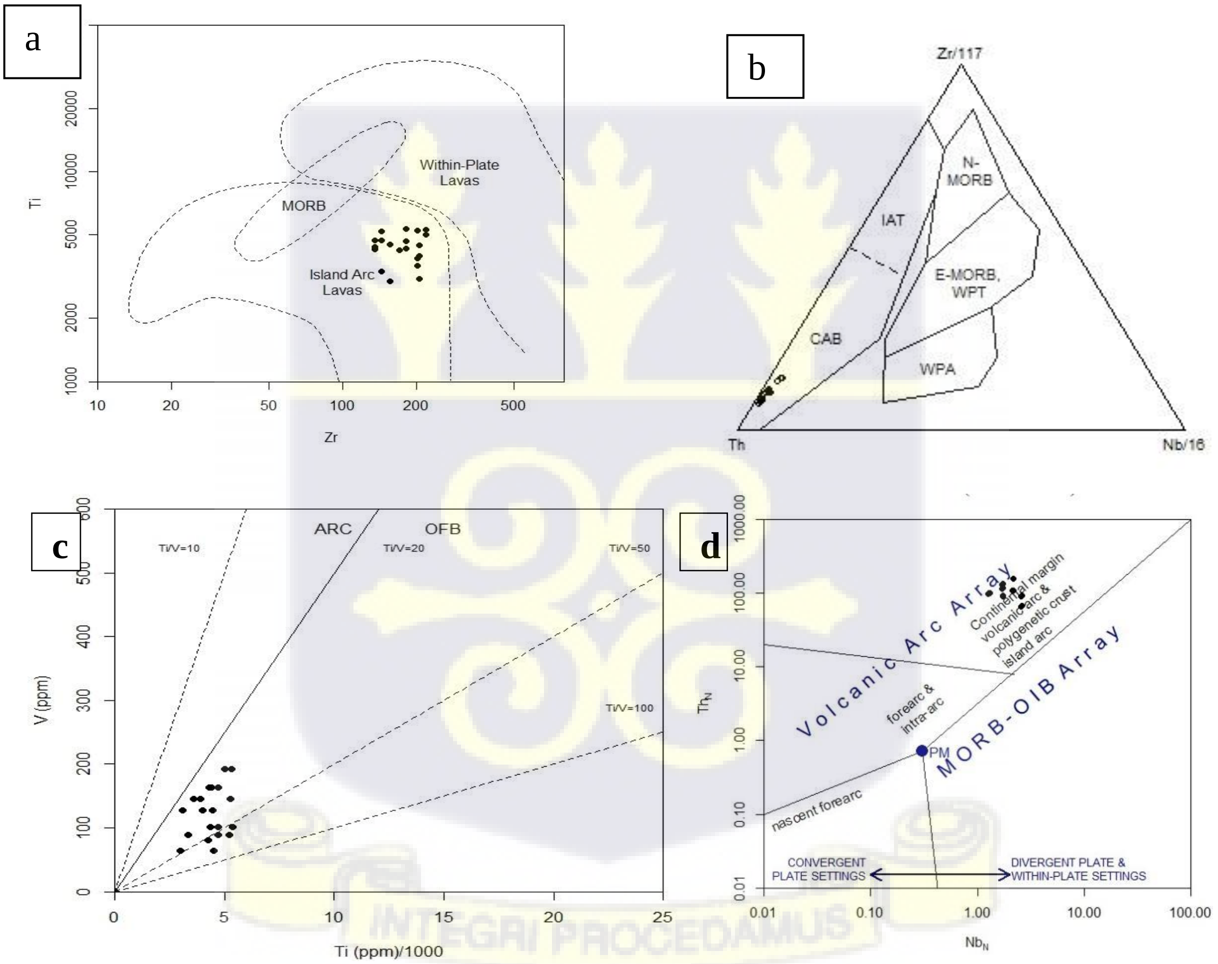

**Figure 4.47: Tectonic setting discrimination diagram for the volcaniclastic rocks in the Kibi gold zone a) Zr-Ti (Pearce et al.,1982) b) Th-Zr/117-Nb/16 plot after Wood (1980) c) V-Ti discriminant diagram, based on Shervais (1982) d) Nb$_N$ verse Th$_N$ (Saccani 2015).**

## 4.11 Major and trace element composition of the hanging and footwall mafic volcanic rocks.

Variable concentrations of the major elements in weight percent (wt. %) for the selected hanging and footwall mafic volcanic rocks are presented in Table 4.11. From the XRF analysis of the hanging wall mafic volcanic rocks, the concentration of $SiO_2$ ranges from 34.2 - 54.50 wt.%, $TiO_2$ (0.54 – 1.44) wt.%, $Al_2O_3$ (8.86-17.81) wt.%, $Fe_2O_3$ (5.17-14.29) wt.%, MnO (0.09 - 0.37) wt.%, MgO (3.73 – 8.28) wt.%, CaO (3.55 – 11.40) wt.%, $Na_2O$ (1.97 – 7.96) wt.% and $K_2O$ (0.32 – 4.41) wt.%.

Comparatively, $SiO_2$ ranges from 33.3-52.4 wt.%, $TiO_2$ (0.61 – 1.57) wt.%, $Al_2O_3$ (9.43-14.44) wt.%, $Fe_2O_3$ (7.85-16.58) wt.%, MnO (0.13 – 0.30) wt.%, MgO (4.9 – 6.49) wt.%, CaO (3.44 – 10.11) wt.%, $Na_2O$ (2.63– 6.01) wt.%, and $K_2O$ (0.19 – 2.57) wt.% in the footwall mafic volcanic rocks. Even though both rock types display a wide range of $SiO_2$, the variation displayed by the hanging wall volcanic rock is enormous. The $SiO_2$ content (33.3- 54.50) wt.% in both volcanic rocks confirms their mafic to intermediate composition as observed in the petrography. High $Al_2O_3$ content can be attributed to the high feldspar content. The low $TiO_2$ contents (Table 1) of the analyzed hanging and footwall mafic volcanic rocks reflect igneous rocks from the magmatic arc environment (Pearce and Cann, 1973).

On the Harker diagram of major oxide versus $SiO_2$ (Figure 4.48), both volcanic rocks display similar trends of decreasing MgO, CaO and $Fe_2O_3$ with a progressive increase in $SiO_2$, while the rest of the major elements ($Na_2O$, $TiO_2$, $Al_2O_3$, MnO, $K_2O$ and $P_2O_5$) produce scattered trends with $SiO_2$. The decline in the contents of $Fe_2O_3$, CaO and MgO against $SiO_2$ indicates fractional crystallization of the ferromagnesian minerals, monoclinic pyroxene and calcic plagioclase. Generally, $P_2O_5$ is low in both hanging wall (0.10 – 0.40) wt.% and footwall mafic

(0.10 – 0.30) wt.% volcanic rocks study varying from and the values are slightly lower in the acid rocks reflecting the fractional crystallization of apatite.

**Table 4.11: Variable concentrations of the major elements in weight percent (wt. %) for the selected hanging and footwall mafic volcanic rocks**

| Sample | $SiO_2$ | $TiO_2$ | $Al_2O_3$ | $Fe_2O_3$ | MnO | MgO | CaO | $Na_2O$ | $K_2O$ | $P_2O_5$ |
|---|---|---|---|---|---|---|---|---|---|---|
| HW001 | 50.9 | 0.78 | 14.76 | 7.36 | 0.11 | 4.53 | 4.47 | 3.76 | 2.84 | 0.3 |
| HW002 | 53.39 | 0.62 | 13.44 | 5.88 | 0.09 | 4.35 | 5.07 | 7.91 | 0.81 | 0.21 |
| HW003 | 34.92 | 0.77 | 12.01 | 11.61 | 0.14 | 8.23 | 8.54 | 4.28 | 0.76 | 0.08 |
| HW004 | 50.93 | 0.54 | 10.03 | 5.84 | 0.13 | 5.36 | 8.11 | 4.74 | 0.92 | 0.23 |
| HW005 | 40.78 | 0.68 | 11.98 | 8.96 | 0.16 | 7.15 | 9.45 | 3.29 | 1.51 | 0.16 |
| HW006 | 54.39 | 0.55 | 17.81 | 5.79 | 0.37 | 3.73 | 3.55 | 1.97 | 4.41 | 0.19 |
| HW007 | 42.72 | 0.78 | 13.44 | 8.45 | 0.17 | 5.77 | 7.67 | 4.44 | 1.78 | 0.26 |
| HW008 | 34.55 | 1.41 | 9.75 | 14.26 | 0.24 | 5.99 | 7.17 | 2.52 | 1.66 | 0.11 |
| HW009 | 34.23 | 1.16 | 8.86 | 12.57 | 0.23 | 6.27 | 11.36 | 5.71 | 0.5 | 0.33 |
| HW010 | 50.95 | 0.83 | 14.81 | 7.41 | 0.16 | 4.58 | 4.52 | 3.81 | 2.89 | 0.35 |
| HW011 | 53.44 | 0.67 | 13.49 | 5.93 | 0.14 | 4.4 | 5.12 | 7.96 | 0.86 | 0.26 |
| HW012 | 34.97 | 0.82 | 12.06 | 11.66 | 0.19 | 8.28 | 8.59 | 4.33 | 0.81 | 0.13 |
| HW013 | 50.98 | 0.59 | 10.08 | 5.89 | 0.18 | 5.41 | 8.16 | 4.79 | 0.97 | 0.28 |
| HW014 | 40.83 | 0.73 | 12.03 | 9.01 | 0.21 | 7.2 | 9.5 | 3.34 | 1.56 | 0.21 |
| HW015 | 42.75 | 0.81 | 13.47 | 8.48 | 0.2 | 5.8 | 7.7 | 4.47 | 1.81 | 0.29 |
| HW016 | 34.58 | 1.44 | 9.78 | 14.29 | 0.27 | 6.02 | 7.2 | 2.55 | 1.69 | 0.14 |
| HW017 | 34.26 | 1.19 | 8.89 | 12.6 | 0.26 | 6.3 | 11.39 | 5.74 | 0.53 | 0.36 |
| HW018 | 50.98 | 0.86 | 14.84 | 7.44 | 0.19 | 4.61 | 4.55 | 3.84 | 2.92 | 0.38 |
| HW019 | 34.27 | 1.2 | 8.9 | 12.61 | 0.27 | 6.31 | 11.4 | 5.75 | 0.54 | 0.37 |
| HW020 | 54.53 | 0.55 | 10.61 | 5.17 | 0.11 | 4.56 | 6.62 | 7.13 | 0.32 | 0.24 |
| FW001 | 45.5 | 0.62 | 11.97 | 7.86 | 0.14 | 5.87 | 7.23 | 5.97 | 0.98 | 0.26 |
| FW002 | 52.21 | 1.34 | 11.21 | 13.92 | 0.2 | 4.11 | 3.46 | 5.09 | 1.2 | 0.12 |
| FW008 | 33.31 | 1.42 | 9.43 | 16.24 | 0.25 | 6.44 | 10.06 | 2.63 | 0.19 | 0.1 |
| FW005 | 33.34 | 1.45 | 9.46 | 16.27 | 0.28 | 6.47 | 10.09 | 2.66 | 0.22 | 0.13 |
| FW003 | 45.7 | 1.28 | 13.85 | 15.27 | 0.24 | 4.21 | 4.37 | 2.98 | 2.55 | 0.14 |
| FW004 | 40.95 | 1.55 | 14.42 | 16.56 | 0.25 | 4.18 | 5.54 | 2.85 | 2.47 | 0.18 |
| FW006 | 45.52 | 0.64 | 11.99 | 7.88 | 0.16 | 5.89 | 7.25 | 5.99 | 1 | 0.28 |
| FW014 | 52.36 | 1.41 | 11.28 | 13.99 | 0.27 | 4.18 | 3.53 | 5.16 | 1.27 | 0.19 |
| FW009 | 45.49 | 0.61 | 11.96 | 7.85 | 0.13 | 5.86 | 7.22 | 5.96 | 0.97 | 0.25 |
| FW010 | 52.26 | 1.39 | 11.26 | 13.97 | 0.25 | 4.16 | 3.51 | 5.14 | 1.25 | 0.17 |
| FW011 | 33.34 | 1.45 | 9.46 | 16.27 | 0.28 | 6.47 | 10.09 | 2.66 | 0.22 | 0.13 |
| FW012 | 52.27 | 1.32 | 11.19 | 13.9 | 0.18 | 4.09 | 3.44 | 5.07 | 1.18 | 0.1 |
| FW007 | 52.23 | 1.36 | 11.23 | 13.94 | 0.22 | 4.13 | 3.48 | 5.11 | 1.22 | 0.14 |
| FW015 | 33.33 | 1.44 | 9.45 | 16.26 | 0.27 | 6.46 | 10.08 | 2.65 | 0.21 | 0.12 |
| FW013 | 33.36 | 1.47 | 9.48 | 16.29 | 0.3 | 6.49 | 10.11 | 2.68 | 0.24 | 0.15 |
| FW016 | 45.72 | 1.3 | 13.87 | 15.29 | 0.26 | 4.23 | 4.39 | 3 | 2.57 | 0.16 |
| FW017 | 40.97 | 1.57 | 14.44 | 16.58 | 0.27 | 4.2 | 5.56 | 2.87 | 2.49 | 0.2 |
| FW018 | 45.54 | 0.66 | 12.01 | 7.9 | 0.18 | 5.91 | 7.27 | 6.01 | 1.02 | 0.3 |
| FW020 | 52.38 | 1.43 | 11.3 | 14.01 | 0.29 | 4.2 | 3.55 | 5.18 | 1.29 | 0.21 |
| FW019 | 45.51 | 0.63 | 11.98 | 7.87 | 0.15 | 5.88 | 7.24 | 5.98 | 0.99 | 0.27 |

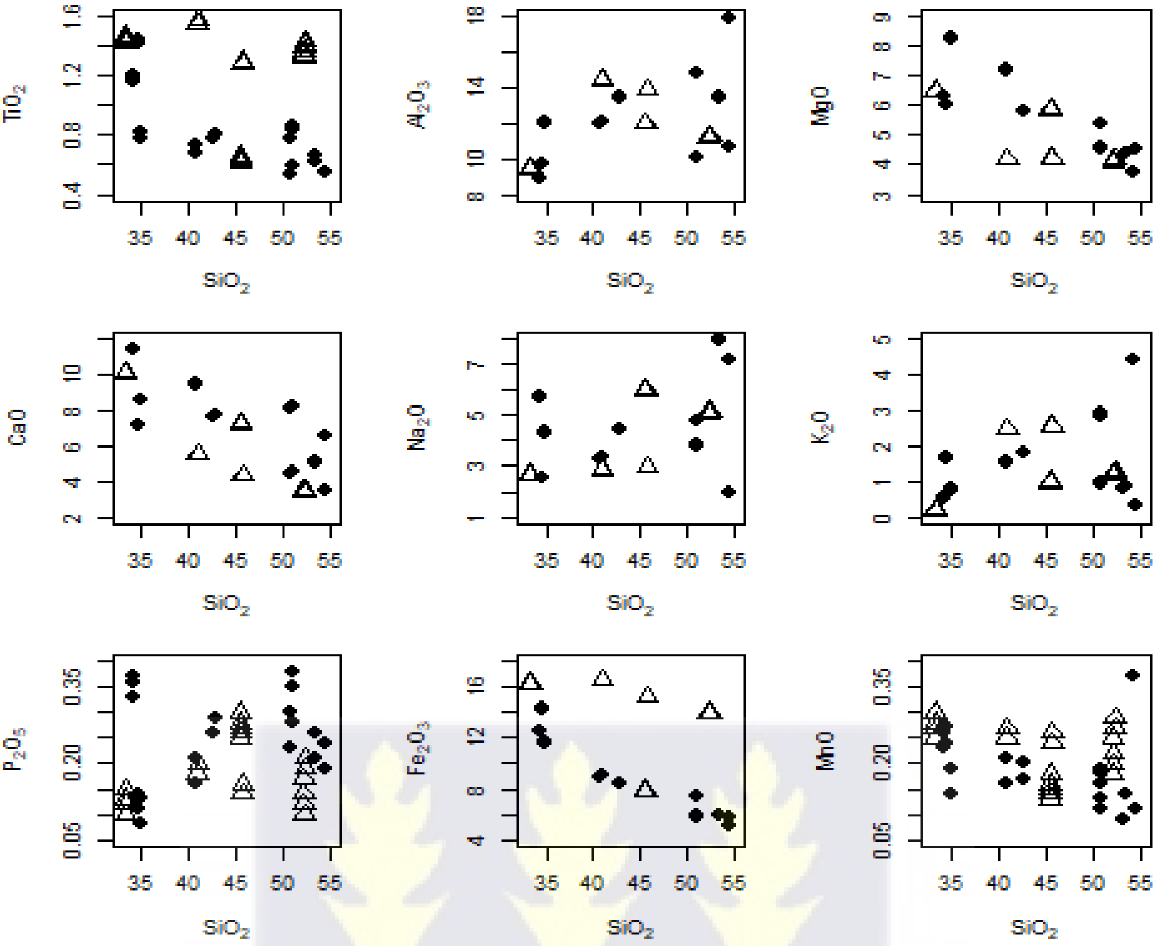

**Figure 4.48: Major elements versus $SiO_2$ diagram of the hanging and footwall mafic volcanic rock sample understudy. Black circle = hanging wall mafic volcanic rock sample, triangle = footwall mafic volcanic rock sample.**

### 4.11.1 Trace elements

#### 4.11.1.1 Large ion lithophile elements (LILE) (Rb, Sr and U)

The contents of selected trace elements in the hanging and footwall mafic volcanic rocks have been presented in Table 4.12. The mean contents of Rb, Sr and U in the hanging wall and footwall rocks are 35.02 ppm, 570.32 ppm, 5.79 ppm and 23.84 ppm, 399.01 ppm and 6.32 ppm respectively. The high Sr content can be attributed to the presence of feldspar as well as the effect of subsequent metamorphism (Gale and Roberts 1974).

### 4.11.1.2 High field strength elements (HFSE) (Y, Zr, Nb and Th)

In this study, the average Y contents in the hanging wall and footwall volcanic rocks are 17.29 ppm and 18.76 ppm respectively. Usually, Y is incorporated into garnet and amphiboles. Zr content in the footwall volcanic rock is slightly higher (83.16 ppm) than the contents in the hanging wall volcanics (78.92pmm). The average Zr content of the footwall mafic volcanic rock (83.16ppm) is slightly higher than that of the hanging wall mafic volcanic rock (78.92ppm). The average concentration of Zr in the basaltic lavas is 88 ppm (Taylor and McLennan, 1995) which is higher than the Zr contents in all the rocks and is indicative of the depletion of heavy minerals, particularly zircon. The average contents of Nb, Th and U in the hanging wall and footwall volcanic rocks are 5.45 ppm, 3.55 ppm, 5.79 ppm and 4.32 ppm, 1.39 ppm, and 6.32 ppm respectively.

### 4.11.1.3 Transitional elements

Average V, Cr, Cu and Ni contents in the hanging wall and footwall are 166.04 ppm, 164.82 ppm, 82.11 ppm, 58.32 ppm and 307.21 ppm, 110.35 ppm, 73.81 ppm and 48.84 ppm respectively. The high contents of Cr and Ni in the rocks suggest the presence of olivine in the source rock (Green, 1980) or probably from mantle rocks. Wrafter and Graham (1989) cautioned that high Cr/Ni ratio is a good indicator of mafic rocks, hence the Cr/Ni ratio (3.2) and (2.1) for the hanging wall and footwall mafic volcanics respectively. These ratios prove that the volcanic rocks understudy are mafic as seen in the petrography. Au in the hanging and footwall mafic volcanic rocks range from 0.1 to 35.21 ppm and 0.1 to 1.5 ppm respectively.

## Table 4. 12: Variable concentrations of the trace elements (ppm) for the selected hanging and footwall mafic volcanic rocks

| Sample | V | Cr | Co | Ni | Cu | Zn | Ga | Rb | Sr | Y | Zr | Nb | Mo | Sb | Cs | Ba | La | Ce | Hf | Ta | Pb | Bi | Th | U | Au | Ag | As |
|---|---|---|---|---|---|---|---|---|---|---|---|---|---|---|---|---|---|---|---|---|---|---|---|---|---|---|---|
| **HW01** | 40.1 | 204.0 | 35.6 | 45.9 | 97.1 | 71.1 | 15.6 | 66.0 | 317.0 | 21.4 | 106.0 | 6.2 | 1.6 | 14.7 | 5.2 | 950.0 | 5.6 | 4.6 | 11.1 | 10.2 | 12.6 | 3.4 | 5.8 | 7.4 | 4.2 | 0.0 | 52.8 |
| **HW02** | 141.0 | 158.0 | 42.8 | 43.1 | 85.6 | 61.2 | 18.5 | 21.9 | 863.0 | 3.7 | 99.0 | 8.1 | 3.4 | 7.6 | 7.0 | 578.0 | 12.0 | 30.4 | 8.2 | 9.2 | 1.5 | 1.3 | 1.2 | 6.9 | 5.7 | 0.1 | 27.6 |
| **HW03** | 219.0 | 237.0 | 68.6 | 138.9 | 98.0 | 106.1 | 14.7 | 19.6 | 299.0 | 19.8 | 41.0 | 3.0 | 1.1 | 8.0 | 1.0 | 108.0 | 3.4 | 3.8 | 6.7 | 13.5 | 9.2 | 4.7 | 3.9 | 5.5 | 0.1 | 0.3 | 1410.0 |
| **HW04** | 81.0 | 152.0 | 35.0 | 28.3 | 77.3 | 63.7 | 16.0 | 20.1 | 363.0 | 16.4 | 60.0 | 4.4 | 7.9 | 8.1 | 2.5 | 414.0 | 4.7 | 4.8 | 10.1 | 12.1 | 12.1 | 4.6 | 4.1 | 6.0 | 6.0 | 2.4 | 2420.0 |
| **HW05** | 181.0 | 249.0 | 83.0 | 69.8 | 58.1 | 101.6 | 18.6 | 34.4 | 465.0 | 2.6 | 67.0 | 4.0 | 3.0 | 5.7 | 6.3 | 615.0 | 13.0 | 24.6 | 8.0 | 8.3 | 1.8 | 0.6 | 1.5 | 8.2 | 4.2 | 0.2 | 669.0 |
| **HW06** | 40.0 | 92.0 | 40.7 | 79.6 | 87.5 | 55.9 | 17.9 | 106.4 | 431.0 | 15.7 | 102.0 | 5.7 | 6.6 | 9.6 | 5.2 | 1241.0 | 7.3 | 5.9 | 10.4 | 12.0 | 10.9 | 4.6 | 5.7 | 8.2 | 6.5 | 1.3 | 1065.0 |
| **HW07** | 192.0 | 227.0 | 46.5 | 64.5 | 90.2 | 94.5 | 21.1 | 40.3 | 1050.0 | 17.5 | 76.0 | 5.7 | 2.4 | 14.5 | 2.2 | 1570.0 | 3.6 | 6.7 | 7.6 | 7.6 | 13.4 | 5.9 | 3.3 | 4.3 | 2.5 | 0.1 | 465.0 |
| **HW08** | 413.0 | 62.0 | 65.9 | 52.1 | 89.3 | 135.8 | 19.2 | 38.9 | 771.0 | 26.5 | 85.0 | 4.3 | 0.6 | 18.6 | 3.4 | 1467.0 | 3.2 | 2.5 | 11.7 | 17.5 | 12.4 | 7.9 | 1.5 | 1.7 | 3.9 | 1.3 | 637.0 |
| **HW09** | 220.0 | 97.0 | 70.1 | 42.7 | 78.4 | 89.1 | 14.6 | 12.6 | 573.0 | 30.7 | 79.0 | 5.5 | 1.9 | 11.5 | 1.5 | 84.0 | 1.9 | 7.0 | 9.0 | 12.5 | 13.4 | 6.1 | 5.3 | 6.1 | 12.0 | 0.0 | 51.4 |
| **HW10** | 40.2 | 204.1 | 35.7 | 46.0 | 97.2 | 71.2 | 15.7 | 66.1 | 317.1 | 21.5 | 106.1 | 6.3 | 1.7 | 14.8 | 5.3 | 950.1 | 5.7 | 4.7 | 11.2 | 10.3 | 12.7 | 3.5 | 5.9 | 7.5 | 10.0 | 6.1 | 0.6 |
| **HW11** | 141.1 | 158.1 | 42.9 | 43.2 | 85.7 | 61.3 | 18.6 | 22.0 | 863.1 | 3.8 | 99.1 | 8.2 | 3.5 | 7.7 | 7.1 | 578.1 | 12.1 | 30.5 | 8.3 | 9.3 | 1.6 | 1.4 | 1.3 | 7.0 | 20.0 | 35.5 | 150.5 |
| **HW12** | 219.1 | 237.1 | 68.7 | 139.0 | 98.1 | 106.2 | 14.8 | 19.7 | 299.1 | 19.9 | 41.1 | 3.1 | 1.2 | 8.1 | 1.1 | 108.1 | 3.5 | 3.9 | 6.8 | 13.6 | 9.3 | 4.8 | 4.0 | 5.6 | 9.3 | 0.1 | 334.0 |
| **HW13** | 81.1 | 152.1 | 35.1 | 28.4 | 77.4 | 63.8 | 16.1 | 20.2 | 363.1 | 16.5 | 60.1 | 4.5 | 8.0 | 8.2 | 2.6 | 414.1 | 4.8 | 4.9 | 10.2 | 12.2 | 12.2 | 4.7 | 4.2 | 6.1 | 16.2 | 0.0 | 180.0 |
| **HW14** | 181.1 | 249.1 | 83.1 | 69.9 | 58.2 | 101.7 | 18.7 | 34.5 | 465.1 | 2.7 | 67.1 | 4.1 | 3.1 | 5.8 | 6.4 | 615.1 | 13.1 | 24.7 | 8.1 | 8.4 | 1.9 | 0.7 | 1.6 | 8.3 | 31.3 | 0.0 | 104.5 |
| **HW15** | 192.0 | 227.0 | 46.5 | 64.5 | 90.2 | 94.5 | 21.1 | 40.3 | 1050.3 | 17.5 | 76.0 | 5.7 | 2.4 | 14.5 | 2.2 | 1570.0 | 3.6 | 6.7 | 7.6 | 7.6 | 13.4 | 5.9 | 3.3 | 4.3 | 35.2 | 0.0 | 178.0 |
| **HW16** | 413.0 | 62.0 | 65.9 | 52.1 | 89.3 | 135.8 | 19.2 | 38.9 | 771.0 | 26.5 | 85.0 | 4.3 | 0.6 | 18.6 | 3.4 | 1467.0 | 3.2 | 2.5 | 11.7 | 17.5 | 12.4 | 7.9 | 1.5 | 1.7 | 35.1 | 0.1 | 1470.0 |
| **HW17** | 220.0 | 97.0 | 70.1 | 42.7 | 78.4 | 89.1 | 14.6 | 12.6 | 573.0 | 30.7 | 79.0 | 5.5 | 1.9 | 11.5 | 1.5 | 84.0 | 1.9 | 7.0 | 9.0 | 12.5 | 13.4 | 6.1 | 5.3 | 6.1 | 12.4 | 0.2 | 542.0 |
| **HW18** | 40.2 | 204.1 | 35.7 | 46.0 | 97.2 | 71.2 | 15.7 | 66.1 | 317.1 | 21.5 | 106.1 | 6.3 | 1.7 | 14.8 | 5.3 | 950.1 | 5.7 | 4.7 | 11.2 | 10.3 | 12.7 | 3.5 | 5.9 | 7.5 | 4.3 | 0.1 | 157.5 |
| **HW19** | 220.0 | 97.0 | 70.1 | 42.7 | 78.4 | 89.1 | 14.6 | 12.6 | 573.0 | 30.7 | 79.0 | 5.5 | 1.9 | 11.5 | 1.5 | 84.0 | 1.9 | 7.0 | 9.0 | 12.5 | 13.4 | 6.1 | 5.3 | 6.1 | 1.3 | 0.0 | 173.5 |
| **HW20** | 46.0 | 131.0 | 30.0 | 27.2 | 30.8 | 39.1 | 17.1 | 7.4 | 683.0 | 0.5 | 65.0 | 8.9 | 6.2 | 18.1 | 7.0 | 320.0 | 14.0 | 18.0 | 8.0 | 6.5 | 1.4 | 1.2 | 0.5 | 1.5 | 0.6 | 0.1 | 0.7 |
| **FW01** | 106.0 | 224.0 | 61.0 | 64.3 | 67.0 | 79.3 | 16.3 | 24.4 | 797.0 | 20.8 | 72.0 | 5.9 | 3.5 | 55.3 | 6.6 | 799.0 | 14.0 | 18.0 | 8.0 | 8.9 | 1.5 | 1.0 | 1.2 | 7.3 | 0.1 | 0.1 | 149.5 |
| **FW02** | 311.0 | 81.3 | 82.0 | 42.9 | 63.4 | 115.3 | 16.8 | 27.2 | 279.0 | 11.8 | 79.0 | 4.0 | 3.2 | 23.2 | 7.0 | 186.0 | 14.0 | 29.0 | 9.0 | 10.0 | 2.0 | 2.2 | 2.0 | 9.0 | 0.1 | 0.1 | 165.5 |
| **FW03** | 419.0 | 51.0 | 70.8 | 45.7 | 91.3 | 114.4 | 15.6 | 5.2 | 285.0 | 28.7 | 89.0 | 4.3 | 1.2 | 34.0 | 1.2 | 12.0 | 1.0 | 8.7 | 12.0 | 17.8 | 7.7 | 9.5 | 1.5 | 1.8 | 0.1 | 0.3 | 545.0 |
| **FW04** | 419.0 | 51.0 | 70.8 | 45.7 | 91.3 | 114.4 | 15.6 | 5.2 | 285.0 | 28.7 | 89.0 | 4.3 | 1.2 | 34.0 | 1.2 | 12.0 | 1.0 | 8.7 | 12.0 | 17.8 | 7.7 | 9.5 | 1.5 | 1.8 | 0.8 | 0.3 | 250.0 |
| **FW05** | 361.0 | 96.0 | 88.0 | 43.9 | 43.6 | 101.9 | 19.9 | 55.3 | 194.0 | 13.9 | 96.0 | 4.2 | 4.0 | 42.4 | 6.5 | 115.0 | 12.0 | 27.3 | 9.2 | 8.9 | 2.5 | 2.0 | 2.0 | 10.0 | 0.2 | 0.1 | 3800.0 |
| **FW06** | 439.0 | 101.0 | 129.0 | 42.3 | 87.1 | 130.3 | 23.2 | 55.0 | 211.0 | 22.2 | 102.0 | 3.9 | 4.1 | 60.5 | 8.5 | 93.0 | 14.0 | 24.3 | 11.0 | 12.0 | 1.9 | 1.6 | 1.8 | 10.0 | 0.5 | 0.2 | 73.6 |
| **FW07** | 106.0 | 224.0 | 61.0 | 64.3 | 67.0 | 79.3 | 16.3 | 24.4 | 797.0 | 18.2 | 72.0 | 5.9 | 3.5 | 55.3 | 6.6 | 799.0 | 14.0 | 18.0 | 8.0 | 8.9 | 1.5 | 1.0 | 1.2 | 7.3 | 1.5 | 0.0 | 144.5 |
| **FW08** | 311.1 | 81.4 | 82.1 | 43.0 | 63.5 | 115.4 | 16.9 | 27.3 | 279.1 | 11.9 | 79.1 | 4.1 | 3.3 | 23.3 | 7.1 | 186.1 | 14.1 | 29.1 | 9.1 | 10.1 | 2.1 | 2.3 | 2.1 | 9.1 | 0.9 | 0.0 | 110.0 |
| **FW09** | 106.0 | 224.0 | 61.0 | 64.3 | 67.0 | 79.3 | 16.3 | 24.4 | 797.0 | 14.8 | 72.0 | 5.9 | 3.5 | 55.3 | 6.6 | 799.0 | 14.0 | 18.0 | 8.0 | 8.9 | 1.5 | 1.0 | 1.2 | 7.3 | 1.0 | 0.0 | 775.0 |
| **FW10** | 311.1 | 81.4 | 82.1 | 43.0 | 63.5 | 115.4 | 16.9 | 27.3 | 279.1 | 11.9 | 79.1 | 4.1 | 3.3 | 23.3 | 7.1 | 186.1 | 14.1 | 29.1 | 9.1 | 10.1 | 2.1 | 2.3 | 2.1 | 9.1 | 1.0 | 0.0 | 987.0 |
| **FW11** | 419.0 | 51.0 | 70.8 | 45.7 | 91.3 | 114.4 | 15.6 | 5.2 | 285.0 | 28.7 | 89.0 | 4.3 | 1.2 | 34.0 | 1.2 | 12.0 | 1.0 | 8.7 | 12.0 | 17.8 | 7.7 | 9.5 | 1.5 | 1.8 | 0.4 | 0.0 | 51.4 |
| **FW12** | 311.0 | 81.3 | 82.0 | 42.9 | 63.4 | 115.3 | 16.8 | 27.2 | 279.0 | 11.8 | 79.0 | 4.0 | 3.2 | 23.2 | 7.0 | 186.0 | 14.0 | 29.0 | 9.0 | 10.0 | 2.0 | 2.2 | 2.0 | 9.0 | 1.3 | 0.9 | 44.6 |
| **FW13** | 311.0 | 81.3 | 82.0 | 42.9 | 63.4 | 115.3 | 16.8 | 27.2 | 279.0 | 11.8 | 79.0 | 4.0 | 3.2 | 23.2 | 7.0 | 186.0 | 14.0 | 29.0 | 9.0 | 10.0 | 2.0 | 2.2 | 2.0 | 9.0 | 1.2 | 0.1 | 140.3 |

| | | | | | | | | | | | | | | | | | | | | | | | | | | | |
|---|---|---|---|---|---|---|---|---|---|---|---|---|---|---|---|---|---|---|---|---|---|---|---|---|---|---|---|
| **FW14** | 105.1 | 223.1 | 60.1 | 63.4 | 66.1 | 78.4 | 15.4 | 23.5 | 796.1 | 12.9 | 71.1 | 5.0 | 2.6 | 54.4 | 5.7 | 798.1 | 13.1 | 17.1 | 7.1 | 8.0 | 0.6 | 0.1 | 0.3 | 6.4 | 1.1 | 0.1 | 364.0 |
| **FW15** | 419.1 | 51.1 | 70.9 | 45.8 | 91.4 | 114.5 | 15.7 | 5.3 | 285.1 | 28.8 | 89.1 | 4.4 | 1.3 | 34.1 | 1.3 | 12.1 | 1.1 | 8.8 | 12.1 | 17.9 | 7.8 | 9.6 | 1.6 | 1.9 | 1.2 | 0.1 | 145.0 |
| **FW16** | 310.1 | 80.4 | 81.1 | 42.0 | 62.5 | 114.4 | 15.9 | 26.3 | 278.1 | 10.9 | 78.1 | 3.1 | 2.3 | 22.3 | 6.1 | 185.1 | 13.1 | 28.1 | 8.1 | 9.1 | 1.1 | 1.3 | 1.1 | 8.1 | 1.0 | 1.3 | 134.8 |
| **FW17** | 418.1 | 50.1 | 69.9 | 44.8 | 90.4 | 113.5 | 14.7 | 4.3 | 284.1 | 27.8 | 88.1 | 3.4 | 0.3 | 33.1 | 0.3 | 11.1 | 0.1 | 7.8 | 11.1 | 16.9 | 6.8 | 8.6 | 0.6 | 0.9 | 1.4 | 0.0 | 79.0 |
| **FW18** | 438.2 | 100.2 | 128.2 | 41.5 | 86.3 | 129.5 | 22.4 | 54.2 | 210.2 | 21.4 | 101.2 | 3.1 | 3.3 | 59.7 | 7.7 | 92.2 | 13.2 | 23.5 | 10.2 | 11.2 | 1.1 | 0.8 | 1.0 | 9.2 | 0.3 | 6.1 | 1470.0 |
| **FW19** | 105.2 | 223.2 | 60.2 | 63.5 | 66.2 | 78.5 | 15.5 | 23.6 | 796.2 | 10.6 | 71.2 | 5.1 | 2.7 | 54.5 | 5.8 | 798.2 | 13.2 | 17.2 | 7.2 | 8.1 | 0.7 | 0.2 | 0.4 | 6.5 | 1.2 | 35.5 | 742.0 |
| **FW20** | 418.2 | 50.2 | 70.0 | 44.9 | 90.5 | 113.6 | 14.8 | 4.4 | 284.2 | 27.9 | 88.2 | 3.5 | 0.4 | 33.2 | 0.4 | 11.2 | 0.2 | 7.9 | 11.2 | 17.0 | 6.9 | 8.7 | 0.7 | 1.0 | 0.6 | 0.1 | 304.5 |

### 4.11.2 Petrogenesis of the mafic volcanic rocks (Footwall and Hanging wall)

The contents of $SiO_2$ in the volcanic rocks (34.2- 54.50) wt.% for the hanging wall mafic volcanic rocks and 33.3-52.4 wt.% for the footwall mafic volcanic rocks) suggest some of them are moderately evolved. The decreasing trends exhibited by MgO, CaO and $Fe_2O_3$ with a progressive increase in $SiO_2$ content may suggest that plagioclase and olivine and/or pyroxene were most likely the major phases that crystallized out during the magma evolution (Yücel et al., 2017).

Pearce (1996) proposed the use of Nb/Y against Zr/Ti for the geochemical classification of volcanic rocks. On the Nb/Y versus Zr/Ti binary diagram (Figure 4.49a) the hanging wall mafic volcanic rocks samples plot mainly in the fields of basalt, basaltic andesite and alkali basalt while the footwall mafic volcanic rocks plot from basalt to basaltic andesite. The andesitic composition could be due to the silicification of the basaltic magma. Because there is no one classification for the two rock types understudy, the terms hanging wall mafic rock and footwall mafic volcanic rocks will be employed throughout this study.

Based on this classification, both rock types may have crystalized from a single magma suite. Kuno (1967) postulated that andesite magmas originate from basalt lavas through fractionation. Sylvester and Attoh (1992) postulated that both tholeiitic and alkali basalts are present in the Birimian terrain. On the $Na_2O$+$K_2O$ – FeOt – MgO (AFM) diagram by Irvine and Baragar (1971) (Figure 4.49b), the hanging wall mafic volcanic rock samples plot as products of calc-alkaline lava series with one sample plotting in the field of tholeiitic suite while the footwall samples are mainly from tholeiitic lava series even though one sample falls in the margin of calc-alkaline lave series. The magma suite that produced the rocks understudy was further confirmed by the $SiO_2$ versus $FeO_t$/MgO binary plot by Miyashiro (1974).

Debon and Le Fort (1983) also proposed the use of K/(Na+K) against Fe+Mg+Ti binary plot to classify volcanic rocks based on their potassium or sodic affinity. On the K/(Na+K) against Fe+Mg+Ti plot (Figure 4.49c) all the rock types understudy have sodic and mesocratic affinities. On the $Al_2O_3/CaO+Na_2O+K_2O$ (A/CNK) versus $Al_2O_3/Na_2O+K_2O$ (ANK) binary plot (Figure 4.49d) the hanging wall mafic volcanic rocks range from metaluminous to slightly peralkaline while the footwall mafic volcanic rocks are predominantly metaluminous.

On the Normal Mid Ocean Ridge Basalt (NMORB) (Figures 4.50 a and b) and normalized primitive mantle (Figures 4.50 c and d) multi-element spider diagrams after Sun and McDonough (1989) and McDonough and Sun (1995) respectively, both rock types understudy are enriched in LILEs (Rb, Ba, K, Pb, and Sr) and depleted in HFSEs (Nb, P, Zr, Th and Ti) (Figures 4.50 a, b, c and d) which is characteristic of volcanic arc related lavas associated with subduction zones. According to Shervais & Jean (2012), The high concentrations of fluid mobile elements (such as Li, B, Be, Rb, Th, and Pb) in volcanic arc rocks are maintained by their constant addition during melting. These elements erupted from a subducted slab. The high depletion of Zr, Ti and Y on the NORM spider diagram (Figures 4.50a and b) suggest that the rocks understudy are tholeiitic arc materials. In general, the calc-alkaline nature of the hanging wall may be due to subsequent hydrothermal alteration (metasomatism) that resulted in the emplacement of gold.

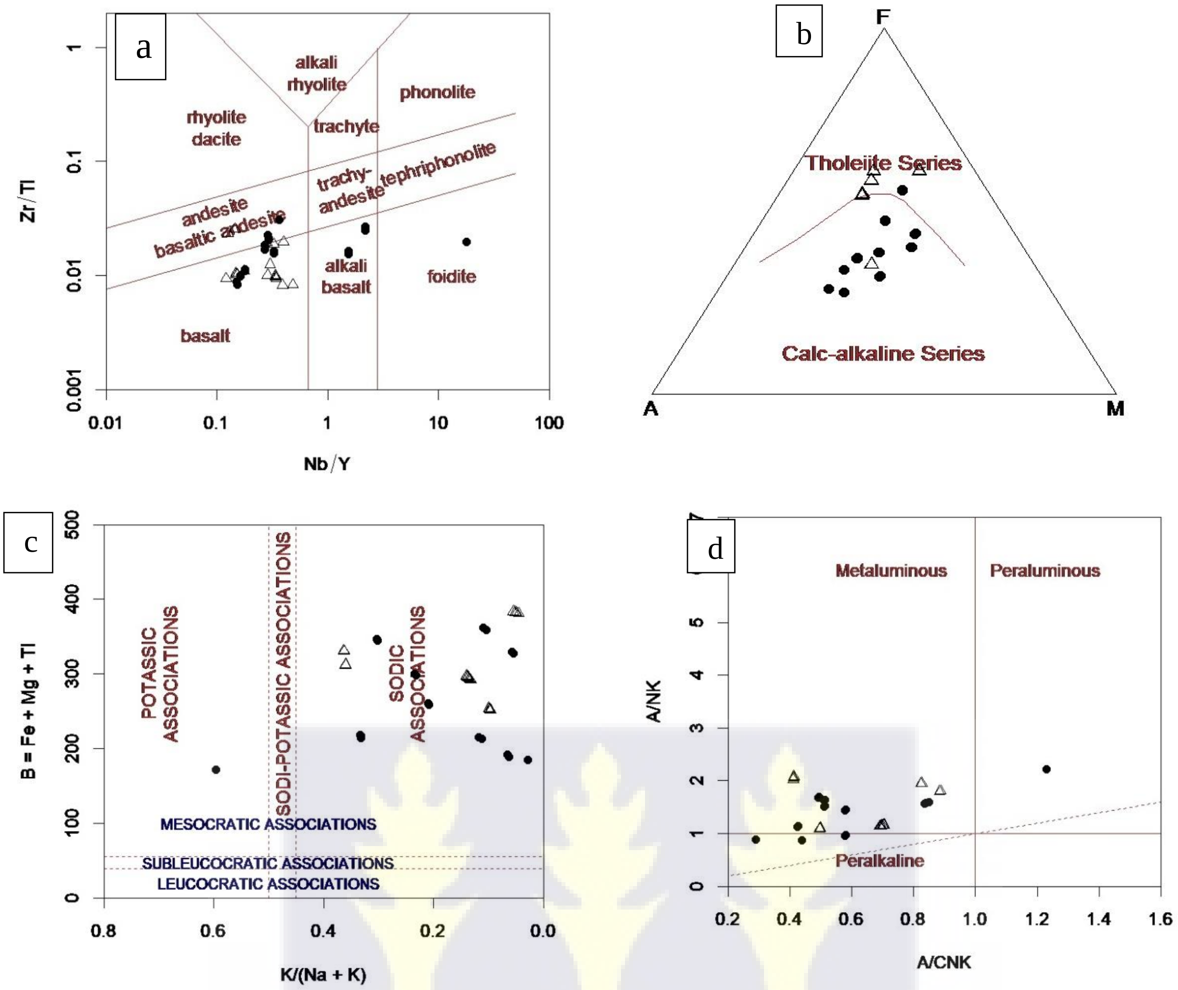

**Figure 4.49:** **a) Nb/Y versus Zr/Ti binary diagram b) $Al_2O_3$ $Na_2O+K_2O$ – FeOt – MgO (AFM) diagram c) K/(Na+K) against Fe+Mg+Ti plot d) $Al_2O_3/CaO+Na_2O+K_2O$ (A/CNK) verus $Al_2O_3/Na_2O+K_2O$ (ANK) binary plot. Black circle = hanging wall mafic volcanic rock sample, triangle = footwall mafic volcanic rock sample.**

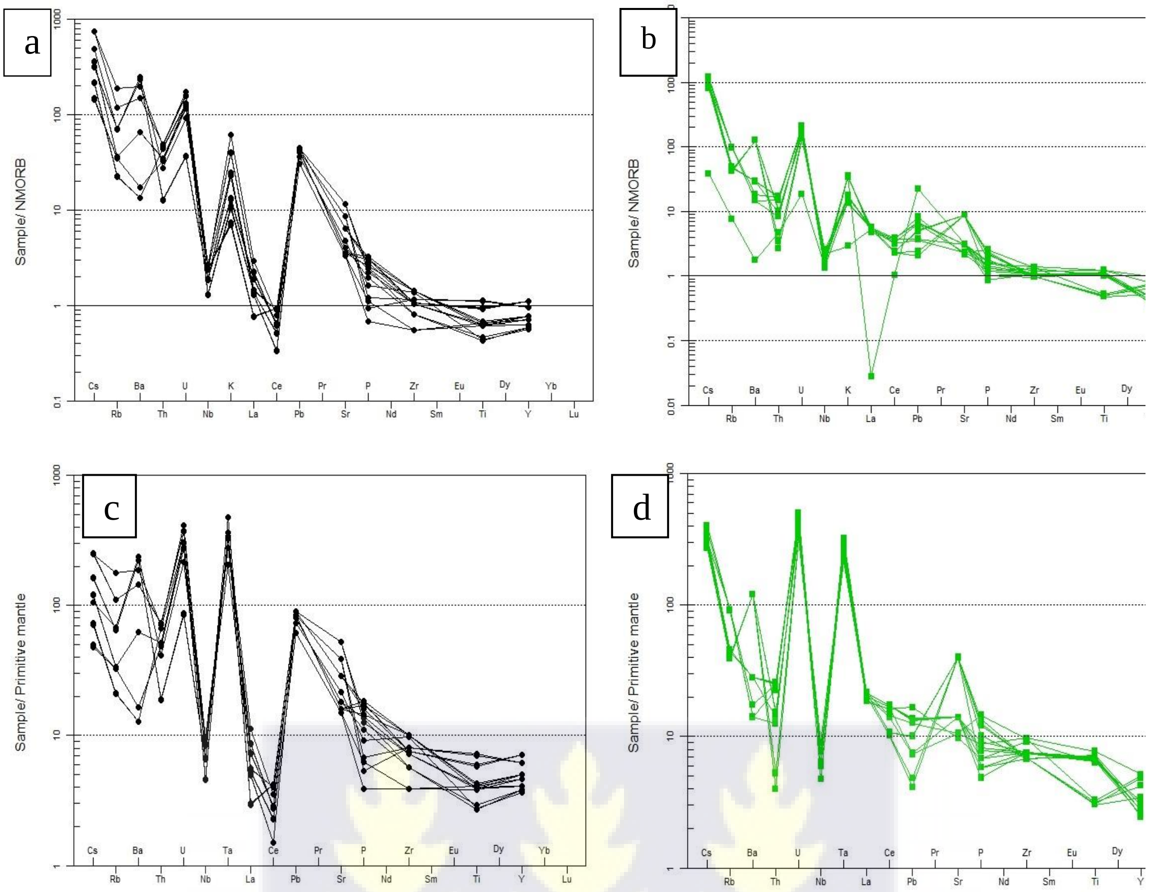

**Figure 4.50: (a and c) NMORB (after Sun and McDonough, 1989) and Primitive mantle (after McDonough and Sun, 1995) normalized multi-element spider diagram for the hanging wall mafic volcanic rocks. (b, and d) Primitive mantle (after McDonough and Sun, 1995) and NMORB (after Sun and McDonough, 1989) normalized multi-element spider diagram for the footwall mafic volcanic rocks in the Kibi area.**

The lava evolution process was determined by bivariate plots of selected compatible elements (Cr, Ni, Rb, Sr and Th) against MgO. On the plot (Figure 4.51) there is little or no correlation between the selected compatible elements and MgO. This implies that the minor and trace elements might have undergone an appreciable degree of remobilization (metasomatism) as a result of subsequent metamorphism or alteration. Based on these correlations it is not advisable to conclude using major and trace elements but rather pay more attention to the rare earth elements (REEs).

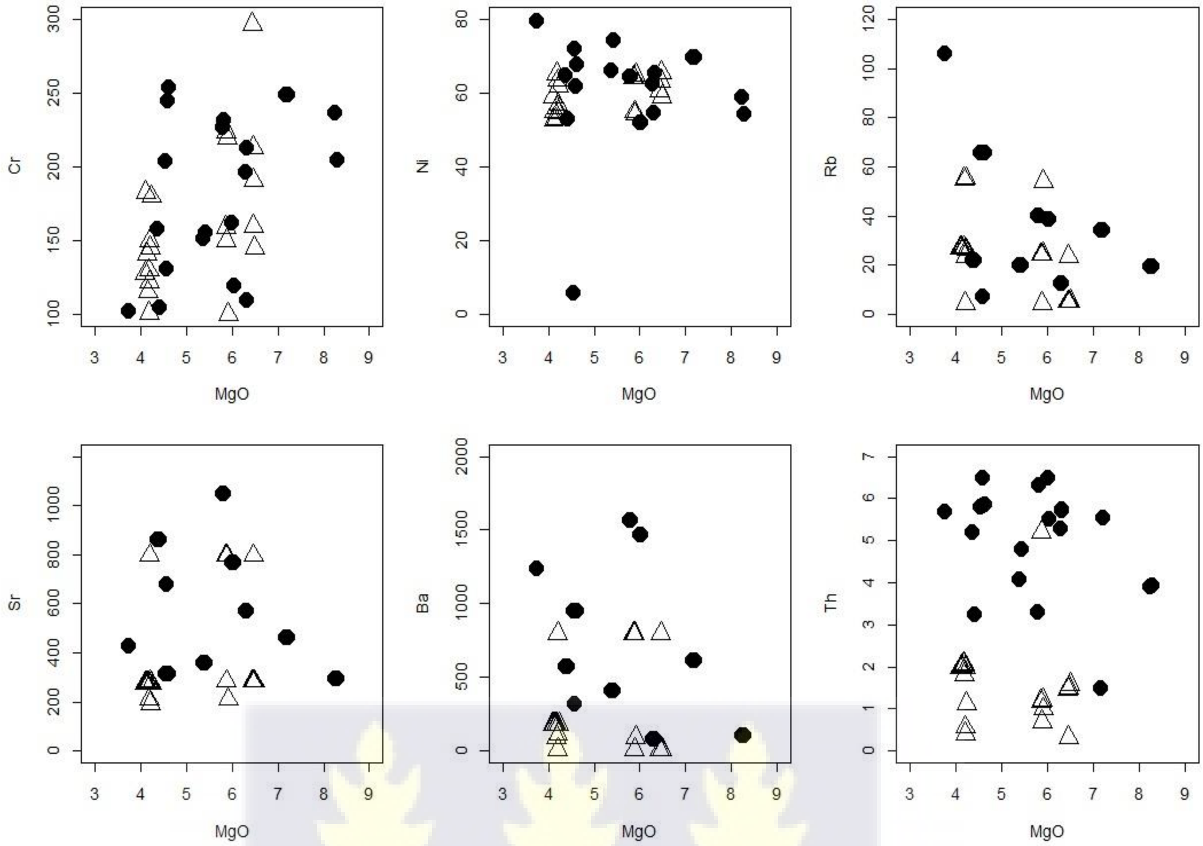

**Figure 4.51: Bivariate plots of selected compatible elements (Cr, Ni, Rb, Sr, Ba and Th) against MgO. Black circle = hanging wall mafic volcanic rock sample, triangle = footwall mafic volcanic rock sample.**

### 4.11.3 Tectonic setting of the mafic volcanic rocks (foot wall and hanging wall)

In the plate tectonic model for the Birimian genesis, various theories consider the Birimian volcanic rocks to be of either plate margin (converging and diverging plates, Pearce and Cann, 1973) or within plate derivatives (intracontinental rifting). Leube et al. (1990) and Alaric, (1990) proposed that the Birimian “greenstone” belts formed from intracontinental rifting while Sylvester and Attoh, (1992) proposed that the Birimian most likely originated from immature island arcs built on the oceanic crust which was subsequently intruded by granitoid during orogenesis. Also, evidence from isotopic studies in Mali indicates that the Mako (Birimian volcanic rocks) Palaeoproterozoic crust is a juvenile arc-related terrain derived from a depleted mantle source, emplaced between 2300Ma and 2079 Ma and subsequently accreted to the growing West African Craton (Dia et al., 1997). This, therefore, gives evidence to arc-related tectonic settings in the Birrimian.

In this study, the Zr - Ti binary diagram by Pearce (1982) has been used to unravel the tectonic setting of the hanging and footwall mafic volcanic rocks. This is because the Zr/Ti ratio is not as strongly affected by alkalinity and calc-alkalinity since Ti is incompatible during basalt fractionation and therefore the ratio increases with increasing fractionation. On the Zr- Ti binary diagram (Figure 4.52a) the hanging wall mafic volcanic rock samples mainly cluster within the island arc lava field even though 4 samples plot as mid-oceanic ridge basalt (MORB) materials. On the other hand, the footwall mafic volcanic rocks plot in the MORB section precisely at the contact between within plate and island arc lavas. On the $Nb_N$ verse $Th_N$ plot after Saccani (2015), the samples generally plot close to the volcanic arc array (Figure 4.52b). Conversely, few samples also plot within the MORB / ocean island basalt margins. The MORB and Arc signatures exhibited by the mafic volcanic rocks (foot wall and hanging wall) can be attributed to the hydrothermal alteration (metasomatism) which is capable of changing the chemistry of the rock. Usually, MORB and arc magmas can also produce arc-back arc signatures as seen in Figure 4.52a. The Ti/1000 versus V plot by Shevias, 1982 (Figure 4.52c) suggests that the samples have MORB affinity. On the La/10 - Yb/15 - Nb/8 ternary pot by Cabanis and Lecolle, 1989 (Figure 4.52d) the mafic volcanic rock samples (hanging wall and foot wall) were predominantly formed in a compressive domain which can be attributed to orogenic events. Orogenic activities might have created pathways for the emplacement of the gold. According to Robert et al. (2007), orogenic gold is restricted to deposits composed of quartz-carbonate veins and associated wall rock replacement associated with compressional or transgressional geological structures such as reverse faults and folds.

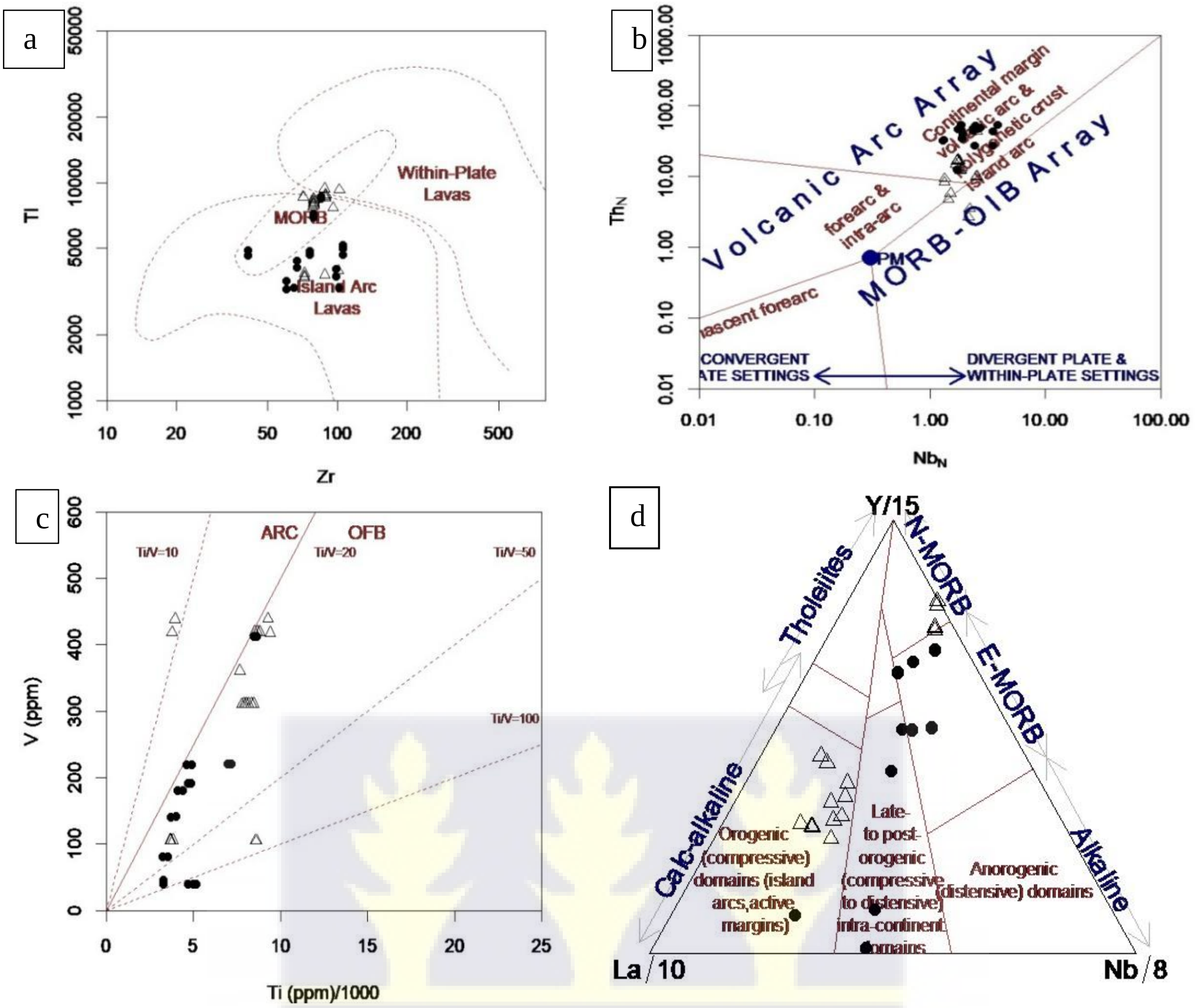

**Figure 4.52: a) Zr versus Ti Tectonic setting discriminating diagram of the hanging wall mafic volcanic rock samples and footwall mafic volcanic rock samples b) Nb$_N$ verse Th$_N$ (Saccani 2015) c) Ti vrs V (Shevias, 1982) d) La/10-Yb/15-Nb/8 ternary pot (Cabanis and Lecolle 1989). Black circle = hanging wall mafic volcanic rock sample, triangle = footwall mafic volcanic rock sample.**

## 4.12 Possible pathfinder elements associated with gold in the study area

Hierarchical Cluster analysis was used to group the selected trace elements in other establish possible pathfinder elements associated with Au in the selected rock types underlying the study area. Ward's Method was employed, which involves an agglomerative clustering algorithm that begins from the leaves and proceeds through the branches and eventually to the trunk. The Squared Euclidean distance was the interval used to measure dissimilarities in the variables. Also, the z-score was used as the standardized transformed value while the orientation of the data was done vertically. The cluster membership employed was the single solution and the number of clusters selected was three (3). The three (3) distinct clusters were identified with the help of the phenon line. From the dendrograms (Figures 4.53a, b, c and d) the best pathfinder elements for gold in the study are Ag and As. Notwithstanding, As, Cs and Sb are closely associated with gold in greywacke (Figure 4.53a) while As, Ni, Pb and Cu can also be used as pathfinder elements in the volcaniclastic rocks (Figure 4.453b). This association (Au - As - Ni – Pb - Cu) within the volcaniclastic rock suggests magmatic influence, possibly calc-alkaline intrusions (Schreiber et al., 1990; Sillitoe & Thompson, 1998). Similarly, the As, Ce, Th, Co, Zn and V and Ag, Nb and Zr are closely associated with gold in the hanging and footwall walls (Figures 4.53c and d) respectively. Considering the individual elements, arsenopyrite (FeAsS) is the most common arsenic (As) sulfide mineral that occurs primarily in hydrothermal and magmatic ore deposits. Cu and Zn can also be related to chalcopyrite and sphalerite respectively. The association between As, Ni, Cu, Pb and Co (Figure 4.53b) is commonly found in sulfide-bearing mineral deposits. In general, the above associations confirm the fact that gold mineralization in the Kibi area resulted mainly from hydrothermal sources with minimal contributions from sedimentary and possibly metamorphic sources probably as a result of the subsequent orogenic activities as seen in Figure 4.52d.

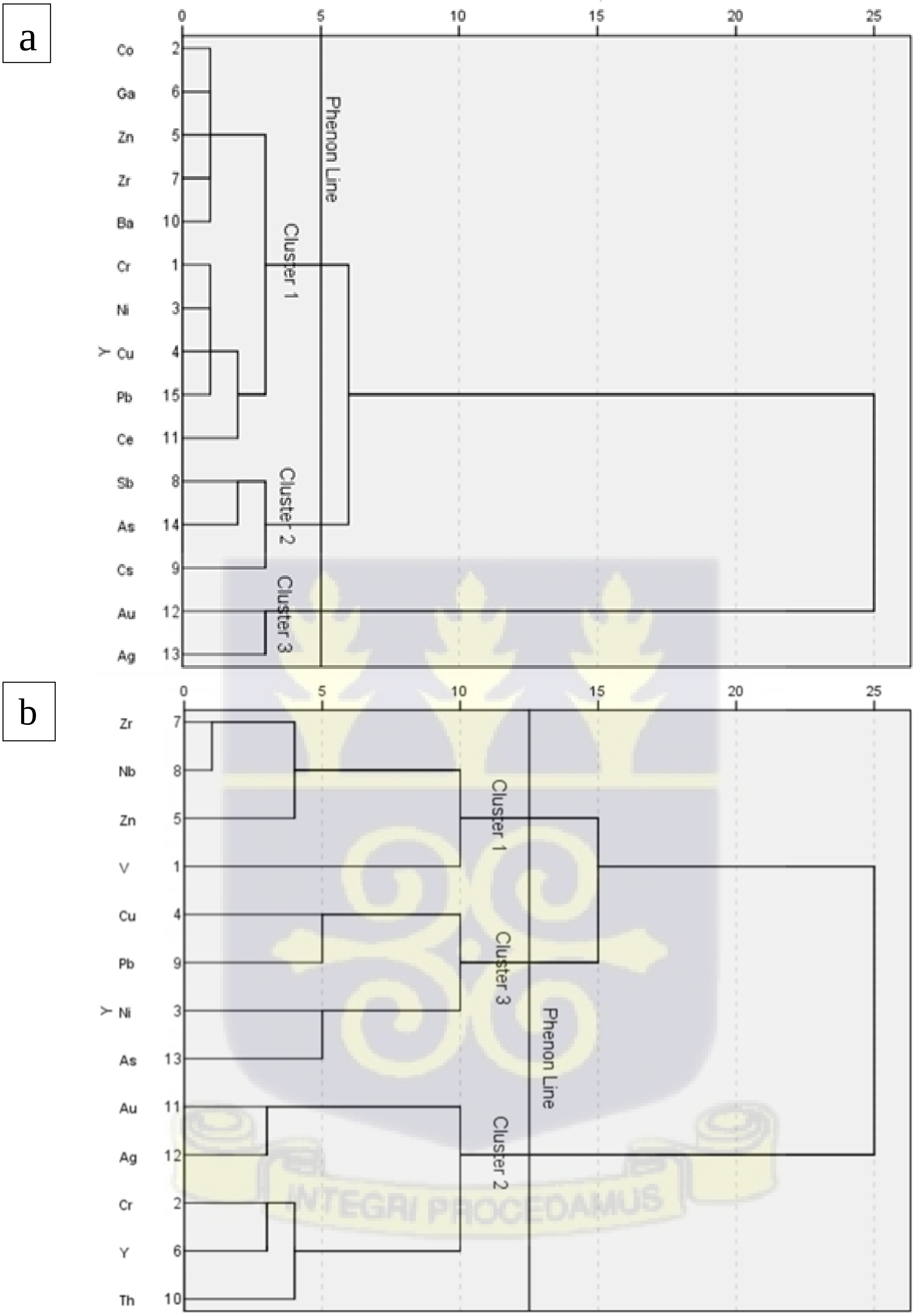

**Figure 4.53: Dendrograms displaying multi-elemental clusters for the a) graywacke and b) volcaniclastic rock samples**

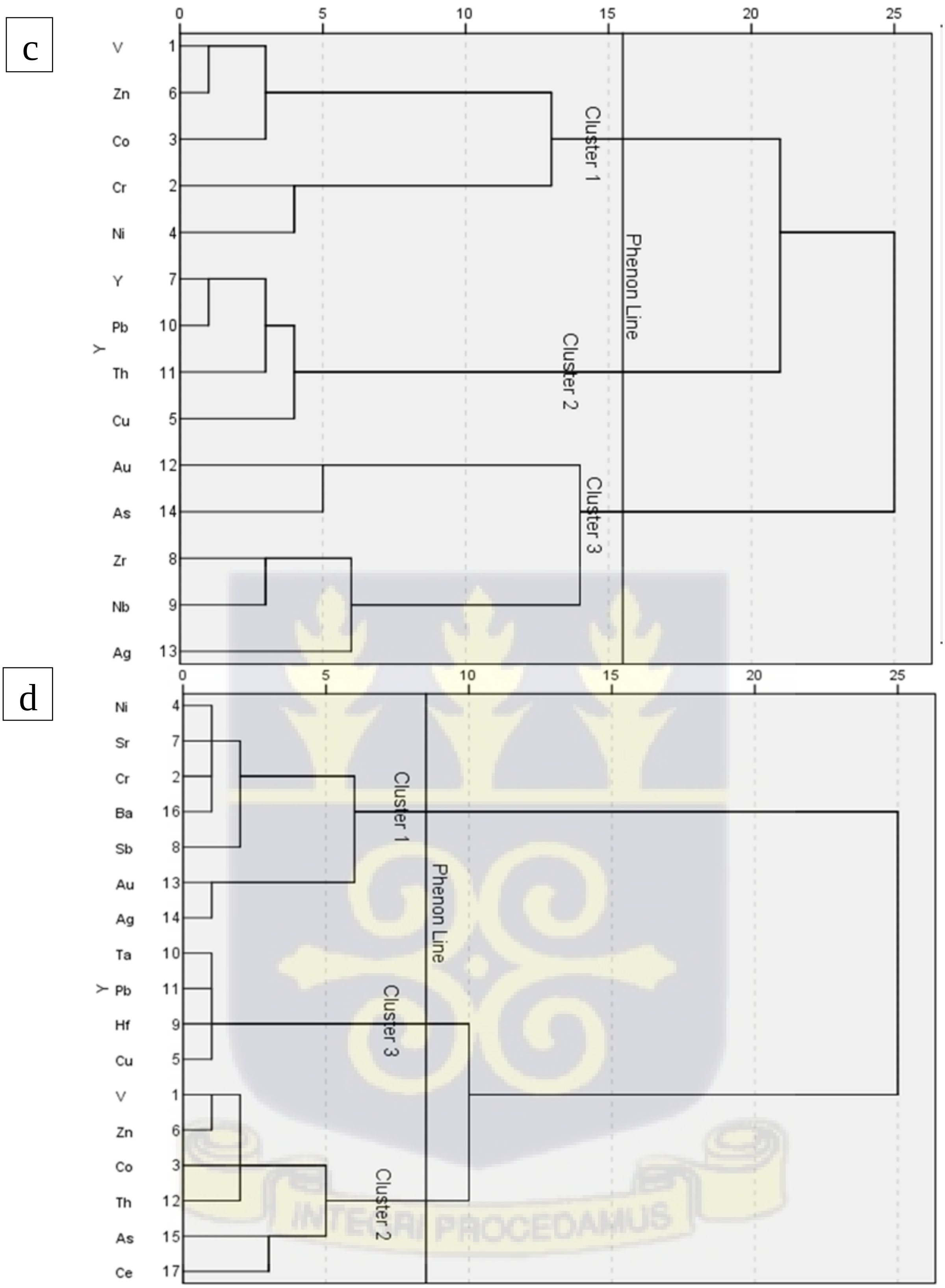

**Figure 4.53 continued: Dendrograms displaying multi-elemental clusters for the c) hanging wall and d) footwall mafic volcanic rocks.**

## 4.13 Proposed origin of the Kibi gold deposit

Inferences from the geophysical, petrographic and geochemical studies point to the fact that the Kibi gold deposit is orogenic based on the phenomenon of emplacement (Figure 54d). Previous workers (Goldfarb & Santosh, 2014; Groves & Santosh, 2016; Groves et al., 2020) used the subduction-diamond model proposed by Wyman et al. (2008) to explain orogenic gold deposits of all ages and terranes. According to the model (Figure 4.54), gold and related metals are likely to have resulted from devolatization of sedimentary rocks. However, the subduction of the oceanic plate and its overlying sedimentary rocks resulted in the irruption of hydrothermal fluid along the weak zones. Wyman et al., 2008 postulated that the presence of gold and pyrite-bearing sedimentary source rocks is a key prerequisite for the formation of orogenic gold deposits. Also, gold and related elements (Ag, As, Bi, Sb, Te and W) are sometimes released into sulphur-bearing fluid through the replacement of pyrite by pyrrhotite (Pitcairn et al., 2006; Large et al., 2009) as observed in Figure 4.54. Occasionally, the over pressured fluids enter deep-seated faults which serve as conduits for these fluids to move upwards and form orogenic gold deposits in back-arc or arc terranes in either second-order structures, veins or in highly fractured rocks. Overall, it is evident from the subduction model (Figure 4.54), that the Kibi gold deposit is orogenic and deposited in an arc or back-arc setting.

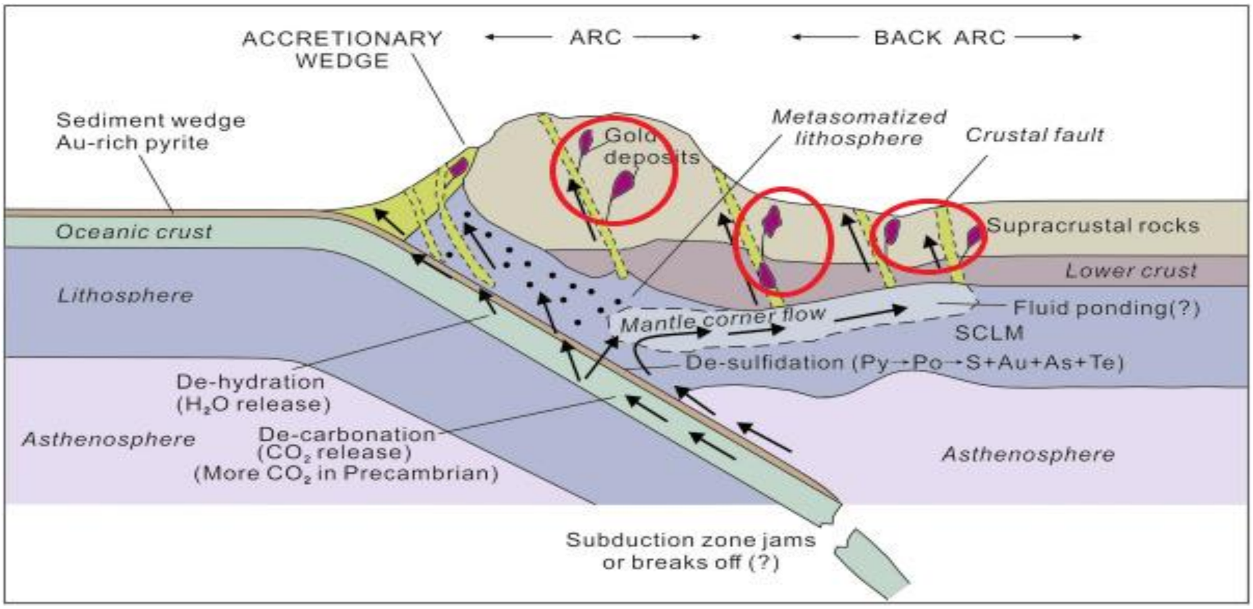

**Figure 4.54: An illustration of the subduction model for the formation of orogenic gold deposits. Red insert circles highlight environments (arc, and back arc) in which gold deposits are most common (modified after Groves et al., 2020).**

However, the individual satellite areas (Afiase (Figure 4.55a) and Ettukrom (Figure 4.55b)) are underlain by metamorphosed and highly deformed greywacke, graphitic phyllite, shale, volcanic rocks (hanging wall and footwall) and granitoids. The compositional variations in the hanging wall (Figures 4.28, 4.55a and b) and footwall (Figures 4.30 and 4.55a and b) may be due to subsequent metasomatism. Both areas show signatures of compression characterized by folds, NW- SE trending faults and shear zones. These structures (shear zone and fault) presented favorable channels for the migration of the mineralizing fluids, which interacted with the rocks thereby altering the composition of the hanging wall and depositing the gold. The fault zones are predominantly composed of sheared carbonated phyllite (Afiase area) and schist (Ettukrom area) and gold mineralization in these units is usually consistent with the brittle-ductile nature of the host rocks. The dominant sulfide types associated with the gold deposit are pyrite and chalcopyrite as observed in Figure 4.25 while the main pathfinder elements are Ag and As (Figure 4.53).

The rocks in the Gold Mountain satellite (Figure 4.55c), Adukrom – Ankomase (Figure 4.55d), Cobra Creek (Figure 4.55e) and Agyapoma (Figure 4.55f) areas are weekly folded and characterized by shear zones trending in the NE-SW direction. In the Gold Mountain and Adukrom – Ankomase satellite areas, native gold occurs within the quartz–tourmaline veins intruding the shear zones which can be attributed to a decrease in pressure, well below the hydrostatic fluid pressure level which was adequate to induce gold precipitation by negligible pH changes (Craw 2013). Generally, the most significant geological structures that control gold mineralization in the study area are faults and share zones, near and within which orebodies are located. Identifying such structures should therefore be the highest priority in the search for gold in the Kibi area. Occasionally, lustrous graphitic materials also serve as markers of mineralized zones. According to Dzigbodi-Adjlmah (1993), these structural features are consistent with the mineralization within the Birimian terrain.

Gold mineralization in the study area is largely constrained by the hangingwall mafic volcanic rock and marked by extensive hydrothermal alteration, which includes carbonate, quartz, schist, pyrite, chlorite, and sericite in varying amounts. From the schematic diagrams (Figure 4.55) the main gold mineralization style in the study area is the shear zone hosted hydrothermal type, specifically, the quartz-carbonate bearing vein and disseminated sulphur types in the metasedimentary rocks with quartz veins or as disseminated in wall rocks without quartz veins.

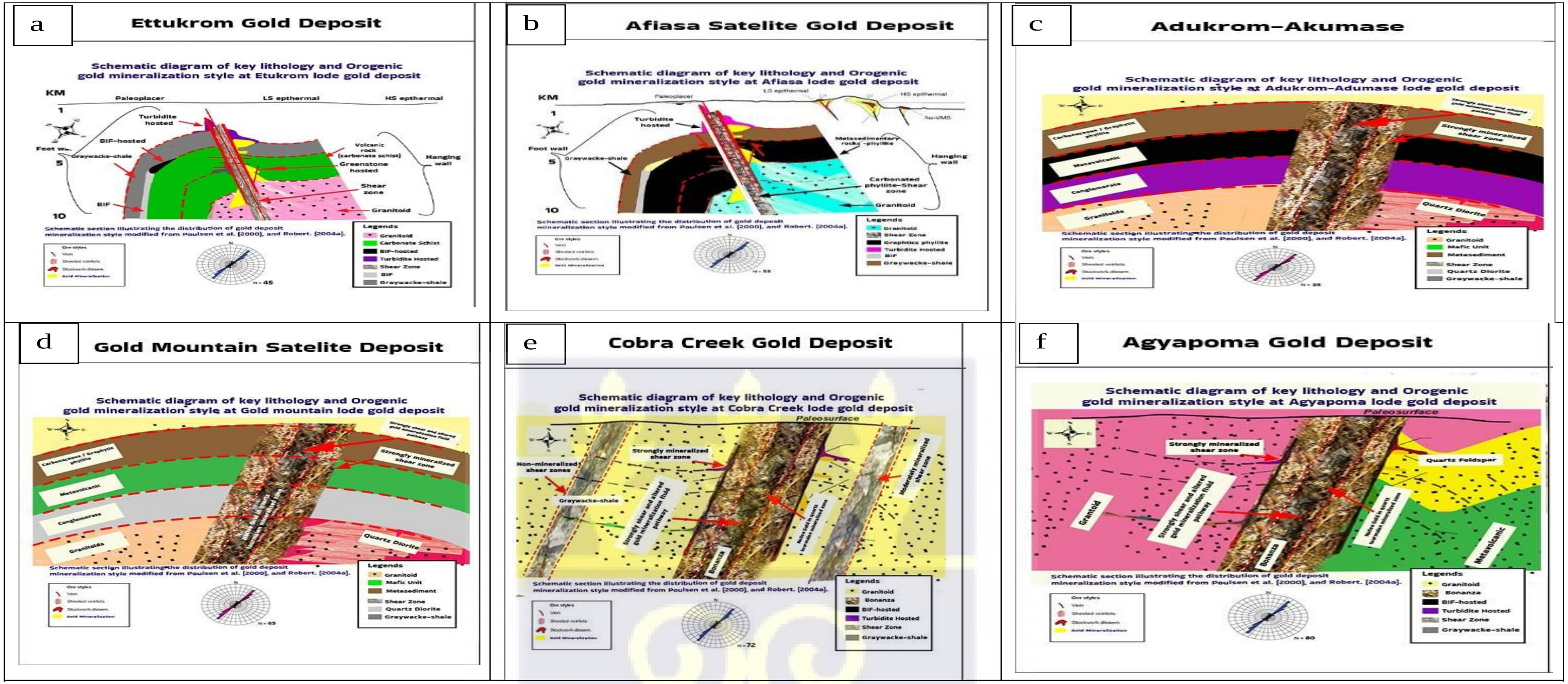

**Figure 4.55: Schematic diagram of key lithologic and orogenic gold mineralization styles occurring within the Kibi area: a) Afiasa b)Gold mountains c) Adukrom –Segyemase d) Cobra Creek e) Agyapoma and f)Ettukrom.**

## 4.14 Exploration guide for the Kibi gold zone based on litho-structural and geochemical characteristics.

In the study area, Au mineralization is observed on major regional faults and shear zones (Figure 4.1). This northeast-southwest trending faults of F2 isoclinal fold plunges are deceptive, considering that their limbs are largely shear-bounded. This could be observed in Kibi, Pano, Asiakwa, Agyapoma, Ettukrom, Osino and Ankaase communities. Similarly, other major faults are present at Cobra creek (Habitat) and Ajomoku. These shear zones indicate that isoclinal folds in the study area may have been kinematically rotated against D2 shear planes/zones. For this thesis, major D2 shear zones are largely delineated by the interpretation of geophysical data (Figure 4.1), as well as major surface lithological or structural trends and patterns relating to discontinuities that were encountered during the field mapping exercise. Gold mineralization within the Ettukrom, Agyapoma and Cobra creek are well-defined on a NE - SW major regional shear zone (Figures 4.55) that are constrained to a fluid pathway serving as a conduit for gold mineralization (Figures 4.6a and b). Subsequent gold mineralization controls include northeast-trending D2 features. These are predominantly hosted in the hanging wall mafic volcanic rocks (ie. basaltic to alkali basalt), greywackes and sills/dykes, which are juxtaposed against a metasedimentary contact at Etukrom and Agyapoma respectively. Local-scale structural controls for auriferous mineralization can be characterized as;

- 1st - Order: regional-scale tight to isoclinal fold hinges.
- 2nd - Order: isoclinal fold and anticlinal hinges that are parallel to D1/S1 foliation and S0 bedding.

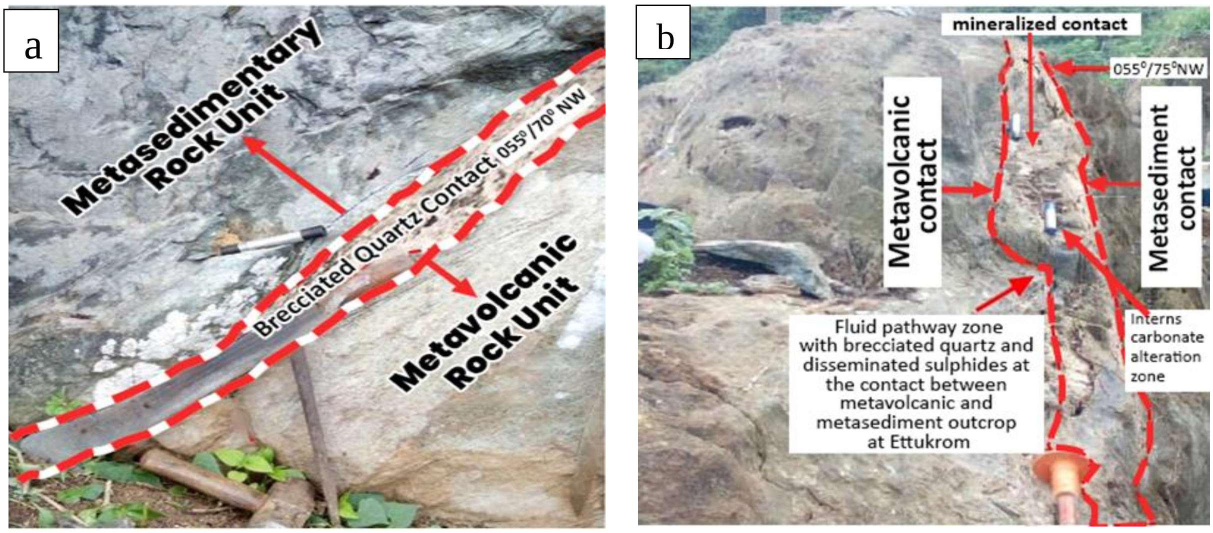

**Figure 4.56: a) Shear zone resulting in brecciated of quartz vein sandwiched between metasedimentary rock unit and metasedimentary rock unit at Ettukrom b) fluid pathway in metavolcanic hanging wall outcrop at Ettukrom gold zone.**

Generally, the study area is underlain by schist (carbonate chlorite schist, quartz-carbonate schist and mylonitized quartz chlorite schist), greywacke, volcaniclastic rock (andesite), hanging and footwall mafic volcanic rocks (basaltic to alkali basalt) which have undergone several deformation and alteration phases involving shearing, fracturing, folding and faulting. The sulfide minerals within the schist occur as amorphous isolated grains and occasionally as aggregates in preferred oriented and within alteration zones. The greywacke is feldspathic (mainly sodic plagioclase) and contains two types of sulphides (pyrite and chalcopyrite). Gold in the greywacke is associated with fractures and pyrite, which occasionally occurs as phenoblast. The greywackes are compositionally immature with minimum recycling, made up of detritus that originated from mafic to intermediate igneous rocks that underwent incipient alteration. The sediments were deposited in a continental rift margin within the island arc or continental field.

Occasionally, the volcaniclastic rock has quartz-carbonate veinlets and contains visible disseminated sulphides. Ankerite in the rock occurs mostly in quartz-albite laminations. Deformed pyrite is the predominant sulfide with occasionally observed replacing magnetite.

Sparse fine-grained chalcopyrite is disseminated in the sample. Gold is found in fractures and is associated with both pyrrhotite and gold. Pyrrhotite was likely part of the fluid that deposited the gold. Geochemically the volcaniclastic rock classifies as andesitic tuff with tholeiitic affinity formed through fractional crystallization in an arc environment within a subduction zone.

Gold grains in the mafic volcanic hanging wall are observed filling fractures in pyrites and sometimes occluded in the pyrite porphyroblast. Occasionally gold grains are also in contact with chalcopyrite and sometimes sphalerite in cavities. Free gold is also observed very close to subhedral fractured and corroded pyrite. The hanging wall volcanic rock is classified as basaltic to alkali basalt with calc alkali composition, metaluminous to slightly peralkaline and exhibits characteristics of volcanic island arc-related lavas associated with subduction zones. The footwall mafic volcanic rock (basalt) contains minor ankeritic, calcitic carbonates, and fractured pyrite with chalcopyrite inclusions in its fragments. Chalcopyrite is the predominant sulfide occurring as anhedral grains with corroded edges. The foot wall mafic volcanic rock is metaluminous, exhibits tholeiitic and volcanic arc-related signatures which are associated with subduction zones.

According to this study, gold mineralization in the Kibi area is mainly trapped within major regional faults and shear zones hosted by the hanging wall mafic volcanic rocks (alkali basalt) (av. 11.04 ppm) and greywackes (av. 2.33 ppm). The host rock alteration, structural control, ore paragenesis, mineral, gangue mineralogy and the arc and back-arc signatures suggest an orogenic metamorphic (transitional mesothermal-epithermal) gold-type mineralization in the Kibi Gold Zone.

## 4. 15 Validation of research findings

An integrated approach as used by this research study involving geophysical, structural, petrographic, ore mineralogy and geochemistry provides a stepwise approach to understanding the geology and ore mineralogy of the previously ill-defined Kibi orogenic gold deposit and outlines the best way for exploration and exploitation. The findings of this research have redefined the previously misleading exploration targets in the Kibi gold zone. Before this study, areas with high-grade gold mineralization were defined as low grade and vice versa (eg. an area with a gold concentration of 9.6g/t occurring at the NW margin of the Kibi area was classified as low grade while 2.56g/t was classified as high grade (Figure 4.57)). A significant financial loss would have resulted from this misclassification. This study has reclassified appropriately the mineral exploration targets in the Kibi gold zone. Hence the findings of this study can serve as guidelines for future exploration work in similar geologic environments.

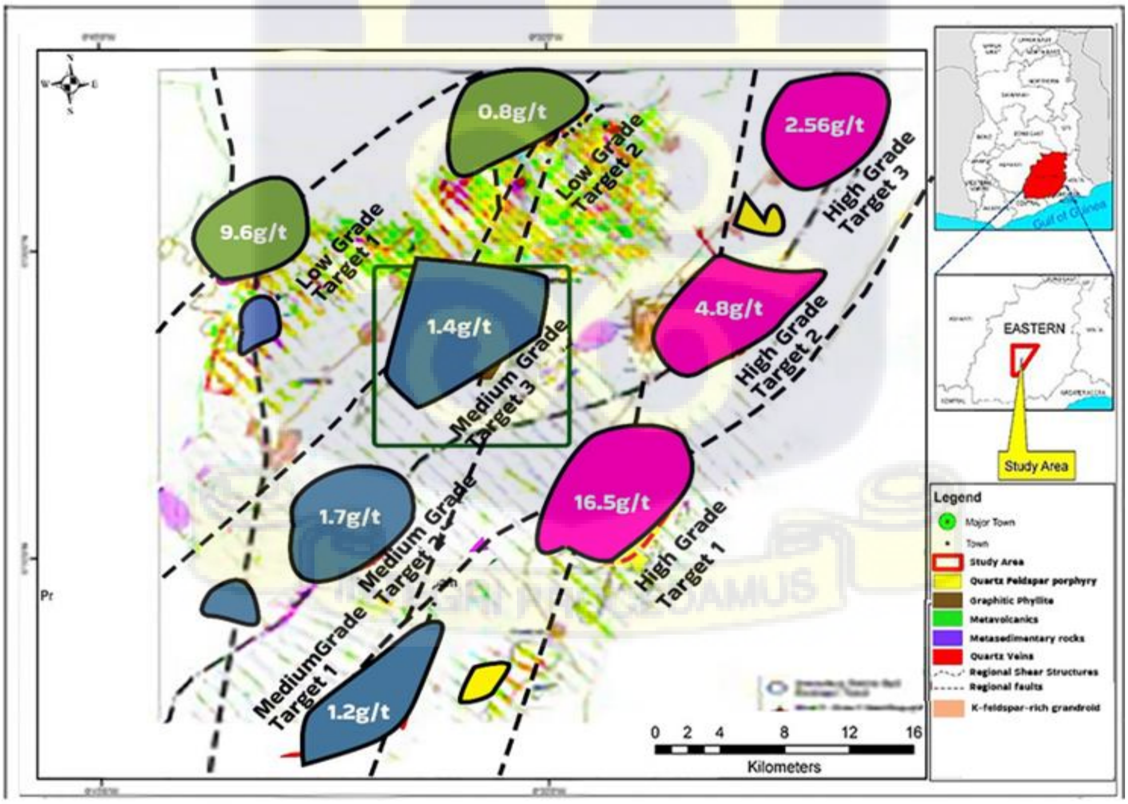

**Figure 4.57: Misclassified lode gold exploration target map for the Kibi area**

## 4.16 Addition to knowledge

This project has been able to uncover the gold mineralization trends and patterns within the Kibi gold zone using an integrated approach (airborne and ground geophysics, field mapping and sampling, structural mapping, petrography and geochemistry) and established appropriate guidelines for future exploration and exploitation in the study area and beyond (similar geologic terrains).

# CHAPTER FIVE

# CONCLUSION AND RECOMMENDATIONS

## 5.1. Conclusion

Based on the geophysical (aeromagnetic and ground geophysical), geological field mapping, petrographical and geochemical datasets gathered from the Kibi area, the following conclusions have been made:

i. The geological structures present in the Kibi area are lineations, foliations, folds, fractures/joints, faults, shear zones and quartz veins. These structures represent at least three major deformation events, namely D1, D2 and D3, The D1 compressional deformation resulted in NNW-SSE oriented sub-horizontal foliations and stretching lineations, as well as, E-W trending tight-isoclinal recumbent folds are observed in Ettukrom, Effiasa and Kibi artisanal lode gold pits. The NW-SE faulty contacts that truncate the Volltain and Birimian rock units on the northeast portions of the study area in a component of the D1 tectonic event. The D2 compressional event created regionally and locally oriented dextral shear zones trending NE-SW, as well as, NE-SW trending asymmetric to upright open folds. Gold mineralization is associated with D2 structures. The faults, quartz veins, shears zones and sampled from the D2 structures in the Tarkwain rock units and contacts recorded higher gold mineralization values. The third produced NS striking fracturing that post-date ductile deformation as observed in Akrofufu, Takyiman, Kwabeng and Bomso.

ii. The Kibi gold district is underlain by schist, sodic greywacke, andesitic tuff (volcaniclastic rock) and basaltic to alkali basalt (hanging and footwall mafic volcanic rocks) which have undergone several deformation phases involving shearing, fracturing, folding and faulting resulting in the mineral alteration and metasomatism.

iii. Hydrothermal alteration along quartz-carbonate veins varies greatly, but in densely veined alkali basalt hanging wall stockworks, the assemblage exhibits moderate to strong silicification, sulphidization, carbonatization, albitization, and sericitization. This is also linked to dispersed pyrrhotite, pyrite, and arsenopyrite (+/- sphalerite) as well as patchy to ubiquitous sulphidization.

iv. The Kibi gold zone gold deposit is an orogenic type deposit occurring along the margins of converging plates within compressional secondary structures that cut across lithologies of all artisanal satellite lode gold deposits being exploited.

v. The mineralization is both hosted, as quartz-bearing veins and disseminations in the metasedimentary rocks with quartz veins or as disseminated in wall rocks without quartz veins. The mineralization is characterized by ore mineral assemblage, which consists of pyrite, chalcopyrite, magnetite in veins; magnetite, tourmaline and micron-sized sulphides in metasedimentary rocks.

vi. Other ore minerals include chalcopyrite, chalcocite, covellite, pyrite, tetrahedrite, tennantite and subordinately pyrrhotite, and pyrite-polymetallic associations. Gangue minerals comprise quartz, muscovite, sericite, and chlorite in veins; quartz, muscovite, sericite, chlorite, and accessory minerals (rutile, titanium, apatite and epidote), in the metasedimentary rocks; quartz, ankerite, calcite, chlorite, albite, epidote, hornblende in the amphibolite.

vii. Pyrite is main the pathfinder for gold even though, chalcopyrite, sphalerite, rutile, haematite, magnetite, pyrrhotite and molybdenite good indicators. Meanwhile, the main pathfinder elements for gold in the Kibi area are Ag and As.

viii. In terms of paragenesis, Chalcopyrite occurs in the first (1) and second (2) generations and partly overlaps the third generation. Rutile and haematite exist in both 1 and 2 generations. Sphalerite and magnetite are associated with generation 1. Gold only occurs in the 2 generation and is associated with 2 generation pyrite which is fractured and has sieve textures.

ix. These mineralizing fluids were transported upwards from deep regions and channeled along regional NE-trending shear zones and faults. Gold is supposed to be transported as sulphides species at oxidation states by near-neutral fluids during the retrograde metamorphism period in metasedimentary rocks. It was transported both as chloride and sulphide complexes in amphibolite during the prograde and retrograde metamorphic period, respectively, suggesting two phases of mineralization in these rocks. Fluid interaction was the possible mechanism for the precipitation of gold in the Kibi Gold district.

x. The host rock alteration, structural control, ore paragenesis, and mineral and gangue mineralogy suggested an orogenic metamorphic (transitional mesothermal-epithermal) gold-type mineralization in the Kibi Gold Zone.

This study has proposed prospecting guides to circumscribe the primary gold deposit and reclassified the gold exploration targets within the Kibi gold zone using an integrated approach.

## 5.2 Recommendations

Mapping out the continuity of the extensive graphitic faults and fissure zones will serve as a guide in finding more deposits along the southeastern margin of the Kibi-Winneba volcanic belt. To better understand the genesis of the Kibi gold zone gold deposit, the following are recommended.

i. $\partial^{13}C$ isotope study should be done to determine whether the elemental C is from an abiogenic or a magmatogenic source.

ii. Absolute ages for the two volcanic rock units should be determined to compare their relative ages.

iii. A fluid inclusion study should be done to get a fair idea about the chemistry of the fluid that deposited the gold as well as the pH-Eh state.

## REFERENCES

Abdelsalam, M. G., & Stern, R. J. (1999). Mineral exploration with satellite remote sensing imagery: Examples from the Neoproterozoic Arabian-Nubian Shield. *Journal of African Earth Sciences*, *28*(4), 1.

Abdel-Hakeem, M., El-Tahir, M., Zeid, E. A., & Rageh, H. (2023). Genetic implications of Th/U, Th/K, and U/K ratios for U mineralizations: A case study from El-Missikat and El-Erediya shear zones, Eastern Desert, Egypt. *Geochemical Transactions*, *24*(1), 3.

Abouchami, W., Boher, M., Michard, A., &Albarede, F. (1990). A major 2.1 Ga event of mafic magmatism in West Africa: an early stage of crustal accretion. *Journal of Geophysical Research: Solid Earth*, *95*(B11), 17605-17629.

Abuakwa South Municipality Assembly (2018) District medium-term development plan 2018–2021. Abuakwa South Municipality (Unpublished)

Adadey, K., Clarke, B., Théveniaut, H., Urien, P., Delor, C., Roig, J.Y., Feybesse, J.L., 2009,

Addo-Fening, R. (2013). Ghana under colonial rule: An outline of the early period and the interwar years. *Transactions of the Historical Society of Ghana*, (15), 39-70.

Ademila, O., Okpoli, C. C., &Ehinmitan, D. (2019). Geological and lithological mapping of part of Igarra schist belt using integrated geophysical methods. *Earth Sciences Pakistan*, *3*, 01-09.

Adewumi, T., & Salako, K. A. (2018). Delineation of mineral potential zone using high resolution aeromagnetic data over part of Nasarawa State, North Central, Nigeria. *Egyptian Journal of petroleum*, *27*(4), 759-767.

Adjlmah, C L, 1988 Petrological studies on the genesis of the gold deposits of Prestea, Ghana Unpubl Dr rer nat Dissertation Technlsche Unlversltat Berlin, 274 pp

Affaton, P., Aguirre, L., & Ménot, R. P. (1997). Thermal and geodynamic setting of the Buem volcanic rocks near Tiélé, Northwest Bénin, West Africa. *Precambrian Research*, *82*(3-4), 191-209.

Affaton, P., 1990. Le basin des Volta (Afrique de l'ouest): une marge passive d'gtge protrozoique suprieur tectonisre au Panafricain (600 + 50 Ma). Edition de I'OSTROM, Collection Etudes et Theses, Paris.

Affaton, P., Lasserre, J. L., Lawson, L. T. et Vincent, P. L. (1978). Notice explicative des cartes geologiques au 1/200000 de la Republique du Togo et de la R6publique du Benin entre les 9e et 10e degr6 de latitude Nord {feuille Bassari-Djougou et feuille Parakou-Nlkki). Rapport B. R. G. M. N°.78 R. D. M. 055AF, Orleans, Fr.,70 p., 2 cartes, 2 annexes, ined.

Affaton, P., Rahaman, M. A., Trompette, R., & Sougy, J. (1991). The Dahomeyide Orogen: tectonothermal evolution and relationships with the Volta Basin. In *The West African orogens and circum-Atlantic correlatives* (pp. 107-122). Berlin, Heidelberg: Springer Berlin Heidelberg.

Agbossoumondé, Y., Ménot, R. P., Paquette, J. L., Guillot, S., Yéssoufou, S., &Perrache, C. (2007). Petrological and geochronological constraints on the origin of the Palimé–Amlamé granitoids (South Togo, West Africa): A segment of the West African Craton Paleoproterozoic margin reactivated during the Pan-African collision. *Gondwana Research*, *12*(4), 476-488.

Agra, N. A., Kwayisi, D., Amponsah, P. O., Dampare, S. B., Asiedu, D & Nude, P. M. (2017). Petrogenetic Evolution of the Eastern Buem Volcanic Rocks, South-Eastern Ghana. *Science and Development*, 1(2)31- 49.

Agyemang, R. N. K., Gordon Foli, P., Gawu, S. K., & Nude, P. M. (2019). Evaluation of Placer Deposits in Ghana: A Case Study of the Kwabeng Placer Gold Deposit North Western Flank of Atewa Range, Eastern Region, Ghana. *Evaluation*, *8*(11).

Ahafo Mineral Resource and Ore Reserve Report (2006). Newmont Ghana Gold Limited, Ahafo Project.

Aidoo, F., Zhang, Q-Q., Zhang, A-B., Nude, P. M. (2022): Identification of UHT granulites in the Pan-African Dahomeyide suture zone in SE Ghana: Implications for evolution of collisional orogens, Journal of Petrology, 2022; 63:1-33, https://doi.org/10.1093/petrology/egac042

Aidoo, F., Nude, P. M., Sun, F.-Y., Liang, T., & Zhang, S-B, (2021). Paleoproterozoic TTG-like metagranites from the Dahomeyide Belt, Ghana: Constraints on the evolution of the Birimian-Eburnean Orogeny, Precambrian Research 353 (2021) 106024. Doi https://doi.org/10.1016/j.precamres.2020.106024.

Aidoo, F., Suna, F-Y., Lianga, T., & Nude, P. M. (2020). New insight into the Dahomeyide Belt of southeastern Ghana, West Africa: Evidence of arc-continental collision and Neoarchaean crustal reworking, Precambrian Research, 347: 105836.

Allibone, A., & Wysoczanski, R. (2002). Initiation of magmatism during the Cambrian–Ordovician Ross orogeny in southern Victoria Land, Antarctica. *Geological Society of America Bulletin*, *114*(8), 1007-1018.

Allibone, A. H., Jongens, R., Turnbull, I. M., Milan, L. A., Daczko, N. R., DePaoli, M. C. & Tulloch, A. J. (2009). Plutonic rocks of Western Fiordland, New Zealand: Field relations, geochemistry, correlation, and nomenclature. *New Zealand Journal of Geology and Geophysics*, *52*(4), 379-415.

Amer, R., Kusky, T., & El Mezayen, A. (2012). Remote sensing detection of gold related alteration zones in Um Rus area, Central Eastern Desert of Egypt. *Advances in Space Research*, *49*(1), 121-134.

Amponsah, P. O., Salvi, S., Béziat, D., Siebenaller, L., Baratoux, L., & Jessell, M. W. (2015). Geology and geochemistry of the shear-hosted Julie gold deposit, NW Ghana. *Journal of African Earth Sciences*, *112*, 505-523.

Amponsah, P. O., Salvi, S., Didier, B., Baratoux, L., Siebenaller, L., Jessell, M., & Gyawu, E. A. (2016). Multistage gold mineralization in the Wa-Lawra greenstone belt, NW Ghana: The Bepkong deposit. *Journal of African Earth Sciences*, *120*, 220-237.

Armstrong-Altrin, J. S., Ramos-Vázquez, M. A., Zavala-León, A. C., & Montiel-García, P. C. (2018). Provenance discrimination between Atasta and Alvarado beach sands, western Gulf of Mexico, Mexico: Constraints from detrital zircon chemistry and U–Pb geochronology. *Geological Journal*, *53*(6), 2824-2848.

Anani, C. Y., Bonsu, S., Kwayisi, D., & Asiedu, D. K. (2019). Geochemistry and provenance of Neoproterozoic metasedimentary rocks from the Togo structural unit, Southeastern Ghana. *Journal of African Earth Sciences*, *153*, 208-218.

Anum, S., Sakyi, P.A., Su, B.-X., Nude, P.M., Nyame, F., Asiedu, D., *Kwayisi, D*. (2015). Geochemistry and geochronology of granitoids in the Kibi-Asamankese area, south of the Kibi-Winneba volcanic belt of Ghana. *Journal of African Earth Sciences*,102: 166-179.

Appiah, H., Norman, D. I., & Boadi, I. (1991). The geology of the Prestea and Ashanti goldfields: A comparative study. In *Symposium Brazil Gold'91* (pp. 247-255).

Arhin, E., Jenkin, G. R. T., Cunningham, D., & Nude, P. (2015). Regolith mapping of deeply weathered terrain in savannah regions of the Birimian Lawra greenstone belt, Ghana. *Journal of Geochemical Exploration*. 159: 194-207.

Asiedu, D. K., Agoe, M., Amponsah, P. O., Nude, P. M., &Anani, C. Y. (2019). Geochemical constraints on provenance and source area weathering of metasedimentary rocks from the Paleoproterozoic (~ 2.1 Ga) Wa-Lawra Belt, southeastern margin of the West African Craton. *Geodinamica Acta*, *31*(1), 27-39.

Asiedu, D. K., Atta-Peters, D., & Peprah, R. (2000). Depositional environment of the Takoradi Sandstone formation of the Sekondian Group, western Ghana, as revealed by textural analysis. *Ghana Mining Journal*, *6*, 53-58.

Attoh, K., Samson, S., Agbossoumondé, Y., Nude, P. M., Morgan, J. (2013). Geochemical characteristics and U-Pb zircon LA-ICPMS ages of granitoids from the Pan-African Dahomeyide orogen, West Africa. *Journal of African Earth Sciences*, 79: 1-9.

Attoh, K., Corfu, F. & Nude, P. M. (2007). U-Pb zircon age of deformed carbonatite and alkaline rocks in the Pan-African Dahomeyide suture zone, West Africa. *Precambrian Research*, 155: 251-260.

Attoh, K. (1998). High-pressure granulite facies metamorphism in the Pan-African Dahomeyide orogen, West Africa. *The Journal of geology*, *106*(2), 236-246.

Attoh, K., & Nude, P. M. (2008). Tectonic significance of carbonatite and ultrahigh-pressure rocks in the Pan-African Dahomeyide suture zone, southeastern Ghana. *Geological Society, London, Special Publications*, *297*(1), 217-231.

Attoh, K., Dallmeyer, R. D., &Affaton, P. (1997). Chronology of nappe assembly in the Pan-African Dahomeyide orogen, West Africa: evidence from 40Ar39Ar mineral ages. *Precambrian research*, *82*(1-2), 153-171

Attoh, K., Evans, M. J., & Bickford, M. E. (2006). Geochemistry of an ultramafic-rodingite rock association in the Paleoproterozoic Dixcove greenstone belt, southwestern Ghana. *Journal of African Earth Sciences*, *45*(3), 333-346.

Aryee, B. N. (2001). Ghana's mining sector: its contribution to the national economy. *Resources Policy*, *27*(2), 61-75.

Barenblitt, A., Payton, A., Lagomasino, D., Fatoyinbo, L., Asare, K., Aidoo, K., ... & Wood, D. (2021). The large footprint of small-scale artisanal gold mining in Ghana. *Science of the Total Environment*, *781*, 146644.

Basu, A., Young, S., Sutner, L., James, W. and Mack, G.H. (1975). Re-evaluation of the use of undulatory extinction and crystallinity in detrital quartz for provenance interpretation, Journal of Sedimentary Petrology, 45, pp. 873-882.

Berge, J. (2011). Paleoproterozoic, turbidite-hosted, gold deposits of the Ashanti gold belt (Ghana, West Africa): Comparative analysis of turbidite-hosted gold deposits and an updated genetic model. *Ore Geology Reviews*, *39*(1-2), 91-100.

Bertrand-Sarfati, J., Moussine-Pouchkine, A., Affaton, P., Trompette, R., & Bellion, Y. (1991). Cover sequences of the West African craton. In *The West African orogens and circum-Atlantic correlatives* (pp. 65-82). Berlin, Heidelberg: Springer Berlin Heidelberg.

Bessoles, B., &Trompette, R. (1980). Geologie De L'afrique, La Chaine Panafricaine" Zone Mobile D'afrique Centrale (Partie Sud) Et Zone Mobile Soudanaise".

Béziat, D., Bourges, F., Debat, P., Lompo, M., Martin, F., & Tollon, F. (2000). A Paleoproterozoic ultramafic-mafic assemblage and associated volcanic rocks of the Boromo greenstone belt: fractionates originating from island-arc volcanic activity in the West African craton. *Precambrian Research*, *101*(1), 25-47.

Bhatia, M.R. and Crook, K.A.W. (1986). Trace element characteristics of and tectonic setting discrimination of sedimentary basins. Contrib. Mineral. Petrol. 92, 181–193.

Binley, A., & Kemna, A. (2005). DC resistivity and induced polarization methods. In *Hydrogeophysics* (pp. 129-156). Dordrecht: Springer Netherlands.

Black, R., & Liégeois, J. P. (1993). Cratons, mobile belts, alkaline rocks and continental lithospheric mantle: the Pan-African testimony. *Journal of the Geological Society*, *150*(1), 89-98.

Blair, T. C., & McPherson, J. G. (1994). Alluvial fans and their natural distinction from rivers based on morphology, hydraulic processes, sedimentary processes, and facies assemblages. *Journal of sedimentary research*, *64*(3a), 450-489.

Boadi, B., Raju, P. S., & Wemegah, D. D. (2022). Analysing multi-index overlay and fuzzy logic models for lode-gold prospectivity mapping in the Ahafo gold district–Southwestern Ghana. *Ore Geology Reviews*, 105059.

Boateng, Daniel & Adabanija, Moruffdeen & Osei Jnr, Edward & Ntori, Clement & Student, Msc & Student,. (2019). Hydrothermal Alteration Mapping, Using the Crosta Technique: Case Study of the Kibi Goldfields Osino Concession, Ghana. International Journal of Engineering Science. 8. 19507.

Bouguettaya, A., Yu, Q., Liu, X., Zhou, X., & Song, A. (2015). Efficient agglomerative hierarchical clustering. *Expert Systems with Applications*, *42*(5), 2785-2797.

Bowell, R. J. (1992). Supergene gold mineralogy at Ashanti, Ghana: Implications for the supergene behaviour of gold. *Mineralogical Magazine*, *56*(385), 545-560.

Brako, B. A., Amadu, C. C., Foli, G., Nude, P. M., & Gawu, S. K. (2022). Petrography and geochemistry of metasedimentary rocks from the Paleoproterozoic Birimian at the Chagupana area, North-West Ghana: implications for provenance and tectonic setting. *Arabian Journal of Geosciences*, *15*(24), 1749.

Boggs, S. (2009). *Petrology of sedimentary rocks*. Cambridge university press.

Briggs, I. C. (1974). Machine contouring using minimum curvature. *Geophysics*, *39*(1), 39-48.

Cabanis, B., & Lecolle, M. (1989). The La/10-Y/15-Nb/8 diagram: a tool for discriminating volcanic series and highlighting the mixing and/or crustal contamination processes. In *Reports From the Academy of Sciences. Series 2, Mechanics, Physics, Chemistry, Universe Sciences, Earth Sciences* (Vol. 309, pp. 2023-2029).

Caby, R. (1987). The Pan-African belt of West Africa from the Sahara desert to the Gulf of Benin. *Anatomy of mountain ranges*, *1*, 129-170.

Cahen, L., Snelling, N.J., Delhal, J. van Vail, J.R., 1984. The Geochronology and Evolution of Africa. Clarendon, Ox-ford, 581 pp

Castaing, C., Triboulet, C., Feybesse, J. L., &Chevremont, P. (1993). Tectonometamorphic evolution of Ghana, Togo and Benin in the light of the Pan-African/Brasiliano orogeny. *Tectonophysics*, *218*(4), 323-342.

Chappell, B. W., & White, A. J. (2001). Two contrasting granite types: 25 years later. *Australian journal of earth sciences*, *48*(4), 489-499.

Chu, M.F., Wang, K.L., Griffin, W. L., Chung, S.L., O'Reilly, S. Y., Pearson, N. J. (2009). Apatite Composition: Tracing Petrogenetic Processes in Transhimalayan Granitoids. J. Petrol. 50 (10), 1829–1855. doi:10.1093/petrology/egp054

Clauer, N., Caby, R., Jeannette, D., &Trompette, R. (1982). Geochronology of sedimentary and metasedimentary Precambrian rocks of the West African craton. *Precambrian Research*, *18*(1-2), 53-71.

Combes, V., Eglinger, A., André-Mayer, A. S., Teitler, Y., Jessell, M., Zeh, A., & Gibert, P. (2022). Integrated geological-geophysical investigation of gold-hosting Rhyacian intrusions (Yaou, French Guiana), from deposit-to district-scale. *Journal of South American Earth Sciences*, *114*, 103708.

Condie, K. C. (1990). Growth and accretion of continental crust: inferences based on Laurentia. *Chemical Geology*, *83*(3-4), 183-194.

Cooper, W. G. G., (1934), "The Geology of the Prestea Goldfleld". *Gold Coast Geological Survey, Memoir*. 3 46 pp.

Cox K.G, Bell J.D & Pankhurst RJ . (1979). Compositional variation in magmas. In: The Interpretation of Igneous Rocks. Springer, Dordrecht, Netherlands, 455 p. DOI: https://doi.org/10.1007/978-94-017-3373-1_2

Cox, R. and Lowe, D.R. (1995). Compositional evaluation of coarse elastic sediments in the South Western United States from 1.8 to 0.2 G.A. and implications for relationships between the development of crustal blocks and their sedimentary cover; J. Sedim. Res. 65A, pp.477-494.

Cullers, R. L. (2000). The geochemistry of shales, siltstones and sandstones of Pennsylvanian–Permian age, Colorado, USA: implications for provenance and metamorphic studies. *Lithos*, *51*(3), 181-203.

Cullers, R.L. (1988). Mineralogical and chemical changes of soil and stream sediment formed by intense weathering of the Danberg granites, Georgia, U.S.A. Lithos 21, pp. 301-314.

Cullers, R. L., & Podkovyrov, V. N. (2000). Geochemistry of the Mesoproterozoic Lakhanda shales in southeastern Yakutia, Russia: implications for mineralogical and provenance control, and recycling. *Precambrian Research, 104*(1-2), 77-93.

Craw, D. (2013). River drainage reorientation during placer gold accumulation, southern New Zealand. *Mineralium Deposita*, *48*, 841-860.

Dampare, S. B., Shibata, T., Asiedu, D. K., Osae, S., &Banoeng-Yakubo, B. (2008). Geochemistry of Paleoproterozoic metavolcanic rocks from the southern Ashanti volcanic belt, Ghana: Petrogenetic and tectonic setting implications. *Precambrian Research*, *162*(3-4), 403-423.

Davis, W. J., Fryers, B. J., & King, J. E. (1994). Geochemistry and evolution of late Archean plutonism and its significance to the tectonic development of the Slave craton. *Precambrian Research*, *67*(3-4), 207-241.

Debon, F., & Le Fort, P. (1983). A chemical–mineralogical classification of common plutonic rocks and associations. *Earth and Environmental Science Transactions of the Royal Society of Edinburgh*, *73*(3), 135-149.

Deksissa, D. J., &Koeberl, C. (2004). Geochemistry, alteration, and genesis of gold mineralization in the Okote area, southern Ethiopia. *Geochemical journal*, *38*(4), 307-331.

deGroot-Hedlin, C., & Constable, S. (1990). Occam's inversion to generate smooth, two-dimensional models from magnetotelluric data. *Geophysics*, *55*(12), 1613-1624.

Delaney, T. A., & Fletcher, W. K. (1999). Efficiency of cyanidation in gold exploration using soils. *Journal of Geochemical Exploration*, *66*(1-2), 229-239.

Dia, A., Van Schmus, W. R., & Kröner, A. (1997). Isotopic constraints on the age and formation of a Palaeoproterozoic volcanic arc complex in the Kedougou Inlier, eastern Senegal, West Africa. *Journal of African Earth Sciences*, *24*(3), 197-213.

Dickson, B. L., & Scott, K. M. (1997). Interpretation of aerial gamma-ray surveys-adding the geochemical factors. *AGSO Journal of Australian Geology and Geophysics*, *17*(2), 187-200.

Direen, N. G., Lyons, P., Korsch, R. J., & Glen, R. A. (2001). Integrated geophysical appraisal of crustal architecture in the eastern Lachlan Orogen. *Exploration Geophysics*, *32*(4), 252-262.

Dzigbodi-Adjimah, K. (1993). Geology and geochemical patterns of the Birimian gold deposits, Ghana, West Africa. *Journal of geochemical exploration*, *47*(1-3), 305-320.

Echague, J., Leão-Santos, M., Melo, R., Mendes, T., & Borges, W. (2024). Application of Geophysical Methods in the Identification of Mineralized Structures and Ranking of

Areas for Drilling as Exemplified by Alto Guaporé Orogenic Gold Province. *Minerals*, *14*(8), 788.

Eisenlohr, B. N., &Hirdes, W. (1992). The structural development of the early Proterozoic Birimian and Tarkwaian rocks of southwest Ghana, West Africa. *Journal of African Earth Sciences (and the Middle East)*, *14*(3), 313-325.

Eldosouky, A. M., El-Qassas, R. A., Pour, A. B., Mohamed, H., &Sekandari, M. (2021). Integration of ASTER satellite imagery and 3D inversion of aeromagnetic data for deep mineral exploration. *Advances in Space Research*, *68*(9), 3641-3662.

Eluwa, N. N., Opara, A. I., Okereke, C. N., Eluwa, J. C., &Onwe, R. M. (2021). Estimation of radioelements concentration in Sokoto Basin for geothermal energy studies using airborne radiometric data. *World Journal of Advanced Research and Reviews*, *12*(1), 315-325.

Ennih, N., &Liégeois, J. P. (2008). The boundaries of the West African craton, with special reference to the basement of the Moroccan metacratonic Anti-Atlas belt. *Geological Society, London, Special Publications*, *297*(1), 1-17.

Ennih, N., &Liégeois, J. P. (2008). The boundaries of the West African craton, with special reference to the basement of the Moroccan metacratonic Anti-Atlas belt. *Geological Society, London, Special Publications*, *297*(1), 1-17.

Fedo, C.M., Nesbitt, H.W. and Young, G.M. (1995). Unraveling the effects of potassium metasomatism in sedimentary rocks and paleosols, with implications for paleoweathering conditions and provenance. Geology 23, 921–924.

Feng, R. and Kerrich, R. (1990). Geochemistry of fine-grained clastic sediments in the Archean Abitibi Greenstone Belt, Canada: Implications for Provenance and Tectonic Setting; Geochimica et Cosmochimica Acta, 54, pp. 1061-1081.

Fertl, W. H. (1983). Gamma ray spectral logging: a new evaluation frontier Part III-Measuring source rock potential. *World Oil; (United States)*, *196*(6).

Feybesse, J. L., Billa, M., Guerrot, C., Duguey, E., Lescuyer, J. L., Milesi, J. P., &Bouchot, V. (2006). The paleoproterozoic Ghanaian province: Geodynamic model and ore controls, including regional stress modeling. *Precambrian Research*, *149*(3-4), 149-196.

Fitton, J. G., James, D., Kempton, P. D., Ormerod, D. S., & Leeman, W. P. (1988). The role of lithospheric mantle in the generation of late Cenozoic basic magmas in the western United States. *Journal of Petrology*, (1), 331-349.

Florio, G. (2020). The estimation of depth to the basement under sedimentary basins from gravity data: Review of approaches and the ITRESC method, with an application to the Yucca Flat Basin (Nevada). *Surveys in Geophysics*, *41*(5), 935-961.

Foli, G., Agyemang, K., Brako, B. A., Gawu, S. K. Y., & Nude, P. M. (2020). Characterisation of alluvial gold exploration data to improve gold recovery in Ghana. *Arabian Journal of Geosciences*, *13*, 1-11.

Foss, C., (2011): Magnetic data Enhancement and Depth Estimation. (H. Gupta, Ed.) Encyclopedia of Earth Sciences Series, 736-746

Fougerouse, D., Micklethwaite, S., Miller, J., McCuaig, T. C., & Ulrich, S. (2013, August). Multistage mineralization of the giant Obuasi gold deposit, Ghana. In *Mineral Deposit Research for a High-Tech World, 12th SGA Biennial Meeting 2013, Proceedings* (Vol. 3, pp. 1105-1108).

Fougerouse, D., Micklethwaite, S., Miller, J., Ulrich, S., & McCuaig, T. C. (2015). WITHDRAWN: The Obuasi gold deposit, Ghana: A West African giant.

Fyfe, W. S., & Kerrich, R. (1976). Geochemical prospecting: extensive versus intensive factors. *Journal of Geochemical Exploration*, *6*(1-2), 177-192.

Gale, G.H., and Roberts, D., (1974). Trace element geochemistry of Norwegian lower Paleozoic basic volcanics and its tectonic implications. Earth Planet. Sci. Lett., 22: pp. 380-390.

Geological map explanation — map sheet 0503 B (1:100000), CGS/BRGM/Geoman, Geological Survey Department of Ghana (GSD). No MSSP/2005/GSD/5a.

Gobashy, M. M., Eldougdoug, A., Abdelwahed, M., Abdelazeem, M., Abd El-Rahman, Y., Abdelhalim, A., & Said, S. (2023). Role of integrated magnetics and geology in tracking and exploring complex structures controlling gold mineralization. Example from the Fawakheir-Atalla Gold Prospects, Eastern Desert, Egypt. *Pure and Applied Geophysics*, *180*(7), 2775-2805.

Gocking, R. (2005). *The history of Ghana*. Greenwood Publishing Group.

Goldfarb, R. J., & Santosh, M. (2014). The dilemma of the Jiaodong gold deposits: Are they unique? *Geoscience Frontiers*, *5*(2), 139-153.

Graham, K. M. (2013). *Geological and structural interpretation of part of the Buem formation, Ghana, using aerogeophysical data* (Doctoral dissertation).

Grant, F. S. (1985). Aeromagnetics, geology and ore environments, I. Magnetite in igneous, sedimentary and metamorphic rocks: an overview. *Geoexploration*, *23*(3), 303-333.

Green, T.H. (1980). Island arc and continent-building magmatism: A review of petrogenetic models based on experimental petrology and geochemistry. Tectonophys, v.63, pp. 367-385.

Griffin, W. L., Belousova, E. A., Walters, S. G., & O'Reilly, S. Y. (2006). Archaean and Proterozoic crustal evolution in the Eastern Succession of the Mt Isa district, Australia: U–Pb and Hf-isotope studies of detrital zircons. *Australian Journal of Earth Sciences*, *53*(1), 125–149.

Griffis, R. J. (1998). Explanatory Notes – Geological Interpretation of Geophysical Data from Southwestern Ghana. Minerals Commission, Accra, 51p

Griffis, R. J., Barning, K., Agezo, F.L. and Akosa, F.K. (2002), Gold Deposits of Ghana, Minerals Commission, Accra, Ghana. 432pp.

Groves, D. and Phillips, N., (1987). The genesis and tectonic control on Archean gold deposits of the Western Australian Shield-- a metamorphic replacement model. Ore Geol. Rev., 2: 287–322.

Groves, D. I., & Santosh, M. (2016). The giant Jiaodong gold province: the key to a unified model for orogenic gold deposits? *Geoscience Frontiers*, *7*(3), 409–417.

Groves, D. I., Santosh, M., & Zhang, L. (2020). A scale-integrated exploration model for orogenic gold deposits based on a mineral system approach. *Geoscience Frontiers*, *11*(3), 719-738.

Grundmann, G., & Scholz, H. (2015). Preparation methods in mineralogy & geology: the preparation of thin sections, polished sections, acetate foil prints. *preparation for elutriation analysis, and staining tests for the optical and electron microscopy.(2015) https://doi. org/10.13140/RG*, *2*(2593.9360).

Gunn, P., 1997, Airborne Magnetic and Radiometric Surveys. AGSO Journal of Australian Geology and geophysics, 17,(2), 216p.

Hammerli, J., Kemp, A. I. S., Barrett, N., Wing, B. A., Roberts, M., Arculus, R. J., Boivin, P., Nude, P. M., & Rankenburg, K. 2017: Sulfur isotope signatures in the lower crust: A SIMS study on S-rich scapolite of granulites. *Chemical Geology*, 454:54–66.

Hart, S. J., Shaffer, R. E., Rose-Pehrsson, S. L., & McDonald, J. R. (2001). Using physics-based modeler outputs to train probabilistic neural networks for unexploded ordnance (UXO) classification in magnetometry surveys. *IEEE Transactions on Geoscience and Remote Sensing*, *39*(4), 797-804.

Hastie, A. R., Kerr, A. C., Pearce, J. A., & Mitchell, S. F. (2007). Classification of altered volcanic island arc rocks using immobile trace elements: development of the Th–Co discrimination diagram. *Journal of petrology*, *48*(12), 2341-2357.

Hinkle, D. E., Wiersma, W., & Jurs, S. G. (2003). Applied statistics for the behavioral sciences. *(No Title)*.

Hirdes, W., Davis, D. W., & Eisenlohr, B. N. (1992). Reassessment of Proterozoic granitoid ages in Ghana on the basis of U/Pb zircon and monazite dating. *Precambrian Research*, *56*(1-2), 89-96.

Hirdes, W., & Nunoo, B. (1994). The Proterozoic paleoplacers at Tarkwa gold mine, SW Ghana: sedimentology, mineralogy, and precise age dating of the Main Reef and West Reef, and bearing of the investigations on source area aspects. *Geologisches Jahrbuch D*, *100*, 247-311.

Hirdes, W., & Davis, D. W. (1998). First U-Pb zircon age of extrusive volcanism in the Birimian Supergroup of Ghana/West Africa. *Journal of African Earth Sciences*, *27*(2), 291-294.

Hirdes, W., Senger, R., Adjei, J., Efa, E., Loh, G. and Tettey, A. (1993). Explanatory notes for the geological map of southwest Ghana. 1:100,000: sheets Wiawso (0603D), Asafo (0603C), Kukuom (0603B), Goaso (0603A), Sunyani (0703D) and Berekum (0703C). Geologisches Jahrbuch B83, 139p. Schweizerbart'sche Vertagsbuchhandlung, Stuttgart.

Hobbs, B.E., Means, W.D. and Williams, P.F. (1976). An Outline of Structural Geology, Wiley, New York, N.Y., 517 pp.

Hofmann, H. J. (1987). PALEOSCENE# 7 Precambrian Biostratigraphy. *Geoscience Canada*, *14*(3), 135-154.

Independent Technical Report of Kibi Gold Project by Xtra Gold Resources Corp, 2012.

Irvine, T. N., & Baragar, W. R. A. (1971). A guide to the chemical classification of the common volcanic rocks. *Canadian journal of earth sciences*, *8*(5), 523-548.

Ji'an, S., Huijuan, J., and Lianhua, X. (1994). Annnalysis on Mechanism of Feldspar Dissolution and Its Influencing Factors in Feldspar-rich Sandstone Reservoir [J]. *Acta Sedimentologica Sinica, 3*.

John, T., Klemd, R., Hirdes, W., & Loh, G. (1999). The metamorphic evolution of the paleoproterozoic (Birimian) volcanic Ashanti belt (Ghana, West Africa). *Precambrian Research*, *98*(1-2), 11-30.

Jones, W. B. (1990). The Buem volcanic and associated sedimentary rocks, Ghana: a field and geochemical investigation. *Journal of African Earth Sciences (and the Middle East)*, *11*(3-4), 373-383.

Junner, N. R. (1932). The geology of the Obuasi Goldfields. *Mem. No. 2 Gold Coast Geol. Surv.*, *43*.

Junner, N. R. (1935). Gold in the Gold Coast‖ Ghana Geological Survey. *Memoir*, *4*(5), 20.

Junner, N.R., 1940. Geology of the Gold Coast and Western Togoland. Gold Coast Geological Survey Bulletin, No. 11, p. 40.

Kalsbeek, F., & Frei, R. (2010). Geochemistry of Precambrian sedimentary rocks used to solve stratigraphical problems: an example from the Neoproterozoic Volta basin, Ghana. *Precambrian Research*, *176*(1-4), 65-76.

Kesse, G. O. (1985). The mineral and rock resources of Ghana.

Kiessling R (1997). Sedimentation and structure in the Tarkwaian group of the Bui Basin in West Ghana. GeolJahrb B, 88:113–182

Koranteng, J. (2019). *Effects of small-scale gold mining on farming in Atiwa West District* (Doctoral dissertation, University of Cape Coast).

Kreuzer, O. P., Buckingham, A., Mortimer, J., Walker, G., Wilde, A., & Appiah, K. (2019). An integrated approach to the search for gold in a mature, data-rich brownfields environment: A case study from Sigma-Lamaque, Quebec. *Ore Geology Reviews*, *111*, 102977.

Kuma, J. S., & Ewusi, E. (2010). Water resources issues in Tarkwa municipality, southwest Ghana. *Ghana Mining Journal*, *11*.

Kuno, H. 1967: Mafic and uitramafic noduh:s from Itinome-gata, Japan, pp. 337-42 in Ultramafic and Related Racier, ed. by P. J. Wyllie. Wiley Press, New York. 4.64 pp.

Kwayisi, D. (2022). *Lithotectonic Evolution of the Buem Structural Unit and Its Relationship to the Suture Zone of the Pan-African Dahomeyide Orogenic Belt, South-Eastern Ghana*. University of Johannesburg (South Africa).

Kwayisi D, Amponsah PO, Agra NA, Nunoo S, Thompson J, Kazapoe RW, Anani CY, Asiedu D, and Nude PM. 2024: Neoproterozoic passive margin formation and evolution during the Rodinia–Gondwana supercontinent cycle at the eastern margin of the West African Craton. Geological Magazine 161(e14): 1–23. https://doi.org/10.1017/S001675682400027X

Kwayisi D, Nyavor E, Dzikunoo EA, Fynn IEM, Kutu J, and Nude PM., 2024: Cryogenian-Ediacaran crustal growth and evolution of the active margin of the Dahomeyide belt, Ghana. Geological Magazine https://doi.org/10.1017/S0016756823000808

Kwayisi, D., Agra, N. A., Dampare, S. B., Asiedu, D. K., Amponsah, P. O., Nude, P. M. 2017: Two suites of gabbros in the Buem Structural Unit, of the Pan-African Dahomeyide orogen, southeastern Ghana: Constraints from new field and geochemical data. *Journal of African Earth Sciences*, 129:45-55.

Large, R. R., Danyushevsky, L., Hollit, C., Maslennikov, V., Meffre, S., Gilbert, S., ... & Foster, J. (2009). Gold and trace element zonation in pyrite using a laser imaging technique: Implications for the timing of gold in orogenic and Carlin-style sediment-hosted deposits. *Economic Geology*, *104*(5), 635-668.

Leube, A., Hirdes, W., Mauer, R., & Kesse, G. O. (1990). The early Proterozoic Birimian Supergroup of Ghana and some aspects of its associated gold mineralization. *Precambrian research*, *46*(1-2), 139-165.

Liégeois, J. P., Latouche, L., Boughrara, M., Navez, J., & Guiraud, M. (2003). The LATEA metacraton (Central Hoggar, Tuareg shield, Algeria): behaviour of an old passive margin during the Pan-African orogeny. *Journal of African Earth Sciences*, *37*(3-4), 161-190.

Loh, G. and Hirdes, W. (1996). Explanatory notes for the geological map of southwest Ghana. sheets Sekondi (0402A) and Axim (0403B). Bulletin 49, 63p. Ghana Geological Survey Department, Accra, Ghana.

Loke, M. H., & Barker, R. D. (1996). Rapid least-squares inversion of apparent resistivity pseudosections by a quasi-Newton method1. *Geophysical prospecting*, *44*(1), 131-152.

Lowell, J. D. (2014). *Intrepid explorer: The autobiography of the world's best mine finder*. University of Arizona Press.

Luo, Y., XUE, D. J., & Wang, M. (2010). Reduction to the pole at the geomagnetic equator. *Chinese Journal of Geophysics*, *53*(6), 1082-1089.

Magalhães, L. A., & Souza Filho, C. R. (2012). Targeting of gold deposits in Amazonian exploration frontiers using knowledge-and data-driven spatial modeling of geophysical, geochemical, and geological data. *Surveys in Geophysics*, *33*(2), 211-241.

Maniar, P. D., & Piccoli, P. M. (1989). Tectonic discrimination of granitoids. *Geological society of America bulletin*, *101*(5), 635-643.

Marston, R. J. (1978). The Geochemistry of Archean clastic sediments in relation to crustal evolution, Northeastern Yilgarn Block, Western Australia. Precambrian Res., 6: pp. 157-175.

Masurel, Q., Eglinger, A., Thébaud, N., Allibone, A., André-Mayer, A. S., McFarlane, H., & Amponsah, P. O. (2022). Paleoproterozoic gold events in the southern West African Craton: review and synopsis. *Mineralium Deposita*, *57*(4), 513-537.

McDonough, W. F., & Sun, S. S. (1995). The composition of the Earth. *Chemical geology*, *120*(3-4), 223-253.

McFaul, S., Xavier, A. M., & Mafu, N. (2013). Supporting mining community development through economic diversification: The adoption of Enterprise Facilitation (EF) in Cobar, Australia. *Sustainable Development in the Minerals Industry*, 14-03.

McLennan, S.M., Nance, W.B. and Taylor, S.R. (1983). Geochemistry of Archaen shales from the Pilbara super group, Western Australia.

McLennan, S.M., (1989). Rare-earth elements in sedimentary rocks: Influence of provenance and sedimentary processes; Rev. Min. 21, pp. 169-200.

Milési, J. P., Ledru, P., Ankrah, P., Johan, V., Marcoux, E., & Vinchon, C. (1991). The metallogenic relationship between Birimian and Tarkwaian gold deposits in Ghana. *Mineralium Deposita*, *26*, 228-238.

Milési, J. P., Ledru, P., Feybesse, J. L., Dommanget, A., & Marcoux, E. (1992). Early Proterozoic ore deposits and tectonics of the Birimian orogenic belt, West Africa. *Precambrian Research*, *58*(1-4), 305-344.

Minty, B. R. S., Luyendyk, A. P. J., & Brodie, R. C. (1997). Calibration and data processing for airborne gamma-ray spectrometry. *AGSO Journal of Australian Geology and Geophysics*, *17*(2), 51-62.

Miyashiro, A. (1974). Volcanic rock series in island arcs and active continental margins. *American journal of science*, *274*(4), 321–355.

Mumin, A. H., Fleet, M. E., & Chryssoulis, S. L. (1994). Gold mineralization in As-rich mesothermal gold ores of the Bogosu-Prestea mining district of the Ashanti gold belt, Ghana: Remobilization of “invisible” gold. *Mineralium Deposita*, *29*, 445-460.

Murtagh, F., & Legendre, P. (2011). Ward's hierarchical clustering method: clustering criterion and agglomerative algorithm. *arXiv preprint arXiv:1111.6285*.

Neuendorf, K. K. (2005). *Glossary of geology*. Springer Science & Business Media.

Milligan, P. R., & Gunn, P. J. (1997). Enhancement and presentation of airborne geophysical data. *AGSO Journal of Australian Geology and Geophysics*, *17*(2), 63-75.

Nesbitt, H. W. & Young, G. M. (1982). Early Proterozoic climates and plate motions inferred from major element chemistry of lutites: Nature, 299, pp. 715 – 717

Neyamadpour, A., Wan Abdullah, W. A. T., Taib, S., & Neyamadpour, B. (2010). Comparison of Wenner and dipole–dipole arrays in the study of an underground three-dimensional cavity. *Journal of Geophysics and Engineering*, *7*(1), 30-40.

Norman, M. D., Leeman, W. P., Blanchard, D. P., Fitton, J. G., & James, D. (1989). Comparison of major and trace element analyses by ICP, XRF, INAA and ID methods. *Geostandards Newsletter*, *13*(2), 283-290.

Ntiamoah-Agyakwa, Y. (1979). Relationship between gold and manganese mineralizations in the Birimian of Ghana, West Africa. *Geological Magazine*, *116*(5), 345-352.

Nude P. M. Kwayisi, D. Taki, N. A, Kutu, J. M., Anani, C., Banoeng-Yakubo, B, & Asiedu, D. K: 2015: Petrography and chemical evidence for multi-stage emplacement of western Buem volcanic rocks in the Dahomeyide orogenic belt, southeastern Ghana, West Africa. *Journal of African Earth Science,* 112: 314-327.

Nude, P. M., Asigri, J. M., Yidana, S. M., Arhin, E., Foli, G., & Kutu, J. M. 2012. Identifying pathfinder elements for gold in multi-element soil geochemical data from the Wa-Lawra belt, northwest Ghana: A multivariate statistical approach. *International Journal of Geosciences,* 3, 62-70.

Nude, P. M., Shervais, J. W. Attoh, K. & Foli, G. 2012. Petrological and geochemical characteristics of mafic granulites associated with alkaline rocks in the Pan-African Dahomeyide suture zone, southeastern Ghana. *In* Ali Ismail Al-Juboury (ed.), *Petrology-New Perspectives and Applications.* ISBN978-953-307-424-5, 21-38.

Nude, P. M., Shervais, J. W., Attoh, K., Vetter, S. K.& Burton, C. 2009. Petrology and geochemistry of nepheline syenite and related carbonate-rich rocks in the Pan African Dahomeyide orogen, southeastern Ghana, West Africa. *Journal of African Earth Sciences,* 55: 147-157.

Nwazelibe, V. E., Unigwe, C. O., & Egbueri, J. C. (2023). Integration and comparison of algorithmic weight of evidence and logistic regression in landslide susceptibility mapping of the orumba north erosion-prone region, nigeria. *Modeling Earth Systems and Environment*, *9*(1), 967-986.

Oberthür, T., Hirdes, W., Höhndorf, A., Schmidt Mumm, A., Vetter, U., Weiser, T., & Loh, G. (1995). A review of gold mineralisation in the Ashanti Belt of Ghana and its relation to the crustal evolution of the terrane. *Communications of the Geological Survey of Namibia*, *10*, 121-127.

Oberthür, T., Hirdes, W., Höhndorf, A., Schmidt Mumm, A., Vetter, U., Weiser, T., & Loh, G. (1995). A review of gold mineralisation in the Ashanti Belt of Ghana and its relation to the crustal evolution of the terrane. *Communications of the Geological Survey of Namibia*, *10*, 121-127.

Oberthür, T., Vetter, U., Davis, D. W., &Amanor, J. A. (1998). Age constraints on gold mineralization and Paleoproterozoic crustal evolution in the Ashanti belt of southern Ghana. *Precambrian Research*, *89*(3-4), 129-143.

Oberthür, T., Vetter, U., Davis, D. W., &Amanor, J. A. (1998). Age constraints on gold mineralization and Paleoproterozoic crustal evolution in the Ashanti belt of southern Ghana. *Precambrian Research*, *89*(3-4), 129-143.

Oberthür, T., Weiser, T., Amanor, J. A., & Chryssoulis, S. L. (1997). Mineralogical siting and distribution of gold in quartz veins and sulfide ores of the Ashanti mine and other deposits in the Ashanti belt of Ghana: genetic implications. *Mineralium Deposita*, *32*, 2-15.

Osae, S., Asiedu, D. K., Banoeng-Yakubo, B., Koeberl, C., & Dampare, S. B. (2006). Provenance and tectonic setting of Late Proterozoic Buem sandstones of southeastern Ghana: Evidence from geochemistry and detrital modes. *Journal of African Earth Sciences*, *44*(1), 85-96.

Pande, C. B., & Moharir, K. (2018). Spatial analysis of groundwater quality mapping in hard rock area in the Akola and Buldhana districts of Maharashtra, India. *Applied Water Science*, *8*, 1-17.

Parra-Avila, L. A., Bourassa, Y., Miller, J., Perrouty, S., Fiorentini, M. L., & McCuaig, T. C. (2015). Age constraints of the Wassa and Benso mesothermal gold deposits, Ashanti belt, Ghana, West Africa. *Journal of African Earth Sciences*, *112*, 524-535.

Pašteka, R., Kušnirák, D., & Karcol, R. (2018). Matlab tool REGCONT2: effective source depth estimation by means of Tikhonov's regularized downwards continuation of potential fields. *Contributions to Geophysics and Geodesy*, *48*(3), 231-254

Pearce, J. A. (1996). A user's guide to basalt discrimination diagrams. *Trace element geochemistry of volcanic rocks: applications for massive sulphide exploration. Geological Association of Canada, Short Course Notes*, *12*(79), 113.

Pearce, J. A., & Cann, J. R. (1973). Tectonic setting of basic volcanic rocks determined using trace element analyses. *Earth and planetary science letters*, *19*(2), 290-300.

Pearce, J. A., Harris, N. B. W. and Tindle, A. G. (1984). Trace element discrimination diagrams for the inetrpretation of granitic rocks. Journal of Petrology. 25, 956- 983.

Perri, F., Borrelli, L., Critelli, S., & Gullà, G. (2012). Investigation of weathering rates and processes affecting plutonic and metamorphic rocks in Sila Massif (Calabria, southern Italy). *Rendiconti Online della Società Geologica Italiana*, *21*, 557-559.

Perrouty, S., Aillères, L., Jessell, M. W., Baratoux, L., Bourassa, Y., & Crawford, B. (2012). Revised Eburnean geodynamic evolution of the gold-rich southern Ashanti Belt, Ghana, with new field and geophysical evidence of pre-Tarkwaian deformations. *Precambrian Research*, *204*, 12-39.

Perrouty, S., Jessell, M. W., Bourassa, Y., Miller, J., Apau, D., Siebenaller, L., ... & Salvi, S. (2015). The Wassa deposit: a poly-deformed orogenic gold system in southwest Ghana–implications for regional exploration. *Journal of African Earth Sciences*, *112*, 536-547.

Perrouty, S., Lindsay, M. D., Jessell, M. W., Aillères, L., Martin, R., & Bourassa, Y. (2014). 3D modeling of the Ashanti Belt, southwest Ghana: Evidence for a litho-stratigraphic control on gold occurrences within the BirimianSefwi Group. *Ore Geology Reviews*, *63*, 252-264.

Petersson, A., Scherstén, A., & Gerdes, A. (2018). Extensive reworking of Archaean crust within the Birimian terrane in Ghana as revealed by combined zircon U-Pb and Lu-Hf isotopes. *Geoscience Frontiers*, *9*(1), 173-189.

Pettijohn, F.J. (1963). Chemical Compositions of Sandstones- Excluding Carbonate and Volcanic Sands: Geol.Soc. America Bull., v.70, p. 593-600.

Pettijohn, F.J. (1972). The Achaean of the Canadian Shield: résumé. Geol. Soc. Am. Mem., 135: pp. 131-149.

Pettijohn, F. J., Potter, P. E., and Siever, R. (2012). *Sand and sandstone*. Springer Science & Business Media.

Phillips, J. D., 1997. Potential-Field Geophysical Software for the PC, version 2.2: U.S. Geological Survey Open-File Report 97-725.

Pigois, J. P., Groves, D. I., Fletcher, I. R., McNaughton, N. J., &Snee, L. W. (2003). Age constraints on Tarkwaian palaeoplacer and lode-gold formation in the Tarkwa-Damang district, SW Ghana. *Mineralium Deposita*, *38*, 695-714.

Pitcairn, I. K., Teagle, D. A., Craw, D., Olivo, G. R., Kerrich, R., & Brewer, T. S. (2006). Sources of metals and fluids in orogenic gold deposits: insights from the Otago and Alpine Schists, New Zealand. *Economic Geology*, *101*(8), 1525-1546.

Potter, P. E. (1978). Petrology and chemistry of modern big river sands. The Journal of Geology, 86(4), 423-449.

Purucker, M., & Whaler, K. (2007). Crustal magnetism. *Treatise on geophysics*, *5*, 195-237.

Qari, M. Y. H. (1989). Lithological mapping and structural analysis of Proterozoic rocks in part of the southern Arabian Shield using Landsat images. *International Journal of Remote Sensing*, *10*(3), 499-503.

Rae, J. Griffis R.J., AgymangK. (2006). Evaluation of the Kwabeng, Pameng and Apampam. Alluvial deposits. Report Prepared for Xtra-Gold Resources Corporation.Unpublished report.

Reeves, G. D., Baker, D. N., Belian, R. D., Blake, J. B., Cayton, T. E., Fennell, J. F., & Spence, H. E. (1998). The global response of relativistic radiation belt electrons to the January 1997 magnetic cloud. *Geophysical Research Letters*, *25*(17), 3265-3268.

Reeves, C.V., Reford, S.W., and Milligan, P.R., (1997). Airborne Geophysics: Old methods, new images in Gubbins, A.G.(Ed.) Proceedings of Exploration 97, Fourth Decennial International Conference on Mineral Exploration, pp. 13-30.

Robert, F., Brommecker, R., Bourne, B.T., Dobak, P.J., McEwan, C.J., Rowe, R.R., Zhou, X. (2007). Models and exploration methods for major gold deposit types, ore deposits and exploration technology. In: Milkereit, B. (Ed.), Proceedings of the 5th Decennial International Conference on Mineral Exploration (Exploration '07),, 48. Ore Deposits and Exploration Technology, pp. 691–71.

Rollinson, H. (1993). Using geochemical data. *Evaluation, presentation, interpretation*, *1*, 23-89.

Roser, B. P., Cooper, R. A., Nathan, S., & Tulloch, A. J. (1996). Reconnaissance sandstone geochemistry, provenance, and tectonic setting of the lower Paleozoic terranes of the West Coast and Nelson, New Zealand. *New Zealand Journal of Geology and Geophysics*, *39*(1), 1-16.

Roser, B. P., & Korsch, R. J. (1988). Provenance signatures of sandstone-mudstone suites determined using discriminant function analysis of major-element data. *Chemical geology*, *67*(1-2), 119-139.

Saccani, E. (2015). A new method of discriminating different types of post-Archean ophiolitic basalts and their tectonic significance using Th-Nb and Ce-Dy-Yb systematics. Geoscience Frontiers 6:481–501. http://dx.doi.org/10.1016/j.gsf.2014.03.006.

Sakyi, P. A., Manu, J., Su, B. X., Kwayisi, D., Nude, P. M., &Dampare, S. B. (2019). Geochemical and Sm–Nd isotopic evidence for the composition of the Palaeoproterozoic crust of the West African Craton in Ghana. *Geological Journal*, *54*(6), 3940-3957.

Sasaki, Y. (1992). Resolution of resistivity tomography inferred from numerical SIMULATION1. *Geophysical prospecting*, *40*(4), 453-463.

Saunders, J. A., Prikryl, J. D., & Posey, H. H. (1988). Mineralogic and isotopic constraints on the origin of strontium-rich cap rock, Tatum dome, Mississippi, USA. *Chemical geology*, *74*(1-2), 137-152.

Sawyer, E.W. (1986). The influence of source rock type, chemical weathering and sorting on the geochemistry of clastic sediments from the Quetico metasedimentary belt, Superior Province, Canada; Chem. Geol. 55; pp. 77-95.

Schonlau, M. (2004). Visualizing non-hierarchical and hierarchical cluster analyses with clustergrams. *Computational Statistics*, *19*, 95-111.

Schreiber, D. W., Fontbote, L., & Lochmann, D. (1990). Geologic setting, paragenesis, and physicochemistry of gold quartz veins hosted by plutonic rocks in the Pataz region. *Economic Geology*, *85*(7), 1328-1347.

Sestini, G. (1973). Sedimentology of a Paleoplacer: The Gold-bearingTarkwaian of Ghana. In *Ores in Sediments: VIII. International Sedimentological Congress, Heidelberg, August 31–September 3, 1971* (pp. 275-305). Berlin, Heidelberg: Springer Berlin Heidelberg.

Shervais, J. W. (1982). Ti-V plots and the petrogenesis of modern and ophiolitic lavas. *Earth and planetary science letters*, *59*(1), 101-118.

Shervais, J. W., & Jean, M. M. (2012). Inside the subduction factory: Modeling fluid mobile element enrichment in the mantle wedge above a subduction zone. *Geochimica et Cosmochimica Acta*, *95*, 270-285.

Sillitoe, R. H., & Thompson, J. F. (1998). Intrusion–Related Vein Gold Deposits: Types, Tectono-Magmatic Settings and Difficulties of Distinction from Orogenic Gold Deposits. *Resource Geology*, *48*(4), 237-250.

Silva, A. M., Pires, A. C. B., Mccafferty, A., de Moraes, R. A. V., & Xia, H. (2003). Application of airborne geophysical data to mineral exploration in the uneven exposed terrains of the Rio Das Velhas greenstone belt. *Brazilian Journal of Geology*, *33*(2), 17-28.

Simon, M.S., Amanor J. and Byrne D. (2012). Independent Technical Report on Apapam Concession, Xtra Gold Project Eastern Region (2013). Unpublished Report.

Smith, A. J., Henry, G., & Frost-Killian, S. (2016). A review of the Birimian Supergroup-and Tarkwaian Group-hosted gold deposits of Ghana. *Episodes Journal of International Geoscience*, *39*(2), 177-197.

Strogen P (1991). The sedimentology, stratigraphy and structure of the Tarkwaian, western region, and its relevance to gold exploration and development. In: Kesse, GO (ed) Proceedings of the International Conference on the Geology of Ghana, Geological Society of Ghana, Accra, 3 R1-R39.

Sun, S. S., & McDonough, W. F. (1989). Chemical and isotopic systematics of oceanic basalts: implications for mantle composition and processes. *Geological Society, London, Special Publications*, *42*(1), 313-345.

Sun, S. S. (1980). Lead isotopic study of young volcanic rocks from mid-ocean ridges, ocean islands and island arcs. *Philosophical Transactions of the Royal Society of London. Series A, Mathematical and Physical Sciences*, *297*(1431), 409-445.

Sylvester, P. J., & Attoh, K. (1992). Lithostratigraphy and composition of 2.1 Ga greenstone belts of the West African Craton and their bearing on crustal evolution and the Archean-Proterozoic boundary. *The Journal of Geology*, *100*(4), 377-393.

Tairou, M. S., Affaton, P., Anum, S., & Fleury, J. (2012). Pan-African paleostresses and reactivation of the Eburnean basement complex in Southeast Ghana (West Africa). *Journal of Geological Research*, *2012*.

Taylor, S.R. & McLennan, S.M. (1995). The geochemical evolution of the continental crust. Review Geophysics, 33, p. 241-265.

Taylor, P. N., Moorbath, S., Leube, A., & Hirdes, W. (1992). Early Proterozoic crustal evolution in the Birimian of Ghana: constraints from geochronology and isotope geochemistry. *Precambrian research*, *56*(1-2), 97-111.

Telford, W.M., Geldart, L.P., Sheriff, R.E. (1990). Applied geophysics, 2nd edn. Cambridge University Press.

Toulmin III, P., & Barton Jr, P. B. (1964). A thermodynamic study of pyrite and pyrrhotite. *Geochimica et Cosmochimica Acta*, *28*(5), 641-671.

Tunks, A., Selley, D., Rogers, J., Brabham, G. (2004). Vein mineralization at the damang gold mine, ghana: controls on mineralization. Journal of Structural Geology 26, 1257–1273.

Voicu, G., & Bardoux, M. (2002). Geochemical behavior under tropical weathering of the Barama–Mazaruni greenstone belt at Omai gold mine, Guiana Shield. *Applied Geochemistry*, *17*(3), 321-336.

Voicu, G., Bardoux, M., & Voicu, D. (1997). Mineralogical norm calculations applied to tropical weathering profiles. *Mineralogical Magazine*, *61*(405), 185-196.

Volesky, J. C., Stern, R. J., & Johnson, P. R. (2003). Geological control of massive sulfide mineralization in the Neoproterozoic Wadi Bidah shear zone, southwestern Saudi Arabia, inferences from orbital remote sensing and field studies. *Precambrian Research*, *123*(2-4), 235-247.

Wang, B.Q., Wang, W. and Zhou, M.F. (2013). Provenance and Tectonic Setting of the Triassic Yidun Group, The Yidun Terrane, Tibet. Geoscience Frontiers 4, 765–777.

Ward, W.T. Geology, geomorphology, and soils of the South-western part of County Adelaide, South Australia. Melbourne, Vic.: CSIRO; 1966. legacy:3359. https://doi.org/10.25919/5db33828b9852

Whiting, T. H. (1986). Aeromagnetics as an aid to geological mapping—a case history from the Arunta Inlier, Northern Territory. *Australian Journal of Earth Sciences*, *33*(2), 271-286.

Wilford, J. R., Bierwirth, P. E., & Craig, M. A. (1997). Application of airborne gamma-ray spectrometry in soil/regolith mapping and applied geomorphology. *AGSO Journal of Australian Geology and Geophysics*, *17*(2), 201-216.

Wilson, M. (1989). Igneous Petrogenesis, A Global Tectonic Approach. Unwin Hyman, London, 400 p

Winchester, J. A., & Floyd, P. A. (1977). Geochemical discrimination of different magma series and their differentiation products using immobile elements. *Chemical geology*, *20*, 325-343.

Wrafter , J. P., & Graham, J. R. (1989). Short paper: ophiolitic detritus in the Ordovician sediments of South Mayo, Ireland. *Journal of the Geological Society*, *146*(2), 213-215.

Wright, J. B., Hastings, D. A., Jones, W. B., & Williams, H. R. (1985). *Geology and mineral resources of West Africa* (Vol. 187). London: Allen & Unwin.

Wood, D.A. (1980). The application of a Th-Hf-Ta diagram to the problems of tectonomagmatic classification and to establishing the nature of crustal contamination of basaltic lavas of the British Tertiary volcanic province. Earth and Planetary Science Letters 50, 11-30.

Wronkiewicz, D. J., & Condie, K. C. (1990). Geochemistry and mineralogy of sediments from the Ventersdorp and Transvaal Supergroups, South Africa: cratonic evolution during the early Proterozoic. *Geochimica et Cosmochimica Acta*, *54*(2), 343-354.

Wyman, D. A., O'Neill, C., & Ayer, J. A. (2008). Evidence for modern-style subduction to 3.1 Ga: a plateau–adakite–gold (diamond) association. *When did plate tectonics begin on planet Earth*, *440*, 129-148.

Yao, Y., & Robb, L. J. (2000). Gold mineralization in Palaeoproterozoic granitoids at Obuasi, Ashanti region, Ghana: Ore geology, geochemistry and fluid characteristics. *South African Journal of Geology*, *103*(3-4), 255-278.

Yao, Y., Murphy, P. J., & Robb, L. J. (2001). Fluid characteristics of granitoid-hosted gold deposits in the Birimian Terrane of Ghana: a fluid inclusion microthermometric and Raman spectroscopic study. *Economic Geology*, *96*(7), 1611-1643.

Yiridomoh, G. Y. (2021). "Illegal" gold mining operations in Ghana: Implication for climate-smart agriculture in northwestern Ghana. *Frontiers in Sustainable Food Systems*, *5*, 745317.

Yuan, S., Williams-Jones, A. E., Mao, J., Zhao, P., Yan, C., & Zhang, D. (2018). The origin of the Zhangjialong tungsten deposit, South China: Implications for W-Sn mineralization in large granite batholiths. *Economic Geology*, *113*(5), 1193-1208.

Yücel, C., Arslan, M., Temizel, I., Yazar, E. A., & Ruffet, G. (2017). Evolution of K-rich magmas derived from a net veined lithospheric mantle in an ongoing extensional setting: Geochronology and geochemistry of Eocene and Miocene volcanic rocks from Eastern Pontides (Turkey). *Gondwana Research*, *45*, 65-86.

Zhang, C., Lü, Q., Yan, J., & Qi, G. (2018). Numerical solutions of the mean-value theorem: New methods for downward continuation of potential fields. *Geophysical Research Letters*, *45*(8), 3461-3470.

Zheng, Y. F., Zhao, Z. F., & Chen, R. X. (2019). Ultrahigh-pressure metamorphic rocks in the Dabie–Sulu orogenic belt: compositional inheritance and metamorphic modification. *Geological Society, London, Special Publications*, *474*(1), 89-132.

Zouaghi, T. (2020). Potential mineral occurrences from airborne geophysical and satellite image data, case study in Asir terrane, Arabian Shield. *IOSR J. Appl. Geol. Geophys.*, *8*(2 Ser. II), 42-52.

Zouaghi, T., & Harbi, H. (2022). Airborne geophysics and remote sensing of an Nimas-Khadra area, southern Arabian shield: New insights into structural framework and mineral occurrences. *Advances in Space Research*, *70*(11), 3649-3673.